Gas Turbine Laboratory
Department of Aeronautics and Astronautics
Massachusetts Institute of Technology
Cambridge, MA 02139

Final Technical Report
on AFOSR Grant #F49620-03-1-0309

entitled

ASPIRATED HIGH PRESSURE COMPRESSOR

submitted to

LTC R. Jefferies
Air Force Office of Scientific Research/NA
875 North Randolph Street
Suite 325, Room 3112
Arlington, VA 22203-1768

INVESTIGATORS: Alan. H. Epstein (PI)
R.C. Maclaurin Professor of Aeronautics and Astronautics
Director, Gas Turbine Laboratory

Jack L. Kerrebrock
Professor Emeritus

PERIOD OF
INVESTIGATION: May 1, 2003 – August 31, 2005

August 2006

20061102512

RECEIVED AUG 1 [illegible] 2006

REPORT DOCUMENTATION PAGE

Form Approved
OMB No. 0704-0188

The public reporting burden for this collection of information is estimated to average 1 hour per response, including the time for reviewing instructions, searching existing data sources, gathering and maintaining the data needed, and completing and reviewing the collection of information. Send comments regarding this burden estimate or any other aspect of this collection of information, including suggestions for reducing the burden, to the Department of Defense, Executive Services and Communications Directorate (0704-0188). Respondents should be aware that notwithstanding any other provision of law, no person shall be subject to any penalty for failing to comply with a collection of information if it does not display a currently valid OMB control number.
PLEASE DO NOT RETURN YOUR FORM TO THE ABOVE ORGANIZATION.

1. REPORT DATE *(DD-MM-YYYY)*	2. REPORT TYPE	3. DATES COVERED *(From - To)*
80-08-2006	Final Technical Report	05-01-2003 - 31-08-2005

4. TITLE AND SUBTITLE
Aspirated High Pressure Compressor

5a. CONTRACT NUMBER

5b. GRANT NUMBER
F49620-03-1-0309

5c. PROGRAM ELEMENT NUMBER

6. AUTHOR(S)
Epstein, Alan H., Professor
Guenette, Gerald R., Dr.
Kerrebrock, Jack L., Professor
Merchant, Ali A., Dr.
Neumayer, Fritz, Dr.
Onnee, Jean-Francois
Parker, David V.

5d. PROJECT NUMBER

5e. TASK NUMBER

5f. WORK UNIT NUMBER

7. PERFORMING ORGANIZATION NAME(S) AND ADDRESS(ES)
Massachusetts Institute of Technology
Department of Aeronautics & Astronautics, Gas Turbine Laboratory, 31-266
77 Massachusetts Avenue,
Cambridge, Massachusetts 02139

8. PERFORMING ORGANIZATION REPORT NUMBER

9. SPONSORING/MONITORING AGENCY NAME(S) AND ADDRESS(ES)
Rhett Jefferies, LtCol, USAF
AFOSR/NA
875 North Randolph Street, Suite 325 Room 3112
Arlington, VA 22203-1768

10. SPONSOR/MONITOR'S ACRONYM(S)

11. SPONSOR/MONITOR'S REPORT NUMBER(S)

12. DISTRIBUTION/AVAILABILITY STATEMENT
unlimited

AFRL-SR-AR-TR-06-0447

13. SUPPLEMENTARY NOTES
none

14. ABSTRACT

The design and test of a two-stage, vane less, aspirated counter-rotating fan is presented in this paper. The fan nominal design objectives were a pressure ratio of 3:1 and adiabatic efficiency of 87%. A pressure ratio of 2.9 at 89% efficiency was measured in the tests. The configuration consists of a counter-swirl-producing inlet guide vane, followed by a high tip speed (1450 feet/sec) non-aspirated rotor, and a counter-rotating low speed (1150 feet/sec) aspirated rotor. The lower tip speed and lower solidity of the second rotor results in a blade loading above conventional limits, but enables a balance between the shock loss and viscous boundary layer loss, the latter of which can be controlled by aspiration. The aspiration slot on the second rotor suction surface extends from the hub up to 80% span, with a conventional tip clearance, and the bleed flow is discharged at the hub. The fan was tested in a short duration blow down facility. Particular attention was given to the design of the instrumentation to obtain efficiency measurements

15. SUBJECT TERMS
flow control, compressor, counter-rotating fan, turbomachinery

16. SECURITY CLASSIFICATION OF:			17. LIMITATION OF ABSTRACT	18. NUMBER OF PAGES	19a. NAME OF RESPONSIBLE PERSON
a. REPORT	b. ABSTRACT	c. THIS PAGE	UU	320	Professor Alan H. Epstein
					19b. TELEPHONE NUMBER *(Include area code)* 617-253-2485

Standard Form 298 (Rev. 8/98)
Prescribed by ANSI Std. Z39.18

[illegible] STATEMENT A
Approved for Public Release
Distribution Unlimited

ABSTRACT (continued from Block14)

within 0.5 percentage points. High response static pressure measurements were taken between the rotors and downstream of the fan to determine the stall behavior. Pressure ratio, mass flow, and efficiency on speed lines from 90% to 102% of the design speed are presented and discussed along with comparison to CFD predictions and design intent. The results presented here complement those presented earlier for two aspirated fan stages with tip shrouds, extending the validated design space for aspirated compressors to include designs with conventional unshrouded rotors and with inward removal of the aspirated flow.

EXECUTIVE SUMMARY

An MIT-NASA team has designed and successfully tested the first two-stage, vaneless, aspirated counter-rotating fan. This work is the last element of a DARPA-sponsored program at the MIT Gas Turbine Laboratory to develop and validate the technology for design of axial compressors that incorporates control of flow separation by aspiration (or suction) of the viscous flows at diffusion-limited locations.

Prior to the work reported here, two aspirated single-stage fans were designed and tested in earlier phases of the program. The first was a transport engine aspirated transonic fan stage, with a pressure ratio of 1.6 at a tip speed of only 750 feet/sec (about 1/2 the speed of conventional fans). The second, high tip speed, stage was designed and tested to assess the feasibility of similarly high loading at a tip speed of 1,500 ft/sec and was designed as a single-stage replacement for the 3-stage F100 (F-15 engine) fan. Rotor-tip shrouds were used in these designs for two reasons: first, to enable an assessment of the benefits of aspiration without the complications of tip clearance flows, and second, to provide a practical means in a first-stage configuration for transporting the aspirated flow outwards from the suction slots on the rotor blades to the rotor housing. Both fan stages validated the concept of aspiration by approximately doubling the stage work over that achievable in a similar stage without aspiration. They also validated the design system as a means for designing aspirated compressors with unusual design parameters, without prior empirical knowledge.

The new proposition addressed here is that aspiration offers additional benefits in application to compressors, either fans or cores, with counter-rotating blade rows, because of the high levels of work enabled by the swirl that enters the second rotor of a pair. This high work results in high aerodynamic loading and high Mach number in the second blade row of such counter-rotating pairs, both of which lead to diffusion problems that can be addressed with aspiration. The result is a potential for higher pressure ratios with fewer blade rows, hence either shorter and lighter compressors or compressors that meet unusual needs.

A configuration of special interest in this context is the counter-rotating fan studied here. It consists of a counter-swirl-producing inlet guide vane, followed by a high tip speed (1450 feet/sec) non-aspirated rotor, and a counter-rotating low speed (1150 feet/sec) aspirated rotor. There are no stators. The lower tip speed of the second rotor results in a blade loading above conventional limits, but delivers a good balance between the shock loss and viscous boundary layer loss, both of which can be controlled by aspiration. In the context of such counter-rotating fans, viscous flow control via aspiration enables the design of high work, compact, and efficient compression systems that are not possible without such viscous flow control. Applications for such fans may be found in variable-cycle engines for multi-mission aircraft and in high-supersonic cruise aircraft. The particular engine design space explored here was that suggested by the General Electric Company based on an advanced military engine concept intended for high speed flight. The resultant high flight temperatures make tip shrouds mechanically difficult to implement, so this is the first unshrouded aspirated compressor which demonstrated the viability of hub discharge of the aspirated flow.

The fan nominal design objectives were a pressure ratio of 3:1 and adiabatic efficiency of 87%. A pressure ratio of 2.9 at 89% efficiency was measured in the tests.

The configuration consists of a counter-swirl-producing inlet guide vane, followed by a high tip speed (1450 feet/sec) non-aspirated rotor, and a counter-rotating low speed (1150 feet/sec) aspirated rotor. The lower tip speed and lower solidity of the second rotor results in a blade loading above conventional limits, but enables a balance between the shock loss and viscous boundary layer loss, the latter of which can be controlled by aspiration. The aspiration slot on the second rotor suction surface extends from the hub up to 80% span, with a conventional tip clearance, and the bleed flow is discharged at the hub. The fan was tested in a short duration blowdown facility. Particular attention was given to the design of the instrumentation to obtain efficiency measurements within 0.5 percentage points. High response static pressure measurements were taken between the rotors and downstream of the fan to determine the stall behavior. Pressure ratio, mass flow, and efficiency on speedlines from 90% to 102% of the design speed are presented and discussed along with comparison to CFD predictions and design intent. The results presented here complement those presented earlier for two aspirated fan stages with tip shrouds, extending the validated design space for aspirated compressors to include designs with conventional unshrouded rotors and with inward removal of the aspirated flow.

The research performed in this program is detailed in the following sections. A technical overview is first presented in the form of a technical paper. The detailed design, analysis, and test results are then present in two theses.

Proceedings of GT2006
ASME Turbo Expo 2006: Power for Land, Sea and Air
May 8-11, 2006, Barcelona, Spain

GT2006-90582

DESIGN AND TEST OF AN ASPIRATED COUNTER-ROTATING FAN

Jack L. Kerrebrock, Alan H. Epstein, Ali A. Merchant, Gerald R. Guenette, David Parker, Jean-Francois Onnee, Fritz Neumayer
Gas Turbine Laboratory
Massachusetts Institute of Technology
Cambridge, Massachusetts 02139, USA

John J. Adamczyk
NASA-Glenn Research Center
Cleveland, Ohio 44135, USA

Aamir Shabbir
University of Toledo
Toledo, Ohio 43606, USA

ABSTRACT

The design and test of a two-stage, vaneless, aspirated counter-rotating fan is presented in this paper. The fan nominal design objectives were a pressure ratio of 3:1 and adiabatic efficiency of 87%. A pressure ratio of 2.9 at 89% efficiency was measured in the tests. The configuration consists of a counter-swirl-producing inlet guide vane, followed by a high tip speed (1450 feet/sec) non-aspirated rotor, and a counter-rotating low speed (1150 feet/sec) aspirated rotor. The lower tip speed and lower solidity of the second rotor results in a blade loading above conventional limits, but enables a balance between the shock loss and viscous boundary layer loss, the latter of which can be controlled by aspiration. The aspiration slot on the second rotor suction surface extends from the hub up to 80% span, with a conventional tip clearance, and the bleed flow is discharged at the hub. The fan was tested in a short duration blowdown facility. Particular attention was given to the design of the instrumentation to obtain efficiency measurements within 0.5 percentage points. High response static pressure measurements were taken between the rotors and downstream of the fan to determine the stall behavior. Pressure ratio, mass flow, and efficiency on speedlines from 90% to 102% of the design speed are presented and discussed along with comparison to CFD predictions and design intent. The results presented here complement those presented earlier for two aspirated fan stages with tip shrouds, extending the validated design space for aspirated compressors to include designs with conventional unshrouded rotors and with inward removal of the aspirated flow.

INTRODUCTION

The work reported here is the latest element of a program being conducted by the MIT Gas Turbine Laboratory and its collaborators to develop and validate the technology for design of axial compressors that incorporates control of flow separation by aspiration (or suction) of the viscous flows at diffusion-limited locations. Prior to the work reported here, two aspirated single-stage fans were designed and tested. The first was a transport engine aspirated transonic fan stage, with a pressure ratio of 1.6 at a tip speed of only 750 feet/sec. It was designed and tested in the Blowdown Compressor at MIT as a first step in assessing the utility of aspiration for increasing stage loading [1]. A second, high tip speed, stage was designed and tested at NASA Glenn Research Center to assess the feasibility of similarly high loading at a tip speed of 1,500 ft/sec [2]. Rotor-tip shrouds were used in these designs for two reasons: first, to enable an assessment of the benefits of aspiration without the complications of tip clearance flows, and second, to provide a practical means in a first-stage configuration for transporting the aspirated flow outwards from the suction slots on the rotor blades to the rotor housing. Both fan stages validated the concept of aspiration by approximately doubling the stage work over that achievable in a similar stage without aspiration. They also validated the design system as a means for designing aspirated compressors with unusual design parameters, without prior empirical knowledge [3].

The new proposition addressed here is that aspiration offers additional benefits in application to compressors, either fans or cores, with counter-rotating blade rows, because of the high levels of work enabled by the swirl that enters the second rotor of a pair. This high work results in high aerodynamic loading and high Mach number in the second blade row of such counter-rotating pairs, both of which lead to diffusion problems that can be addressed with aspiration. The result is a potential for higher pressure ratios with fewer blade rows, hence either shorter and lighter compressors or compressors that meet unusual needs.

A configuration of special interest in this context is the counter-rotating fan studied here. It consists of a counter-swirl-producing inlet guide vane, followed by a high tip speed (1450 feet/sec) non-aspirated rotor, and a counter-rotating low speed (1150 feet/sec) aspirated rotor. There are no stators. The lower tip speed of the second rotor results in a blade loading above conventional limits, but delivers a good balance between the shock loss and viscous boundary layer loss, both of which can be controlled by aspiration. In the context of such counter-

rotating fans, viscous flow control via aspiration enables the design of high work, compact, and efficient compression systems that are not possible without such viscous flow control. Applications for such fans may be found in variable-cycle engines for multi-mission aircraft and in high-supersonic cruise aircraft [4,5].

Such counter-rotating configurations are not readily configured with tip shrouds, in part because of high temperatures in some potential applications, so the rotors were designed with conventional tip clearance and with provision for discharging the aspirated flow from the second rotor inward, rather than outward as in the previous aspirated stages. In addition to meeting the needs of potential applications, this choice enables a generic assessment of the feasibility of such inward discharge, which in general is desirable for energy recovery from the aspirated flow.

To minimize the time and cost of testing the counter-rotating fan, which will be described in more detail below, the evaluation has been carried out in a short test duration blowdown facility at MIT. As discussed in more detail below, the several hundred milliseconds test duration of this facility enables evaluation of the performance of the compressor in terms of its pressure ratio, mass flow, and efficiency by means of conventional instrumentation such as is used in continuously operating test facilities. The key requirement is for thermocouple response fast enough to achieve essentially steady measurements during the blowdown time. All temperature measurements reported here meet this requirement. Therefore the measurements of pressure ratio, mass flow, and efficiency are directly comparable to those that would be obtained for the same configuration in a steady test facility.

Efficiency being an important component of such a comparison, it is important to note that in this paper, to isolate the effect of aspiration on efficiency, we quote the through-flow adiabatic efficiency. Specifically, this is the adiabatic efficiency of the compressor based on the stator (or rotor) outflow. This through-flow efficiency includes the effects of shock losses in the core flow and viscous losses that influence the entropy of the outflow of the compressor. It does not embrace the effects of losses that raise the entropy of the aspirated flow, or the work associated with it. The overall impact of these (secondary) effects of aspiration can be properly quantified only in the context of a complete engine design, in which the handling of the aspirated flows is explicated. Merchant *et al.* [6] qualitatively explore the key issues of aspiration on the engine efficiency, and Kirtley *et al.* [7] has also examined the impact of flow control in the context of efficiency of multistage compressors. This said, we do comment on the impact of bleed on efficiency later in the paper.

The structure of the remainder of this paper is as follows. The aerodynamic design is summarized first, followed by a brief description of the mechanical design of the stage and facility. The overall compressor performance is discussed and compared with the predictions of multi-stage CFD analyses. The operability and off-design behavior is discussed briefly. Lastly, the important conclusions and implications of the results of the test program are enumerated.

AERODYNAMIC DESIGN

The nominal design objectives for the counter-rotating fan based on engine concept studies are presented in Table 1. The desired pressure ratio was 3:1 with an adiabatic efficiency goal of 87%. The RPM ratio for the rotors was approximately 0.8, and the corresponding tip speed ranges are given in the table. The design point stall margin was 20%. An inlet guide vane was included in the engine concept for off-design operation, and this was exploited in optimizing the performance at the design point. The exit swirl from the second rotor was constrained to less than 15 deg, consistent with either a mechanical strut that could remove the residual swirl or entry into a core.

Table 1: Nominal fan design objectives

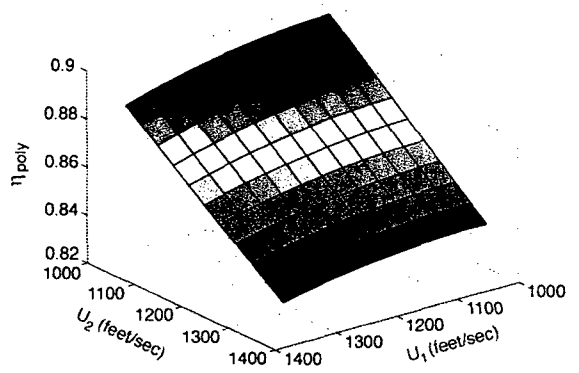
Pressure Ratio	3:1
Adiabatic Efficiency	87%
Rotor 1 Speed Range	1400-1500 ft/sec
Rotor 2 Speed Range	1100-1250 ft/sec
Specific Flow	41.5 lbm/sec/ft^2
Exit Mach No.	0.5
Exit Swirl Angle	<15 deg

In contrast to the design of a conventional fan, this design was complicated by the introduction of the second independent rotor with its tip speed and work coefficient as additional design variables. The absence of a vane between the rotors added further complexity to the design effort due to the very high relative supersonic Mach numbers into the second rotor.

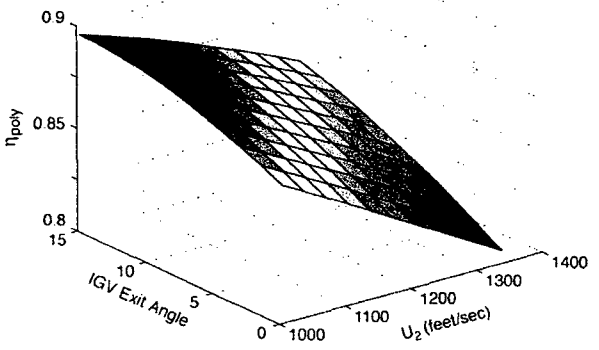
In order to clarify the roles of design variables such as rotor speed ratio, a preliminary design study and optimization of design parameters was performed using a one-dimensional model of the fan. The model included compressibility, area change, shock loss, and viscous loss models. Parametric studies were carried out using rotor speeds, rotor work coefficients, and inlet guide vane swirl as variables to explore the design space. Finally, a constrained optimization was performed to arrive at the optimum values for the preliminary design.

The parametric study showed that the speed of the second rotor has a strong impact on the efficiency, mainly due to the shock loss at high relative Mach numbers at the rotor face (Figure 1). The speed of the first rotor has a relatively small impact on the overall efficiency, since the average Mach number varies only from 0.95 to 1.15 over the speed range. In contrast, the average Mach number in the second rotor varies from 1.4 to 1.6. Note that this variation was calculated without any counter-swirl in the first rotor. Lowering the blade speed of the second rotor to manage the Mach number, while maintaining the design pressure ratio, results in a higher work coefficient and blade loading than is found in conventional supersonic rotors.

Adding counter-swirl via the inlet guide vane increases the relative Mach number into the first rotor, but lowers the relative Mach number into the second rotor. As shown in Figure 1b, the efficiency reaches a peak at about 15 degrees of counter-swirl. A linear counter-swirl variation from 10 degrees at the hub to 0 degrees at the tip was used in the final design.



(a) Efficiency variation with Rotor 1 and 2 tip speeds.



(b) Efficiency variation with IGV counter-swirl and Rotor 2 tip speed.

Figure 1: Design calculations of the effect of rotor speeds and IGV counter-swirl on fan efficiency.

The optimized 1D design was used as the starting point for a coupled axisymmetric-quasi-3D design of the fan. Fan design parameters are shown in Table 2. The flowpath was designed to provide sufficient flow contraction to maintain an acceptable meanline axial velocity decrease. The inlet radius ratio was constrained by the test facility and the exit radius ratio was selected to achieve an exit Mach number of 0.5 at design conditions. The casing flowpath was sloped 2% across each rotor to unload the tip sections, especially that of the second rotor. The aerodynamic design of the blades was carried out using the aspirated blade design system described in Merchant [3].

Three-dimensional viscous analysis of the stage, using the multi-stage average passage APNASA code developed by Adamczyk [8], was a critical component in the design process. The high supersonic Mach numbers in the blade rows, close blade row spacing, coupled with the very high blade loading demanded more accurate blade row matching than is possible with mixing-plane approaches. While the blade design was carried out using the quasi-3D design system, modifications to blade geometry, primarily incidence changes, were made using information extracted from the 3D APNASA solution.

Table 2: Fan aerodynamic design parameters

Rotor Speeds	1450 fps	1150 fps
Work Coefficient	0.34	0.5
Diffusion Factor	0.48	0.55
Hub Relative Mach	1.0	1.3
Tip Relative Mach	1.5	1.45
Blade Count	20	29
Avg. Solidity	1.9	1.7
Avg. Aspect Ratio	1.6	1.75
Inlet Radius Ratio	0.5	0.65

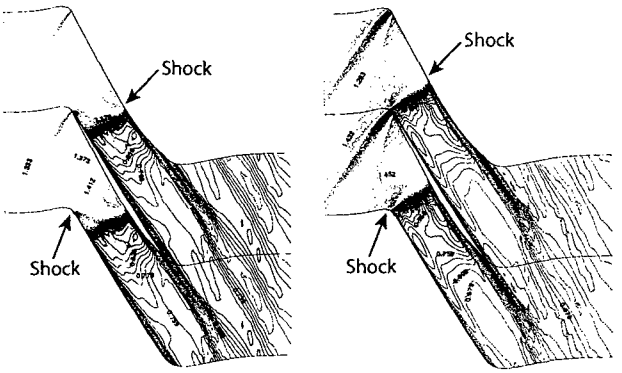
The predicted nominal design point performance for the fan calculated using APNASA is shown in Table 3. The tip clearances for the rotors were approximately 0.6% (Rotor 1) and 0.9% (Rotor 2) of the tip chord. The fan predictions exceeded the efficiency goal by 1.2% at the design pressure ratio, and achieved a peak adiabatic efficiency of 89% at a pressure ratio of 3.16.

Table 3: CFD predicted nominal design point performance

	Rotor 1	Rotor 2	Overall
Pressure Ratio	1.92	1.6	3.02
Adiab. Efficiency %	91.2	86.6	88.2
Poly. Efficiency %	92.3	87.5	90.0
Aspiration %	0	1.0	1.0

It is interesting to compare the design parameters of the two rotors shown in Table 2. Although the first rotor parameters are in the range of conventional supersonic fans, the aspect ratio is higher due to a lower average solidity [9]. The average Mach number of the first rotor is also higher than for conventional fans due to the counter-swirl from the inlet guide vane. The second rotor has a 40% higher work coefficient and 20% higher average Mach number than the first rotor. The average solidity is also significantly lower than for conventional fans. This is due to a combination of reduced blade count and reduced chord length, both enabled by aspiration.

The detailed design process revealed that a started shock system in the second rotor was critical to meeting the performance goals. This was complicated by three issues: 1) excessive hub boundary layer growth at the shock impingement location leading to shock unstart at the hub, 2) achieving the correct blade throat margin to maintain started flow at design and part speed conditions, and 3) managing the blade blockage by keeping the blade count low while maintaining sufficient solidity to meet the high loading requirement. Aspiration was critical in addressing these issues. First, the position of the passage shock was stabilized by aspiration. This approach has been utilized in the form of "shock traps" in supersonic inlets and was also incorporated in previous aspirated compressors [6]. Second, aspiration enabled blade designs with 20% lower solidity at diffusion factors of 0.55. This resulted in reduced blade blockage and enabled a blade design with sufficient throat margin [10]. Increasing the throat margin results in a stronger shock system that could be tolerated with aspiration.



(a) Peak efficiency (b) Peak pressure ratio

Figure 2: Contours of Mach number in Rotor 2 at mid-span.

To illustrate the shock locations and boundary layer thicknesses, Figure 2 presents relative Mach number contours at mid-span, from the APNASA calculation. The peak efficiency point (Figure 2a) has a started shock and a well-attached suction side boundary layer, and the peak pressure ratio point is the last computed CFD point, which shows a spilled shock system. A mid-span quasi-3D analysis of the impact of aspiration on the characteristics of the rotor showed that 1% aspiration resulted in a gain of 2 percentage points in efficiency and 6% in pressure ratio before shock unstart.

Figure 3 shows the predicted design speed pressure ratio and adiabatic efficiency with different levels of aspiration (percent of inlet mass flow). The mass flow variation at 0% aspiration indicates that both rotors are unchoked at the computed points. The peak pressure ratio is 3.08 and the peak efficiency potential is 84%. Comparing the speedlines at 0.5% and 1% aspiration, there is little difference in the peak efficiency, but the pressure ratio at 0.5% aspiration at which the speedline rolls off is 4% lower than at 1% aspiration. The predicted stall margin potential based on the last computed CFD point, calculated using the method in Wadia *et al.* [9], is 15% at the design bleed, 11% at 0.5% bleed, and 6% at 0% bleed.

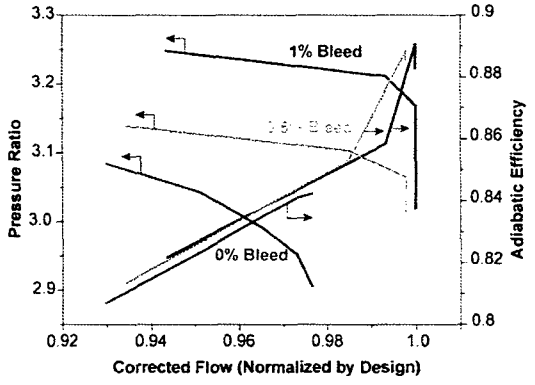


Figure 3: Predicted fan design speed pressure ratio and efficiency at different levels of aspiration.

EXPERIMENT DESCRIPTION

The theory and first application of blowdown compressor testing is described in Kerrebrock [11]. This blowdown facility is shown in Figure 4, and its test section details in Figure 5. The facility consists of a supply tank, initially separated by a fast-acting annular valve from the counter-rotating compressor stages and the dump tank into which they discharge. A choked perforated plate placed between the valve and test section was used to tailor the transient characteristics of the facility to the flow requirements of the compressor. A choked, adjustable area throttle downstream of the stage set the operating point. For this experiment, a sufficient the test time was required to permit accurate measurements of temperatures at the entrance to and exit from the compressor. In this facility, the measurement uncertainty of efficiency is dominated by temperature rise uncertainty. For these experiments, the target for efficiency measurement was 0.5%, which requires measurement of the temperature rise to about the same accuracy. Such instrumentation had been demonstrated for blowdown turbine stage testing [12]. This established a 100 ms test time requirement. This short test time precludes aeromechanical problems with the test hardware over the life of a typical test program.

A characteristic of blowdown compressors as used at MIT is that the decrease of the temperature of the gas in the supply tank during the test time is matched by slowing of the rotor, which is driven by its angular inertia, so that the Mach number of rotation is nearly constant during the blowdown. The relatively long test time of these experiments required the addition of a flywheel on each of the spindles carrying the rotors.

The test section, consisting of the two rotors, each on an independent, electric motor-driven spindle, is shown in Figure 5. The need to provide sufficient inertia to drive these high work stages for the required test time sized the flywheel inertia. The desire to keep the rotating systems' critical speeds above their operating range thus imposed a minimum hub-to-tip ratio on the first rotor of about 0.5. The tungsten flywheels, around which the test section was designed, failed during proof test, necessitating their replacement with maraging steel units. The resultant reduction in flywheel inertia was compensated for by reducing the inlet pressure and thus the test Reynolds number by about 20%.

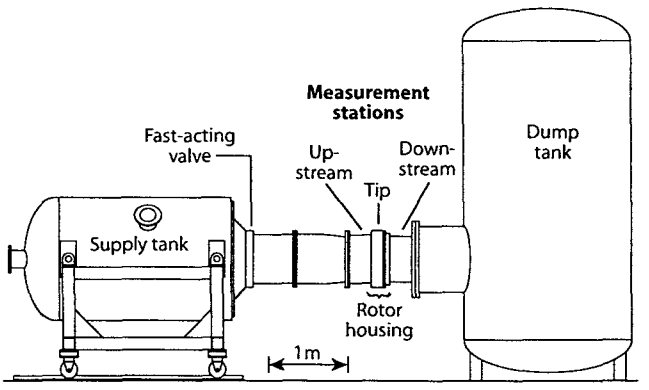


Figure 4: Blowdown facility.

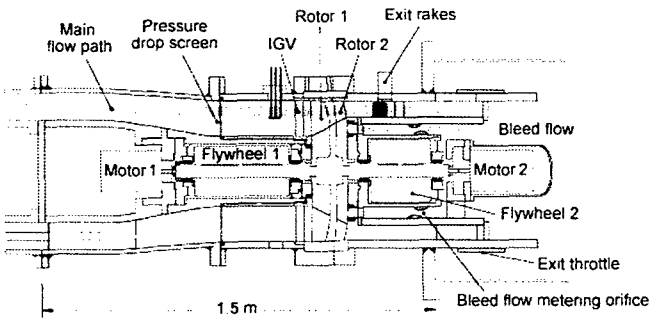


Figure 5: Counter-rotating fan test section.

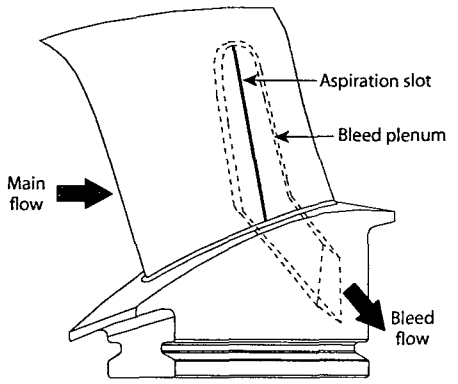


Figure 6: Aspiration passage geometry in Rotor 2.

The first rotor is an integrated bladed steel disk. The second rotor dovetails steel blades to a steel disk. Steel was chosen for the second rotor blades to ease construction of the hollow airfoils. They were fabricated by milling a bleed passage within a partially finished blade, e-beam welding on a cover, and then finish machining. The bleed air is removed through a passage electro-discharge-machined through the rear blade tang as shown in Figure 6. The bleed flowpath was designed to choke the suction surface slot so as to establish the bleed flow rate. Details of the mechanical design were given by Parker [13].

Primary performance instrumentation consisted of static and total pressure probes and rakes, and stagnation temperature rakes located ahead of the first rotor and behind the second rotor. (This test-section did not have torque-meters.) Also, high frequency response wall static pressure transducers were located in the casing between the two rotors, and just downstream of the second rotor. The rotor speeds and tank pressures were recorded as well. The pressure across an annular orifice in the bleed flowpath downstream of the second rotor was measured to monitor the aspirated bleed flow but programmatic constraints precluded proper bleed flowpath calibration so the bleed flow estimates in this paper are from the bleed flowpath design CFD calculations.

For these tests, a gas mixture of CO_2 and Argon with a ratio of specific heats, γ, of 1.4 was used in place of air to reduce the speed of sound (and thus mechanical stresses) while maintaining aerodynamic and thermodynamic similarity with air at flight conditions. During data reduction, the mixture was treated as real gas with properties estimated from NIST data (γ changes by about 3% from the stage inlet to outlet). Details of the construction and calibration of the instrumentation along with the test error analysis were given by Onnee [14].

BLOWDOWN OPERATION

Insofar as we are aware, this is the first two-rotor configuration tested in a transient facility and some effort was required to realize the desired test behavior. Given fixed rotor inertia and geometry, the operating condition of the fan during the test time is set by the initial rotor speeds, the supply tank pressure and temperature, and throttle areas downstream of the second rotor and in the bleed flowpath (which are adjustable). Figure 7 shows a typical simulated test time history. While the pressures and temperatures vary during the test, the pressure and temperature ratios across the stage remain close to constant for a sufficient period to enable accurate measurement of the fan performance. The useful test time is after the initial startup transient, from 250 ms to approximately 350 ms. The rise of the dump tank pressure then results in unchoking of the throttle and eventual stall of the fan.

The corrected flow is derived from a survey of the stagnation and static pressures upstream of the first rotor, and is essentially a measure of the Mach number at that point. Corrected speed is derived from the measured rotative speed and the measured temperature upstream of the first rotor. All of the measured values, including the rotative speed, are variable in time during the run, so a point on the map is defined by selecting a time near the middle of the test time, when the rotative and flow Mach numbers are nearly constant, and calculating the operating point from the values measured at that time. Typical variation in corrected speed and weight flow during the nominal 100 ms test time is shown in Figure 8, which shows a variation of less than ±0.5% in corrected speed and ±1.6% in corrected flow.

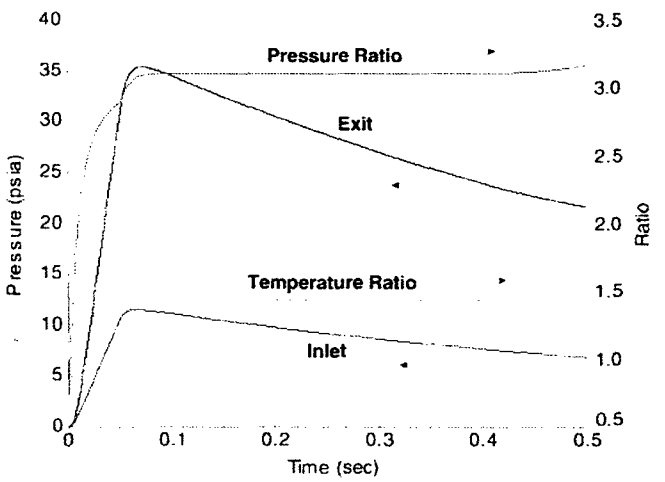


Figure 7: Typical variation of flow conditions during a blowdown test.

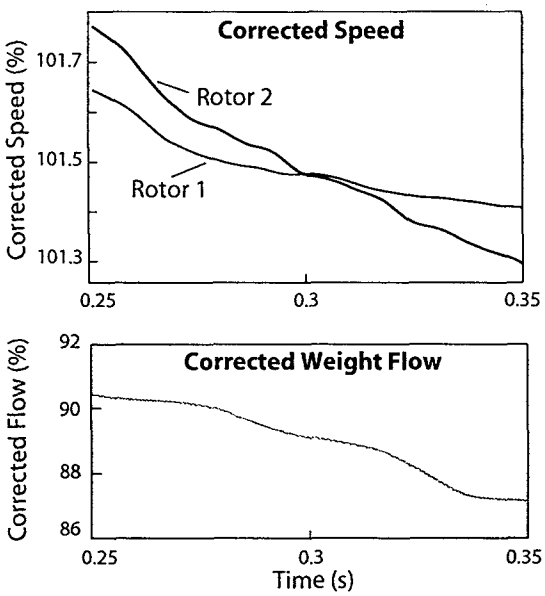


Figure 8: Measured corrected rotor speed variations.

After this 100 ms test period, the operating point changes as the throttles unchoke, resulting in the fan stalling after several hundred milliseconds. Conceptually, data from this period could be used to map out the stage behavior over the operating line followed. Such analysis has yet to be done however, and all data reported herein is that averaged over the 100 ms matched test time.

RESULTS AND DISCUSSION

In this section we present and discuss the overall fan performance map. The experimental results are compared and reconciled with CFD calculations carried out using APNASA. The stall behavior of the fan is also discussed from a first principles analysis. In order to assist in understanding the measured performance of the fan, a simple one-dimensional model, which includes shock loss, diffusion loss, and a coupling of the mass flow to the rotor speed (assuming that both rotors operate with a unique incidence condition), was used. The model was calibrated by adjusting the blade metal angles to match the design pressure ratio. The corresponding predicted efficiency from the loss model was found to be in reasonable agreement.

1) Overall Fan Performance

The overall measured performance of the counter-rotating compressor is summarized in Figures 9 and 10, which respectively show the pressure ratio and efficiency as functions of corrected speed and corrected flow. The pressure ratio was derived by area-averaging the measured upstream/downstream spanwise pressure profiles. The reported efficiency was calculated from total enthalpy and entropy from NIST tables based on area-averaged total pressure and temperature [13,14]. The predicted APNASA performance was calculated from area-averaging the flow solution. Excluding the effect of the

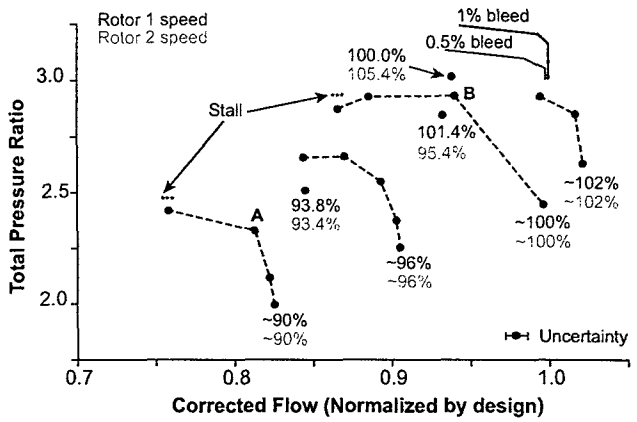


Figure 9: Compressor pressure ratio as predicted by APNASA (solid lines) and as measured (points).

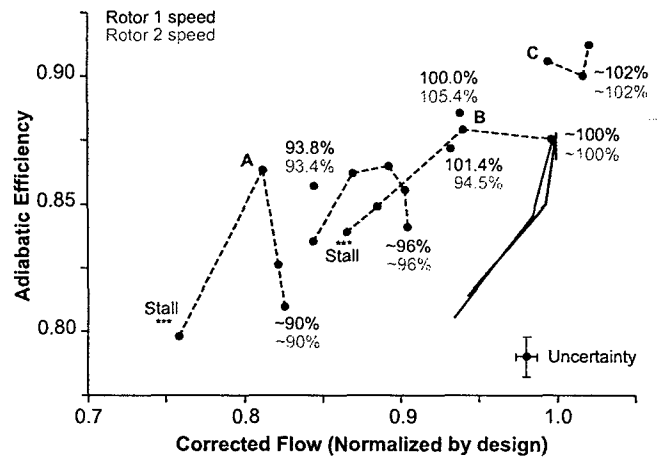


Figure 10: Adiabatic efficiency as predicted using APNASA (solid lines) and as measured (points).

boundary layers outside the radius of the hub and tip rake measurements resulted in an increase of about 0.3% in the predicted efficiency.

The nominal speeds of the two rotors as percent of the design speed are both shown (R1, top red and R2, bottom green). The design speed ratio between the rotors was maintained on each of the speedlines, and perturbations from the design speed ratio were tested at the individual points indicated on the map. The operating points on the speedlines were obtained by adjusting the downstream throttle setting. The APNASA calculations presented are all predictions made prior to the start of the test program. Because of the complexity of the dual-shaft test rig, it was difficult at first to set operating points to a precision greater than 2% in speed and mass flow prior to the test (although the precision improved with experience and there was no difficulty in reducing the data to 0.1% precision). The predictions were made at an inlet Reynolds number of 2.6×10^6 while tests were run at about 1.6×10^6 at design speed. The rotor tip clearance used in the

calculations was 0.6% and 0.9% of the tip chord for the first and second rotors respectively, while that in the tests is estimated to 60% lower than the calculation. The effect of the tighter clearance on the efficiency is estimated to be 0.6% increase based on the tip leakage model by Denton [15]. The result is that the CFD solutions are not exactly at the test conditions (resource limitations precluded rerunning the CFD at the measured operating points).

Figure 9 shows that the fan achieved a peak pressure ratio of 2.94 at design speed. This is 3% below the predicted design pressure ratio, and implies a difference of approximately 1% in the temperature ratio. Comparing this to the predicted peak efficiency points, the measured pressure ratio is 7% below the pressure ratio predicted for 1% aspiration, and 4% below the pressure ratio predicted for 0.5% aspiration. This implies a difference of approximately 2% between the measured and predicted temperature ratios. The one-dimensional fan model described above was used to relate the sensitivity of the stage temperature ratio or work to the flow angle deviation. The model indicated that the stage was very sensitive to changes in exit flow angles, and a rotor deviation change of approximately 1 degrees was sufficient to explain the observed differences in the measured and predicted performance. The increase in deviation may be caused by lower than design aspirated flow. An additional point to note is the strong coupling between the rotors due to absence of a stator, which typically constrains the absolute flow angle into a downstream rotor. Thus, in the counter-rotating compressor, a change in deviation of the first rotor will have a larger impact on the downstream rotor, and thus the overall stage performance than in a conventional multistage compressor.

The measured choking mass flow at the design speed is within 1% of the predicted design mass flow. The measurements show a flow range of 14% from choke to stall, which is approximately twice the range of the predicted speedline. Typical supersonic stages show a mass flow variation of about 7% at design speed conditions [9,16]. At 102% design speed, the measured choking mass flow is about 2% higher than design. This flow is determined solely by the choking mass flow in the first rotor and the increase in corrected flow is consistent with the speed increase of the first rotor. At 90% speed, the measured flow range from choke to stall is 10%, and the measured choking flow rate is within 2% of the value predicted by APNASA. It should be noted that the rotor geometry changes with mechanical speed; specifically, the stagger in supersonic fans increases as the blade speed drops, so the choking mass flow will drop as well. Variations in the geometry due to mechanical speed variations were not accounted for in the CFD calculations, which may explain the lower choking mass flow in the predictions.

The peak stage adiabatic efficiency measured was 91% (Figure 10). The variation in efficiency on the nominal design speedline (100% and 102% design speedlines), as the stage is throttled to stall, is qualitatively in agreement with the trend predicted by the APNASA calculation, although the lowest measured efficiency is about 3 percentage points higher than the lowest predicted efficiency. At 90% speed, only one efficiency prediction was available, and this is about 3 to 6 points lower

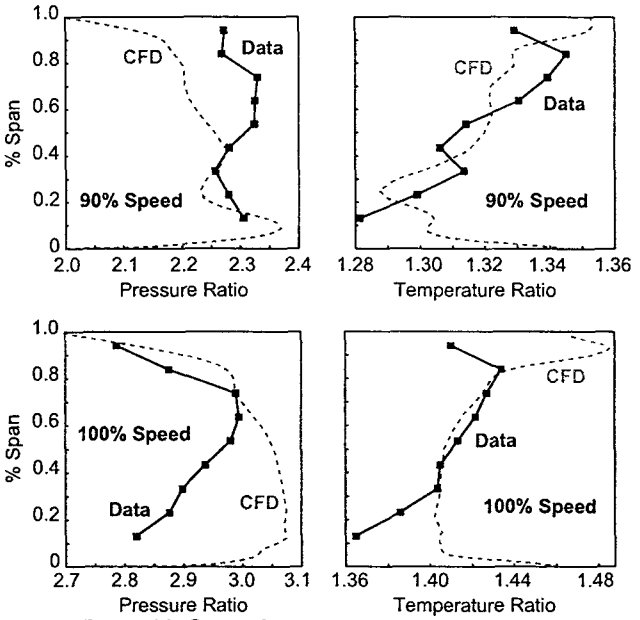


Figure 11: Spanwise pressure and temperature distributions.

than the measurement, depending on the operating point chosen for comparison.

The CFD and test data spanwise distribution of the rotor 2 exit temperature and pressure are given in Figure 11 for point B on the 100% speedline and point A on the 90% speedline. At 100% speed, the CFD over predicts the pressure rise along the inner half of the span while under predicting the temperature rise. At 90% speed, the outer span pressure rise is over predicted.

Given the sensitive supersonic operating condition of both rotors, the measured and predicted performance are in good agreement. Thus, we conclude that the overall aspirated compressor aerodynamic design system gives useful results even in new and unusual sectors of design space such as that selected for this fan.

2) Casing Static Pressure Measurements

In the tests to date, the outer casing static pressure measurements provide the only independent assessment of the performance of the first rotor. At the choking mass flow on the nominal design speed, where the first rotor is choked, the measured ratio of wall static to upstream total pressure is 1.39 while the value predicted by APNASA is 1.41. At the stall point, the measured static pressure ratio is 1.45 and the predicted value at the last computed point is 1.44. At 90% speed, the measured normalized static pressure is 1.3 and the predicted value is 1.31. This comparison indicates that this measure of first rotor performance is in agreement with prediction at both speeds.

3) Speed Ratio Perturbations

Although the stage was nominally designed and tested for a speed ratio of 0.8, changes in the speed ratio will occur in an

engine environment. Two speed ratio perturbations were examined about point B on the compressor map. Increasing the speed of the second rotor while maintaining the speed of the first rotor results in an increase in pressure ratio and efficiency. The second rotor effectively acts as a throttle for the first rotor, so increasing the speed ratio moves the operating point of the first rotor closer to choke. This can be seen in the decrease in the normalized static pressure downstream of the first rotor shown in Table 4. It is interesting to note that the overall flow rate does not change even though the first rotor is being throttled down. This unusual behavior can be explained by noting that an increase in the exit deviation of rotor 1, caused by throttling down, can change the absolute flow angle without necessarily changing the axial velocity (mass flow). The overall result is that the inlet corrected flow of rotor 2 can change as the blade speed is increased without changing the overall mass flow rate of the compressor. This behavior does not occur in a conventional stage since the stators constrain the absolute flow angles into downstream rotors.

Table 4: Comparison of casing static pressures at speed ratio perturbations about the design speed

% Speed	Rotor 1	Rotor 2	Overall
100-100	1.41	1.82	2.57
100-105	1.38	1.89	2.61
101-95	1.46	1.73	2.52

Conversely, decreasing the speed ratio results in throttling up of the first rotor, moving it closer to stall. The static pressure rise downstream of the first rotor at 100-95% speeds is greater than the normalized static pressure at the stall point of the stage at the design speed ratio. The key point is that changes in speed ratio can have a large impact on the stage performance, in particular of the first rotor. The design implication is that the first rotor must be designed with the appropriate stall margin to withstand the throttling effect caused by reductions in the speed ratio in an engine environment.

4) Stall Behavior

As is common practice, high frequency response pressure measurements on the outer casing downstream of the stage were used to detect rotating stall. The quasi-steady test window contains about 20 revolutions of the first rotor and 16 revolutions of the second rotor. Stall was detected during the test time for operating points with a sufficiently closed throttle. The rotating stall frequency observed was approximately 35% of the first rotor speed.

Figure 12 show the measured stall margin of the fan as defined in [9]. The stalling pressure ratio was taken as the last operating point on each speedline. (Note, that stall was not observed on the 95% and 102% speediness, so these are excluded from this discussion) The fan exhibits a stall margin of at least 25% on the three speedlines depending on the operating pressure ratio. The stall margin at peak efficiency on the speedlines is approximately 12%. At the nominal design speed, the stall margin is 15% at a pressure ratio of 2.8 and

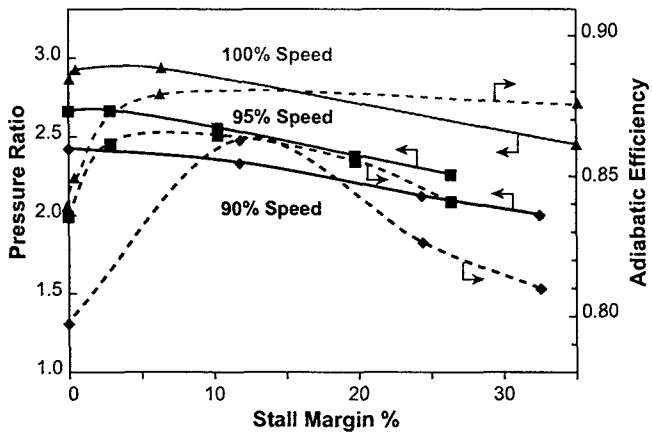


Figure 12: Measured stall margin vs. pressure ratio.

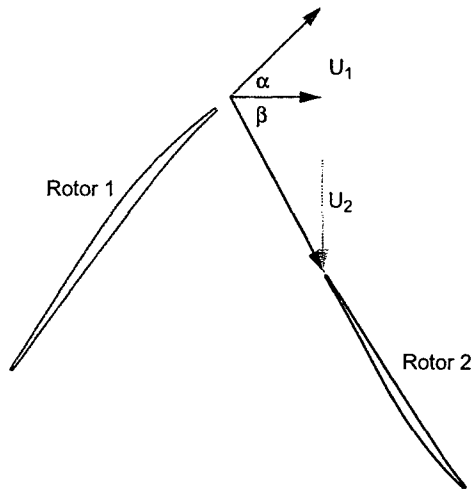


Figure 13: Velocity triangles in the frame of reference of the first rotor.

adiabatic efficiency of 88%.

This is the first counter-rotating fan reported in the literature and, for a high pressure ratio supersonic fan, this stage has considerable flow range and stall margin. This behavior merits some examination. Cumpsty [17] presents a simple explanation that a steeper pressure rise characteristic smoothes out non-uniformities in the flow and therefore is advantageous in delaying stall. The slope of the ideal characteristic of a vaneless counter-rotating fan is:

$$\frac{\partial \psi}{\partial \phi_{inlet}} = -\left(\frac{U_2}{U_1}\right)\tan(\alpha) - \left(1 - \frac{U_2}{U_1}\right)\tan(\beta) \cdot$$

Here, U is the blade speed, α is the relative exit angle of rotor 1, and β is the blade relative inlet angle of rotor 2. For simplicity, it is assumed that there is no inlet swirl and the axial velocity is constant. Substituting appropriate flow angles

Design and Operation of a Counter-Rotating Aspirated Compressor Blowdown Test Facility

by
David V. Parker

B.S., Mechanical Engineering (2003)
University of New Hampshire

Submitted to the Department of Aeronautics and Astronautics in partial fulfillment of the degree of

Master of Science

at the
MASSACHUSETTES INSTITUTE OF TECHNOLOGY

June 2005

© Massachusetts Institute of Technology 2005. All rights reserved.

Author.....
Department of Aeronautics and Astronautics
May 20, 2005

Certified by.....
Alan H. Epstein
R.C. Maclaurin Professor of Aeronautics and Astronautics
Thesis Supervisor

Certified by.....
Jaime Peraire
Professor of Aeronautics and Astronautics
Chair, Committee on Graduate Students

Design and Operation of a Counter-Rotating Aspirated Compressor Blowdown Test Facility

by
David V. Parker

Submitted to the Department of Aeronautics and Astronautics on
May 20, 2005 in partial fulfillment of the degree of
Master of Science

Abstract

A unique counter-rotating aspirated compressor was tested in a blowdown facility at the Gas Turbine Laboratory at MIT. The facility expanded on experience from previous blowdown turbine and blowdown compressor experiments. Advances in thermocouple and facility designs enabled efficiency estimates through total temperature and total pressure measurements. The facility was designed to provide at least 100 ms of available test time, approximately a factor of five greater than previous blowdown compressor facilities.

The adiabatic core efficiency of the compressor was estimated with an uncertainty of 0.8% and the corrected flow was estimated with an uncertainty of 1.0%. The compressor was tested at several operating conditions and two speed lines were partially mapped. The maximum measured total pressure ratio across the two stages was 3.02 to 1. The measured adiabatic efficiency for that point was 0.885.

The span-wise total pressure, total temperature, and efficiency profiles were compared to the predicted profiles for runs with the corrected speeds of the two rotors at 90% of design and 100% design. There appears to be reasonable agreement between the predictions and the measurements.

Thesis Supervisor: Dr. Alan H. Epstein
Title: R.C. Maclaurin Professor of Aeronautics and Astronautics

Acknowledgments

The author would like to thank Prof. Alan H Epstein, Dr. Gerald Guenette, and Prof. Jack Kerrebrock for the opportunity to work on this project. Also, they were invaluable resources for insight and guidance when looking for solutions to problems. Without their experience with blowdown facilities this project would not have succeeded. Also, Dr. Fritz Neumayer and Dr. Ali Merchant deserve thanks for their work on the data acquisition system and the rotors, respectively.

Thanks to JF Onnee for spending long days working in the lab, thinking through problems, and getting through this process.

A special thanks to Jack Costa, James Letendre, and Victor Dubrowski for their tireless work in the lab. The instruments were partially the result of many hours Mr. Costa spent staring through the microscope soldering wires. Similarly, Mr. Dubrowski's skills with a Bridgeport and lathe where highly valued while manufacturing the instruments. Finally, Mr. Letendre showed the author how to safely and effectively work in the lab.

On a personal note the author would like to thank his family, who have always supported and pushed him; Debbie, she is an amazing blessing and support; and his church for the friendship and community that they have provided.

Finally, the author would like to thank Dr. S. Walker, program manager at the Defense Advanced Research Program Agency, for funding this research.

Table of Contents

Acknowledgments 5
Table of Contents 7
Table of Figures 11
Table of Tables 15
Nomenclature 17
1 Introduction 19
1.1 Motivation of Work 19
1.2 Contents of This Work 19
2 Experimental Facility Design 21
2.1 Facility Requirements 23
2.2 Facility Scaling Parameters 23
2.2.1 Matching Corrected Flow and Mach Number 24
2.2.2 Matching Corrected Speed 25
2.2.3 Matching Ratio of Specific Heats 26
2.2.4 Matching Reynolds' Number 27
2.3 Facility Packaging 27
2.3.1 Supply Tank Sizing 27
2.3.2 Fast-Acting Valve Area 27
2.3.3 Fitting Flywheels within the Flow path 28
3 Detailed Facility Description 29
3.1 Tanks and Accessory Systems 29
3.2 Fast Acting Valve 30
3.3 Test Sections 32
3.3.1 The Forward Test Section 32
3.3.2 The Aft Test Section 35
3.4 Rotating Assemblies 36
3.4.1 Bearings and Drive Shaft Assemblies 37
3.4.2 Flywheel Design 38
3.4.3 Motors and Motor Control Architecture 44
4 Design and Manufacture of Bladed Components 47
4.1 Blade Design 47
4.1.1 Counter-Rotation Benefits and Challenges 47
4.1.2 Inlet Guide Vanes 48
4.1.3 Rotor One 49
4.1.4 Rotor Two 52
4.1.5 "Hot-to-Cold" Geometry Transformations 54
4.2 Five-Axis Machining of Blisks 55
4.2.1 Selection of Profile Tolerance 56
4.2.2 Surface Finish Tolerance 57
4.2.3 Non-Conformities of Manufactured Parts 58
4.3 Manufacturing Process for Aspirated Blades 59
4.3.1 Challenges Associated with Aspiration 59
4.3.2 Order of Operations 63
5 Instrumentation and Data Acquisition 69

5.1 Measurement Locations 69
5.2 Temperature Probes 71
5.3 Pressure Probes 71
5.3.1 Rated Transducer Properties 71
5.3.2 Total Pressure Rake Design 72
5.3.3 Pitot Pressure Probes 73
5.3.4 Wall Static Pressure Taps 74
5.4 Data Acquisition System 76
5.4.1 Low-Speed A/D Cards 76
5.4.2 High Speed A/D Card 76
5.4.3 80 MHz Counter Card 76
6 Facility Operation and Initial Results 77
6.1 Data Reduction Methods 77
6.1.1 Filtering 77
6.1.2 Corrected Flow 78
6.1.3 Efficiency 81
6.2 Facility Operation 82
6.2.1 Operational Constraints Due to Inertia Ratios 82
6.2.2 Throttle Behavior 85
6.2.3 Rotor Interactions 86
6.3 Inlet Distortion 87
6.3.1 Thermal Boundary Layers 87
6.3.2 Total Pressure Distortion 88
6.4 Uncertainty Analysis 91
6.4.1 Measurement Uncertainty 92
6.4.2 Non-Instrument Related Uncertainties 93
6.5 Initial Test Results 95
6.5.1 90%-90% Corrected Speeds 96
6.5.2 100%-100% Corrected Speeds 98
6.5.3 100%-105% Corrected Speeds 101
6.5.4 Summary of Performance Results 102
6.5.5 Change in Operating Point during the Test Time 105
6.5.6 High Frequency Data Analysis 106
7 Conclusions and Future Recommendations 109
7.1 Results 109
7.2 Recommendations 109
7.2.1 Further Analysis 109
7.2.2 Further Measurements 110
Works Cited 111
Appendix A: Blowdown Equations 113
Appendix B: Uncertainty Analysis Derivations 115
Uncertainty Propagation In Corrected Flow Measurement 115
Uncertainty Propagation in Corrected Speed 118
Appendix C: Measurement Uncertainties 119
Pressure Uncertainties that Result form Probe Geometry 119
Pressure Transducer Qualification 119

Summary of Pressure Uncertainties 121
Summary of Temperature Uncertainties 123
Summary of Gas Mixture Uncertainties 124
Appendix D: Blowdown Test Details 125
Sequence of Test Operations 125
Calibration Method 126
Appendix E: Raw Data Documentation 127
Raw Data 127
Facility Conditions & Test Time Selection 134
Corrected Flow 137
Pressure Ratio & Temperature Ratio 139

Table of Figures

Figure 2.1: Sketch of CRAspC Blowdown Test Facility 22
Figure 2.2: Estimated Corrected Flow During Blowdown 25
Figure 2.3: Estimated Variation in Corrected Speed During Blowdown 26
Figure 3.1: Blowdown Counter-Rotating Aspirated Compressor Facility, flow goes from right to left 29
Figure 3.2: Schematic drawing of the Fast-Acting Valve [9] 31
Figure 3.3: Sequence of events for the Fast-Acting Valve while opening [9] 31
Figure 3.4: Sketch of Both Sections 32
Figure 3.5: Forward Test Section 33
Figure 3.6: First Mode - 151 Hz (9060 RPM) [10] 34
Figure 3.7: Aft Test Section 35
Figure 3.8: Forward Rotating Assembly 36
Figure 3.9: Aft Rotating Assembly 36
Figure 3.10: Aft bearing and spring-plate assembly 38
Figure 3.11: One piece of a tungsten flywheel after bursting. 39
Figure 3.12: One of the Inertia Centering Plates 40
Figure 3.13: Von-Mises Equivalent Stress (psi) in the ICPs [10] 41
Figure 3.14: FEA Estimate of Spring Stiffness for Different Geometries 41
Figure 3.15: Forward Flywheel 43
Figure 3.16: Radial Deflections of the Forward Flywheel (m) 43
Figure 3.17: Forward motor housing, showing water and electrical lines through the struts. 45
Figure 4.1: Velocity Triangles for a counter-rotating compressor [16] 47
Figure 4.2: Streamlines that define the Inlet Guide Vanes 48
Figure 4.3: Rotor One Streamlines 50
Figure 4.4: Relative Mach Number Contours of Rotor One at Hub, D=0.53 [17] 50
Figure 4.5: Rotor One Relative Mach Number contours, Mid-Span [17] 51
Figure 4.6: Rotor One Relative Mach Number Contours, Tip [17] 51
Figure 4.7: Effect of Aspiration on boundary layer growth 52
Figure 4.8: Streamlines for Rotor Two 53
Figure 4.9: Relative Mach Number contours for Rotor Two at hub [17] 53
Figure 4.10: Mid-Span Relative Mach number contours, Rotor Two [17] 54
Figure 4.11: Rotor Two Relative Mach number contours at tip [17] 54
Figure 4.12: IGV while still on the machine 55
Figure 4.13: Sketch that illustrates the concept of a profile tolerance 56
Figure 4.14: Tool markings and surface finish for Rotor One 57
Figure 4.15: Probe data for one stream line of Rotor One 58
Figure 4.16: Sketch of scheme for removing aspiration flow radially inward [16] 60
Figure 4.17: Stress in Rotor Two, Pressure Side, Alum.- Yield Stress ~120 MPa (Max 340 MPa) [18] 61
Figure 4.18: Stress in Rotor Two, Pressure Side, 17-4 PH - Yield Stress = 162 ksi (Max 150 ksi) [19] 62
Figure 4.19: Aluminum test blade with section of leading edge due to distortion during welding 64

Figure 4.20: Inadequate weld joints in fillet because of control issues with the electron beam 65
Figure 4.21: Aspirated Rotor after assembly and balance 67
Figure 5.1: Instrument Locations in the Blowdown CRAspC Facility 70
Figure 5.2: Cross-Section view of pressure tubes within the Upstream Rake 72
Figure 5.3: Sketch showing impact heads and tubes of a Downstream Rake 73
Figure 5.4: United Sensor Pitot Probe [24] 74
Figure 5.5: Wall static pressure taps, dimensions in inches 74
Figure 5.6: Upstream static pressure measurement for Run 014 75
Figure 5.7: Difference in upstream static pressures normalized by the pitot static pressure, Run 014 75
Figure 6.1: Response of random data to the digital filter used in data analysis 78
Figure 6.2: Total and Static Pressures for each window in Run 013 79
Figure 6.3: Mass flow for each window during Run 013 80
Figure 6.4: Corrected Flow by Window for Run 013 80
Figure 6.5: Assumed profile for area averaging 81
Figure 6.6: Corrected Speeds for Run 005 83
Figure 6.7: Corrected Speeds for Run 006 84
Figure 6.8: Corrected Speeds for Run 007 84
Figure 6.9: Throttling effect of Rotor Two on Rotor One 87
Figure 6.10: Thermal boundary layers during Run 010 88
Figure 6.11: Circumferential total pressure variation, normalized by average total pressure 88
Figure 6.12 Circumferential static pressure variation, normalized by average total pressure 89
Figure 6.13: Circumferential variation in velocity head, normalized by the average 89
Figure 6.14: Prediction of loss coefficient [27] 90
Figure 6.15: Correlation between area variation and total pressure 91
Figure 6.16: CFD result used to estimate uncertainty from radial sampling 94
Figure 6.17: Performance Of CRAspC during Run 007 96
Figure 6.18: Span-wise Total Pressure Ratio Profile compared to CFD, 90%-90% Corrected Speeds 97
Figure 6.19: Span-wise Total Temperature Ratio Profile compared to CFD, 90%-90% Corrected Speeds 97
Figure 6.20: Span-wise Efficiency Profile compared to CFD, 90%-90% Corrected Speeds 98
Figure 6.21: Compressor Performance at Design Point 99
Figure 6.22: Span-wise Total Pressure Profile compared to CFD, Design Point 100
Figure 6.23: Span-wise Total Temperate Profile compared to CFD, Design Point 100
Figure 6.24: Span-wise Adiabatic Efficiency Profile compared to CFD, Design Point 101
Figure 6.25: Compressor Performance for Run 009 102
Figure 6.26: Compressor Map, Pressure Ratio vs. Corrected Flow 103
Figure 6.27: Compressor Map, Adiabatic Efficiency vs. Corrected Flow 104
Figure 6.28: Compressor Map, Polytropic Efficiency vs. Corrected Flow 104
Figure 6.29: High-Frequency wall static pressure measurement between rotors, Run 010 107

Figure 6.30: High-Frequency wall static pressure, ensemble averaged, Run 010 107
Figure C.1: Pressure history of Heise 015 during transducer qualification 120
Figure E.1: Supply Tank Pressures, Run 013 128
Figure E.2: Upstream Total Pressure Singles, Run 013 128
Figure E.3: Upstream Static Pressures, Run 013 129
Figure E.4: Upstream Total Pressure, Rakes Run 013 129
Figure E.5: Upstream Total Temperature Singles, Run 013 130
Figure E.6: Upstream Total Temperature Rake Measurements, Run 013 130
Figure E.7:High frequency casing static pressure measurements, Run 013 131
Figure E.8: Downstream mid-stream Pitot Probe, Run 013 131
Figure E.9: Downstream Total Pressures, Run 013 132
Figure E.10: Downstream Total Temperatures, Run 013 132
Figure E.11: Dump Tank Pressures, Run 013 133
Figure E.12: Bleed Flow Total Pressure, Run 013 133
Figure E.13: Rotor speeds during Run 013 134
Figure E.14: Corrected Speeds During Run 013 135
Figure E.15: Corrected speeds between 250 ms and 350 ms for Run 013 136
Figure E.16: Important pressure ratios in the facility for Run 013 136
Figure E.17: Entropy entering Compressor, normalized by $s(0.250)$, Run 013 137
Figure E.18: Mass flow at each measurement location, Run 013 138
Figure E.19: Corrected flow normalized by the design value at each measurement location, Run 013 138
Figure E.20: Mach Number at each measurement location, Run 013 139
Figure E.21: Pressure Ratio and Temperature Ratio during Run 013 140
Figure E.22: Adiabatic efficiency, average inlet corrected flow, and inlet Reynolds' number for Run 013 141

Table of Tables

Table 2.1 Important Non-Dimensional Parameters for Scaling Test Facility 24
Table 4.1: Rotor One Aero-Design Summary [16] 49
Table 4.2: Rotor Two Aero-Design Summary [16] 52
Table 4.3 Blade Row Length Scales 56
Table 4.4: Probe Data From One Streamline of Rotor One 59
Table 6.1: Variations of the discharge coefficient model 86
Table 6.2: Pressure Loss Coefficient for the screen 90
Table 6.3: Uncertainties in Corrected Flow 92
Table 6.4: Uncertainties in adiabatic efficiency measurements 93
Table 6.5: Uncertainty from discrete radial measurements 94
Table 6.6: Comparison of performance parameters for two operating points 102
Table 6.7: Change in operating conditions during test time 105
Table C.1: Relative uncertainties in pressure measurements due to probe geometry 119
Table C.2: Qualification Data For Upstream Pressure Transducers 120
Table C.3: Qualification Data for Downstream Pressure Transducers 121
Table C.4: Up Stream Total Pressure Uncertainty 121
Table C.5: Down Stream Total Pressure Uncertainty 122
Table C.6: Up Stream Static Pressure Uncertainty 122
Table C.7: Summary of Absolute Temperature Uncertainty 123
Table C.8: Uncertainty in gas mixture 124

Nomenclature

η	adiabatic efficiency
ρ	density
δ	fraction of mass flow
γ	ratio of specific heats
σ	rotor solidity
Ω	rotor speed (rad/sec)
κ	thermal conductivity
π	total pressure ratio
μ	viscosity
τ_b	blowdown time constant
τ_c	total temperature ratio
A_C	area of annulus entering compressor
C_P	specific heat at a constant pressure
C_V	specific heat at a constant volume
D	diameter
D_F	diffusion factor
M	Mach number
$\dot{m}$	mass flow
N	rotor speed (Hz)
N_C	corrected speed
P	power
P_T	total pressure
P_{T_ref}	reference total pressure (1 atm)
R_{air}	gas constant of air
Re	Reynolds' number
Rg	gas constant of the gas mixture
T_T	total temperature
T_{T_ref}	reference total temperature (288 K)
V	volume
v	velocity
W_C	corrected mass flow

1 Introduction

1.1 Motivation of Work

In axial compressors the total pressure rise across a stage is directly related to the wheel speed and the turning of the flow. As the wheel speed is increased the velocity of the flow relative to the blade increases, increasing the Mach number. Increasing the Mach number too much can lead to unacceptable losses in efficiency. The limit on turning the flow is typically related to boundary layer separation [1]. A useful measure for relating the pressure rise, relative velocities, and turning in a compressor is the Diffusion Factor, first defined by Lieblein et al. [1] as:

$$D = 1 - \frac{V_2}{V_1} + \frac{|v_2 - v_1|}{2 \cdot \sigma \cdot V_1} \qquad \text{Eqn (1.1) [2]}$$

In equation 1.1 station '1' is entering the blade row and station '2' is exiting the blade row; V_i is the velocity relative to the blade, v_i is the circumferential velocity, and σ is the solidity of the blade row. The diffusion factor can be thought of as a relationship between the maximum velocity on the suction surface of the blade and the velocity of the fluid at the trailing edge of the blade. Losses increase dramatically when the diffusion factor exceeds 0.6 [2, 3].

It has been recognized since at least as early as 1950 that counter-rotation is a method for dramatically increasing the turning of the flow across the rotor. The fundamental problem with counter-rotation is that it results in supersonic relative Mach numbers in the second rotor. The advantage of counter-rotation is increasing the pressure ratio for the two stages; or the pressure ratio of current technology can be achieved while lowering the wheel speeds of the two rotors. Recently, reducing engine noise has received attention. A significant component of the noise generated by engines comes from the first stage fan. There has been a push within industry to reduce fan noise by reducing wheel speed through counter-rotation [4]. In the early 1950's Curtiss-Wright attempted, unsuccessfully, to produce a highly loaded counter-rotating compressor [1].

Since the mid 1990s investigators at MIT have been investigating the use of aspiration, removing low-momentum flow from boundary layers, to increase the pressure ratio per stage and extend the diffusion factor design space [6]. To date three aspirated compressors have been built and tested; one 'low-speed stage' that was tested at the MIT Gas Turbine Lab, one 'high-speed stage' that was tested at the NASA-Glenn Research Center, and a counter-rotating fan stage that is the subject of this current work.

1.2 Contents of This Work

One goal for this project was to measure the adiabatic efficiency of a counter-rotating aspirated compressor using a blowdown test facility. To accomplish this meant designing a new facility, rotors, and instruments. This thesis discusses the design of the facility (Chapters 2-3), the design and manufacture of the two rotors (Chapter 4), a cursory

treatment of the instrumentation and data acquisition systems (Chapter 5), and the results from the first series of tests (Chapter 6). Chapter 7 contains recommendations for future work. For details about the facility instrumentation consult "Aerodynamic Performance Measurements in a Counter-Rotating Aspirated Compressor" [5].

Some of the content of this thesis is the work of the author while other sections are descriptions of other people's work that are necessary for a comprehensive discussion of the facility. While the facility was being designed the author was primarily responsible for the design of the flywheels and pressure screen. The author also provided support designing the remainder of the test section. The author worked on a team to establish the mechanical design of the Inlet Guide Vanes, Rotor One, and Rotor Two. Interfacing with the manufacturer and managing the production of the bladed components was spearheaded by author. The author designed the total pressure rakes and manufactured the profiles for both the total pressure rakes and the total temperature rakes. Finally the author developed a system to reduce the data to engineering units and then analyze the data.

2 Experimental Facility Design

Short duration blowdown tests of compressors and turbines have been occurring at the Gas Turbine Laboratory at MIT since the early 1970s. Much has been learned about blowdown test dynamics and the solutions to problems associated with these test facilities. This knowledge base was heavily relied upon while designing the Blowdown Counter-Rotating Aspirated Compressor Facility (CRAspC), however, counter-rotation and aspiration presented new problems to be solved on this project.

Figure 2.1 is a basic sketch of the facility. The facility consists of the supply tank (A); the fast-acting valve (B); the pressure screen (C); the rotating assemblies, with consist of motors, inertias, and rotors (D,E); the throttle (F); and the dump tank(G). The order of operations for a blowdown test is that the entire facility is evacuated, then the valve is closed and the supply tank is filled to an initial pressure. The rotors are then brought to a set speed and the valve opens in less than 50 ms. Approximately 100 ms later the test is finished when the temperature of the gas mixture drops below 250° K.

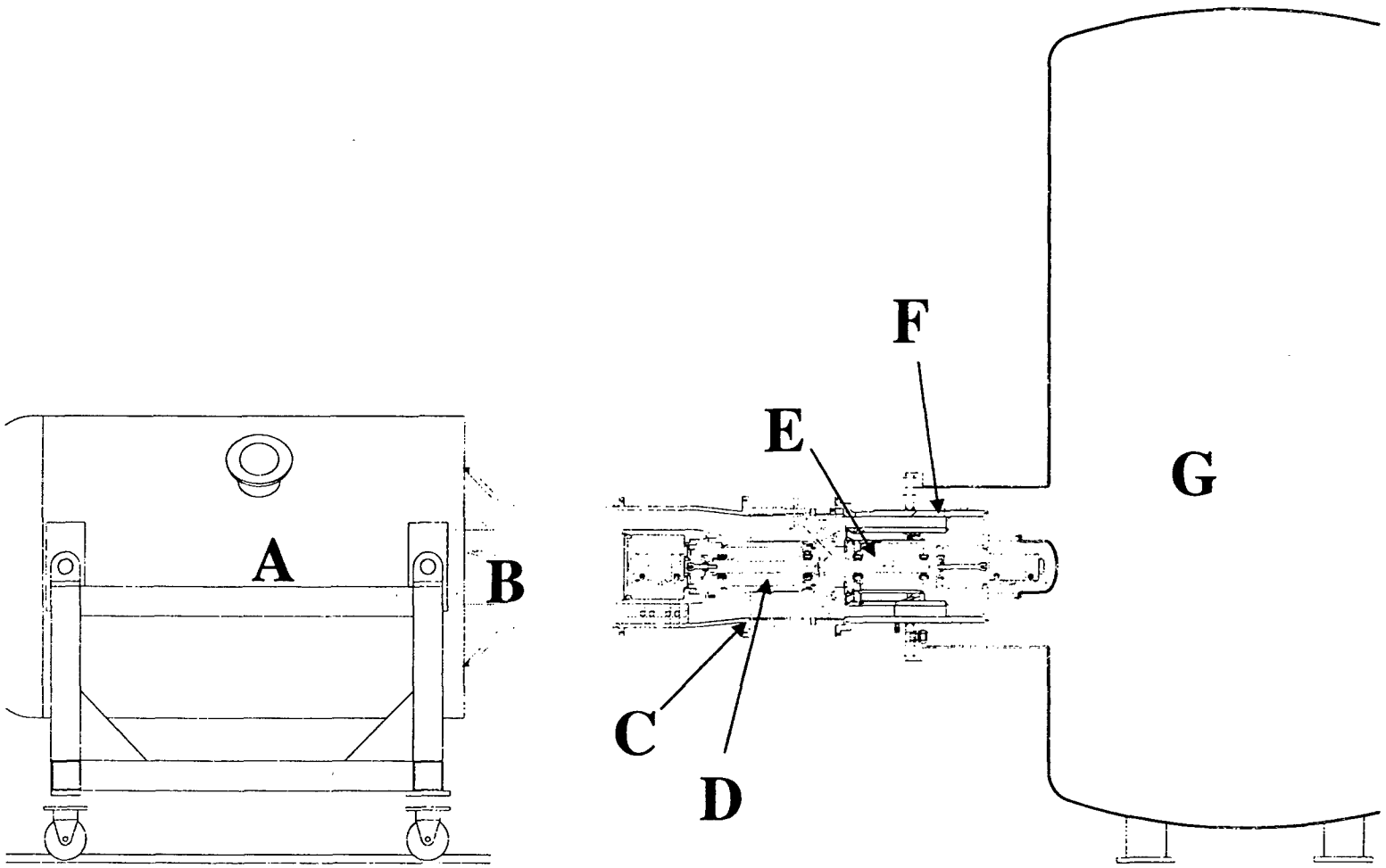


Figure 2.1: Sketch of CRAspC Blowdown Test Facility

This chapter discusses the underlying principles in the design of a blowdown compressor facility. Section 2.1 looks at the specific requirements of this facility. Section 2.2 discusses the non-dimensional groupings of variables that are used for scaling the facility and Section 2.3 discusses the some of the physical constraints on the facility that influenced the scales that the compressor was designed to.

2.1 Facility Requirements

One goal of this project was to accurately measure the important parameters of a counter-rotating aspirated compressor that would be appealing to industry. Economics and schedule dictated that the test be conducted in a blowdown facility. The requirements of the facility are enumerated below.

1. The facility must be scaled such that all pertinent non-dimensional parameters are matched during the test.
2. Non-Dimensional parameters must be constant during the test period.
3. The test must have a relatively long duration (400-500 ms) so that efficiency can be precisely measured with total temperature probes.
4. The facility was to be designed in such a manner that instrumentation capable of measuring more detailed flow phenomenon could be added at a later date.
5. All operational stresses must be kept within safe limits.
6. The compressors must be un-shrouded.

2.2 Facility Scaling Parameters

In a conventional steady-state compressor test facility inlet and exit conditions are held essentially constant. Inlet total temperature, total pressure, and mass flow do not vary (unless some dynamic phenomena is specifically investigated). The nature of blowdown experiments dictate that these parameters vary throughout the duration of the test. Previous work, by many investigators, has shown that characteristics of the fluid flow within the compressor are dictated not by dimensional, but rather, by non-dimensional parameters. These parameters are listed in Table 2.1. In blowdown experiments the facility is designed with the intent that these non-dimensional parameters, with the exception of Reynolds Number, remain relatively constant during the test. This section discusses how different facility dimensional variables affect the behavior of non-dimensional parameters over time during a test. The facility was scaled based on the predicted performance of the compressor at the design point. The impact of this scaling on the off-design performance is discussed in Section 6.2.

Table 2.1 Important Non-Dimensional Parameters for Scaling Test Facility

Parameter	Formula	What It Measures
Corrected Flow	$Wc = \frac{\dot{m} \cdot \sqrt{\frac{R_g \cdot T_T}{R_{air} \cdot T_{T\_Ref}}}}{A \cdot \frac{P_T}{P_{T\_Ref}}}$	mass flow through compressor corrected to standard day conditions
Corrected Speed	$Nc = \frac{N \cdot \pi \cdot D}{\sqrt{R_g \cdot T_T}}$	tip speed relative to speed of sound
Ratio of Specific Heats	$\gamma = \frac{C_p}{C_v}$	defines 1-D compressible flow relationships
Mach Number	$M = v/c$	velocity of flow relative to speed of sound
Reynolds Number	$\mathrm{Re} = \frac{\rho \cdot v \cdot D}{\mu}$	momentum of the fluid relative to the viscosity

2.2.1 Matching Corrected Flow and Mach Number

For an ideal gas with constant γ corrected flow can be expressed as:

$$Wc = f(M,\gamma) \cdot \frac{P_{T\_Ref}}{\sqrt{R_g \cdot T_{T\_Ref}}}$$

$$f(M,\gamma) = \sqrt{\gamma} M \cdot \left(1 + \frac{\gamma - 1}{2} \cdot M^2\right)^{-\frac{\gamma+1}{2(\gamma-1)}}$$

Eqn (2.1) [7]

The corrected flow in the facility is set with a choked throttle between the test section and the dump tank. As long as the flow remains choked the Mach number is constant making the corrected flow constant. Therefore, one significant influence on the available test time is the size of the dump tank. The larger the tank the longer it will be before the pressure in the dump tank rises above the critical pressure where the orifice unchokes. The throttle is designed so that the area can be changed between runs. Before the first test CFD compressor models and an estimate of the throttle discharge coefficient are used in combination with steady and unsteady models (both of which assume the compressor operates at a specific operating point from the CFD) of the facility to set a nominal throttle position. Analysis after the run allows the investigators to view where the compressor operated and adjust the throttle accordingly. A quasi-steady lumped parameter model of the facility was developed to investigate how changing different variables affected the entire system. Figure 2.2 shows some of the results of the unsteady model for the compressor design point. It is easy to see from Equation 2.1 that if the corrected flow is constant then the inlet Mach number also remains constant.

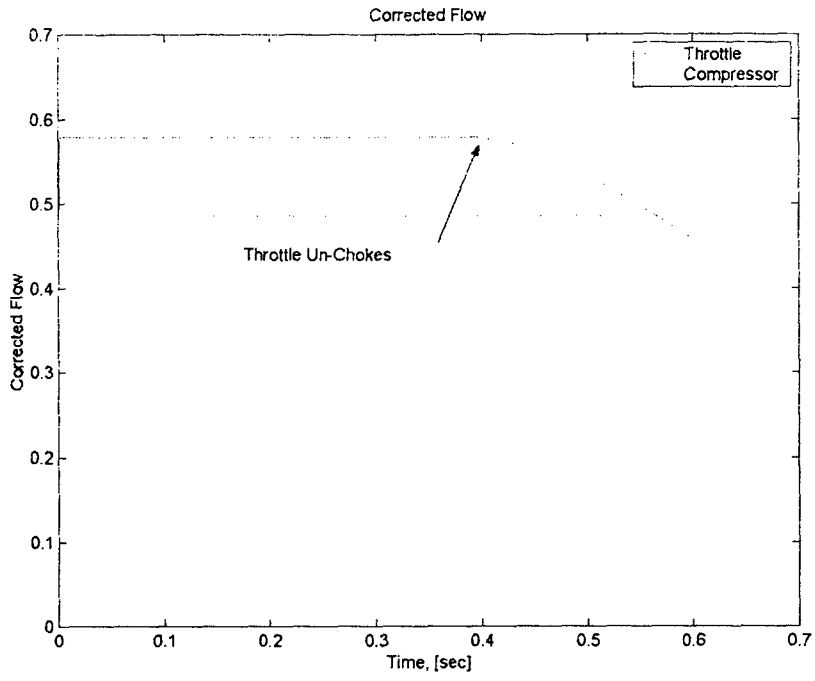


Figure 2.2: Estimated Corrected Flow During Blowdown

2.2.2 Matching Corrected Speed

Taking the derivate of Corrected Speed with respect to time shows that:

$$\frac{dN_C}{dt} = \frac{D}{\sqrt{R_g T_T}} \cdot \frac{dN}{dt} - \frac{ND}{2\left(R_g T_T\right)^{3/2}} \cdot \frac{dT_T}{dt} \qquad \text{Eqn (2.2)}$$

Thus to keep the corrected speed constant during the test it is evident that:

$$\frac{dN}{dt} = \frac{N}{2R_g T_T} \cdot \frac{dT_T}{dt} \qquad \text{Eqn (2.3)}$$

Assuming an isentropic expansion within the tank and choked flow across the pressure screen yields the total temperature of the flow as a function of time expressed by Equation 2.4. The derivation for this equation is in Appendix A.

$$T_T(t) = T_T(0)(1 + t/\tau_b)^{-2} \qquad \text{Eqn. (2.4)}$$

Where τ_b is the blowdown time constant and defined by:

$$\tau_b = \left[\left(\frac{\gamma - 1}{2}\right)\frac{W_{Sc} A_{Sc} \sqrt{R_g T_T(0)}}{V_S}\right]^{-1} \qquad \text{Eqn. (2.5)}$$

V_S = Supply Tank Volume
W_{Sc} = Corrected flow through pressure screen
A_{Sc} = Open area of pressure screen

The power consumed by each compressor stage can be expressed as:

$$P = \dot{m} \cdot C_P \cdot T_T \cdot (\tau_c - 1) = W_{Sc} A_{Sc} P_T \frac{\gamma \sqrt{R_g T_T}}{1+\gamma} (\tau_c - 1)$$

Eqn. (2.6)

Power consumption is related to deceleration of the rotor by:

$$P = -I \cdot N \frac{dN}{dt}$$

Eqn. (2.7)

Solving for the compressor speeds leads to complicated expressions involving the corrected flow, screen open area, blowdown time constant, and inertia. This analysis was previously done for a single rotor by J.L. Kerrebrock [8]. His work showed that the corrected flow cannot be held constant but careful selection of design parameters, primarily the inertias of the rotational systems, can keep the deviation of the corrected speed from the design corrected speed within acceptable limits. Numerical models were used to examine how modifying parameters changed the behavior of the corrected speed of the two rotors. Figure 2.3 shows the estimated corrected speed from the unsteady lumped parameter model for a test of the compressor at the design point.

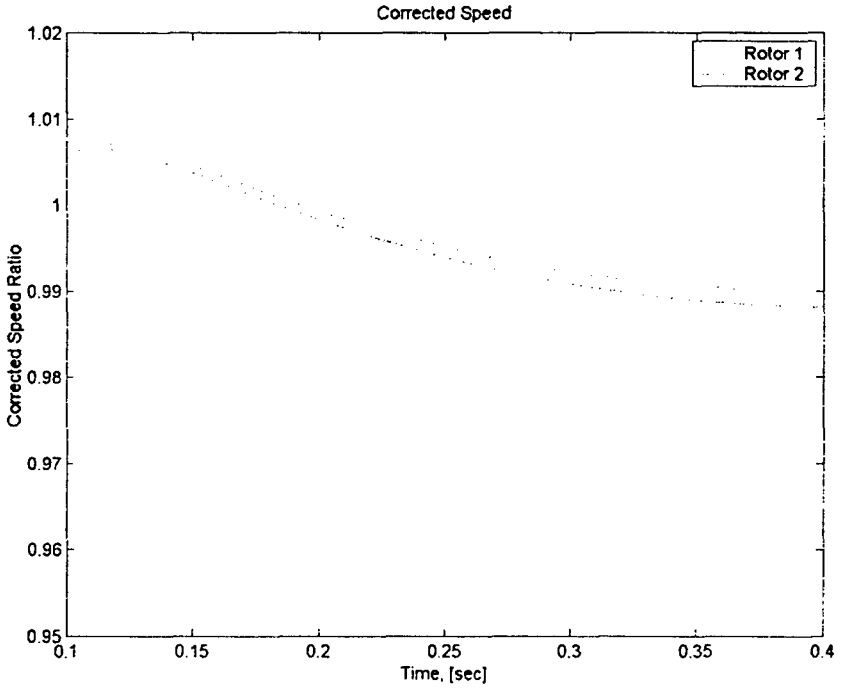


Figure 2.3: Estimated Variation in Corrected Speed During Blowdown

2.2.3 Matching Ratio of Specific Heats

The ratio of specific heats (γ) of the working gas determine the 1-D compressible flow relationships that govern the fluid. The simplest way to match the working gas to the design gas is to use air. Looking at the equation for corrected speed (in Table 2.1) shows

that increasing the molecular weight of the working gas lowers the physical rotor speed for a given corrected speed. Operating the facility at lower physical speeds lowers stresses in the rotors and flywheels. A mixture of carbon dioxide and argon can match the γ of air at a modest price and is 44% heavier than air. Using this mixture there is a concern is that temperature of the supply tank not drop below 220 K during blowdown because of concerns that the CO_2 might solidify. It is also important to note that the mixture ratio is set so that at standard day conditions the ratio of specific heats of the mixture matches that of air. This value changes 2% with the changing temperature across the compressor.

2.2.4 Matching Reynolds' Number

As mentioned earlier Reynolds' number cannot be held constant during the blowdown. It is entirely dependant on the density and velocity into the compressor. Above a certain value changes in Reynolds' number have small impacts on compressor performance. The way to increase the Reynolds' number is to increase the initial supply tank pressure. The initial supply tank pressure is linked to the inertia of the two rotating systems by Equation 2.8, thus along with the benefit of longer test times increasing the available inertia also increases the Reynolds' number.

2.3 Facility Packaging

As shown above, for a given compressor design, there are a limited number variables available to adjust the scaling and maximize available test time. These variables are initial supply tank pressure, supply and dump tank volume, rotational inertia, and throttle area. Throttle area and initial pressure are varied from test to test while volume and inertias are fixed. Selecting these parameters such that they could be packaged in a realizable manner proved to be challenging.

2.3.1 Supply Tank Sizing

Early in the program it was decided to make a minimum number of modifications to the existing GTL Blowdown Turbine Facility because of schedule and a desire for longer test times. The intent was to focus solely on building a new test section. Analysis showed that the blowdown time constant (τ_b) of the Blowdown Turbine Facility would be about four times greater than τ_b of the Blowdown Compressor Facility. Further analysis showed that this configuration would require inertias nearly three times larger than those used in the final design. These simply could not be packaged within the test section so a smaller supply tank was purchased.

2.3.2 Fast-Acting Valve Area

The Fast-Acting Valve separates the test section and dump tank (maintained at vacuum) from the supply tank (at initial pressure) during the spin-up of the rotors then opens

quickly providing a smooth expansion path from the supply tank to the inlet of the compressor. The minimum area of this expansion path is less than the minimum area of the compressor. This means that there would be very high velocity flow within the valve leading to large boundary layers and losses. In order to lower the fluid velocity in the valve (and increase the initial pressure in the supply tank) a screen was placed between the compressor inlet and the valve. This lowers the Mach number in the valve and increases the pressure in the supply tank, improving the operability of the fast-acting valve. The influence of supply tank pressure on the fast-acting valve is described in Section 3.2.

2.3.3 Fitting Flywheels within the Flow path

It was decided to connect the rotor, flywheel, and motor by one shaft because gearing introduces unwanted dynamics to the system. This dictated that the flywheels had to fit inside the inner diameter of the flow path. When one notes that inertia scales as radius to the fourth power it is easy to see that this maximum diameter is a severe constraint on the inertia and ultimately a limit on available test time. Inertia can also be modified, to first order, by changing the length and density. Increasing inertia through length is limited by the shaft and trying to keep the frequency of its first bending mode safely above the operating speed. Increasing the density is limited by available materials and the strength properties of those materials. Section 3.4.2 describes attempts to maximize inertia by using a high-density tungsten nickel alloy.

3 Detailed Facility Description

This chapter discusses the some of the details of the facility. Credit must be given to Dr. J.L. Kerrebrock, Dr. G.R. Guenette, and Prof. A.H. Epstein and others who pioneered blowdown test facilities. Without the experience of those investigators this facility could not have been fabricated on the time scale that it was. Elements of this facility that were not part of other blowdown facilities are the pressure screen and the inertia elements.

The final facility design consisted of supply and dump tanks; gas bottles, vacuum pumps, and a piping system; and a separate test section for each rotor. The tanks and test sections sit on a track system. When bolted together their centerlines are aligned within 0.003 inches and the entire facility can hold a vacuum of better than 100 millitorr, with the vacuum pump running. The Blowdown Counter-Rotating Aspirated Compressor Facility is shown in Figure 3.1



Figure 3.1: Blowdown Counter-Rotating Aspirated Compressor Facility, flow goes from right to left

3.1 Tanks and Accessory Systems

As discussed in Chapter 2 the volumes of the supply and dump tanks set the blowdown time constant and the time that the corrected flow through the compressor is constant, respectively. The dump tank is the same tank that was used for the Blowdown Turbine Facility. It has a volume of 570 ft^3 and can safely hold pressures up to 60 psia. The supply tank was specifically sized for this project. It has a volume of 157 ft^3 and can safely hold pressures up to 100 psia. The dump tank is bolted to the floor and serves as a datum for the assembly of the rest of the facility. The supply tank sits on wheels that mount to a 12 ft wide track and can travel up to 10 ft.

Vacuum is pulled through four inch pipes by an industrial pump that is capable of pumping 150 cubic feet per minute. Each tank was individually vacuum tested and were pulled down to about 60 millitorr.

The working gas in the facility is a 51.09%-48.91% mix (by mole) of Argon and Carbon Dioxide. There is a bottle farm for each gas. The piping system that connects the tanks, vacuum pump, and bottle farm is controlled by a series of solenoid actuated ball valves. The facility operator is capable pulling vacuum on one or both of the tanks, filling the supply tank to a specific pressure, and venting one or both of the tanks through two vents of different sizes. In the event of a power failure the valves are set in a manner so that both tanks and the bottle farm (if open) will vent to atmosphere, avoiding a dangerous over pressurization of the tanks.

3.2 Fast Acting Valve

The Fast Acting Valve was designed and built in 1981 by Guenette. The valve was designed to open in less than 50 ms, seal a pressure of 10 atm. in the tank against vacuum in the test section, provide a smooth expansion path for the gas exiting the tank, and operate in temperatures up to 530° F. The pressure and temperature requirements of the valve are less stringent for the CRAspC facility. The operating temperature is the ambient 70° F and the operating pressure is around 2 atm.

The valve consists of an outer annulus, a slider cone which seals against the outer annulus and a pilot cylinder which holds the actuators that move the slider. Figure 3.2 is a sketch of the valve. Inside the pilot cylinder is a pneumatic actuator that can hold the valve closed and initiates the acceleration of the slider. The slider is made of mild steel and weighs about 100 kg. In order to open the valve in 50 ms a force between 10,000 and 20,000 lb is required for accelerating the slider. A more detailed description of the valve can be found in "A Fully Scaled Short Duration Turbine Experiment" [9].

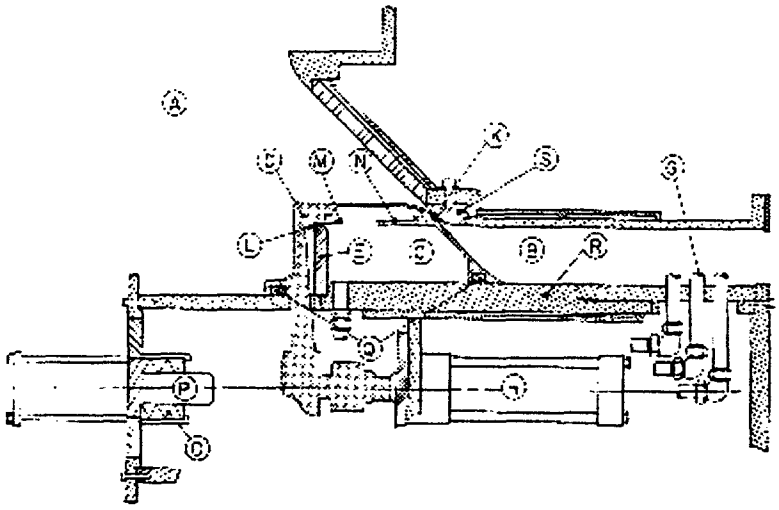


Figure 3.2: Schematic drawing of the Fast-Acting Valve [9]

There are three stages for the valve opening. These three stages are illustrated in Figure 3.3. The first stage is when the pneumatic actuator is fired, this opens the valve slightly. At this point the pressure in the chamber behind the slider is ~0 and the pressure on the dump tank side of the valve is the same as the pressure in the tank. This creates a large force that accelerates the slider. Next the chamber fills so that there is no pressure difference and the slider coasts. Finally the gap in the chamber closes so that as the slider moves backwards the gas in the chamber is compress and the slider decelerates. On the pilot cylinder there is a series of springs to absorb any energy still in the slider before it runs out of travel.

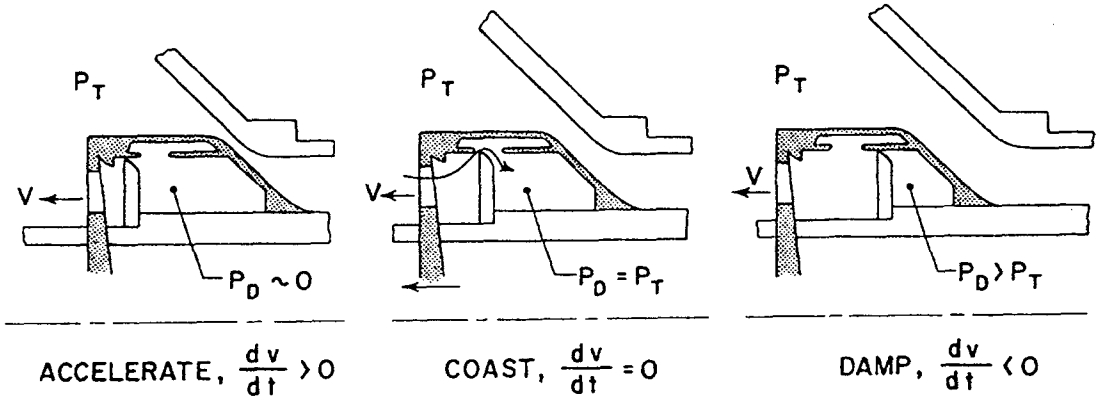


Figure 3.3: Sequence of events for the Fast-Acting Valve while opening [9]

Operating the fast acting valve with tank pressures of between 30 and 40 psi presented two challenges. The first was that there was less force available for use in creating a seal. To improve the seal two steps were taken. First, all elastomer o-rings in the valve were replaced and a seal plate that had been damaged was also replaced. Second, operational

procedures were modified and pressure inside the pilot cylinder was used to press the valve shut. Experiments showed that after the modifications, with 200 psi in the pilot cylinder and 1 atm in the supply tank, a vacuum of less than 100 millitorr could be maintained in the test section and dump tank.

The other challenge was that because of the lower pressure there was less force available for accelerating the slider and less gas in the chamber for damping. This problem was addressed by modifying the pressure in the pilot cylinder used to open the valve.

3.3 Test Sections

There is a separate assembly for housing each rotor and its flywheel and drive motor. Each section consists of flow paths, instrumentation ports, and the rotating assembly. Figure 3.4 shows details of both sections. Each assembly sits on a stand that moves along a track that is aligned with the track the supply tank runs on but is narrower in width. The tip casing is mounted into the aft section and acts as a guide when the forward section is bolted to the aft section. Elastomer o-rings are used at all interfaces to provide seals when pulling vacuum.

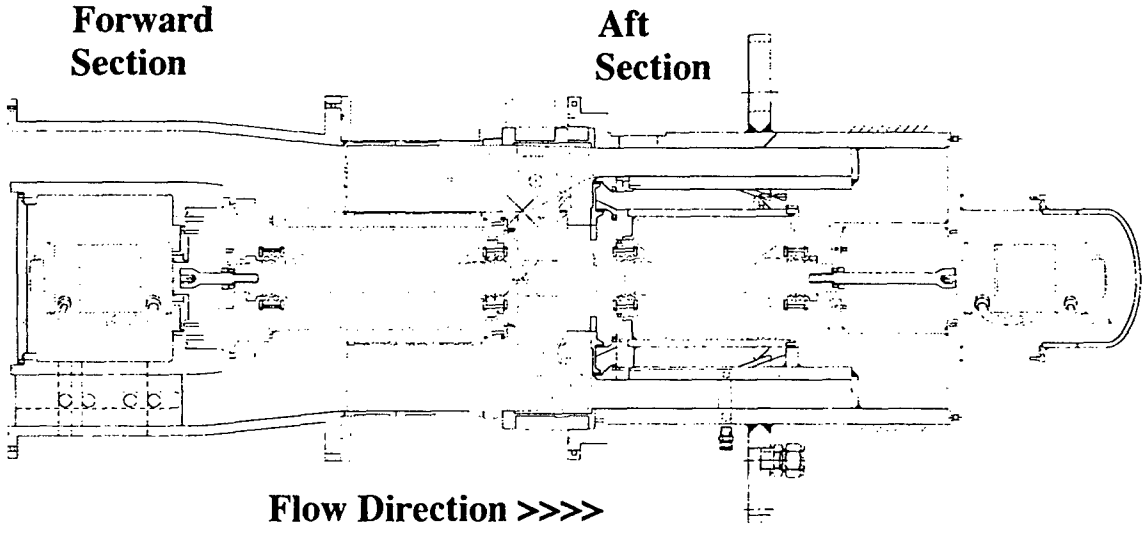


Figure 3.4: Sketch of Both Sections

3.3.1 The Forward Test Section

The forward section is shown in Figure 3.5. Important aspects of the design of the forward section are the pressure screen, the cantilevered nature of the housing for the

flywheel, and choosing tolerances of critical interfaces so that the appropriate parts were concentric about an axis.

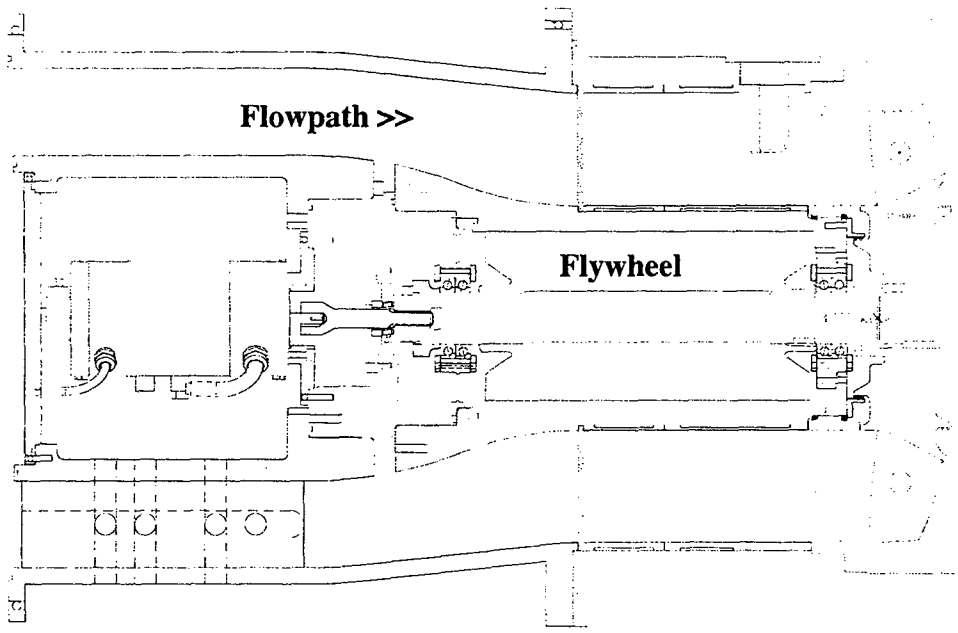


Figure 3.5: Forward Test Section

3.3.1.1 Vibration Analysis

The only connections between the inner and outer annuli of the forward test section are three thirteen inch long struts near the valve that are aligned with struts in the valve. Struts were not used at the rotor end of the test section because of a desire to keep the flow entering the compressor uniform. Early in the design process Dr. Michael Glynn, of the MIT Lincoln Laboratories, created a basic 3-D model of the test section and analyzed the vibration modes, natural frequencies, and static deflections of the test section. This analysis proved to be critical and lead to several design changes. Figure 3.6 shows the first vibration mode of the original forward test section design. This mode is one where the rotor bounces up and down. The frequency of this mode was 151 Hz (9060 rpm) which is lower than the 14,000 rpm design speed of the first rotor [10]. To solve this problem the struts were made longer and the slope where the inner diameter of the flow path is reduced from the valve ID to the first rotor ID was increased. Stiffness of a cantilevered beam decreases as length cubed. Changing the slope made the entire assembly shorter, therefore stiffer, increasing the frequency of the first mode so that it is greater than the design speed of the rotor.

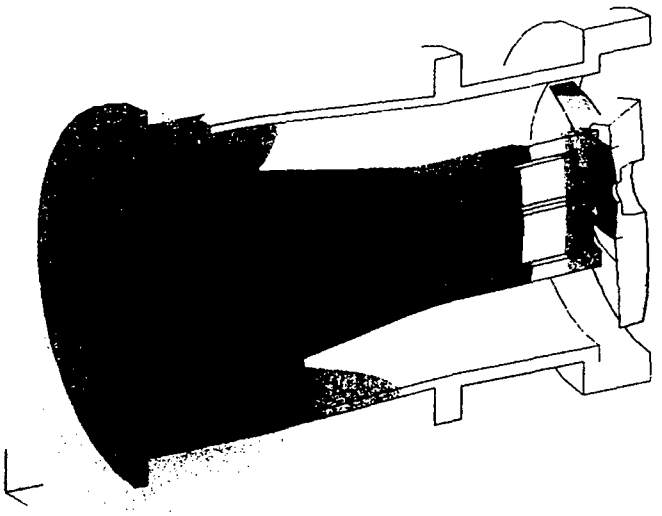


Figure 3.6: First Mode - 151 Hz (9060 RPM) [10]

3.3.1.2 Pressure Screen

The requirements of the pressure screen are that it must have the correct total pressure loss, pass the correct mass flow, and provide uniform flow to the compressor. Literature showed that sub-sonic jets exiting perforated plates required a length of about 40 hole diameters to mix out and that sonic jets exiting perforated plates required about 80 hole diameters to mix out [11]. The first attempts focused around using two subsonic screens with a combined pressure ratio between 2 and 3 (upstream total pressure to downstream total pressure). A handbook for pressure losses through various flow obstructions was consulted [12]. After investigation it was decided that the flow seen by the screen was not in the range of that described by the handbook, therefore a more reliable solution could be obtained with a choked screen. While the screen is choked the conditions entering the compressor are determined by the corrected speeds of the two rotors because they are supersonic and choked, not the supply tank pressure. The biggest challenge in designing the pressure screen was finding a commercially available stamped sheet of steel with small enough holes and but thick enough to withstand the pressure difference. The limiter on the thickness was the diameter of the holes. As the diameter of the holes decrease the thickness of the sheet that the dies can punch through decreases. It was found that for the same hole diameter the sheet thickness could be increased by using mild steel instead of hardened steel. The stress in the perforated plate goes as the inverse of the thickness cubed [13]. It was found that even though the mild steel has a yield stress that is almost half that of the hardened steel the stress in the plate decreased to a safe level because of the increased thickness.

Before the rotating assemblies were in the test sections the pressure screen was installed and run through several blowdowns with increasing dump tank pressures to verify the strength of the plate and determine the discharge coefficient. During these tests the only element controlling the flow was the choked screen. Stagnation pressures were measured

upstream and downstream. The thermocouples were too valuable to risk in these tests so it was assumed that the tank temperature and pressure were related isentropically. The mass flow through the tank was estimated from the pressure history in the tank. The discharge coefficient was calculated from the mass flow rate of the air exiting the tank. During preliminary calculations the discharge coefficient was assumed to be 0.62, from the tests it was calculated to be approximately 0.73.

3.3.2 The Aft Test Section

The aft test section is shown in Figure 3.7. Differences between the aft and forward sections include separate flow paths to the dump tank for the main flow and bleed flow and an absence of cantilevered structures. After the exit measurement plane flow disruptions like struts are acceptable, allowing for a much stiffer structure. The canister that holds the rotating assembly was designed so that it could fit in the assembly fixture used for the Blowdown Turbine Facility.

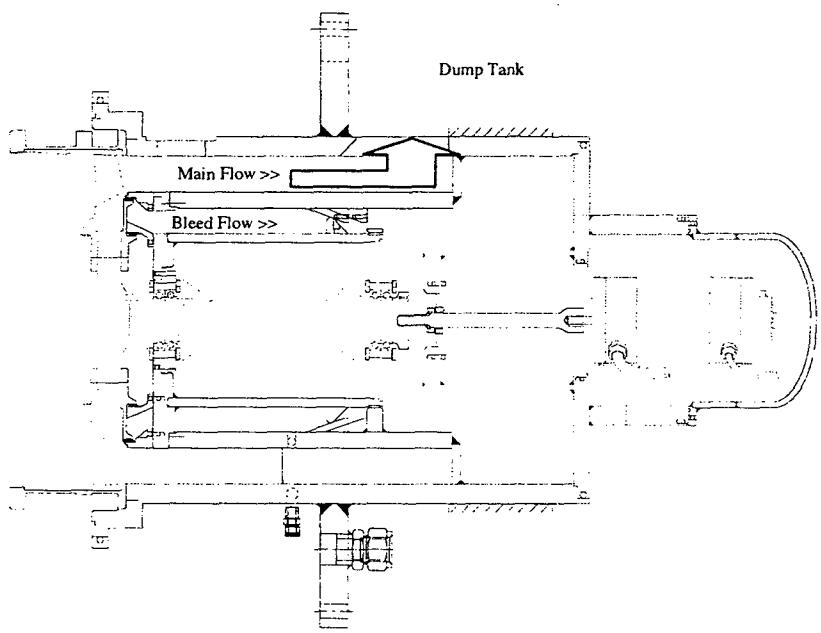


Figure 3.7: Aft Test Section

After exiting the root of the blades of the second rotor the aspiration bleed flow is kept separate from the main flow by two labyrinth seals. The bleed flow then passes between the main flow and the flywheel and passes through a variable area orifice that is used to meter the amount of aspirated flow. The bleed flow then passes by the motor housing into the dump tank without going through the main throttle.

The throttle that sets the corrected flow is an aluminum ring that rides on two hardened rods with linear bearings. A third rod is attached to the throttle and exits through the flange. This rod is used to open and close the throttle without disassembling the facility. Measuring the open area of the throttle comes from the displacement of this rod from a set point. A Cajon© fitting is used to seal the area around the rod and hold the throttle in place.

3.4 Rotating Assemblies

The rotating assemblies of the forward and aft test sections are very similar and will be discussed together. Important dimensions such as the bearings, tolerances, and drive motors are identical. Dimensions such as the rotational inertia and shaft lengths vary slightly between the two assemblies. Figure 3.8 is the forward rotating assembly and Figure 3.9 is the aft rotating assembly.

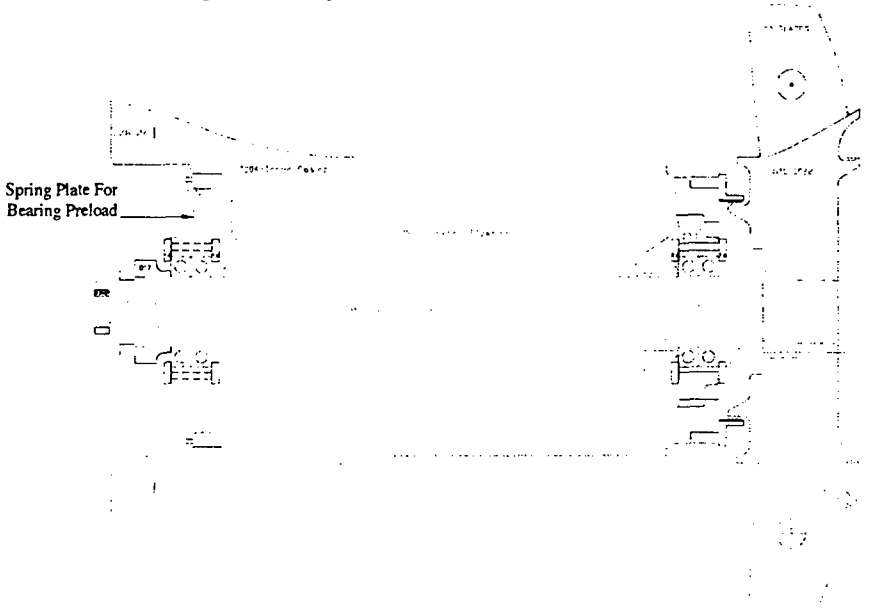


Figure 3.8: Forward Rotating Assembly

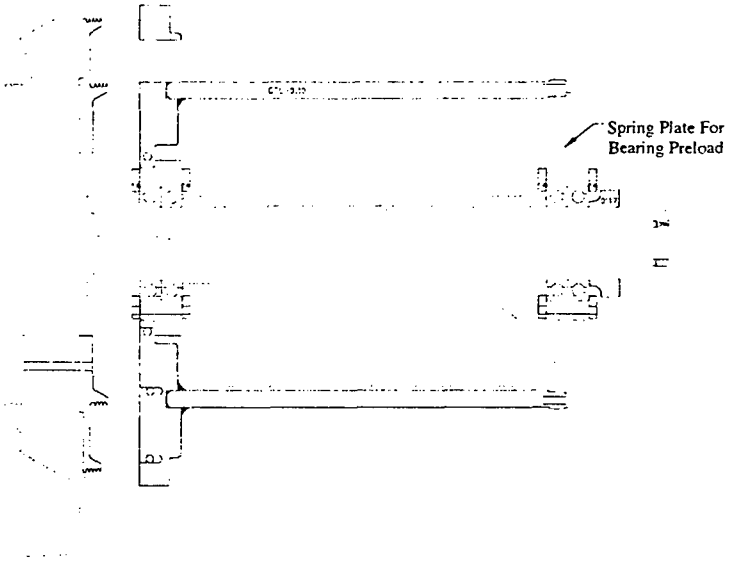


Figure 3.9: Aft Rotating Assembly

3.4.1 Bearings and Drive Shaft Assemblies

Choosing the proper bearings is critical to the operation of the test facility. The choice of what bearings to use was primarily based on experience from previous Blowdown Compressor Facilities. Fafnir super precision angular contact bearings were chosen. These bearings have angular contacts which makes them very stiff under axial loads. The rotors generate axial loads during operation so it is important that the bearings are stiff enough that the rotors do not move, possibly into each other, during the blowdown. The bearings are dual tandem mounted for maximum stiffness. Dual tandem mounting means that the thrust surfaces of both bearings in the pair face the same direction. This provides increased thrust loading capability in that direction. Two pairs of bearings are used for each shaft and the pairs are mounted in opposite directions.

The rated static radial loading of the bearings is 6,860 lbf. The rated permissible speed is 13,600 rpm. The design speed of the first rotor is 13,800 rpm; greater than the rated bearing speed. GTL experience had shown that during blowdown testing bearings can be operated beyond their rated range because of the low number of cycles they experience. A bearing with higher rated speed was available by decreasing the shaft diameter 5 mm. Vibration analysis showed that decreasing the shaft diameter reduced the frequency of the first shaft bending mode below the operating speed of the rotor. During shake-down testing the rotating assemblies were brought to their design speeds without incident. The expected life of the bearings was not calculated because the design speed was greater than the rated speed and expected number of cycles on the bearings was expected to be on the order of $8x10^5$, low compared to typical bearing applications. This corresponds to ~20 tests plus 30 minutes of facility shake-down tests.

One important aspect of the operation of the bearings is the amount of grease that is used. Minimizing heating in the bearings is important to prevent melting of the balls. Too much grease increases heat generation in the bearings. Not enough grease results in too much friction. GTL experience has shown that the proper amount of grease is about one dab (~0.1 g) of SKF LGLT 2/0.2 grease per ball.

At operating speed radial forces generated by the balls in the bearings, combined with the angular contact surface, generate an axial force that tends to separate the inner and outer races resulting in bearing failure. The bearings need to be preloaded to prevent this separation. The bearing manufacture recommends different levels of force for preload. The lightest was selected to limit friction and heating. The axial preload force is created by a spring that doubles as a bearing mount (labeled in Figures 3.8 and 3.9). Sixteen 0.75 inch holes were drilled in the 0.062 inch thick membrane to tailor the axial spring constant. Finite element analysis predicted, and tests confirmed, that the springs have a stiffness of 50 lbf per 0.001 inch. During assembly measurements were made of the spring-bearing assembly and of the distances to each mating surface. A spacer ring was then made to create the correct displacement of the spring when the shaft nut is tightened.

When everything is touching there is approximately 100 lbf of pre-load on the bearings. The aft spring is shown in Figure 3.10 with the bearings.

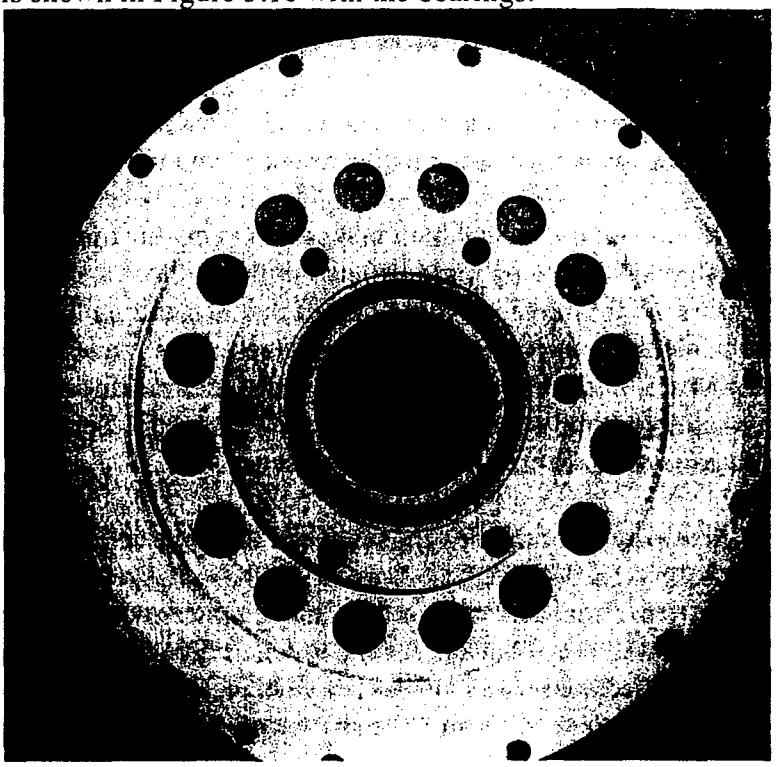


Figure 3.10: Aft bearing and spring-plate assembly

3.4.2 Flywheel Design

Designing the flywheels to maximize the inertia within the size constraints, and minimizing forces due to imbalance, required a considerable amount of effort. Various high density materials were investigated including tungsten alloys and depleted uranium. Flywheels made of tungsten-nickel alloy, which would have operated super-critically on springs, were designed and manufactured. The strength of the alloy billets was less than reported by the alloy manufacturer and they burst near design speeds during over-speed tests. The flywheels were then redesigned and made with 17-4 PH stainless steel. The steel flywheels have a lower inertia and were designed in such a manner that springs were not required.

3.4.2.1 The Tungsten Solution

3.4.2.1.1 Material Challenges

As mentioned above multiple high-density materials were investigated for maximizing the flywheels inertia. An alloy of 97% tungsten and 2% nickel was selected. The tungsten had a high density (~2.5 times more than stainless steel), a high advertised yield strength (85,000 psi), and the nickel made it machinable. Both flywheels burst at a stress condition of approximately 35,000 psi, approximately one third the predicted yield stress. The author believes that the lower stress at which it burst is due to two factors. The first

factor is that tungsten is a brittle material, therefore the statistics of the stress for failure have a larger variation than a ductile material. These statistics for the specific alloy were unavailable to the author. Second, the billets were relatively large. This could have led to problems in adequately controlling the sintering process. The billets were ultrasonically inspected. In the forward flywheel no voids were found and in the aft flywheel 8 voids ranging from 0.020 in. to 0.032 in. were indicated. The manufacturer of the billet indicated that voids this small should not deteriorate the strength of the billets [15]. Figure 3.11 is a piece of one of the flywheels after bursting.



Figure 3.11: One piece of a tungsten flywheel after bursting.

3.4.2.1.2 Design Challenges

Another challenge in designing the flywheels was establishing a way to maintain centrality during operation. At design speed the bore of the flywheels grew nearly 0.0005 inches more than the shaft. Without something to keep the flywheel centered a clearance that large would lead to an imbalance force of ~1,500 lbf. A cyclic force this large is unacceptable, especially considering that the bearings operate at their limit. Many options for centering the flywheel were investigated. Most involved trying to clamp onto the flywheel at a larger diameter, none of these were satisfactory. The chosen solution was to operate the flywheels 'super-critically'. The flywheels were to be attached to the shaft by plates, given the name Inertia Centering Plates (ICP), with spiral arms cut out of them that made the plates radial springs. Figure 3.12 shows one of the ICPs.

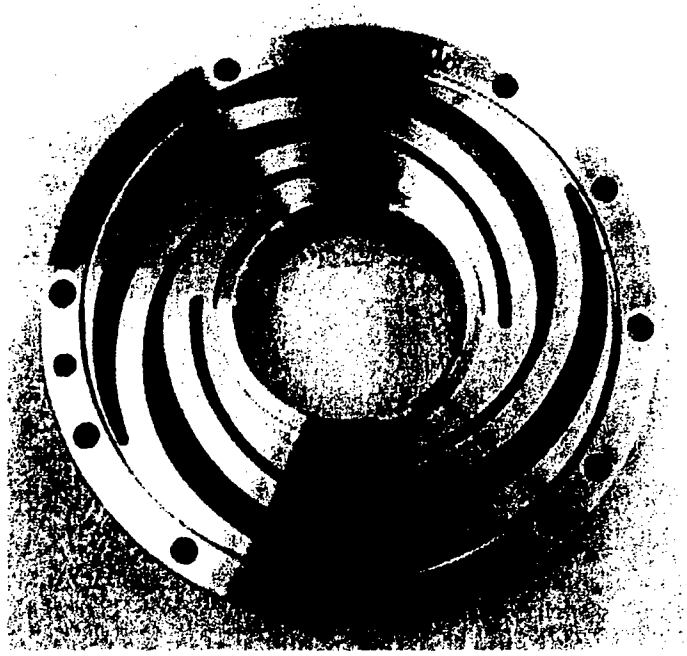


Figure 3.12: One of the Inertia Centering Plates

The goal was to operate the flywheels between the first and second vibration modes of the spring and flywheel system. Vibration theory shows that after going through the critical frequency the response of the system to a cyclic input decreases as the frequency of the forcing increases [14]. In this system the cyclic force is a result of an un-avoidable imbalance in the flywheel. The radius of the bore of the flywheel was designed to be 0.003 inches larger than the radius of the shaft. A gap is necessary to allow the flywheel to move and settle to a steady operating condition during the acceleration. The gap size was selected with the constraints that it be small to minimize the force on the bearings while passing through the critical frequency and larger than the static deflection of the flywheel on the springs. The mass of the flywheel, combined with the desire that the critical frequency be ~1/4 the design speed, set the necessary stiffness of the flywheel.

Dr. Michael Glynn was asked to perform the Finite Element Analysis of the ICPs. Figure 3.13 shows the estimated stress in the final design of the springs. After three design iterations it was found that the radial stiffness of the springs of the springs was approximately linear with the following dimensional grouping of design variables, referred to as the 'geometric constant': $K \propto \frac{E \cdot I}{\alpha \cdot R^3}$ Where E is the elastic modulus of the material, I is the bending moment of a cross section of the arms, R is the radius of the arms, and α is the angle that the arm extends across. After this relationship was established the next design met the requirements for radial stiffness. Figure 3.14 is a plot of predicted stiffness from FEA vs. the value of the geometric constant.

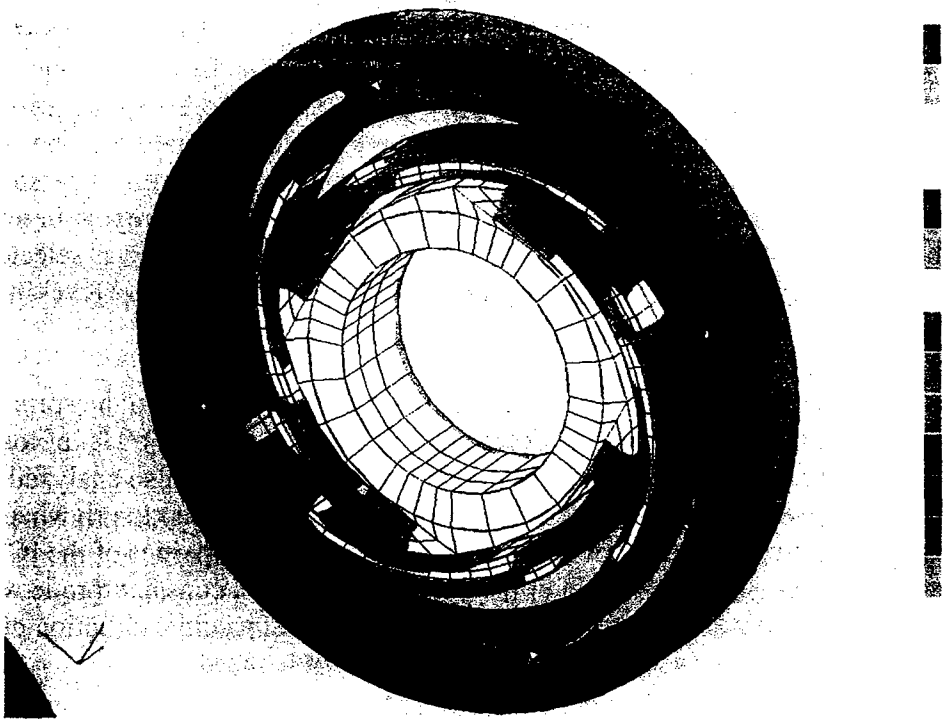


Figure 3.13: Von-Mises Equivalent Stress (psi) in the ICPs [10]

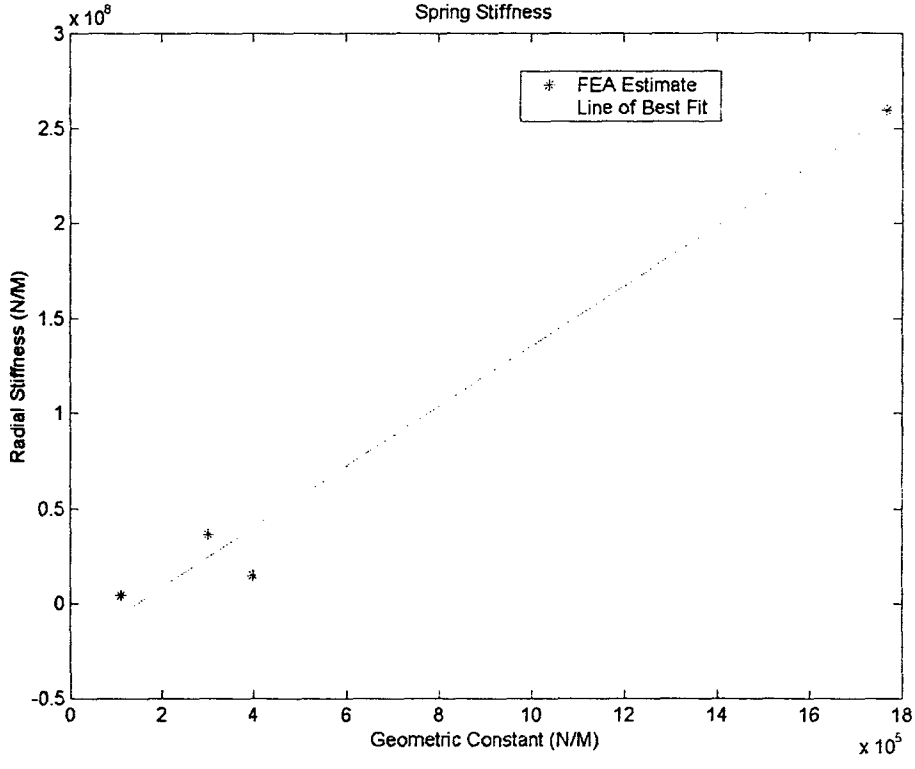


Figure 3.14: FEA Estimate of Spring Stiffness for Different Geometries

Near the hub of the springs there is a tight radius where the spring arms attach to the hub. In these areas the stress from supporting the flywheels is large. There is also a stress that results from torque that transfers rotational momentum from the flywheel to the compressor. Depending on the direction that the torque is applied the spiral arms are placed in either compression or tension. The compression/tension nature of the stress due to holding the flywheel is independent of the direction of the spiral arms. The stresses are assumed to be linear in nature so adding a compression stress to a region in tension lowers the stress level in the material. The direction of the spiral arms was selected so that when the torque from the rotor was applied it lowered the total stress level in the ICP.

The ICPs were designed to be a spring in the radial direction but, due to the spiral design, they are also torsion springs. During the test they essentially see a 1,000 ft-lbf torque in the form of a step function. The rotational stiffness of the ICPs was also analyzed by Dr Glynn. A simple model was developed with two rotational elements (the flywheel and the rotor/shaft system) connected by a torsion spring with the properties of the ICPs. The system was given the initial condition of the design speed and a constant torque was applied to the rotor. It was found that although there was a sinusoidal variation of the rotor speed the variation was less than 1% of the mean rotor speed.

Analysis predicted that as the flywheels passed through the critical speed approximately 850 lbf and 630 lbf would be imparted to the shaft and bearings by the forward and aft flywheels respectively. Balancing the flywheels to better than 1 oz-in would limit the imbalance forces at full speed to 315 lbf and 220 lbf (Forward, Aft). Unfortunately, the material failed during over-speed tests, and the operation of the system in the blowdown rig was never observed.

3.4.2.2 The Steel Solution

After the tungsten flywheels burst using tungsten was abandoned because of time and economic constraints. 17-4 PH stainless steel, heat treated to an H1150 condition, was chosen as a substitute material because of its well known properties and high strength. The lower density of 17-4 decreased the inertia and required that the facility be run with a lower initial pressure in the supply tank, reducing the expected Reynolds' number. Also the method of running the flywheels super-critically was not an option with the steel flywheels because the lower mass increased the critical frequencies to an unacceptable speed.

The bore of a steel cylinder with the dimensions of the flywheels, rotating at the design speeds, grows ~7×10^{-4} and 5×10^{-4} inches (Forward, Aft). While less than the growth of the tungsten flywheel this is still too much. During the re-design process it was noted that the growth of the bore goes as the outer radius squared. By having a section at each end that is only ~ 3/8 in. thick the growth of these lands is almost negligible. Furthermore, not all the material above these lands had to be removed, just enough to separate the lands from the material at the higher radii. This meant that the removed material, at the lower radii, has a small impact on the inertia. Without the ICPs the

flywheels can be made slightly longer further increasing the available inertia. Figure 3.15 is an outline of the forward flywheel.

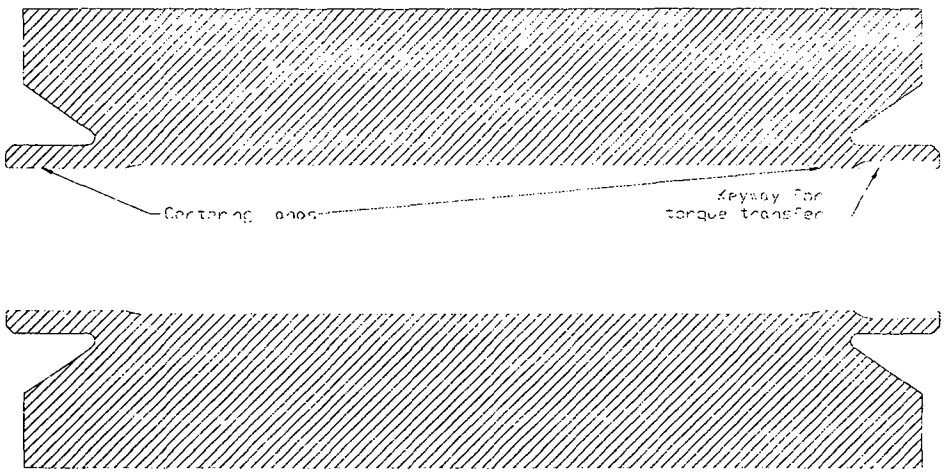


Figure 3.15: Forward Flywheel

Finite element analysis showed that the radial growth of the lands is in fact slightly negative. This is shown in Figure 3.16, the FEA of the forward flywheel. The pinching in of the centering lands is a result of material above them pulling upwards. During the initial shake down tests of the rotating systems no imbalance problems were experienced.

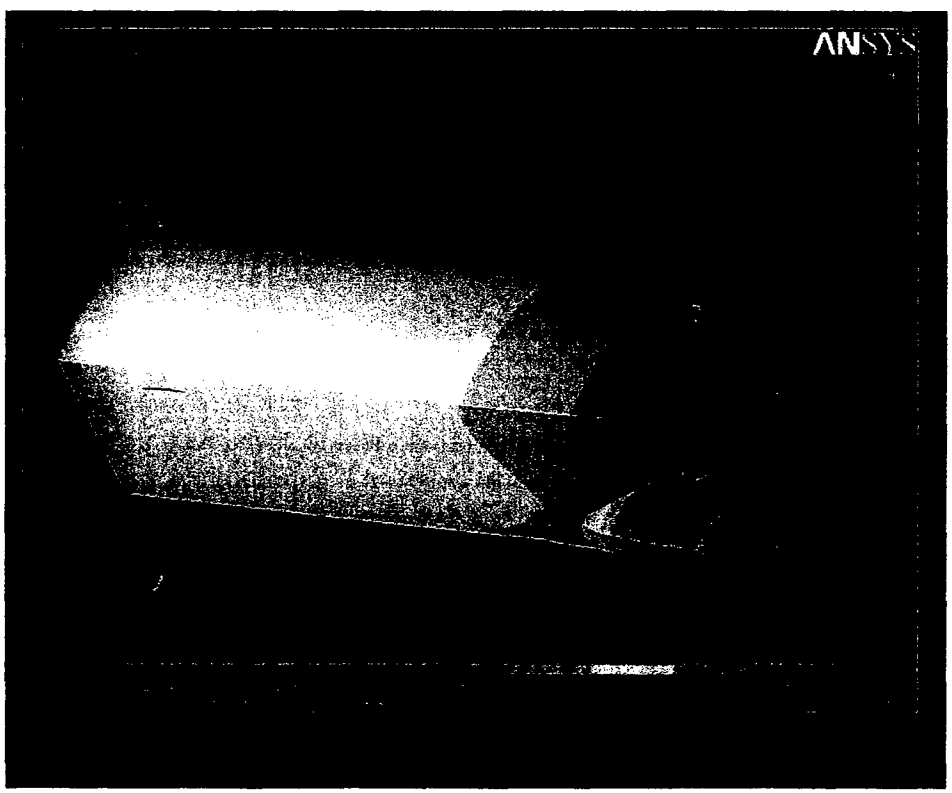


Figure 3.16: Radial Deflections of the Forward Flywheel (m)

The most significant challenge involving the stainless steel flywheels was encountered during assembly. The flywheel and shaft were designed so that the radial gap between them would be 0.0000 to 0.0003 inches. When manufactured there was a slight gap (within tolerance) but they would not go together, partly because they were made of the same material. Because both pieces have the same hardness trying to force the shaft into the flywheel would have resulted in galling. The first step to solving this problem was turning down the shaft, coating it with chrome (a harder material), then re-grinding it to the specified diameter. Then the bores were given another honing pass to increase the diameters by 0.0001 in. Finally the shafts were cooled before being inserted into the flywheels. The shafts can be removed from the flywheels without tooling.

3.4.3 Motors and Motor Control Architecture

The motors used in the Blowdown Compressor Facility are 15 hp motors made by Reuland Electric. These motors use 440 volt AC power. They are rated for 16 amps and 16,000 rpm. Power is supplied to the motors by a Yaskawa GPD-515 motor drive. A LabView© program was written to send commands from a computer to the GPD-515 such as set speed, acceleration rates, 'coast', and 'stop'. The computer that runs this LabView© program is physically located next to the computer that operates the Data Acquisition System (DAQ) so that the motors and DAQ can be run by the same person.

Temperatures in the motors are monitored manually, although the drives have the capability to accept input commands related to overheating this functionality was not used. The motors have six thermocouple outputs. They are located on the motor bearings at multiple locations on the windings. Temperatures in the motors were not allowed to exceed 250 F.

The encoders on the motors were designed for this facility. Each encoder has two outputs; a once per revolution signal and another where the number of pulses is equal to 16 times the number of blades. The number of pulses was chosen so that future high speed measurements could be correlated to blade passages.

3.4.3.1 Requirements for Motor Operation

The motors are cooled with cold process water and must operate in air because of internal lubricants. The rotors must be in vacuum to bring them to speed with a 15 hp motor therefore there needs to be a mechanical seal between the motor housing and the rest of the test section. This seal is created with a carbon face ring where the main shaft mates with the quill shaft. The carbon face seal can be run dry but a thin layer of Shell Turbo T68 oil was placed on the face during assembly. Water lines, power cables, encoder signals, and thermocouples are fed into the motor housing through four ¾ inch holes in one of the struts of the forward section. This meant the welds for these struts had to be vacuum tight. Figure 3.17 shows the forward motor housing with support hoses coming through the strut. These lines for the aft motor are brought in through 1 inch flex tubes connected with Swagelock© fittings.



Figure 3.17: Forward motor housing, showing water and electrical lines through the struts.

3.4.3.2 Motor Control

There were two requirements for motor control in the Blowdown Compressor Facility. First, the motors needed to hold the design speed within 1%. Second, the motors had to be brought to speed and slowed down as quickly as possible to limit the amount of wear on the bearings. Also, the system cannot be allowed to slow down through bearing friction, this would take too long and the heat generated in the bearings could cause them to melt. The drives are able to decelerate the motors. 5,000 Ω resistors are utilized during deceleration to dissipate some of the power.

The motors are controlled by setting a set speed and acceleration schedules. Operators can choose a set speed, high and low speed acceleration rates, high and low speed deceleration rates, and a switching speed. Typically the two deceleration rates are set to the same value. The low speed acceleration is set to the calculated maximum acceleration (based on the available motor power and the inertia of the system), the high speed acceleration is set to a very low value (typically 0.3 Hz/sec), and the switching speed is set to approximately 5 Hz less than the set speed. Switching to a low acceleration rate before the set speed prevents the motor from over-shooting the set speed. At any point while the motor is running the operator can select 'coast' or 'stop'. If 'stop' is selected then the motor is decelerated at a rate that is dependant on the speed

and the set deceleration rate. When 'coast' is selected power to the motor is removed and it is allowed to slowly decelerate due to bearing friction. Typical operation sequence for a test is that the rotors are brought and held at the design speed, the DAQ is then armed, the motors set to coast, and the valve fired. The motors are then used to stop the rotors. Typically it takes about five minutes to bring the rotors up to the set speed.

4 Design and Manufacture of Bladed Components

The primary focus of this chapter is the manufacturing of the bladed components of the Counter-Rotating Aspirated Compressor (CRAspC). The author was involved with the mechanical designs of the blade and managing the production process. The aero-dynamic design is discussed in Section 4.1 because mechanical design and manufacturing decisions must be influenced by the aerodynamic design. The bladed components of the test facility are the Inlet Guide Vanes (IGV), first stage rotor (non-aspirated), and second stage rotor (aspirated). Producing these components required a synthesis of aerodynamic design, structural analysis, and advanced manufacturing processes.

4.1 Blade Design

Aerodynamic design of the blades in the CRAspC is the work of Dr. Ali Merchant. The methodology and code used to design and predict the performance of aspirated blades was developed by Dr. Drela and Dr. Merchant from first principles. Unlike most industry designs there was no database of previous design knowledge to use in designing these stages. The designs were also analyzed by Dr. John Adamczyk of NASA Glenn using APNASA, a 3-D viscous code.

4.1.1 Counter-Rotation Benefits and Challenges

The pressure rise across an axial compressor is a result of the change in angular momentum of the fluid. Typically between stages the swirl is removed from the flow by stators. By not removing the swirl and counter-rotating the next stage a much larger change in angular momentum can be achieved with lower physical speeds. A common method for conceptualizing the change in angular momentum for a stage is velocity triangles. The velocity triangles for the counter-rotating compressor are shown in Figure 4.1 [16].

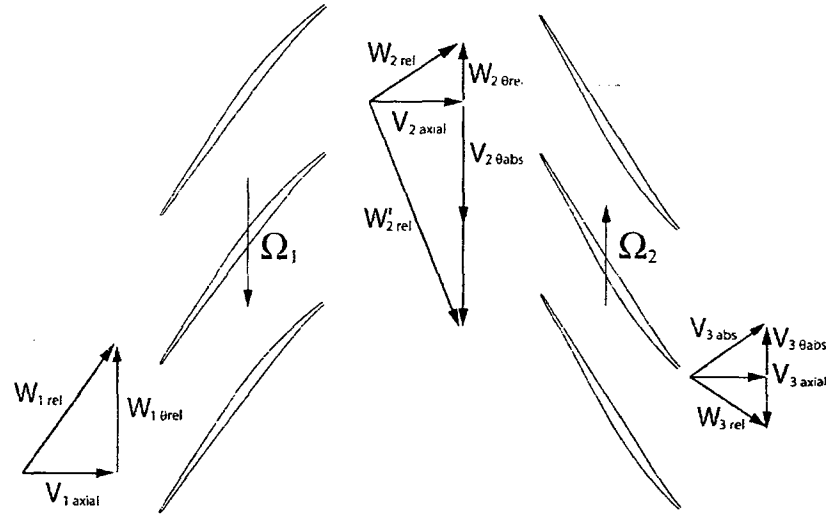


Figure 4.1: Velocity Triangles for a counter-rotating compressor [16]

The benefits of counter-rotation have been known since at least the 1950's with the Curtiss-Wright Counter-Rotating Compressor [1]. To date attempts at counter-rotation have been unsuccessful. The characteristics of the flow that have prevented success are high relative Mach numbers in the second rotor, separation (typically indicated by high diffusion factors), sensitivity to shock un-start, and finally matching the two rotors is more difficult when the stator between them is removed. Section 4.1.4 discusses how predictions show that aspiration might be a solution to these difficulties.

4.1.2 Inlet Guide Vanes

The Inlet Guide Vanes were employed to introduce a slight counter swirl into the hub of Rotor One. This increased the loading at the hub of Rotor One and decreased the loading of the hub of Rotor Two; increasing the overall performance of the machine. Above the hub the IGV does nothing to modify the flow. Figure 4.2 shows the hub, mid-span, and tip streamlines of the IGV.

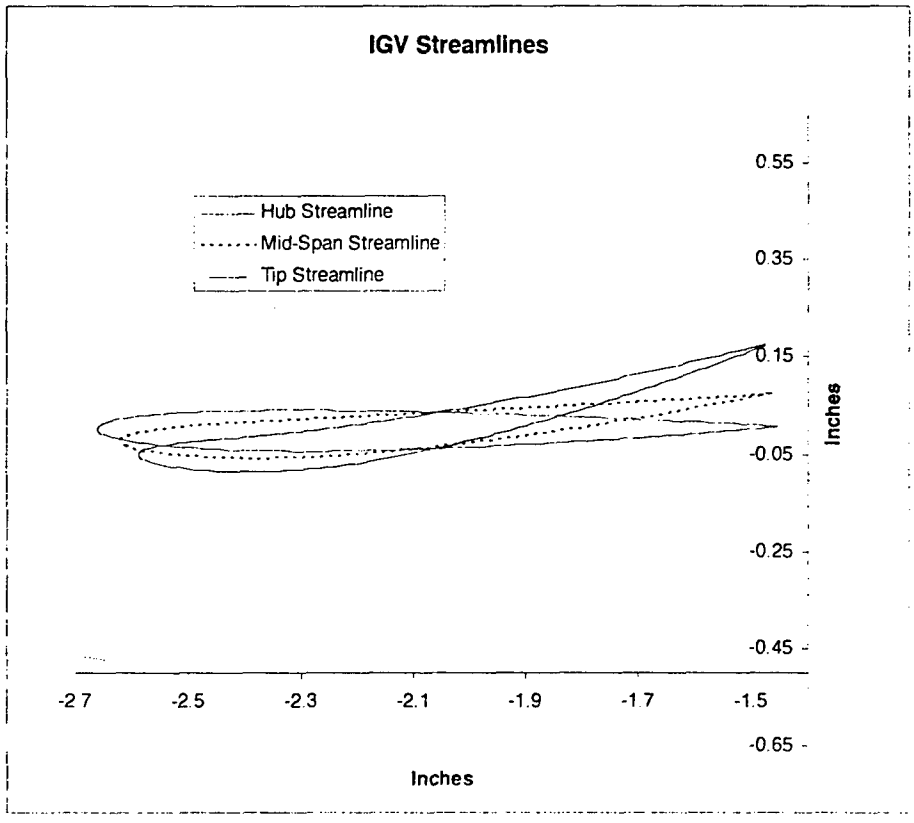


Figure 4.2: Streamlines that define the Inlet Guide Vanes

After it was decided to use an IGV there was a need to be able to measurements across an entire IGV pitch in the downstream measurement plane. This is due to IGV wakes passing through both rotors. In previous Blowdown Turbine experiments a translator was built that moved the downstream instruments circumferentially so that the circumferential variation due to the nozzle guide vane wakes could be measured. Designing and building

the translator requires a large amount of time and resources that were unavailable. It was believed that by placing the IGV on bearings, and tailoring its inertia for a certain acceleration rate, that the translator could be replaced. Fundamentally there is no difference between a rotating IGV with stationary probes and a stationary IGV and rotating probes. During early shake-down tests it was noticed that while the IGV did accelerate as predicted due to the incoming flow there were interactions with the first rotor that were not modeled that resulted in the speed of the IGV exceeding the rated speed of it's bearings after the test time. In order to maintain a safe operating situation and protect the rotors the capacitance probe that had been used to measure the IGV speed was replaced with an aluminum rod that fixed the IGV in place.

4.1.3 Rotor One

The first rotor is an un-aspirated fan that has supersonic tip relative Mach numbers. Rotor One has 20 blades, a hub to tip ratio of 0.5 and an average aspect ratio of about 1.6. The design tip speed (in air) is 1450 feet per second. The design pressure ratio is 1.92 with a polytropic efficiency of 0.923. Table 4.1 summarizes the aero-design parameters of Rotor One. An important measure of compressors is their diffusion factor (recall Eqn. 1.1). The diffusion factor is a zero-th order indicator of how efficient the compressor will be. Typically, compressors with diffusion factors greater than 0.6 experience separation and unacceptably low efficiencies [2]. The diffusion factor for the first rotor is .48 and the average relative Mach number across the span of the first rotor is 1.26 [16]. Figure 4.3 is the hub, mid-span, and tip streamlines of the first rotor. Figures 4.4 – 4.6 show lines of constant Mach number within the rotor passage for three different streamlines.

Table 4.1: Rotor One Aero-Design Summary [16]

Rotor One Stage Aero-Design	
N Blades	20
Hub to Tip Ratio	0.5
Tip Speed	1450 fps
Polytropic Eff.	0.923
Aspect Ratio	~1.6
D Factor	0.48
Pressure Ratio	1.92
$\Delta H/U^2$	0.34

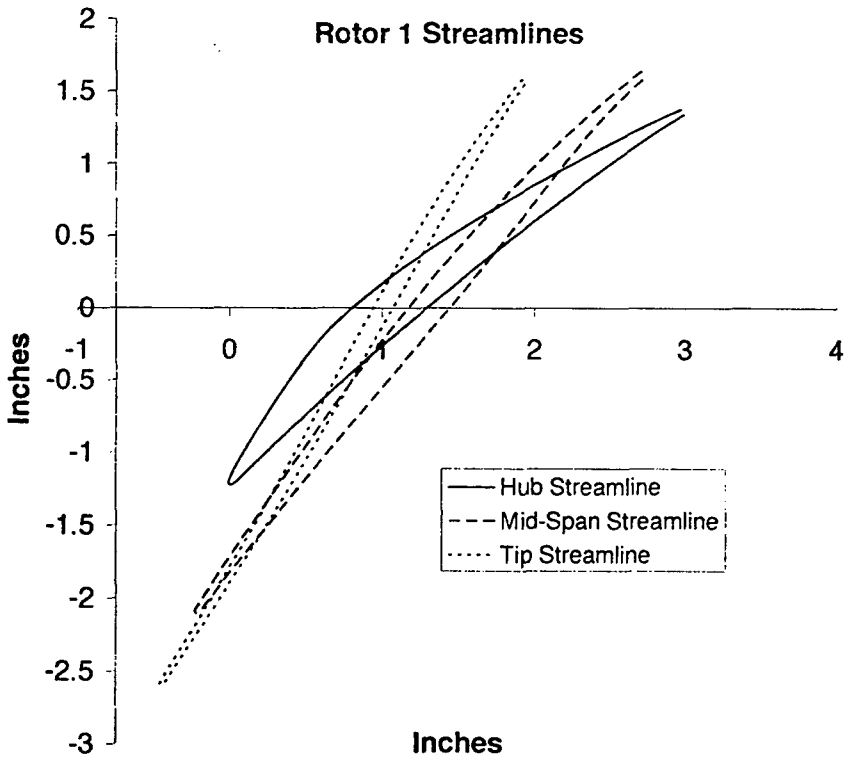


Figure 4.3: Rotor One Streamlines



Figure 4.4: Relative Mach Number Contours of Rotor One at Hub, D=0.53 [17]

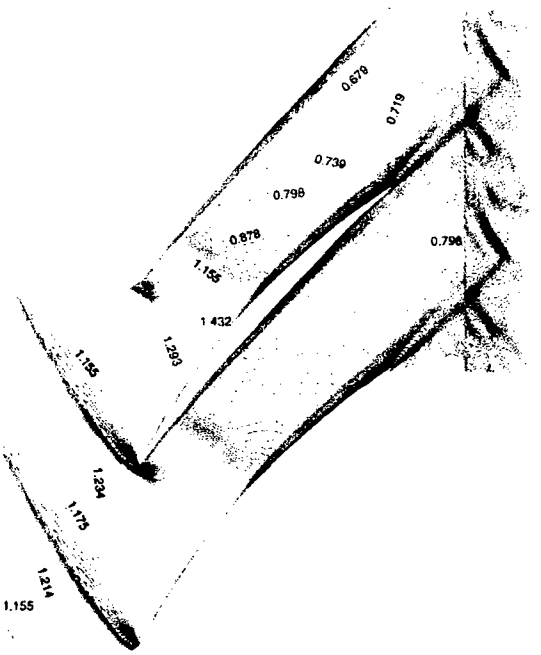


Figure 4.5: Rotor One Relative Mach Number contours, Mid-Span [17]

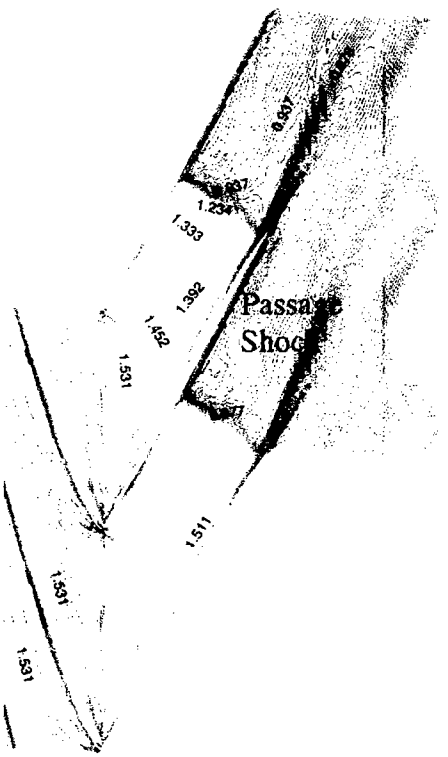


Figure 4.6: Rotor One Relative Mach Number Contours, Tip [17]

4.1.4 Rotor Two

The second rotor is aspirated and the flow is supersonic relative to the blade across its entire span. Rotor Two has 29 blades with an aspect ratio of 1.75 and operates at a tip speed of 1150 fps. The pressure ratio is 1.6 with a polytropic efficiency of 0.902. The diffusion factor for this stage is 0.52, higher than rotor one and typical compressors [16]. Approximately 1% of the stage inlet mass flow is used in aspiration. CFD results indicate that aspiration technology is a solution to many of the hurdles in counter-rotation. First, aspiration removes low-momentum boundary layer fluid which delays or even prevents separation effectively increasing the range of diffusion factor available to a designer. This concept is illustrated in Figure 4.7. Second, as with supersonic inlets, the aspiration slot sets the shock position within the rotor passage. This is illustrated in Figures 4.9 – 4.11. Figure 4.8 shows three streamlines for the second rotor.

Table 4.2: Rotor Two Aero-Design Summary [16]

Rotor Two Stage Aero-Design	
N Blades	29
Hub to Tip Ratio	0.7
Tip Speed	1150 fps
Polytropic Eff.	0.902
Aspect Ratio	~1.75
D Factor	0.52
Pressure Ratio	1.6
$\Delta H/U^2$	.50

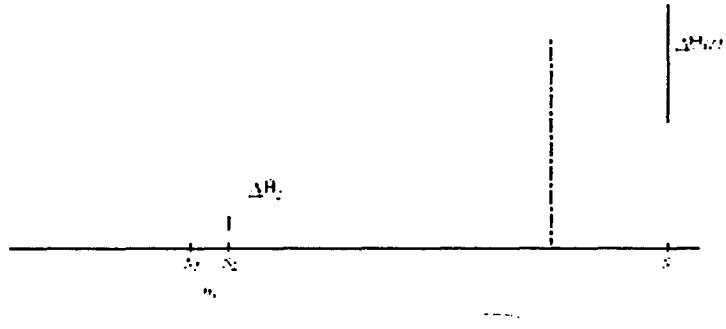


Figure 4.7: Effect of Aspiration on boundary layer growth

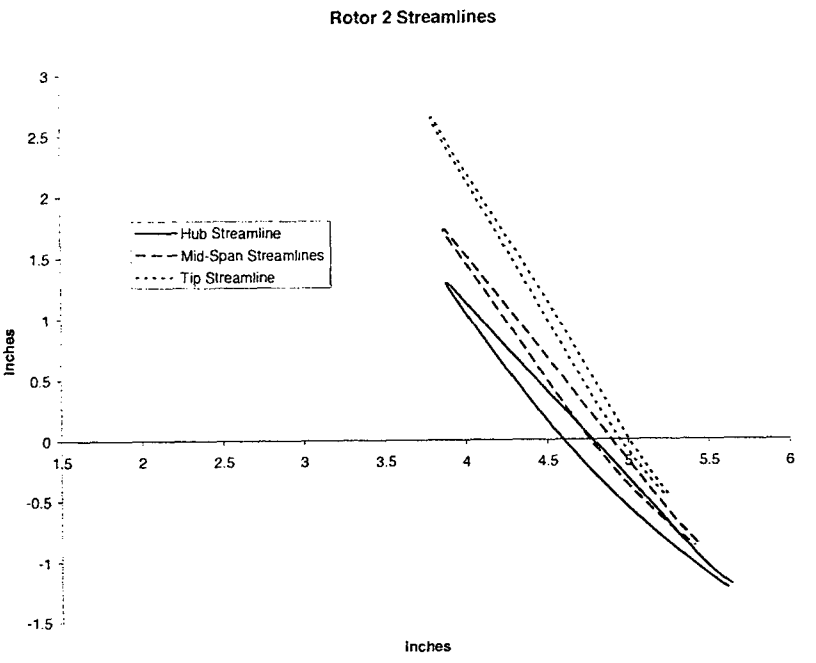


Figure 4.8: Streamlines for Rotor Two

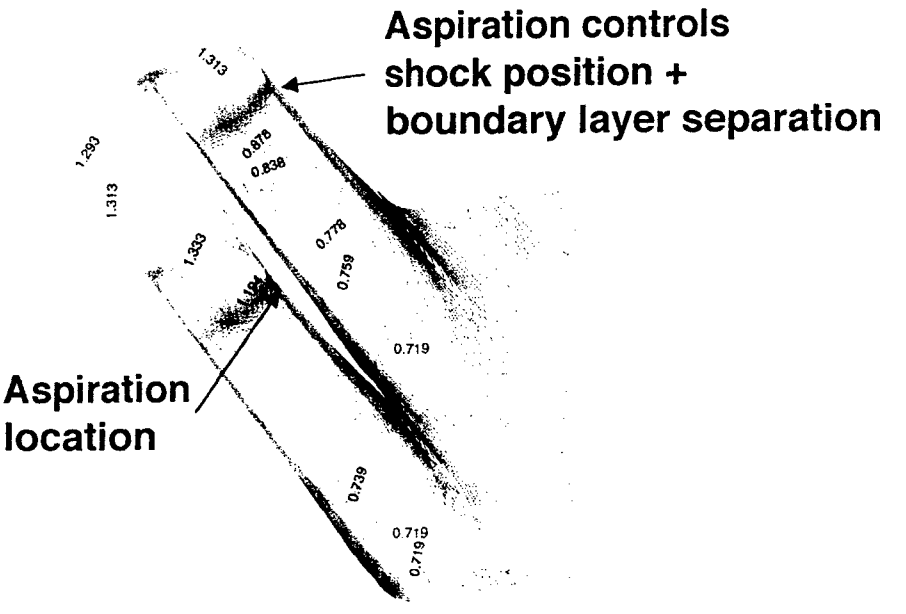


Figure 4.9: Relative Mach Number contours for Rotor Two at hub [17]

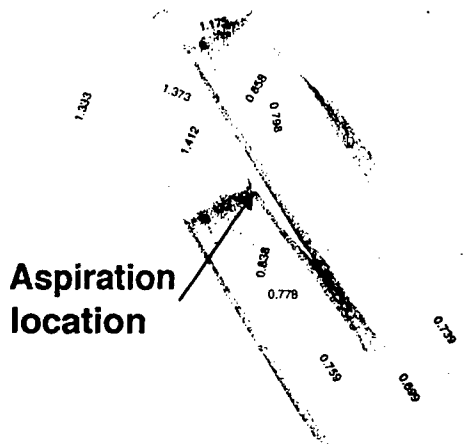


Figure 4.10: Mid-Span Relative Mach number contours, Rotor Two [17]

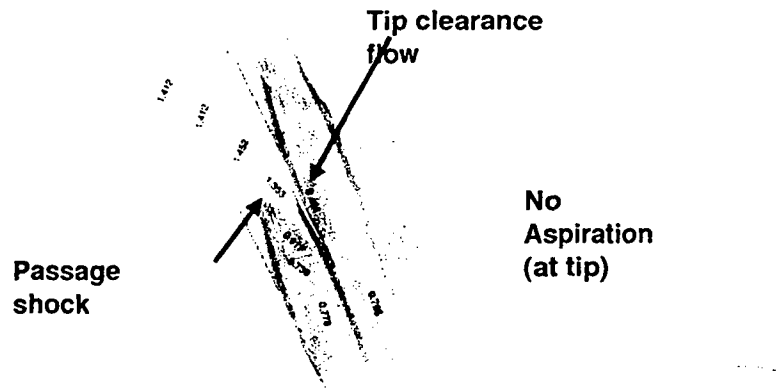


Figure 4.11: Rotor Two Relative Mach number contours at tip [17]

4.1.5 "Hot-to-Cold" Geometry Transformations

It is important to note that the aerodynamic geometry generated by the aero-design codes is not the final data that is used for manufacturing the compressors. When placed under centrifugal and aerodynamic loads the blade geometry changes. The geometry used for manufacture was generated by putting the aero geometry into a finite element code and applying centrifugal and aerodynamic loads in a direction opposite of what the blades experience. Care had to be taken to apply these loads in a non-linear manner because the

as the blade deforms the center of mass changes, changing the effect of the centrifugal loads. In these two rotors the tips grow nearly 0.015 inches and un-twist.

4.2 Five-Axis Machining of Blisks

The IGV and first rotor are both blisks. Blisks, also known as integrally bladed rotors (IBRs), are components where the blades and disk are one piece, typically machined from a forging. Blisks are gaining popularity in use in axial compressors. Blisks reduce part counts, complexity, and eliminate problems of wear at the blade-disk interfaces. For this project using blisks where possible was attractive because it reduced manufacturing cost per rotor by reducing the number of machine set-ups. There are a few variables that determine the cost of the blisk. These are the fillet radius, surface finish, and profile tolerance. Ultimately all of these variables influence machine time.

Figure 4.12 shows the IGV while still on the machine. Normally integrally machining the shroud and blades together makes the process more difficult. This is due to the fact that the part must be flipped at least once (increasing setups), that when roughing material a tool that is not designed for plunging will be expected to plunge, and typically non-optimized roughing patterns are used. However, in this specific case adding the integral shroud for inertia simplified the machining process. The blades have a very high aspect ratio. These long short blades would not provide enough resistance to the cutting forces. The shroud provides another clamped boundary condition and makes the blades much stiffer. Without this holding tolerances on these blades would have been difficult due deflections. Section (4.2.1) gives a more detailed description of how blade mechanics affect the machining process.

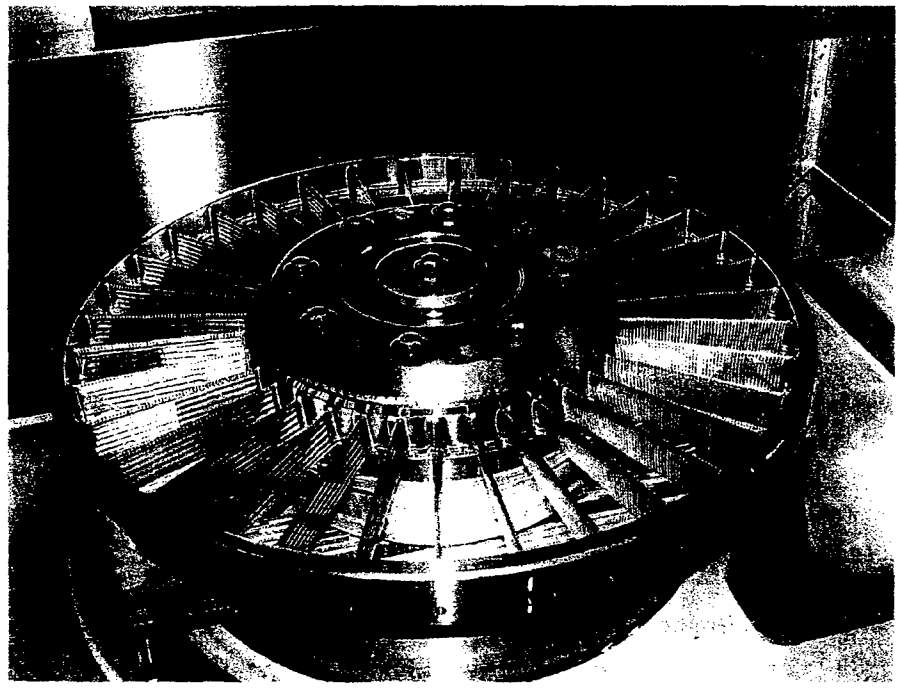


Figure 4.12: IGV while still on the machine

4.2.1 Selection of Profile Tolerance

Profile tolerances are a method of controlling deviations of a three dimensional surface. The best way to think about profile tolerancing is to imagine offsetting the design surface on both sides by the amount of the tolerance. A surface that fits within this envelope meets the tolerance. Figure 4.13 is a two-dimensional sketch of this concept. The profile tolerance for the blades was selected based on the length scale that could be resolved by the CFD design codes and what could reasonably be maintained by the machines that would be used. Table 4.3 lists the length scales of each blade section and the profile tolerance.

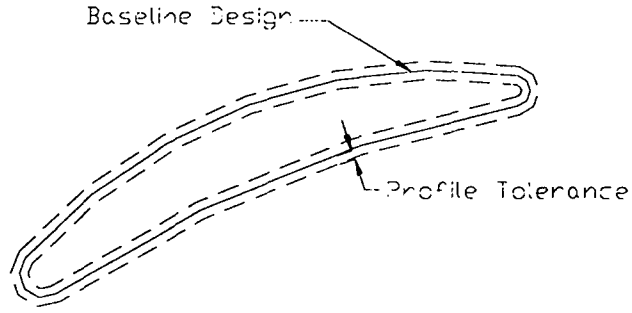


Figure 4.13: Sketch that illustrates the concept of a profile tolerance

Table 4.3 Blade Row Length Scales

Blade Row	Diameter	Chord	Span	Profile Tolerance
IGV	21"	1.14"	5.18"	0.010 in.
Rotor One	21"	4.5"	4.62"	0.006 in.
Rotor Two	21"	3.0"	2.72"	0.004 in.

For the manufacturer holding the blade tolerance is a matter of balancing multiple deflections. First the tool is essentially a beam, when cutting forces are applied to the tip of the tool it bends. The longer the tool is, and normally tool length is a function of blade height, the greater the deflection is. Second, the blade also acts as a beam and bends under the cutting forces. Generally the machine tool path is created so that if everything in the system was perfectly rigid a blade thinner than the design would be produced. The decision for the magnitude of this undercut is based on the blade material, the ratio of tool length to diameter, machine specific considerations and experience.

One of the major developments of the design code that was used for these blades is that it shapes the leading edge in a manner that minimizes shock strength. The controlling feature is not the surface position but the derivatives of the surface profile. A problem

with maintaining profile tolerance is that it does not hold the surface derivatives to the design. If this design concept is to be used in real engines it will be important to investigate how tightly the surface derivatives need to be held to achieve the desired performance. Depending on the result of that investigation new methods of manufacturing, tolerancing, and measurement may need to be developed.

4.2.2 Surface Finish Tolerance

Surface finish is defined as the average deviation of the surface from a mean-line surface. The standard for surface finish, and almost all correlations between surface finish and performance, is based on a 'sand grain finish'. This is a surface that would be created by a typical casting and the value is on the order of the largest grain of the casting die material. Surfaces of machined blades are fundamentally different. These surfaces are often machined with ball endmills, because of they allow better machine dynamics and can hold tighter profile tolerances. Machining with a ball-end mill leaves cusps on the surface, see Figure 4.14. The surface finish of a machined surface is often defined as the measured roughness across these cusps. Cusp height is a function of tool radius and the distance between machine path lines; surface roughness is approximately ¼ of the cusp height.

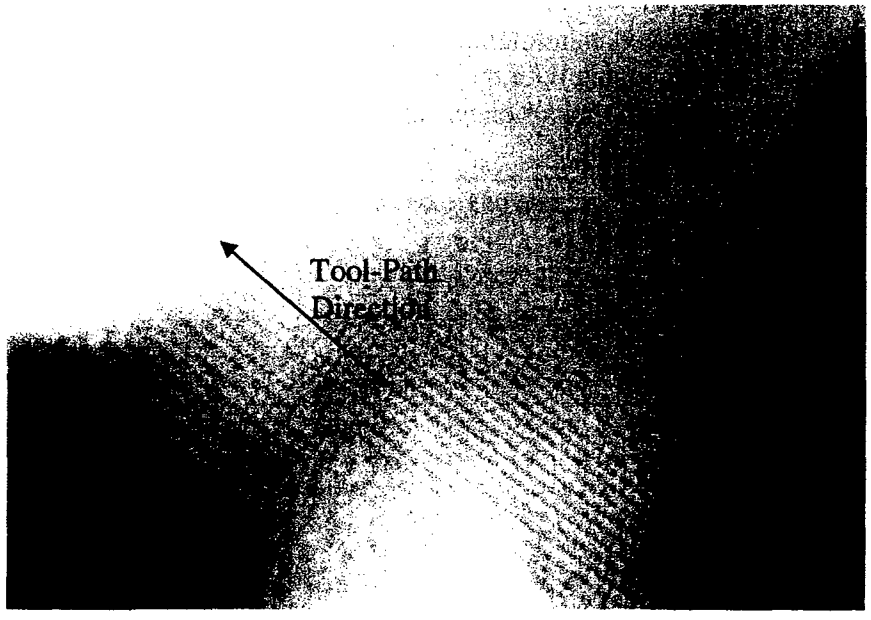


Figure 4.14: Tool markings and surface finish for Rotor One

A surface roughness of 125 μ-inches was specified for the IGV and Rotor One and 63 μ-inches for Rotor Two. This is much rougher than most engine airfoils. The rougher surface finish was chosen because it allowed for significant reductions in machine time and cost. Turbocam, the shop who machined all the blades for this project, has demonstrated that they typically achieve a surface finish of 32 μinches (close to a typical airfoil roughness) parallel to the machine lines. Turbocam was required to machine the blades so that the machine paths were parametrically spaced. This way the machine lines

approximately match flow streamlines, reducing the roughness in the direction of flow. The flow velocity perpendicular to machine lines should be small therefore the cusps should not start thicker boundary layers. An additional benefit of specifying parametric machine paths is that the heights of the blades decrease from the leading edge to the trailing edge. This results in a smoother finish, perpendicular to the cusps, at the trailing edge.

4.2.3 Non-Conformities of Manufactured Parts

The profile tolerance for the first stage was inspected through a process known as "on machine probing". A Renishaw probe was used to interrogate the surface. The blades are inspected while still on the machine so that if the blades are thick measures can be taken to correct them without additional set-ups. Points on streamlines defined the blades for production. A sampling of these definition points were used for inspection.

The drawback of on-machine-probing is that it extends the time on the machine, this makes the process expensive. Five of the first rotor's 20 blades were probed. On each blade three streamlines were probed with 7 points on each side and 4 points around the leading edge. The blades were within tolerance with the exception of the tip streamlines behind the leading edge. Most of these points that were out of tolerance were thick but because the rest of the blade was in tolerance the problem could not be fixed by taking a skim cut. The rotor was accepted with the non-conformities. Figure 4.15 shows the design intent and the probed points of one of these streamlines, Table 4.4 lists the points and their deviation from the design.

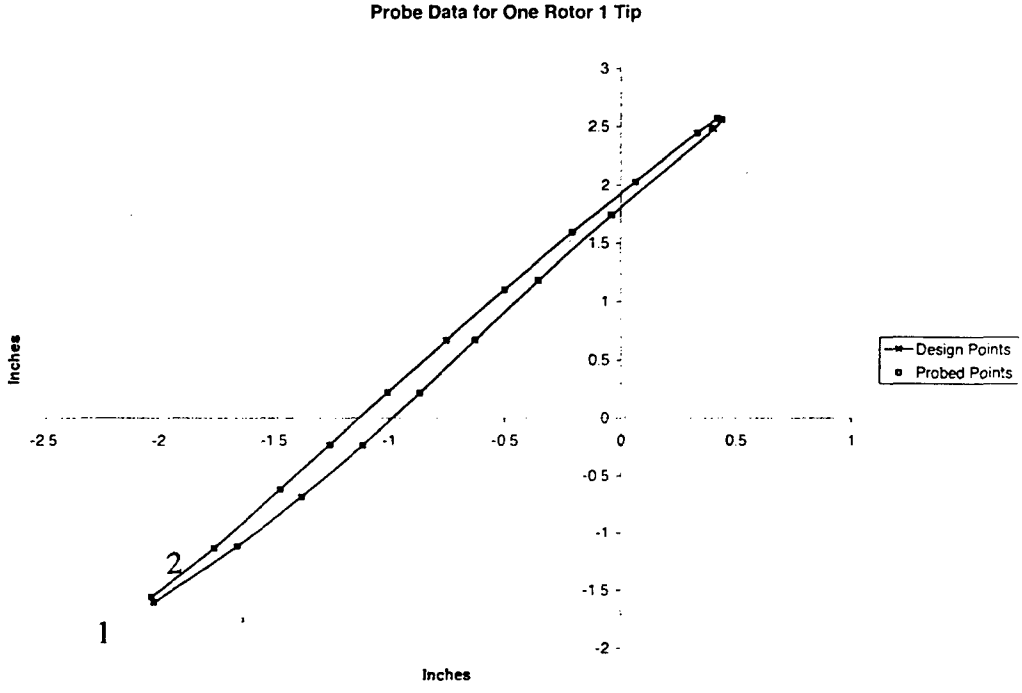


Figure 4.15: Probe data for one stream line of Rotor One

Table 4.4: Probe Data From One Streamline of Rotor One

Point Number	Deviation (in)
6	0.001
7	0.0022
8	0.0023
9	0.0038
10 (LE)	0.0064
11 (LE)	-0.0031
12 (LE)	0.0013
13 (LE)	0.0081
14 (LE)	0.0035
15	0.0023
16	0.0016
17	0.0004
18	-0.0004

4.3 Manufacturing Process for Aspirated Blades

The passage for the aspirated flow in these blades was through the root of the blade. Previous aspirated blades removed the aspiration flow through the shroud. Producing the aspirated blades for the second rotor required an orchestration of several diverse manufacturing and design disciplines including, five-axis machining, electron-beam welding, electric discharge milling, material selection and heat treatment, and finite element analysis. During the process there were multiple set-backs. This section discusses the sources and solutions to these problems, the final process for how the blades were manufactured, and how the blades would be manufactured in the future based on what the author learned from this process.

4.3.1 Challenges Associated with Aspiration

The two causes of most of the issues that were dealt with during the production process were the lean of the blades and the requirement that the aspiration flow be removed without taking it through the tips. In previous aspirated compressors the blades were shrouded and the aspiration flow was removed radially outward. Figure 4.16 is a sketch showing the pathway for the bleed flow through the blade.

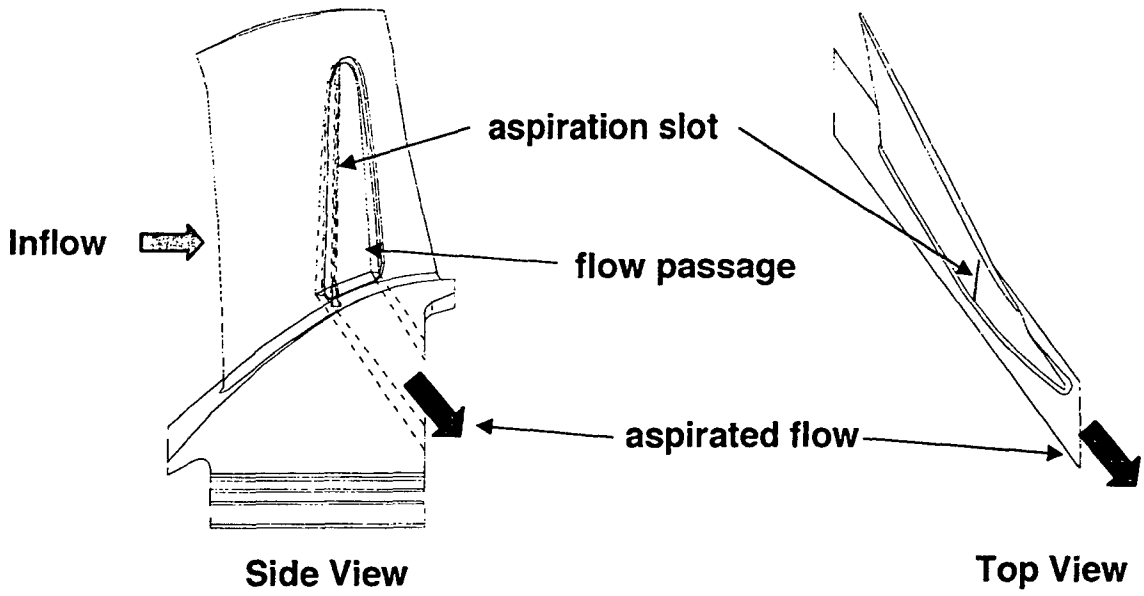


Figure 4.16: Sketch of scheme for removing aspiration flow radially inward [16]

4.3.1.1 Blade Lean and Root Stress

There is about 5° of lean in the second rotor. This lean increases the bending stress in the root, where the blade is attached to the foot. The bending stress is a result of centrifugal forces acting on the center of mass of the blade, which is not radially above the root, and the pressure difference between the pressure and suction sides of the blades. In early designs and trials the aspirated blades were to be made of aluminum. This decision was made because it was believed that using aluminum simplified the design. As a result of aluminums lower density the rotational stresses would be lower, making the design of several critical areas simpler. These areas included the dovetails where the blades fit into the disc, the root of the blade, and the passage through the blade for the bleed flow. Also aluminum would have lowered the cost of the blades through its lower material cost and better machining qualities. During the initial design of the blades it was believed that the only problem with aluminum would be its weld-ability in the electron beam process (more about e-beam welding in section 4.3.2.1). Aluminum alloy 5083 was selected for its welding properties and the experience of the vendor with it.

The problem with aluminum was that it's relatively low yield stress was unable to handle the bending stress in the thin areas of the root near the bleed passage. Throughout the design process it was known that stresses due to rotation were significant compared to the yield stress of the material at the full design speed, it was believed that the stress due to the blade loading would be negligible. During the final stress analysis, performed by Dr. F. Neumayer, it was discovered that the aero loads on the blades increased the maximum stress beyond the ultimate stress of the material. Initially it was believed that, because the highest stresses were near the bleed passage, modifying the passage and increasing minimum wall thickness on the pressure side of the blade could reduce these stresses to

acceptable levels. Figure 4.17 shows FEA results for the aluminum blade. After several iterations it was realized that because the prime contributor to the stress was a bending stress the second area moment needed to be increased, not the area. Modifying the passage only nominally changed the stress. To lower the stress levels below the yield stress would require thickening the blade, requiring a redesign of the aero. This was not an option because of schedule and budget constraints. Turbocam, the machine shop producing these blades, had already been given the geometry and invested engineering time developing the CNC programs. Changing the external blade shape would have required paying them to re-perform this work.

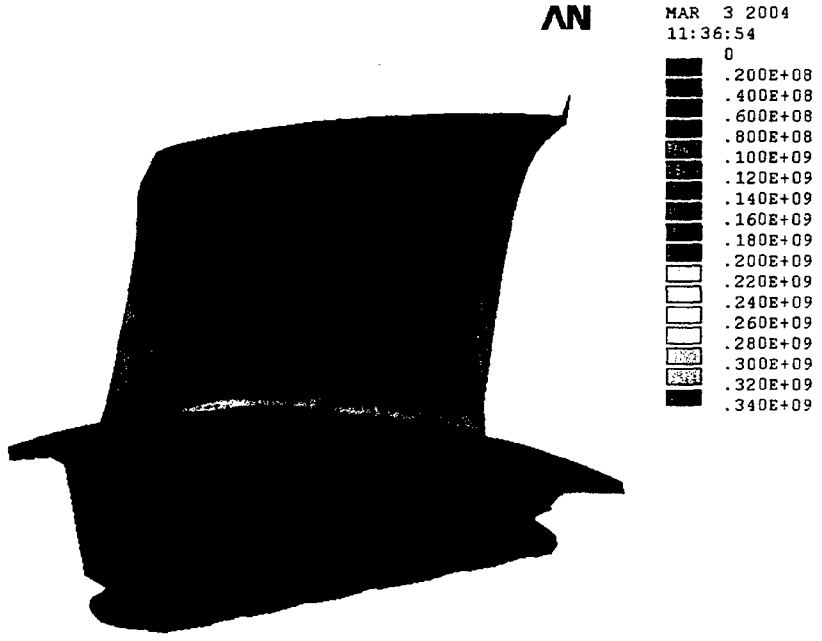


Figure 4.17: Stress in Rotor Two, Pressure Side, Alum.- Yield Stress ~120 MPa (Max 340 MPa) [18]

Instead of modifying the geometry it was decided to change the blade from aluminum to a steel alloy. The finite element analysis was done again with basic steel properties, shown in Figure 4.18. 17-4 PH with an H1150 heat treatment was selected because it's yield stress is high enough to handle the maximum predicted stress. Changing to steel doubled the weight of each blade; this in turn doubled the stress in the dovetails in the disc requiring the addition of a H1150 heat treatment of the disc to ensure that the dovetails would not fail at design speed. The e-beam welding essentially anneals the material and the weld joint is near the area of highest stress in the blade, this required that the blades be heat treated mid-way through the manufacturing process. This is discussed in greater detail in Section 4.3.2.

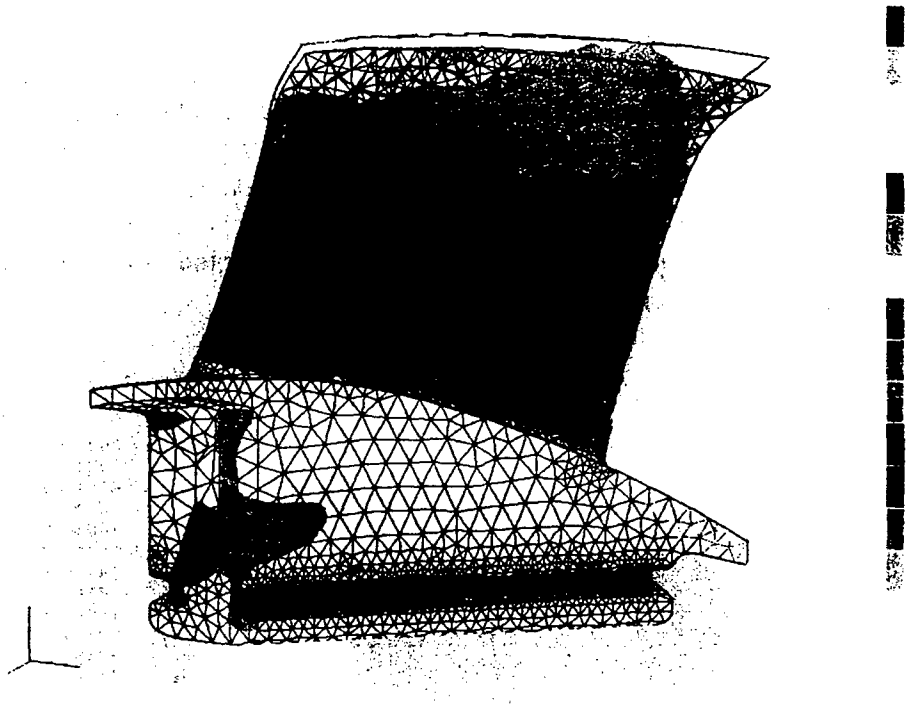


Figure 4.18: Stress in Rotor Two, Pressure Side, 17-4 PH - Yield Stress = 162 ksi (Max 150 ksi) [19]

A material option that was not given much consideration was titanium. Titanium was unattractive because it is a difficult material to machine and the development time of the manufacturing process probably would have been longer. The yield strength to density ratio of aluminum is ~$4X10^4$ m^2/s^2, for 17-4PH steel the value of this ratio is ~$1.4X10^5$ m^2/s^2, and for titanium the strength to density ratio is ~$2.7X10^5$ m^2/s^2. The components of stress due to rotation scale linearly with density thus it is evident that using titanium would have nearly halved the stress in the blades.

4.3.1.2 The Bleed Passage and Plunge EDM

The biggest difficulty in manufacturing the aspirated blades was the passage from the cavity within the blade to the back of the foot of the blade. This passage is approximately 0.080 in wide and 1.0 in long at the blade root and approximately 2 in. deep. The length to diameter ratio of a tool that could fit into this passage to break through to the cavity in the blade would have to be on the order of 30. There is simply not enough strength in tool with these dimensions to machine this passage. The chosen solution was electrical discharge milling (EDM). Electrical discharge milling removes metal by creating an electrical arc between the tool and the work-piece that erodes away the work-piece material. The tool and work-piece are immersed in a dielectric fluid. The fluid between the tool and work-piece must be continually flushed and free of particles otherwise a short circuit is created between the tool and work-piece.

The original design of the bleed passage was a passage that was convergent from the exit to where it meets the pocket inside the blade and was defined by four planes. The

reasoning was that a simple tool could be made that matched this panel, burning material with the tip and sides at the same time. This decision was made with a lack of experience with the EDM process. While the vendor tested the process it was discovered that the method for burning this geometry was to burn up through the center and then use different tools to burn the sides. This process required ~24 hours on the machine. To reduce the cycle time the passage geometry was redefined so that it is a simple projection from the blade root to the back of the foot. A second simple burn was added to widen the passage near where it exits from the foot to match the original geometry.

After changing the passage geometry there were still problems with the process. During the plunge fluid must continually flow past the tool; otherwise the burned particles create a short circuit. During the plunge there is no natural process for creating this flow. One traditional solution to this problem is to make the tool in two halves with a passage in the middle. The dielectric fluid is then pumped into the tool, comes out the center where it is burning, and exits along the exterior of the tool. This method was attempted without success. The tool was too long and thin and the pressure required to drive the flow split the tool at the tip. Attempts were made to weld the two halves of the tool together but this could not be done without bending the tool. The solution was to use EMD drilling to drill from the foot into the cavity and then burn the bleed slots. Then a fixture, connected to a pump, was placed on the side of the blade that was able to pull fluid through the holes, into the cavity, and out the bleed slots. Once this was done a solid tool was used to burn through. The first few blades were used as trials to optimize the burn time through the number and diameter of the holes.

It took between forty-five seconds and a minute to burn one hole, and about eight hours to burn the passage way. In retrospect the simplest, and quickest, way to bring the bleed flow from the internal cavity to the exit in the foot would have been to EDM drill multiple holes. This assumes that enough holes could be drilled to pass the required bleed flow and that the pressure losses across each hole would be acceptable.

4.3.2 Order of Operations

The manufacturing process for the aspirated blades was an integration of three distinct manufacturing methods and material heat treatment management. The process is described in detail below.

4.3.2.1 Rough Machining

Annealed steel is easier to machine than heat treat hardened steel and the e-beam welding process annealed the weld joint. Therefore, the steel alloy was received in an annealed state. The foot and dovetail were machined to finish dimension to create datums for future operations. The pressure side of the blade was rough machined with about 0.020 in. of stock remaining. The pocket for the bleed flow was machined to finish dimensions, as was the interior of the cover-plate for the pocket. The cover plate was also left with

about 0.020 in. of stock on the exterior. The suction side of the blade was not rough machined. In an early trial both sides of the blade were rough machined to within 0.050 of the final dimensions before the cover-plate was welded. It was discovered that there was a deflection of the blade during the weld process. There was so much deflection that the tips of the blade were no longer within the envelope of the finish blade and portions of the blade were missing. This is shown in Figure 4.19. Not rough machining the suction side of the blade left a large mass of metal that prevented deflection and created a way to dissipate more of the heat generated during the welding.



Figure 4.19: Aluminum test blade with section of leading edge due to distortion during welding

4.3.2.2 Electron-Beam Welding of the Cover-Plate

After rough machining the two pieces, blade and cover-plate, were sent to the weld vendor to be joined together. The method used for joining them together was electron-beam welding (EBW). In EBW heat generation for fusing the two pieces of material comes from a stream of electrons generated by a hot cathode and accelerated by a voltage somewhere in the range of 30,000 to 200,000 volts. Typically these beams generate heat on the order of 30 kW/mm^2. The beams are focused and directed to the work-piece by a magnetic field within a vacuum. Welding in a vacuum environment prevents oxidation in the material at the weld. The EBW process has the advantage of being able to weld through joints up to 200 mm thick. The EBW process results in a joint that is homogenous in properties with the rest of the work-piece. Since the weld join will be in or near the blade root, where stresses are highest, the homogeneous nature of an EB weld makes it very appealing for this application. [20]

The only hurdle was the location of the bottom weld. During trials it was discovered that it was difficult to control the position of the weld beam in the corner by the fillet. Both the blade and the root were at the same potential and the beam oscillated between the two. The inability to control the electron beam resulted in the porous weld shown in Figure 4.20. This required that the bottom of the cavity be moved slightly higher in the blade requiring a slightly longer EDM passage from the exit of the foot to the bottom of the cavity.



Figure 4.20: Inadequate weld joints in fillet because of control issues with the electron beam

4.3.2.3 Heat Treat

The material was received in an annealed condition and remained annealed after the welding. After the welding the blades were sent out for heat treatment and heat treated to an H1150 condition. This treatment was selected for its high yield stress and because the material remained machinable after the process.

4.3.2.4 Finish Machining

Following welding and heat treatment the blades were returned to the machine shop where they were machined to finish dimensions. Large amounts of stock, ~1/4 in. were left on the suction side of the blade to ensure that the internal pocket did not move relative to the datum planes used for alignment due to heat stresses during welding. This stock was removed first, then blades were finished with tool paths that were continuous around the blade and parametrically spaced. Similar to the first rotor the surface finish in the direction of the tool paths is better than in the span-wise direction. The surface finish in the span-wise direction was specified to be 63 μin. This is better than the specified surface finish for the first rotor because the second rotor is supersonic across the entire span and more highly loaded.

4.3.2.5 EDM Process

The final step in the manufacturing process of the aspirated blades was to EDM the aspiration slots and the passage from the back of the foot to the base of the interior pocket. As previously mentioned when plunge EDMing there must be a flow of the dielectric fluid around the tool to remove the burnt material and prevent short circuits between the tool and work-piece. This was the primary driver in deciding the order and method of the burns.

Before being placed on the CNC EDM machine several small (0.060 in. diameter) holes were ED drilled from the back of the blade foot into the internal pocket. Changing the number of pre-drilled holes changed the amount of time required to plunge the passage. The number of holes was chosen to minimize the total process time, more was not necessarily better. Next the aspiration slots were burned into the suction side of the blade on a CNC EDM machine. After this step a fixture was clamped onto the surface of the blade so low pressure could be applied to the aspiration slots and pull fluid through the drilled holes, into the blade cavity and out through the aspiration slots. This flow path was crucial to keep fluid moving past the tool as it plunged and burned the exit passage. In total the EDM processes required three different fixtures and about 10 hours per blade. As mentioned previously it is believed by the author that the better way to connect the blade cavity to the foot exit is by using the ED drilling process to drill as many holes as needed to get the proper flow area.

4.3.2.6 Assembly and Balancing

The second rotor was assembled at the GTL. Each blade was placed in a supersonic bath and then cleaned with pipe cleaners. This was to ensure that there was no debris within the aspiration passage that might be jarred loose during operation and possibly end up in the bearings. This process yielded nothing except for a little residual soot from the EDM process. After cleaning each blade was inspected and weighed. They were then placed in the disc in an order that accounted for variation in masses and resulted in a minimum imbalance. The calculated imbalance due to blade non-uniformity was 20.4 gram-inches. The rotor was then balanced on a dummy shaft in two planes so that the final imbalance was less than 1.4 gram-in. The assembled aspirated rotor is shown in Figure 4.21.



Figure 4.21: Aspirated Rotor after assembly and balance

5 Instrumentation and Data Acquisition

The primary measurement goal was to determine the adiabatic core efficiency of the compressor with less than 0.5% uncertainty. This chapter discusses the instruments and data acquisition systems used in the facility.

The efficiency of a compressor is defined as the inverse of the work required by the compressor to achieve a certain pressure ratio divided by the work required to achieve that pressure ratio in an isentropic process. If adiabatic operation and constant thermodynamic fluid properties are assumed and the working fluid is an ideal gas then the adiabatic efficiency of the compressor is:

$$\eta_C = \frac{\pi^{\frac{\gamma-1}{\gamma}} - 1}{\tau - 1} \qquad \text{Eqn. (5.1)}$$

where τ is the ratio of total temperatures and π is the ratio of total pressures. Thus to measure the efficiency the inlet and exit total temperatures and total pressures must be known. The accuracy that they must be measured with is discussed in Section 6.4.1 and detailed in [5].

5.1 Measurement Locations

Upstream of the compressor there are six instrument windows, three pairs separated by 120°. One of each pair is a window of 'singles'. These windows each contain one mid-span total temperature measurement, one mid-span low frequency total pressure measurement, one low frequency wall static pressure measurement, and at least one of the windows contains a pitot probe manufactured by United Sensor Corp., also positioned at the mid-span. In addition to these single measurements there are two span wise rakes, one that measures total temperature and another that is a low frequency total pressure measurement. The bodies of these rakes were machined so that they had an aerodynamic profile that minimizes the disturbance into the compressor.

Similar to the upstream measurement plane the downstream measurement also has six measurement windows that have the same circumferential positions as the upstream windows. Downstream of the compressor the span-wise height is 43% of the upstream annulus height. The required diameter of the heads of the downstream thermocouples results in requiring two downstream rakes to achieve similar measurement density downstream and upstream. Therefore, downstream there is only one window of singles. Figure 5.1 shows the location of all the instruments on the rig.

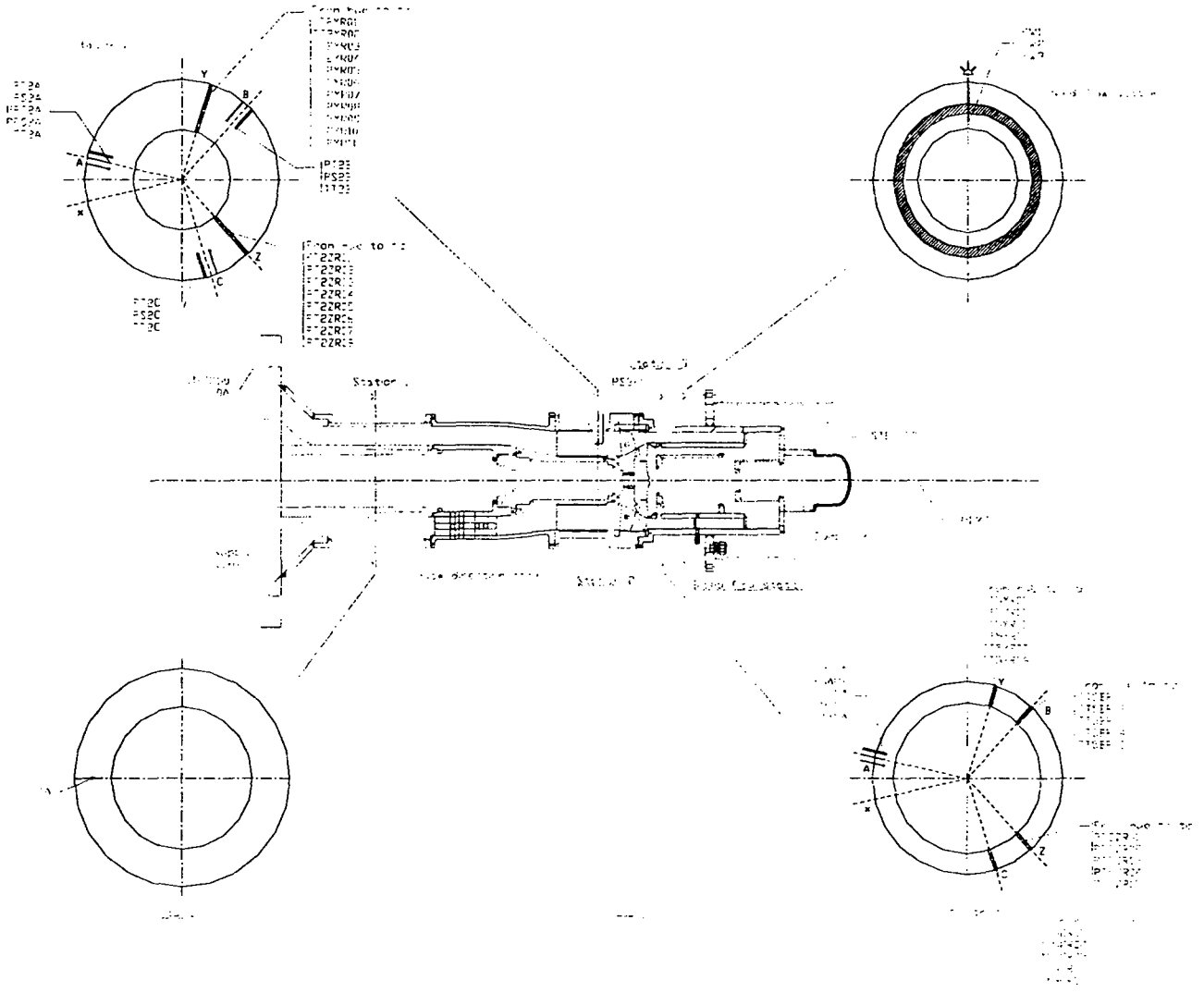


Figure 5.1: Instrument Locations in the Blowdown CRAspC Facility

In addition to these low frequency upstream and downstream measurements there are two high frequency static pressure measurements. One in on the casing between the two rotors and the other is a wall static measurement in one of the downstream instrument windows. High frequency response (~100 KHz) is achieved by fixturing the diaphragm of a .062 in. diameter Kulite pressure transducer flush with the wall.

In the bleed flow passage there is three way wedge probe to measure the total pressure and swirl in the passage. Also in this passage is a variable area orifice that was meant to choke the bleed mass flow. It was believed that with the total pressure measurement, knowledge of the swirl, and a chocked orifice an estimate of the bleed flow could be made. The first test revealed that the bleed passage was too large for the amount of bleed flow. The orifice was not choked, in fact the measured total pressure in the bleed passage was less than the pressure in the dump tank for most of the test time.

After initial tests a distortion of both the inlet total pressure and static pressure was noticed. After several runs additional inlet pitot probes were added to improve the circumferential measurement density. It is believed that the inlet distortion is due to non-uniformities in the hole pattern of the pressure screen. The analysis of this problem is discussed in Section 6.3.

5.2 Temperature Probes

The temperature transducers used in this facility were designed and built in the GTL. The probes are made of 0.0005 in. diameter type K thermocouple wire. The thermocouple beads are mounted within heads with vent holes that slow the flow enough to protect the fragile bead, provide adequate time response and reduce errors. The temperature probes were shown to be accurate to at least 0.3 K throughout the operational range and demonstrated a response time of better than 30 ms. Details about the design, manufacture, calibration and operation of the thermocouples used in this rig can be found in JF Onnee's master's thesis [5].

5.3 Pressure Probes

Probes that measure total pressure, wall static pressure, and pitot probes that measure static and total pressure at one location are placed throughout the facility, as seen in Figure 5.1.

5.3.1 Rated Transducer Properties

All of the pressure transducers used on the rig, both for the high frequency response and the low frequency response probes, are XCQ-062 transducers manufactured Kulite. These probes have a rated response frequency of better than 200 KHz. These transducers measure the pressure difference between the pressure being measured and a variable reference pressure behind the transducer membrane. A vacuum pump is used to set the reference pressure of all the transducers at ~0 psia. Transducers with pressure difference ranges of 15 PSI and 50 PSI were used in the facility. The rated linearity and

repeatability of the relationship between pressure difference and voltage of the transducers is 0.1 % of the transducer range [21]. Details of how the transducers where qualified can be found in Appendix C.

The zeros of Kulite transducers have been shown to drift with temperature [25]. The transducers used in the facility were temperature compensated between 70°F and -350°F (294°K to 61°K). Work by prior investigators has shown that the drift of Kulite transducers can be as much as 2.5% but for the low frequency probes, with the transducers mounted externally to the facility, the temperature at the face of the probe does not vary much from room temperature [25]. Initially during a test the tubes that carry pressure from the probe head to the transducer are evacuated. After the valve opens they are filled with gas that is nearly room temperature. After the initial fill there is no flow within the tubes thus to change the temperature of the transducer heat must be transferred either along the gas column or through the steel of the tubes. The time scale for this is L^2/α, with the minimum L being ~3 inches. For the gas column $\alpha = \kappa/(\rho \cdot C_p)$ $\alpha \sim 1.4 \times 10^{-5}$ m^2/s and for the steel $\alpha \sim 3.5 \times 10^{-6}$ m^2/s. Thus, the time scales for heat transfer are ~ 6 minutes for the gas column and ~ 27 minutes for the steel passage. Because it is assumed there is no temperature variation of the transducer the effect of temperature changes on the transducers was not measured.

5.3.2 Total Pressure Rake Design

The pressure rakes upstream and down stream are extremely similar. Both use the same impact head, steel tubing, and blade profile. The difference is in the number of heads per rake and the ability of the downstream rakes to be rotated ±15° to adjust them to the different levels of swirl at different corrected speeds. Figure 5.3 is a side view of one of the aft rakes with the impact tubes and heads exposed. For the upstream rake the number of impact heads was determined by the thickness of the profile and the number of steel tubes that could be fit into the cross section. Figure 5.2 is a cross section of the upstream rake that shows how the outer diameter of the tubes, combined with the dimension of the cross-section, limits the number of upstream pressure probes. For a sense of scale in these two figures the outer diameter of the tubing is 0.094 in.

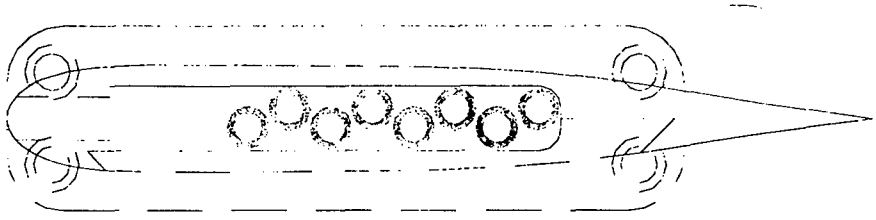


Figure 5.2: Cross-Section view of pressure tubes within the Upstream Rake

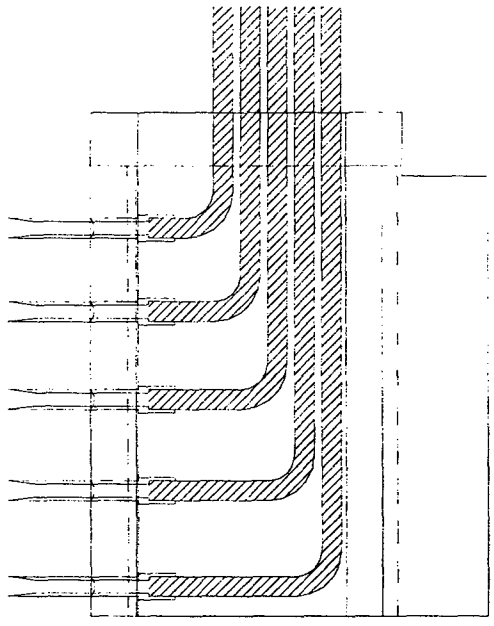


Figure 5.3: Sketch showing impact heads and tubes of a Downstream Rake

The inlet of the impact heads was designed to precisely measure the total pressure of the flow even if the flow was not aligned with the axis of the probe. According to the CFD results the swirl exiting Rotor Two could vary 5°-10° across the span. The 15° bevel on the inlet of the impact heads provide a range 27.5° of misalignment between the flow and the probe where the uncertainty in total pressure measurement is less than 1% of the velocity head [23]. The analytical form of this error is Equation 5.2.

$$\frac{U_{Pt}}{P_t} = \frac{1/2 \cdot \rho \cdot v^2}{P_t} \cdot 1\% = \frac{\gamma \cdot M^2}{2 \cdot \left(1 + \frac{\gamma - 1}{2} M^2\right)^{\frac{\gamma}{\gamma - 1}}} \cdot 1\% \qquad \text{Eqn. (5.2)}$$

5.3.3 Pitot Pressure Probes

Pitot probes are used to measure the static pressure and total pressure at a point. These probes are manufactured by United Sensor Corp and shown in Figure 5.4. According to the calibration curves provided by United Sensor Corp a conservative estimate of errors due to alignment and Mach number reveal that the error in total and static pressures are 1% of the velocity head [24]. The form for the relative uncertainty in static pressure based on Mach number is shown in Equation 5.3; Equation 5.2 is the uncertainty for the total pressure measurement of the pitot probes. Table C.1 in Appendix C shows the uncertainty in pressure measurement due to probe geometry for several runs.

$$\frac{U_{Ps}}{P_s} = \frac{1/2 \cdot \rho \cdot v^2}{P_s} \cdot 1\% = \frac{\gamma \cdot M^2}{2} \cdot 1\% \qquad \text{Eqn. (5.3)}$$

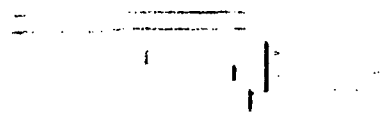


Figure 5.4: United Sensor Pitot Probe [24]

5.3.4 Wall Static Pressure Taps

Figure 5.5 is a sketch of the method for measuring the wall static pressure. This method assumes that the static pressure through the boundary layer is constant and that the diameter of the hole is small enough that the flow does not turn into it. Analyzing data from the runs shows a difference between the wall static pressure measurement and the mid-stream static pressure measurement from the pitot probes. Figure 5.6 is the unfiltered readings from every upstream static pressure measurement between 250 ms and 350 ms for Run 014. Figure 5.7 shows the difference between the wall static pressure measurement and the pitot static pressure measurement at each window normalized by the pitot static pressure measurement at each window. For each window the static pressure measurement at the wall is higher than the mid-stream static pressure measurement. In theory, if the flow is uniform, the static pressure measurement should be the same across the span. One theory for the wall static pressure measurement being higher than the mid-stream measurement is that a component of the velocity head could be entering the static pressure hole, increasing the measured static pressure. Alternatively, there is a circumferential variation of static pressure that seems to be related to variations in the percent open area of the pressure screen, the screen might also be creating span-wise variations of the static pressure.

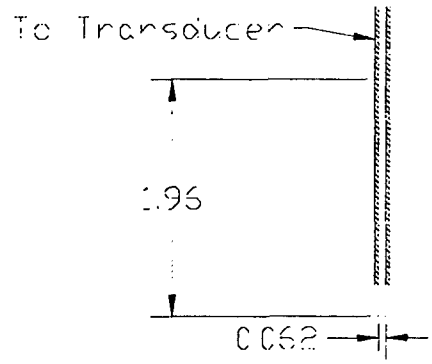


Figure 5.5: Wall static pressure taps, dimensions in inches.

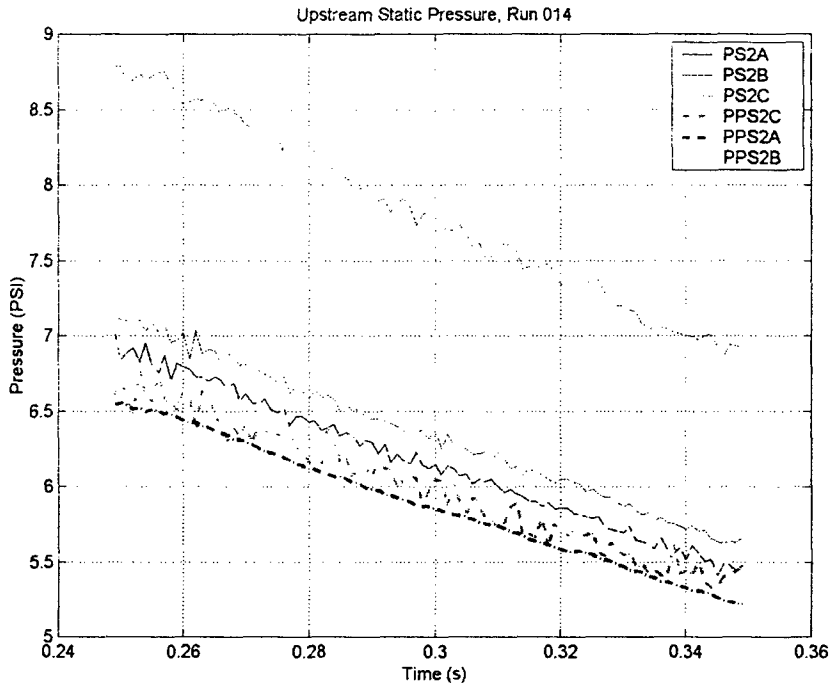


Figure 5.6: Upstream static pressure measurement for Run 014

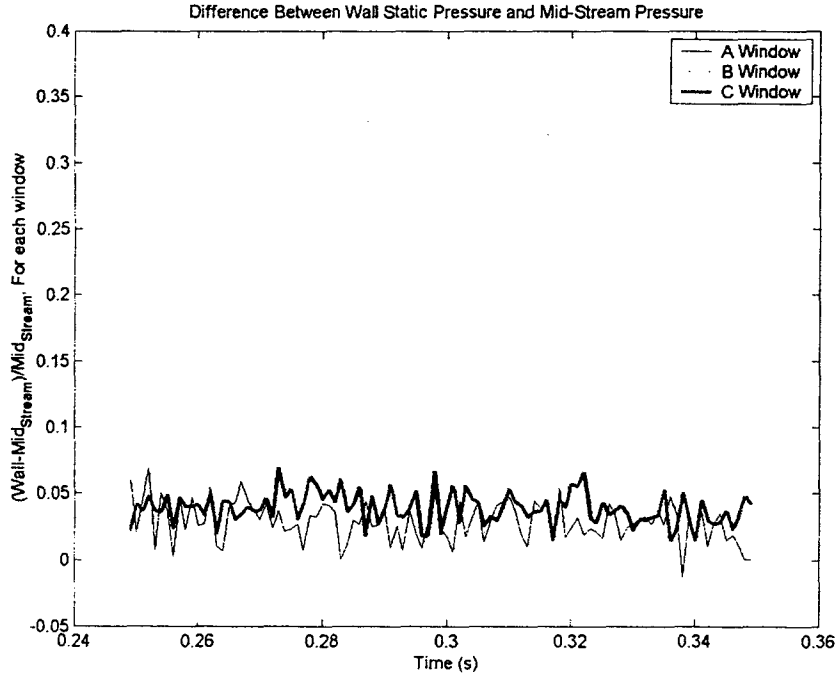


Figure 5.7: Difference in upstream static pressures normalized by the pitot static pressure, Run 014

5.4 Data Acquisition System

In early 1970's recording the data of blowdown compressor tests required high speed tapes, multiple A/D systems and computers, and careful analysis to ensure that all the data was on the same time scale. Retrieving and backing up the data required hours. Currently, technological advances allow the use of one computer for all the A/D cards in the facility. Retrieving and backing up the data for one run now requires ~90 seconds.

There are three different A/D systems used in the facility. There are two 'low-speed' cards (1 KHz), one 'high-speed' card (100 KHz), and one 80 MHz counter card.

5.4.1 Low-Speed A/D Cards

Two 16-bit National Instrument model PCI-6031E A/D cards are used to record the low frequency 'steady-state' pressure and temperature measurements. Each card has 64 channels and can sample the data at 1 KHz [22]. One card is dedicated to pressure measurements and the other card is dedicated to temperature measurements.

5.4.2 High Speed A/D Card

There is one high speed A/D card to capture the data from the two wall mounted high frequency static pressure probes. This card is an 8 channel 16-bit National Instruments PCI-6143. It has a maximum sampling rate of 250 KHz [22]. The sampling rate is set to 100 KHz during tests and two seconds of data is recorded. Also attached to this card is a once-per-rev signal from each rotor. This signal is used as a backup for rotor speed measurement and to provide a time base for rotor revolution based averaging.

5.4.3 80 MHz Counter Card

Finally, there is an 8-channel 32-bit 80 MHz counter card that is used to measure rotor speed. This card is model PCI-6602, made by National Instruments [22]. The input to the card is the full encoder signal (16 pulses per blade) and the output is the number of 80 MHz pulses between encoder pulses. In essence this provides a time between pulses thus the speed of the rotor is the angle between two pulses divided by the time between those pulses.

6 Facility Operation and Initial Results

To date fourteen tests have been run in the blowdown facility. These tests have provided insight into both the performance of the compressor and general principals for how to operate the facility. Section 6.2 discusses the experience learned about how the facility reacted to changes in initial conditions and the interactions observed between the two rotors. Also discussed in this chapter are the results from the initial tests and the uncertainty in the reported performance variables. Appendix D outlines the order of operations for a blowdown test.

6.1 Data Reduction Methods

During the test a limited number of parameters are measured, from these measurements the flow properties of interest are inferred. How the data is treated, along with the methods used for computing the flow properties influence the confidence in the final reported values. This section will discuss how the data is treated. Section 6.3 discusses the how the uncertainty in the measurements is propagated into the reported values. Appendix E examines all the data channels for a single run (Run 013) and then discusses the analysis process and how the test time is established.

6.1.1 Filtering

With the exception of the two high frequency static pressure measurements behind each rotor the purpose of the instrumentation on the rig is to measure the steady-state performance of the compressor. To remove high frequency instrument noise (some of it 60 Hz electrical hum) and non-steady flow structures measured by the instruments all of the low frequency data channels are digitally filtered before the data is reduced. The filter is a running 17 point average. At a 1000 Hz sampling rate 17 points are required to cover one 60 Hz cycle. This running average is done forward and backwards so that the phase lag of the filtered data is zero. Filtering in the forward direction, then the backward direction effectively creates at 34 point running average and everything above 30 Hz is attenuated. To test this filter a random set of data was generated and put through the filter. The original data, and the filtered data, were analyzed with a Discrete Fourier Transform. The response of the filtered data, compared to the response of the random data, is shown in Figure 6.1. Frequencies below 10 Hz are not modified by the filter. Above 10 Hz the filter attenuates the data at a rate of 20 dB per decade. Before entering the A/D cards some of the low frequency pressure transducer amplifiers have electronic 3-pole low pass filters with a break frequency of 500 Hz. The other amplifiers do nothing to modify the frequency spectrum of the signal before entering the A/D.

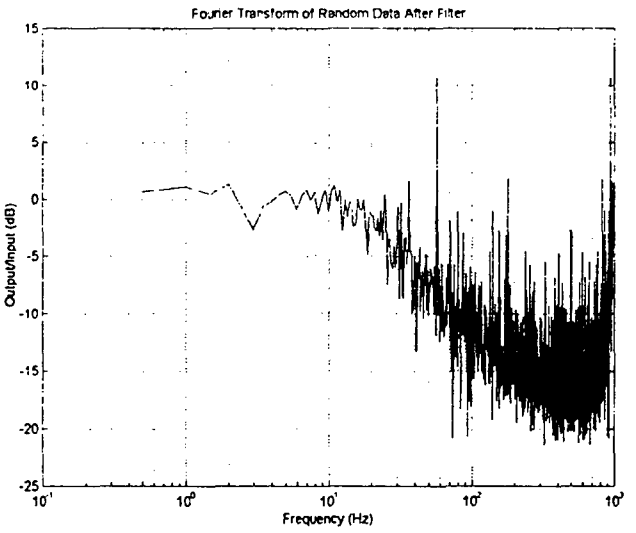


Figure 6.1: Response of random data to the digital filter used in data analysis

6.1.2 Corrected Flow

Between the pressure screen and the first rotor there are three circumferential measurement stations, all in the same axial plane. At each of these locations the total pressure, total temperature, and static pressure is measured. The static pressure is measured with both pitot probes in the center of the flow, and with wall static pressure taps. The wall static taps are not used in calculations because of the uncertainties discussed in Section 5.3.4.

For each measurement window the mass flow is estimated. First, the static temperature is inferred from the total temperature, total pressure, and static pressure. The total temperature and pressure are defined as the temperature and pressure of a fluid particle in the flow that is brought to zero velocity by an isentropic process. This isentropic constraint, along with table of gas properties [26], is used to estimate the static temperature. A Matlab© function was written that interrogates a properties table at the total temperature and total pressure. Once the entropy of the flow is known the function essentially moves along a line of constant entropy until the static temperature is found, such that $entropy(T_S, P_S) = entropy(T_T, P_T)$.

Once the static temperature is known the properties such as density, speed of sound, viscosity, enthalpy, and the ratio of specific heats come directly from the property tables. The last parameter that needs to be calculated to define the corrected flow is the velocity. The velocity is calculated as follows:

$$h = enthalpy(T_S, P_S)$$

$$h_0 = enthalpy(T_T, P_T) = h + \frac{v^2}{2} \qquad \text{Eqn (6.1)}$$

$$v = \sqrt{2 \cdot (h_0 - h)}$$

The mass flow ($\dot{m} = \rho \cdot A_c \cdot v$) is calculated for each window assuming that the total pressure, total temperature, and static pressure are constant radially and circumferentially within the 120° window. The average upstream conditions, mass flow, Mach number, density, etc. are then calculated as an average of these parameters from each window, weighted by the mass flow for each window. It is important to note that there is a four percent variation in the total pressure of the 'A' window compared to the 'B' and 'C' windows. This inlet distortion is discussed in detail in Section 6.3. Figures 6.2-6.4 show the pressures, mass flows, and corrected flows, respectively for each window during the test time in Run 013.

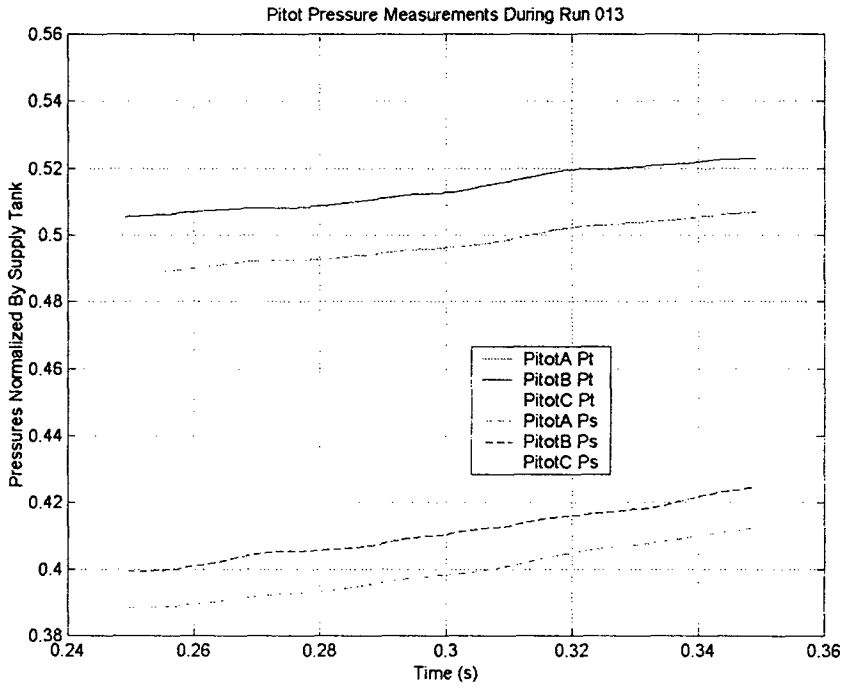


Figure 6.2: Total and Static Pressures for each window in Run 013

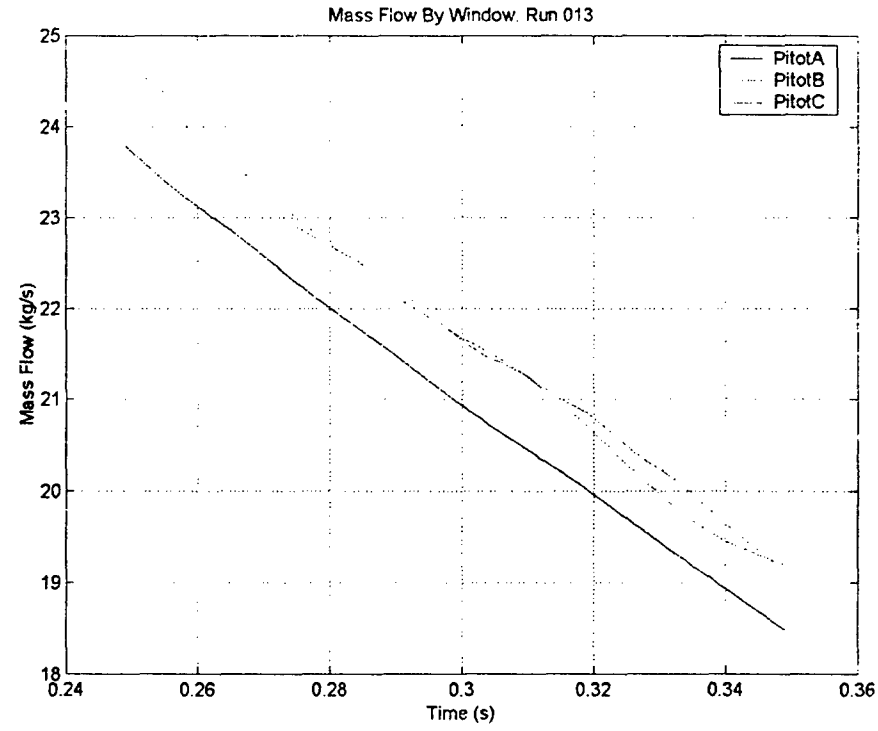


Figure 6.3: Mass flow for each window during Run 013

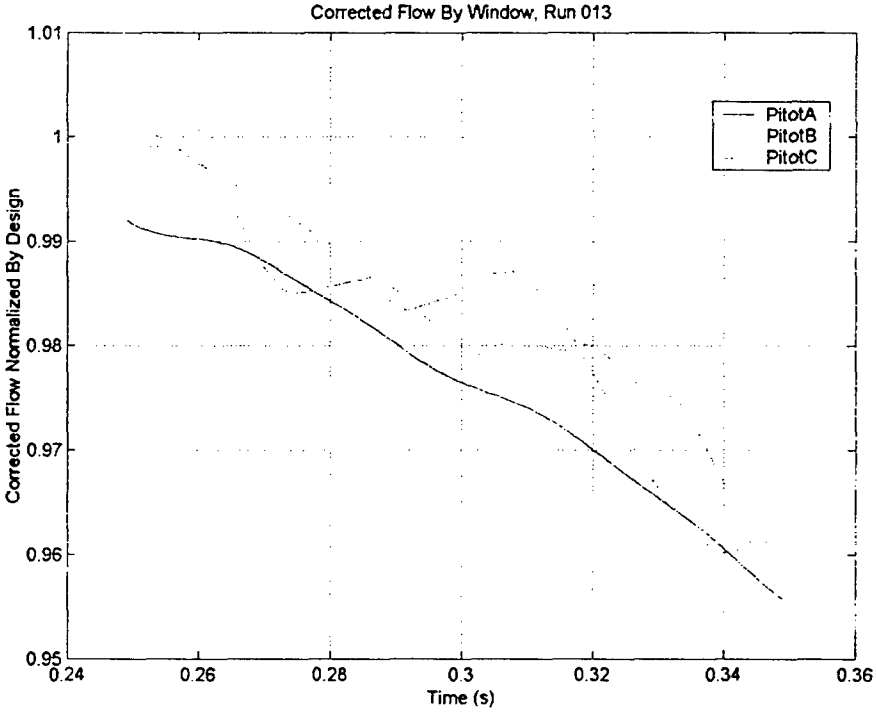


Figure 6.4: Corrected Flow by Window for Run 013

6.1.3 Efficiency

The adiabatic core efficiency numbers reported in Section 6.5 are 'area averaged' values. In the upstream measurement plane the measured values of the total pressure and total temperature rakes are assumed to be constant circumferentially. In the radial direction the measured values are assumed to be constant between measurement positions. Total pressure and temperature are averaged upstream with each measurement given a weight proportional to the area that it is measuring. Downstream the total pressure and total temperature measurements are area averaged with the same assumptions. Figure 6.5 shows the downstream total pressure measurements for Run 007 and the assumed profile used for area averaging. The author would have preferred to mass average the upstream and downstream measurements but there was no practical way to measure the downstream static pressure profile thus there is not any information about downstream mass flow. With the area averaged upstream and downstream total pressure and total temperature measurements the NIST tables are used to determine the total enthalpy and entropy into the compressor and then the total enthalpy out of the compressor and the total exit enthalpy of a compressor that operated isentropically. The core efficiency is the calculated from:

$$\eta = \frac{h_{0\_exit\_Isen} - h_{0\_in}}{h_{0\_exit} - h_{0\_in}} \qquad \text{Eqn. 6.2}$$

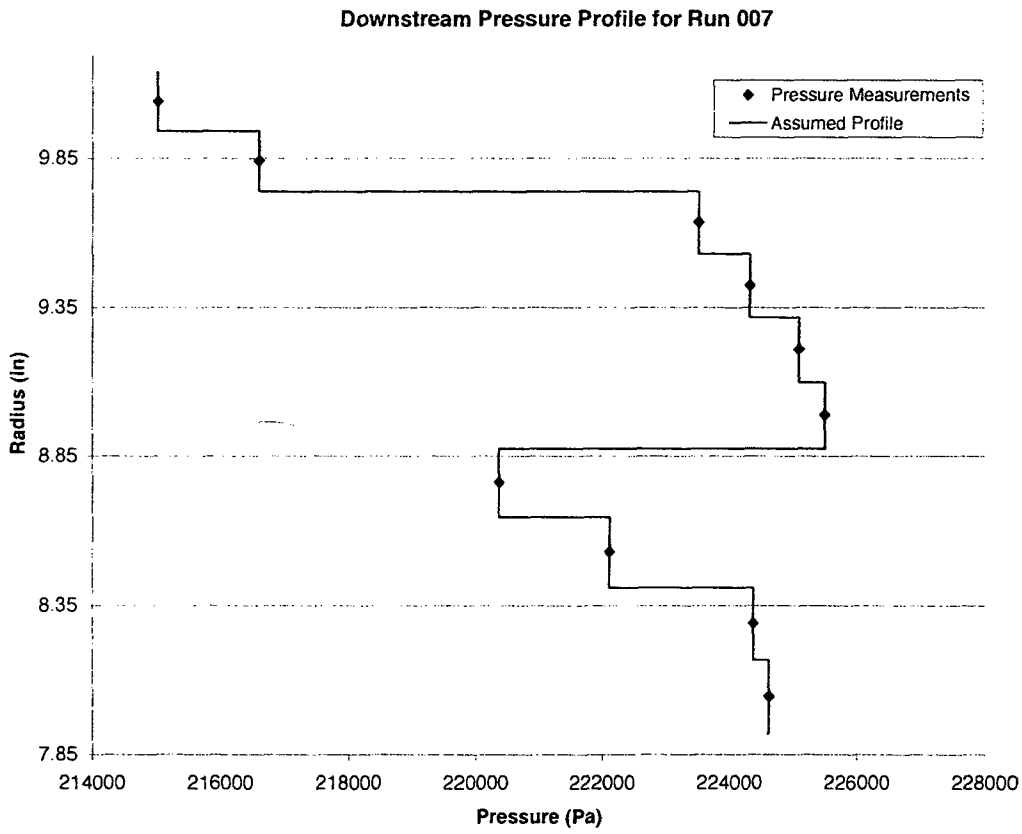


Figure 6.5: Assumed profile for area averaging

6.2 Facility Operation

Trying to measure a specific operating condition with this facility is difficult. It must be noted that in the blowdown facility there is no control of the compressor while it is running. Initial conditions must be set so that between 250 and 350 ms the compressor is operating where desired. There are only four variables that can be set. These are the initial supply tank pressure, the initial speed, and the open area of the throttle between the exit of the two rotors and the dump tank. When the facility was designed it was scaled to the design point of the compressor. This section discusses the effect of the scaling when operating the compressor in off design conditions.

6.2.1 Operational Constraints Due to Inertia Ratios

As described in Section 2.2.2, in order to maintain the corrected speed constant during a test the deceleration of the rotor must match the square root of the change in inlet temperature. The rotor deceleration is very dependant on the inertia of the rotational system. The inertia of the two rotating systems is fixed. Therefore, to keep both rotors at a constant corrected speed the ratio of work for the two rotors must match the ratio of inertia of the two rotating systems. The result is that a finite number of points on the map can be tested.

This principle was seen during early tests as the throttle was changed to get to the design throttle position. As the throttle is opened the back pressure on the second rotor decreases and the total pressure ratio across the second rotor, along with the energy it puts into the fluid, decreases. This means that if the initial pressure in the tank is correct for a given operating point, and the initial speeds of the two rotors are correct, but the throttle is too open, then after the initial transient the corrected speeds will match the desired condition, and rotor one will have a relatively constant corrected speed but rotor two will increase in corrected speed during the test time. This is shown in Figure 6.6. Figure 6.6 is the corrected speeds, normalized by the design corrected speeds, during Run 005. (In Figures 6.6-6.8 there are bumps in the corrected speed, these are related to changes in total temperature.) Run 005 was an attempt at a 90%-90% run, the initial speed of rotor two was low and the throttle was too open. For Run 006 the initial speed of rotor two was increased and the throttle was closed. The corrected speeds for this run are shown in Figure 6.7. Examining Figure 6.7 shows that the corrected speed of rotor two is still increasing, although at a slower rate than in Run 005, and the corrected speed of rotor two still did not match the corrected speed of rotor one at 250 ms. The reason the corrected speed still increased was because the caution was used in closing the throttle. It was closed incrementally to avoid stalling the second rotor at the beginning of the test. The initial speed of rotor two was adjusted linearly from Run 005 to Run 006 to match the normalized rotor one corrected speed. The corrected speed of rotor two was low at 250 ms in Run 006 because closing the throttle increased the work done by the second rotor during the transient therefore lowering the corrected speed at 250 ms during Run

006. From Run 006 to Run 007 the throttle was further closed and the initial speed was again increased. The corrected speeds for Run 007 are shown in Figure 6.8. In Run 007 the normalized corrected speeds of both rotors were matched to 90% of their design speeds, and during the test time (250 ms to 350 ms) the normalized corrected speeds did not deviate from 90% by more than 0.5%.

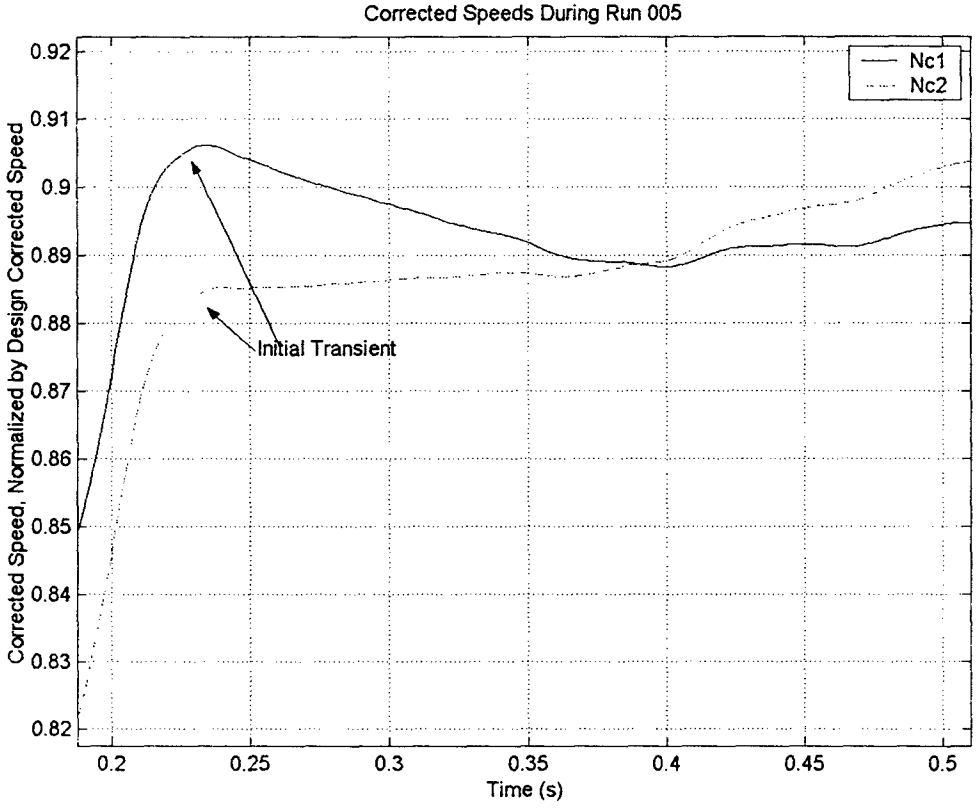


Figure 6.6: Corrected Speeds for Run 005

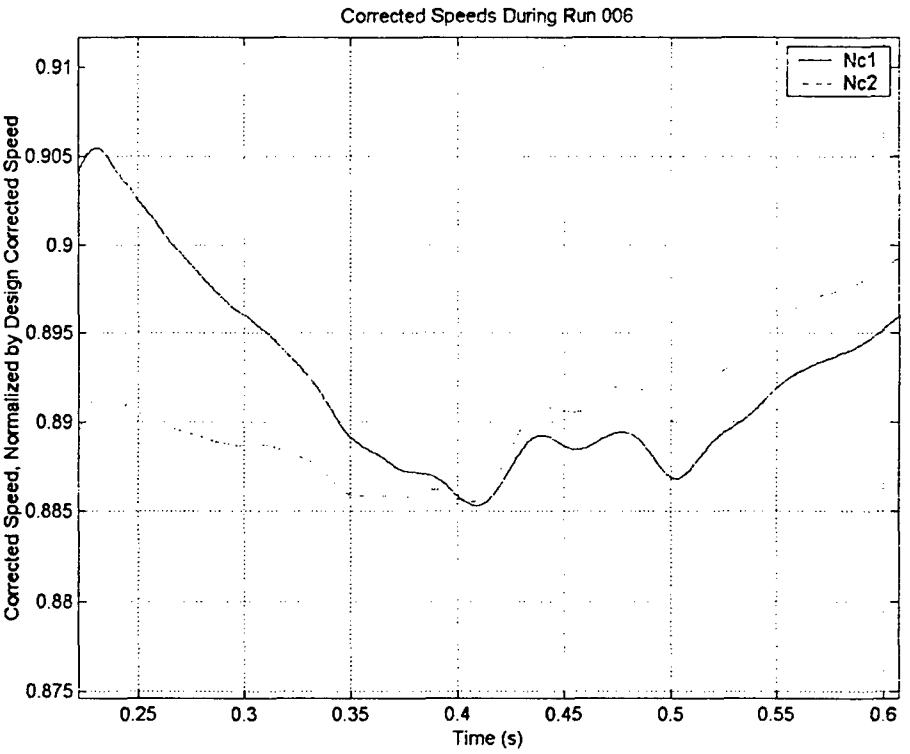


Figure 6.7: Corrected Speeds for Run 006

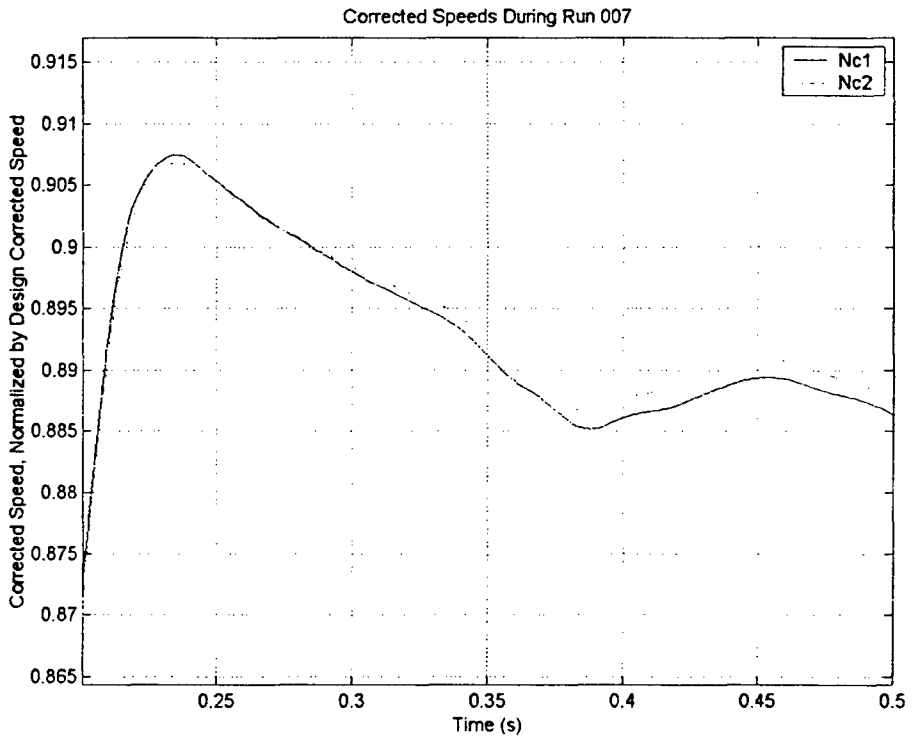


Figure 6.8: Corrected Speeds for Run 007

6.2.2 Throttle Behavior

Before any tests were run the throttle behavior was modeled as a choked orifice in a one dimensional flow. The mass flow through the throttle was modeled with the following relationship, which assumes an ideal gas:

$$\dot{m} = \frac{f(\gamma, M) \cdot A \cdot P_0}{\sqrt{R_g \cdot T_0}}$$

$$f(\gamma, M) = \frac{\sqrt{\gamma} M}{(1 + \frac{\gamma - 1}{2} M^2)^{\frac{\gamma+1}{2\gamma-2}}} \qquad \text{(Eqn. 6.3)}$$

Equating the mass flow into the compressor to the mass flow through the throttle (accurate to ~1% due to the bleed flow) gives that the ratio of throttle area to inlet area as:

$$\frac{A_T}{A_{in}} = \frac{f(\gamma_{in}, M_{in}) \cdot \sqrt{TR}}{f(\gamma_T, 1) \cdot PR} \qquad \text{(Eqn. 6.4)}$$

As gasses pass through an orifice it constricts and the effective area of the orifice is less than the physical area. The ratio of the effective area to the physical area is known as the discharge coefficient. A conservative discharge coefficient was applied to the throttle area to avoid setting the throttle area too small and stalling the compressor. There are several problems with this model. First, the flow is not an ideal gas, especially upstream were the gas becomes very cold. More importantly there are several flow features that are not contained in the one dimensional model. As shown in Figure 3.7 the flow exiting the compressor has to make a 90° turn into the dump tank, which leads to pressure head losses, and there is swirl in flow coming out of rotor two.

Despite the inadequacies of the model the discharge coefficient is consistent enough to be useful for setting the throttle. Table 6.1 shows the discharge coefficient for several runs and the operating condition of the compressor. For small changes in operating conditions (~5% in speeds or pressure ratio) the model is consistent to within ~2%-3%. Larger changes in operating conditions result in 5%-7% variation in the discharge coefficient. When deciding the throttle setting from one run to the next the inlet flow was assumed to remain constant and Equation 6.5 was manipulated to the form of Eqn 6.5, where values for Run(i+1) are desired values.

$$\frac{A_{T\_Run(i+1)}}{A_{T\_Run(i)}} = \frac{PR_{Run(i+1)} \cdot \sqrt{TR_{Run(i)}}}{\sqrt{TR_{Run(i+1)}} \cdot PR_{Run(i)}} \qquad \text{Eqn (6.5)}$$

Table 6.1: Variations of the discharge coefficient model

Run	Throttle Setting (in2)	Wc	Nc Rotor 1	Nc Rotor 2	PR	Discharge Coeff.
005	98.15	81.9%	89.9%	88.7%	1.98	98.3%
006	88.88	81.5%	89.7%	88.9%	2.10	102.6%
007	82.44	80.2%	90.0%	90.0%	2.30	100.7%
008	82.44	83.3%	93.2%	92.8%	2.47	98.6%
009	82.44	92.3%	99.5%	104.8%	2.97	91.0%
010	82.44	92.5%	100.5%	100.6%	2.91	93.0%
011	78.44	87.9%	100.4%	100.5%	2.90	94.9%
013	86.58	98.2%	101.5%	101.5%	2.91	96.2%
014	90.68	100.6%	101.7%	102.1%	2.84	96.4%
*Corrected flow and corrected speed values are normalized by the design value						

6.2.3 Rotor Interactions

It is very important to note the two rotors are highly coupled. If one attempts to consider operating points as two rotors operating independently, each with their own map, then important rotor interactions could be ignored. Thinking about the maps of each compressor only works if the interactions between the two rotors are also considered. There is no stator between the two rotors, so the swirl into the second rotor is dependant on the speed of rotor one. At the design corrected speed the first rotor is supersonic across nearly the entire span, therefore, to first order the corrected speed of rotor one sets the corrected flow entering it. Similarly the second rotor is fully supersonic across its entire span. Therefore, Rotor Two also sets its corrected flow, thus it acts as a throttle on the first rotor. For a given rotor one corrected speed there is a corrected speed for the second rotor where the flows match. Increasing the speed of rotor two from this set speed will lower the static to total pressure ratio of Rotor One, dropping its operating point. Similarly, if the corrected speed of the second rotor is decreased, then the static to total pressure ratio of rotor one will increase, pushing it further towards stall. This is shown in Figure 6.9. Run 009 and Run 010 had essentially the same Rotor One corrected speed (100%) and throttle setting. In Run 009 the corrected speed of Rotor Two was 5% above design, decreasing the speed of Rotor Two increased the backpressure of Rotor One.

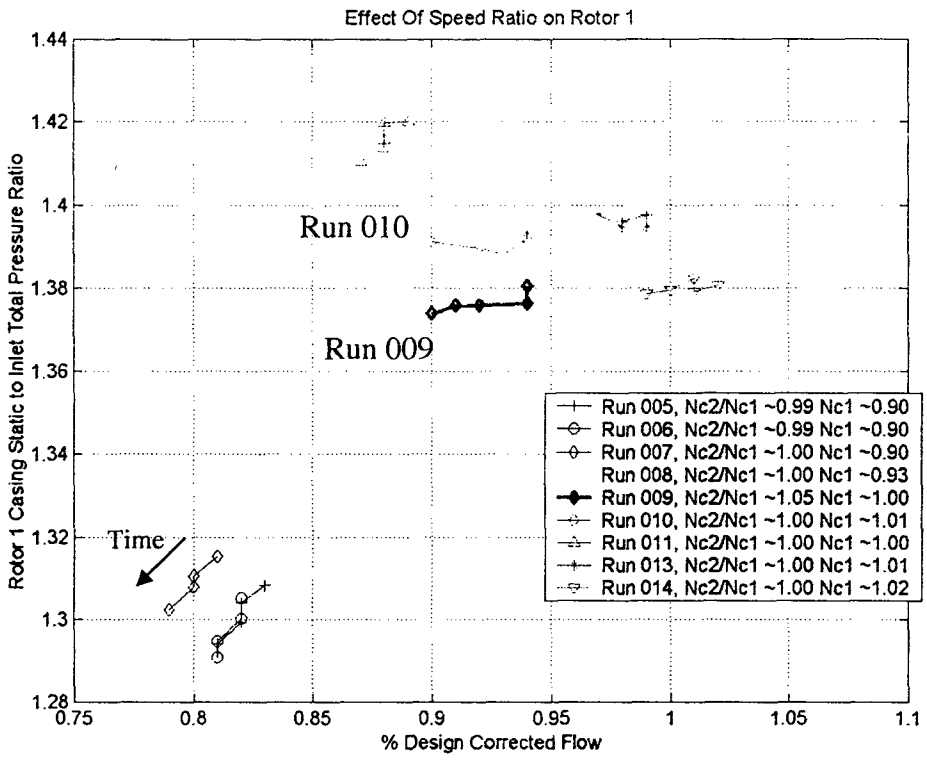


Figure 6.9: Throttling effect of Rotor Two on Rotor One

6.3 Inlet Distortion

An important aspect of testing the steady-state performance of the compressor at the design point is that the flow entering the compressor needs to be uniform in total pressure and total temperature. Unfortunately, neither of these is uniform. This section discusses the thermal boundary layers and the inlet pressure distortion.

6.3.1 Thermal Boundary Layers

In the radial direction there are hot boundary layers due to the fact that the gas is cold (~260 K) relative to the metal of the rig (~300 K). The mass of the rig, combined with the blowdown time scale, results in a nearly constant metal temperature but the gas temperature drops. This means that the thermal boundary layers grow during the test time. Typically the magnitude of the thermal distortion increases from ~1% of the center gas temperature at 250 ms to ~3% of the center gas temperature at 350 ms. Figure 6.10 is the inlet total temperature during Run 010 normalized by the total temperature at the center of the flow at each time.

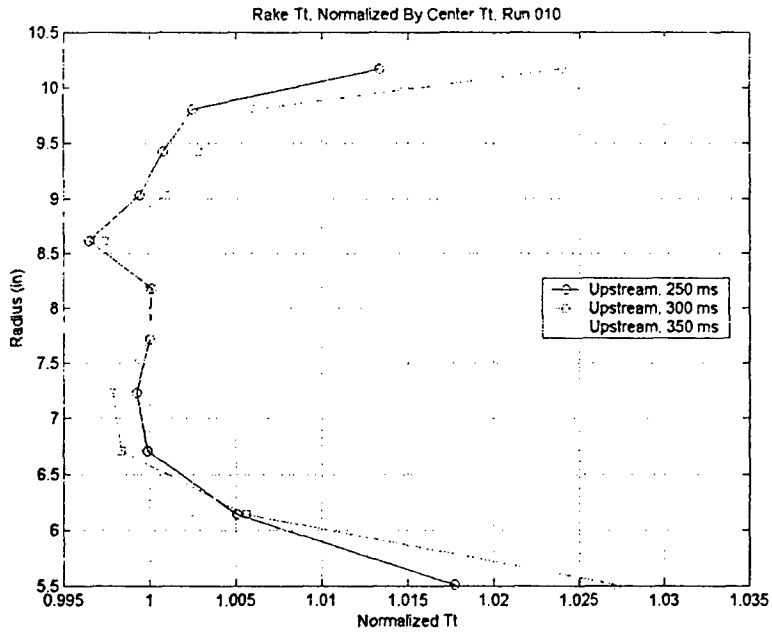


Figure 6.10: Thermal boundary layers during Run 010

6.3.2 Total Pressure Distortion

There are four circumferential points where the upstream total pressure is measured and there was as much as 4% variation among these measurements. After Run 011 pitot probes were added to increase the static pressure measurement density. Analysis showed that there is also a variation in the static pressure and velocity head entering the compressor. Figures 6.11 through 6.13 show the measured variation in these parameters for different runs. It is important to note that outside of the boundary layers there is no radial variation of total pressure measured by the rake.

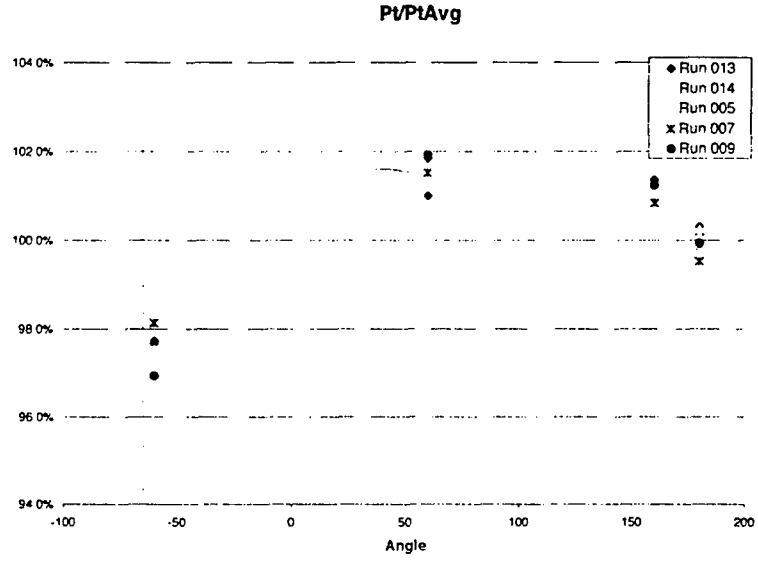


Figure 6.11: Circumferential total pressure variation, normalized by average total pressure

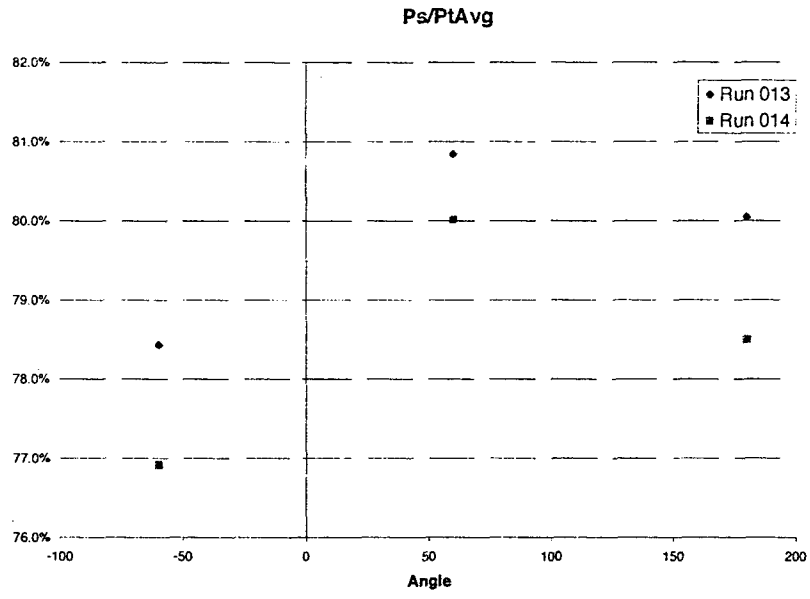


Figure 6.12 Circumferential static pressure variation, normalized by average total pressure

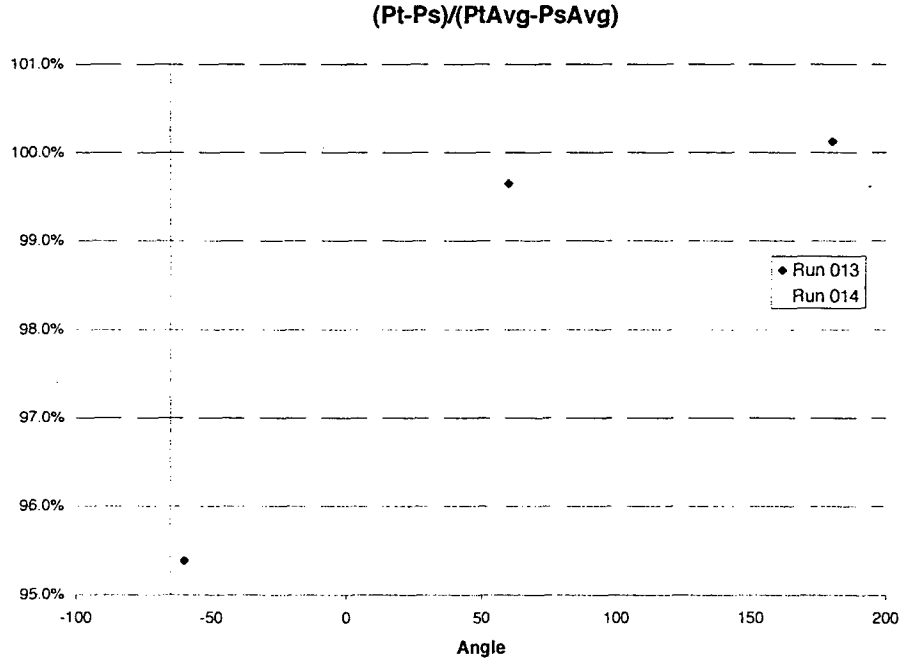


Figure 6.13: Circumferential variation in velocity head, normalized by the average

The measured variation is significant. N.A. Cumpsty defines a parameter for quantifying distortion (DC(60)) which is the change in total pressure divided by the average inlet velocity head. He says that typical engine contracts guarantee maintained operability for values of DC(60) ~ 0.5 [3]. For this facility DC(60) ~0.15. Establishing the source and extent of this distortion was a priority.

With only four circumferential measurements it was very difficult to make a statement about the extent of the distortion. It could have been 120° wide or possibly as small as a single jet. There are 60 hole diameters between the pressure screen and the measurement plane. This long length scale combined with the radial uniformity of the rake convinced the author that the jets were mixed out in the measurement plane. Figure 6.11 shows the consistency of the distortion for several runs. For these runs the rotor speeds, inlet Mach number, supply tank pressure, and throttle position all vary. The only consistent element from run to run was the pressure screen. Searching the literature for a model of losses through perforated plate the author found a paper by W.G. Cornell that presented a model for total pressure loss through a perforated plate with nearly sonic jets. This model says that the total pressure drop across the screen is linear with the percent open area of the screen. Cornell defines a loss factor by:

$$\lambda = \frac{P_{TUp} - P_{TDn}}{1/2 \cdot \rho_{Up} \cdot v_{Up}^2} \qquad \text{Eqn (6.6) [27]}$$

Table 6.1 shows the loss factor for several runs from the data. Figure 6.14 is Cornell's predicted loss factor based on Mach number entering the screen and percent closed area of the screen. These numbers seem to show that average loss across the screen roughly agrees with the model.

Table 6.2: Pressure Loss Coefficient for the screen

Run	Up Stream Mach #	Lambda
003	0.248	9.04
004	0.253	8.70
007	0.247	8.60
013	0.245	11.89
014	0.246	11.99

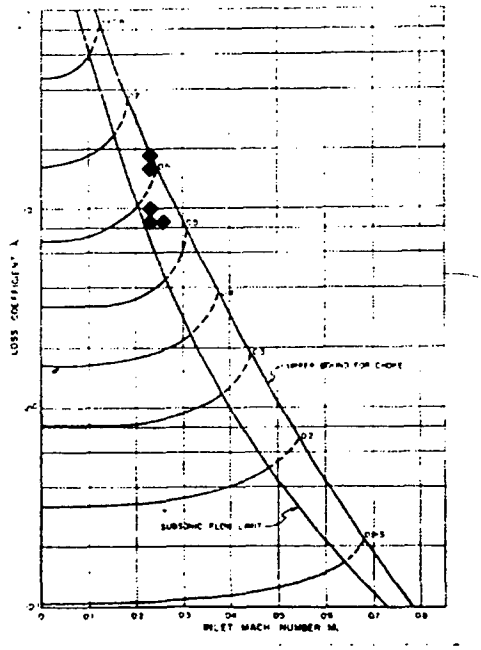


Figure 6.14: Prediction of loss coefficient [27]

The similarity between the model and the data suggests that the distortion is due to a variation in the open area of the screen. One simple approach, though not most accurate, to measure the open area was to count the number of holes. Eighteen 15° sectors with equal area were marked out on the screen and the number of holes in each sector were counted. In Figure 6.15 the measured circumferential variation in open area, along with error bars from the counting, is plotted on top of the previous plot of total pressure variation. There appears to be a strong correlation between total pressure variation and open area variation.

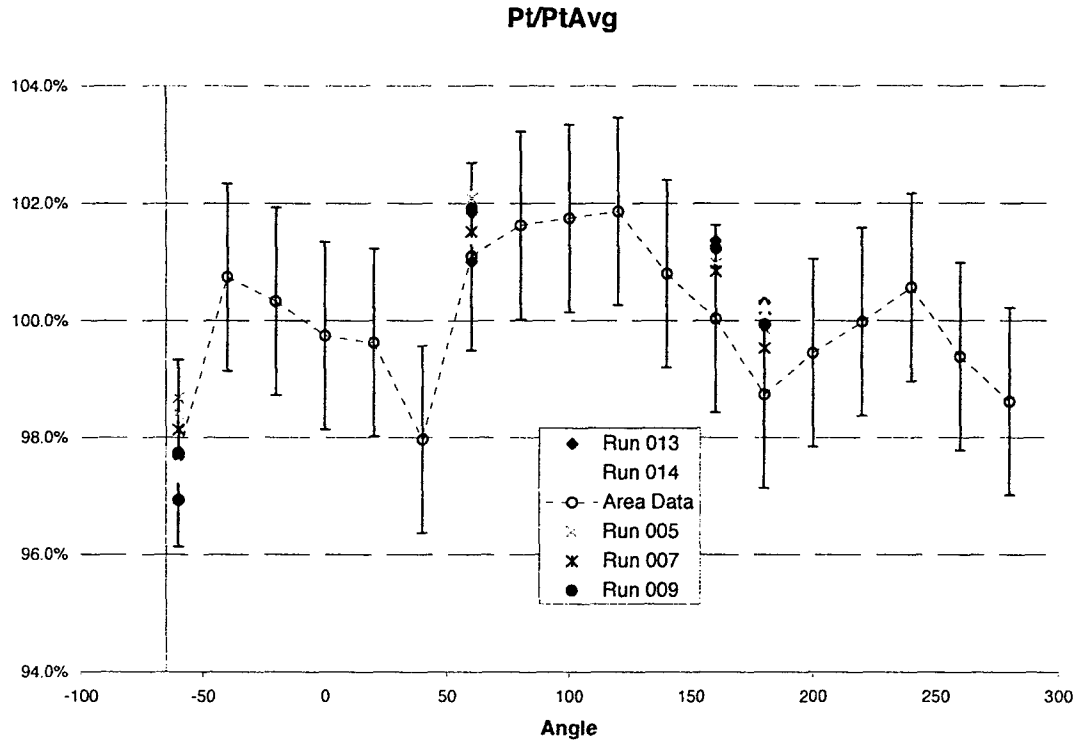


Figure 6.15: Correlation between area variation and total pressure

This data suggests that the total pressure variation is not a 4% distortion that extends 120° degrees but rather two 2% distortions. One is above the mean and extends for ~60° and another below the mean that extends for ~40°. Results shown in Section 6.5 seem to indicate that the compressor operates as designed in spite of the distortion.

6.4 Uncertainty Analysis

As important as the measured values of corrected flow, pressure ratio, and efficiency is the confidence that those numbers are the performance numbers of the machine. In this rig there are two sources of uncertainty. One source is the instrument measurement uncertainty and the other source is related to the flow properties and the discrete nature of the measurements. These sources are treated separately in the following sections.

6.4.1 Measurement Uncertainty

Uncertainty in the measurements of pressures and temperatures result in uncertainty in the final values for corrected flow and efficiency. Much of the work for determining uncertainty has already been performed by previous investigators. It should be noted that when calculating performance parameters the NIST gas tables for the mixture are relied upon. In order to make the uncertainty analysis a tractable problem it is necessary to assume that the working fluid is an ideal gas and that certain properties are constant. This yields analytical expressions for corrected flow and efficiency that can be manipulated to establish uncertainties. These analytical expressions and their derivations are found in Appendix B. Appendix C discusses the qualification procedure for the pressure transducers and contains Tables that list all the pressure transducers and the uncertainties associated with them. The uncertainties associated with the total pressure measurements are discussed in [5]. The results of his work are also tabulated in Appendix C.

Table 6.2 is the uncertainties in the corrected flow measurements due to measurement uncertainties. The Uncertainty Magnification Factors (UMF) show the relative weight of the uncertainty of each measurement [28]. These factors, and some of the measurement uncertainties, change from run to run because of variable flow conditions. It is interesting to note that because mass flow is corrected by inlet total temperature that term drops out of the analytical expression and the uncertainty in total temperature does not affect the corrected mass flow. Table 6.3 shows the uncertainty in the measured adiabatic efficiency. Efforts were made by Onnee to reduce the uncertainties in the total temperature measurement because the importance of total temperature uncertainty is 2.5X to 3X that of the total pressure uncertainty. For both sets of measurements the uncertainty could be reduced by creating a separate set of thermodynamic tables for the specific gas mixture ratio of each run.

Table 6.3: Uncertainties in Corrected Flow

		Rel. Measurement Uncertainties			UMF			
Run	Wc (% of Des)	Pt	Ps	λ	Pt	Ps	λ	Relative Uncertainty
005	81.7%	0.28%	0.29%	0.15%	2.940	-2.940	0.071	**1.17%**
006	81.4%	0.28%	0.28%	0.16%	2.973	-2.973	0.070	**1.18%**
007	80.0%	0.27%	0.28%	0.23%	3.138	-3.138	0.067	**1.23%**
008	83.0%	0.28%	0.29%	0.29%	2.788	-2.788	0.074	**1.13%**
009	91.9%	0.33%	0.32%	0.03%	1.935	-1.935	0.097	**0.88%**
010	92.3%	0.33%	0.32%	0.15%	1.894	-1.894	0.099	**0.86%**
011	87.9%	0.30%	0.30%	0.01%	2.285	-2.285	0.086	**0.97%**
013	98.0%	0.37%	0.34%	0.05%	1.467	-1.467	0.117	**0.74%**
014	100.5%	0.39%	0.35%	0.10%	1.302	-1.302	0.127	**0.69%**

Table 6.4: Uncertainties in adiabatic efficiency measurements

		Relative Uncertainty					UMF			
Run	Meas. Ad. Eff	Up Pt	Dn Pt	Up Tt	Dn Tt	γ	Pt	Tt	γ	Uncertainty
005	0.792	0.31%	0.42%	0.05%	0.10%	0.15%	1.347	-3.142	2.225	**0.85%**
006	0.811	0.31%	0.39%	0.05%	0.09%	0.16%	1.267	-2.952	2.280	**0.80%**
007	0.842	0.31%	0.36%	0.05%	0.09%	0.23%	1.182	-2.780	2.393	**0.84%**
008	0.840	0.32%	0.36%	0.05%	0.09%	0.29%	1.080	-2.446	2.375	**0.90%**
009	0.868	0.36%	0.37%	0.05%	0.09%	0.03%	0.959	-2.159	2.558	**0.54%**
010	0.873	0.36%	0.37%	0.05%	0.09%	0.15%	0.973	-2.205	2.552	**0.66%**
011	0.836	0.34%	0.37%	0.05%	0.09%	0.01%	0.935	-2.032	2.442	**0.51%**
013	0.888	0.40%	0.38%	0.05%	0.09%	0.05%	0.995	-2.297	2.598	**0.61%**
014	0.885	0.42%	0.38%	0.05%	0.09%	0.10%	1.033	-2.433	2.622	**0.69%**

6.4.2 Non-Instrument Related Uncertainties

There are other uncertainties that are not related to instruments but rather result from a lack of instrument density or fundamental aspects of the facility. The uncertainties that are considered are those related to discrete span-wise sampling of the flow, the discrete circumferential sampling of the inlet flow and the uncertainty that arises from the non-adiabatic performance of the compressor. Also discussed is accounting of the bleed flow in the reported adiabatic efficiency.

6.4.2.1 Uncertainty Related to Span-wise Sampling

The downstream temperature and pressure profiles are measured at discrete points and between measurement points the profile is assumed constant. To quantify the uncertainty that this process introduces to the measurement the author examined the difference between the area averaged efficiency from the CFD results when measured at the measurement points and when the entire CFD grid was used. Figure 6.16 shows this process for the CFD run where both rotors were at 90% of their corrected speeds. Table 6.4 lists the difference between the predicted area averaged core adiabatic efficiency and an area averaged adiabatic efficiency using just the values where there are instruments. The difference between the two values decreases towards the design point because as the pressure ratio profile is essentially flat (with exception of the end walls) thus the variation between points decreases. CFD data for this analysis was supplied by Dr. Merchant. It is important to remind the reader that values labeled as "measured" in this section are not measured data points but rather the CFD prediction at points where there are instruments.

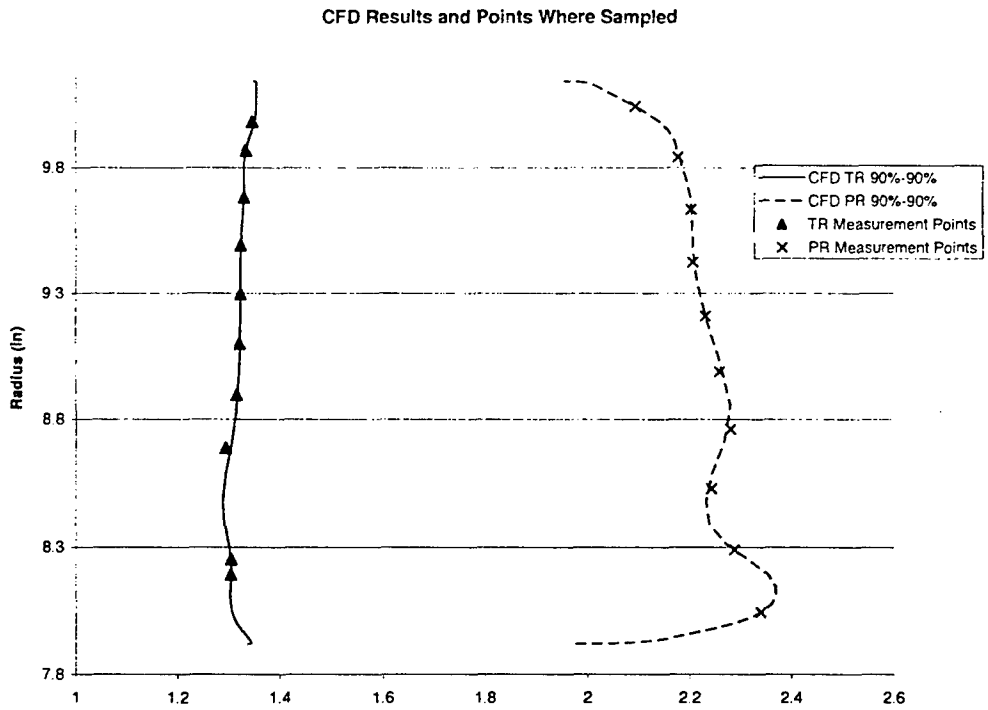


Figure 6.16: CFD result used to estimate uncertainty from radial sampling

Table 6.5: Uncertainty from discrete radial measurements

CFD Run	Predicted Eff	"Meas" Eff	Difference
90%-90%	80.70%	81.93%	1.24%
95%-95%	84.67%	85.41%	0.74%
100%-100%	87.33%	87.89%	0.56%

6.4.2.2 Uncertainty Resulting From Circumferential Sampling of Inlet Distortion

The total temperature and total pressure rakes sample the flow at one circumferential location. Because of this there is a difference between the measured upstream conditions and the true upstream conditions. When the efficiency analysis was done the total pressure rake values were not modified to reflect the average upstream total pressure because at the time the extent and shape of the inlet distortion was not fully known. This results in yet another uncertainty in the efficiency measurements. To quantify this uncertainty JF Onnee used the open area data to establish a baseline total pressure profile then used a parallel compressor analysis to compare the measured adiabatic efficiency to the adiabatic efficiency predicted by the parallel compressor model [5]. The result is that the inlet distortion results in an uncertainty in adiabatic efficiency on the order of 0.95%.

6.4.2.3 Uncertainty due to Non-Adiabatic Operation

Typically compressors operate adiabatically. In steady-state test rigs the temperatures of the compressor metal nearly match the temperatures of the working fluid and the heat transfer to the working fluid is negligible. In the blowdown test environment the temperature of the working fluid entering the compressor is as cold as 250° K. The ambient temperature of the facility is ~290° K. The mass of the compressors is large enough that they can be considered isothermal during the test time [5]. As the working fluid enters the compressor it is first heated by the metal, and then, due to compression heating, the temperature of the fluid rises above the metal temperature and heat is transferred from the fluid to the facility metal. J.F. Onnee estimated how the net heat transfer into the fluid would change the indicated efficiency relative to an adiabatic efficiency for the same compressor. This work is summarized in his master's thesis; the result is that the difference between the indicated efficiency and the adiabatic efficiency is ~0.01% [5].

6.4.2.4 Bleed Flow Accounting

As aspirated compressors have developed there has been discussion as to how to account for the mass flow when reporting efficiency [6]. J.L. Kerrebrock recommends that the efficiency of the machine should be expressed as the efficiency of core flow modified by the bleed flow as shown in Eqn. 6.6. (δ_i is the mass fraction of bleed flow i relative to the inlet mass flow, π_i and τ_i are the pressure ratio and temperature ratio of bleed flow i)

$$\eta_{overall} = \eta_{core}\left[1+\sum_i \delta_i\left(\pi_i^{\frac{\gamma-1}{\gamma}} - \tau_i\right)\right] \qquad \text{Eqn. (6.7)}$$

In this facility attempts were made to measure the bleed flow but they were unsuccessful. Equation 6.6 says that uncertainty in the bleed flow measurement does not affect the measurement of the core efficiency.

6.5 Initial Test Results

Fourteen tests have been run to date. The first seven tests were spent establishing how to operate the facility and moving up the 90%-90% speed line until the throttle position that matched the design throttle condition was found. Once the design throttle condition was found the rotor speeds were increased to the design speeds. For the first attempted test at design speed the second rotor over-sped to a corrected speed of 105% this test produced the highest pressure ratio. The data from these tests will be looked at and compared to CFD results. The CFD results are the analysis of John Adamczyk, using the APNASA code. Also, data from the high frequency wall static pressure measurements, located between and behind the rotors is analyzed.

6.5.1 90%-90% Corrected Speeds

Figure 6.17 shows the quasi-steady performance of the compressors during Run 007. The reported efficiency is the adiabatic core efficiency. This is an area averaged value from the rakes. Between 250 ms and 350 ms both the corrected speed for both rotors is 90% of the design value ±0.5%. During the test time the total pressure ratio varies from 2.34 2.26, a change of 3.4%. The adiabatic core efficiency varies from 87% to 82% during the test time. The corrected flow drops from 81% of the design value to 78% of the design value. It is expected that as the pressure ratio changes the corrected flow into the compressor would also change but typically a decrease in pressure ratio would lead to an increase in the corrected flow. During the test time the Reynolds' number entering the compressor varies 5%. The value used for normalizing Reynolds' number is the Reynolds' number used for designing and analyzing the rotors, ~8 x 10^5 based on chord.

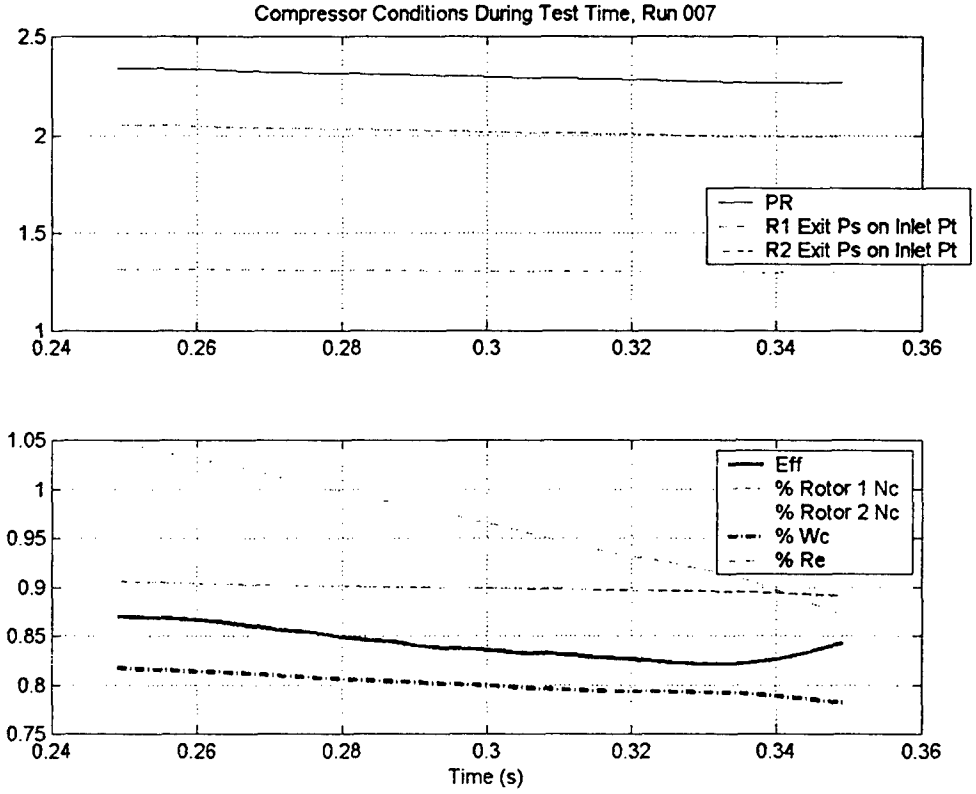


Figure 6.17: Performance Of CRAspC during Run 007

Figures 6.18-6.20 show comparisons of the measured span-wise pressure ratio, temperature ratio, and efficiency profiles of the compressor to the CFD predictions with the corrected speeds at 90%-90%. Below mid-span the measured total pressure ratio roughly agrees with the CFD. Above mid-span the total pressure ratio is as much as 4% higher than the predicted profile. The measured total temperature and efficiency profiles seem to agree well with the predicted profiles with the exception of the point nearest the tip casing.

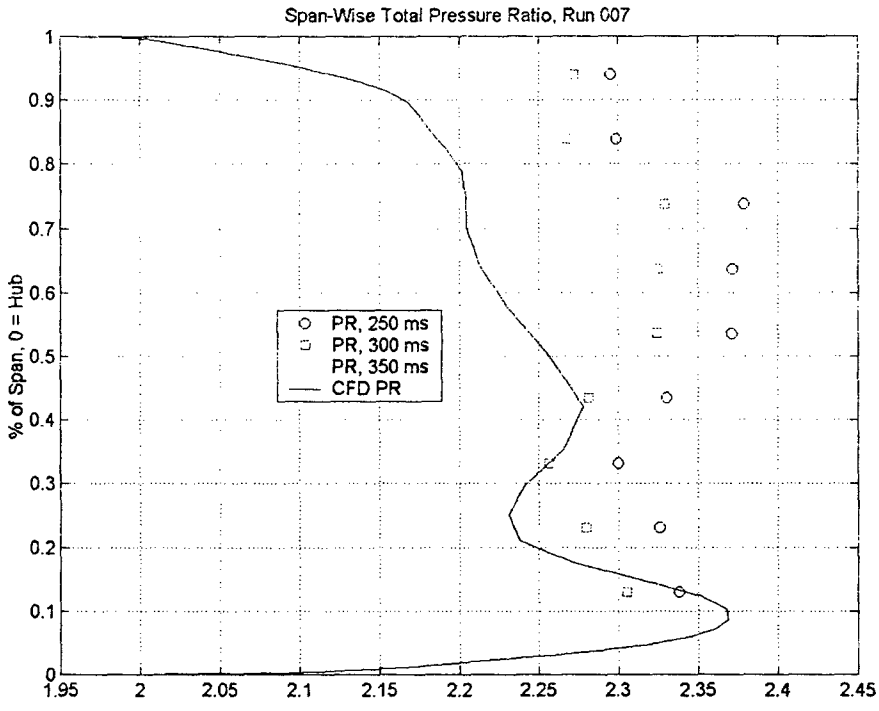


Figure 6.18: Span-wise Total Pressure Ratio Profile compared to CFD, 90%-90% Corrected Speeds

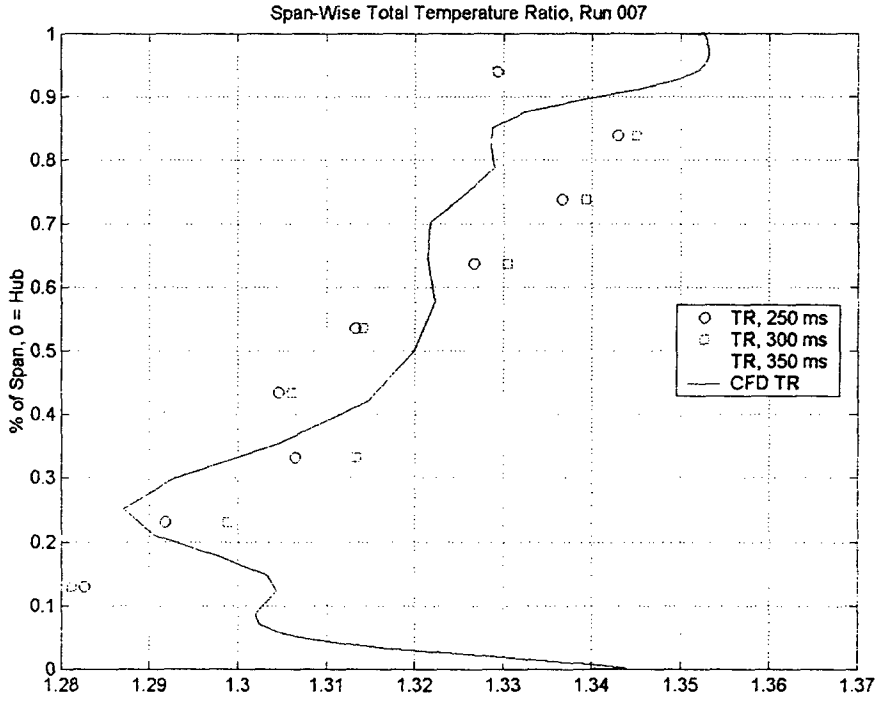


Figure 6.19: Span-wise Total Temperature Ratio Profile compared to CFD, 90%-90% Corrected Speeds

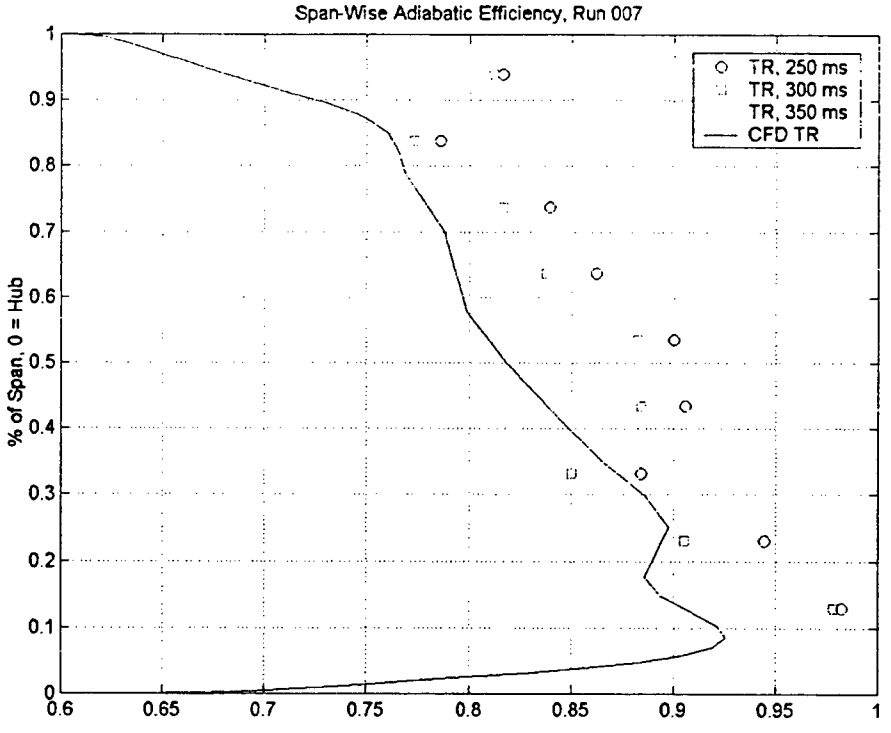


Figure 6.20: Span-wise Efficiency Profile compared to CFD, 90%-90% Corrected Speeds

6.5.2 100%-100% Corrected Speeds

Figure 6.21 shows the quasi-steady performance of the compressor at the design point. The corrected speeds start at 101% of their design values and at the end of the run they are at 100% of their design value. During the run the ratio of corrected speeds is constant. The corrected inlet flow drops 4% from 94% of the design corrected flow to 90% of the design corrected flow. During the test time the total pressure ratio across the compressor drops 1.7% from 2.95 to 2.90. The ratio of compressor exit static pressure to inlet total pressure is nearly constant during the run, dropping 1.9% from 2.58 to 2.53. The adiabatic efficiency of the core flow is 0.885 at the start of the test and drops as low as 0.865 near the end of the test time.

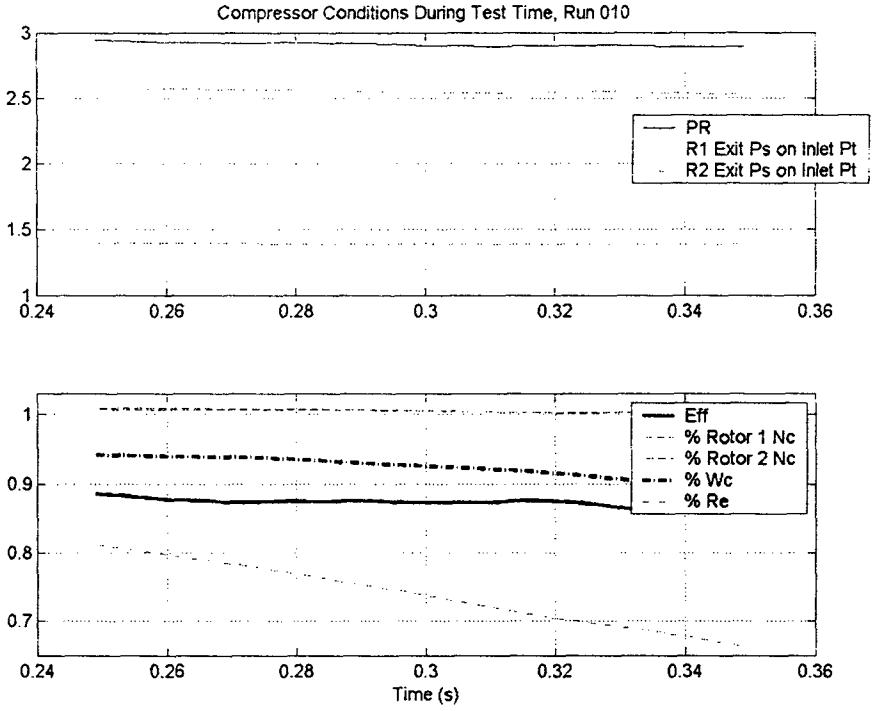


Figure 6.21: Compressor Performance at Design Point

Figures 6.22-6.24 show comparisons of the measured span-wise pressure ratio, temperature ratio, and efficiency profiles to the CFD predictions. It needs to be stated that the measured ratio of exit static pressure to inlet total pressure is lower for the test than for the CFD. The measured pressure ratio profile is lower than the predicted profile. Also of note is that in the CFD predicted pressure profile below 70% of the span the predicted pressure ratio increases slightly but the measured pressure ratio decreases slightly. The measured temperature ratio profile matches the predicted profile, with the exception of the hub and tip were it is lower. Similarly, the measured adiabatic efficiency profile generally matches the CFD efficiency profile except at the hub and tip. Similar to Run 007 the low tip total temperature ratio can be explained by the high inlet temperature; from the thermal boundary layer. The adiabatic efficiency near the hub approaches unity, in a region where one would expect end wall effects to lower the efficiency. The author believes that this is due to a combination of two factors. The reasons are fundamentally related to the fact that in when the profiles are generated there is an assumption that there is no radial mixing of the fluid in the compressor. Similar measurements for transonic, and supersonic compressors have shown that a combination of radial transport and vortex shedding move higher entropy fluid away from the hub to the center of the flow [29]. At this point these hypotheses are simply conjecture; there has been no modeling that demonstrates they are plausible explanations for the phenomena seen in this compressor.

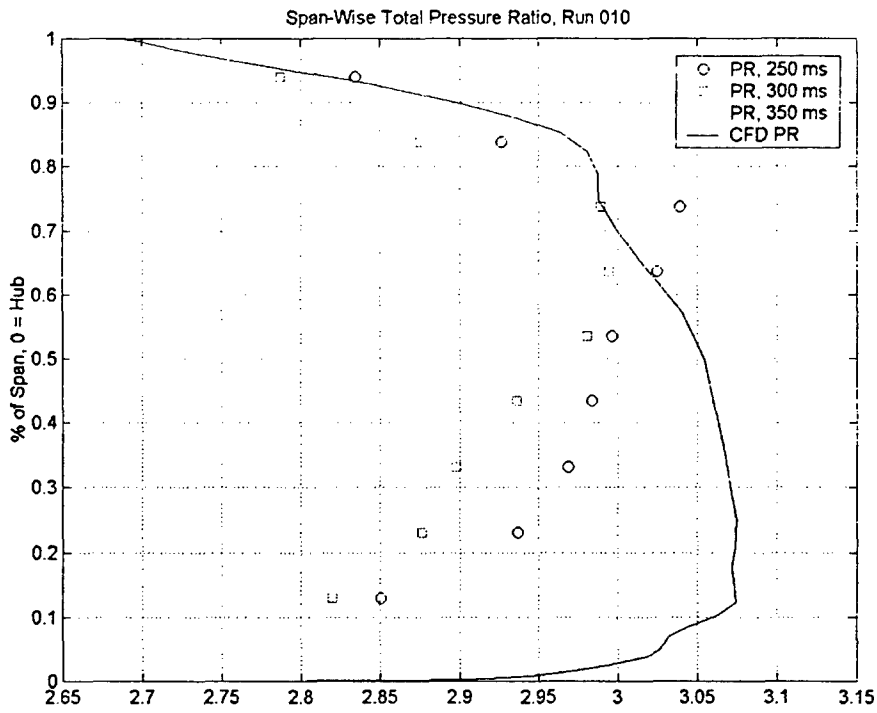


Figure 6.22: Span-wise Total Pressure Profile compared to CFD, Design Point

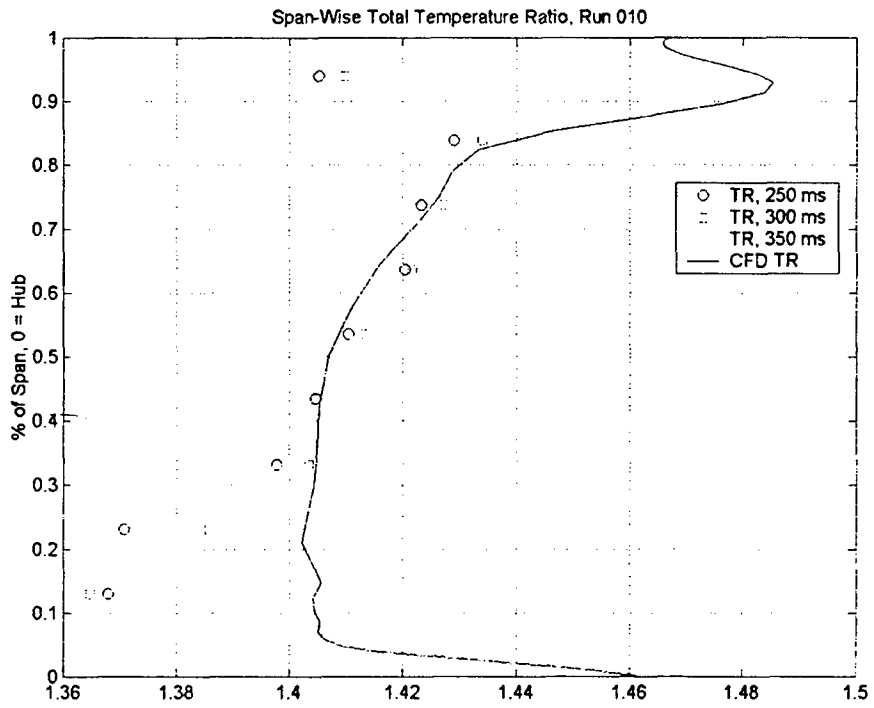


Figure 6.23: Span-wise Total Temperate Profile compared to CFD, Design Point

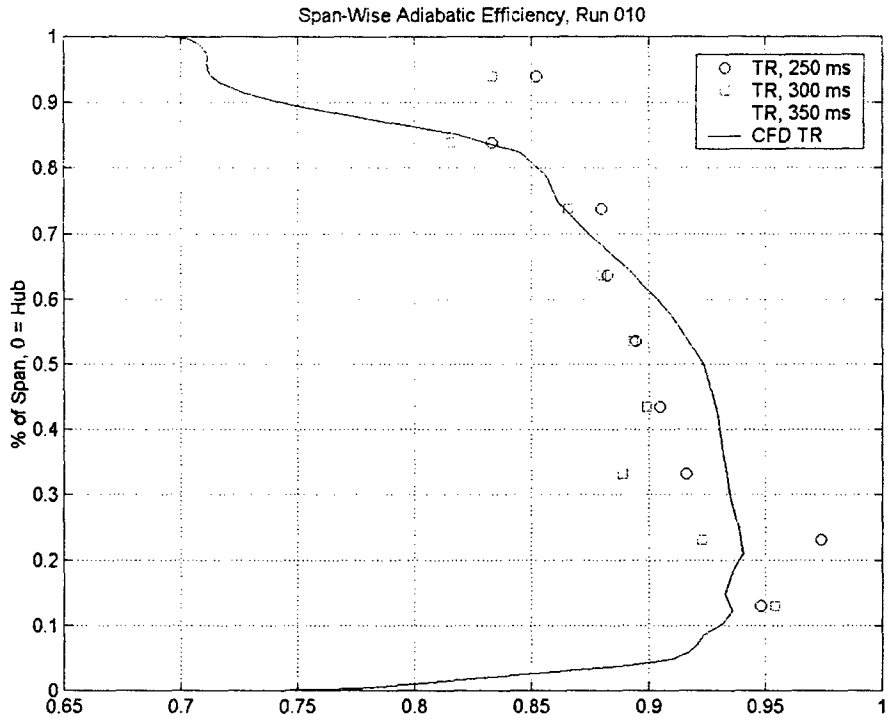


Figure 6.24: Span-wise Adiabatic Efficiency Profile compared to CFD, Design Point

6.5.3 100%-105% Corrected Speeds

Running Rotor One at 100% of its design corrected speed, Rotor Two at 105% of its design corrected speed , and the throttle at the design position (82.44 in^2) resulted in the highest pressure ratio seen during this series of tests. This occurred in Run 009 due to attempts to extrapolate initial conditions from corrected speeds of 90% to corrected speeds of 100%. Figure 6.25 shows the quasi-steady performance of the compressor at this condition. During the test time the total pressure ratio ranged from 3.03 to 2.90 and the adiabatic core efficiency started at 0.887 and dropped to 0.838.

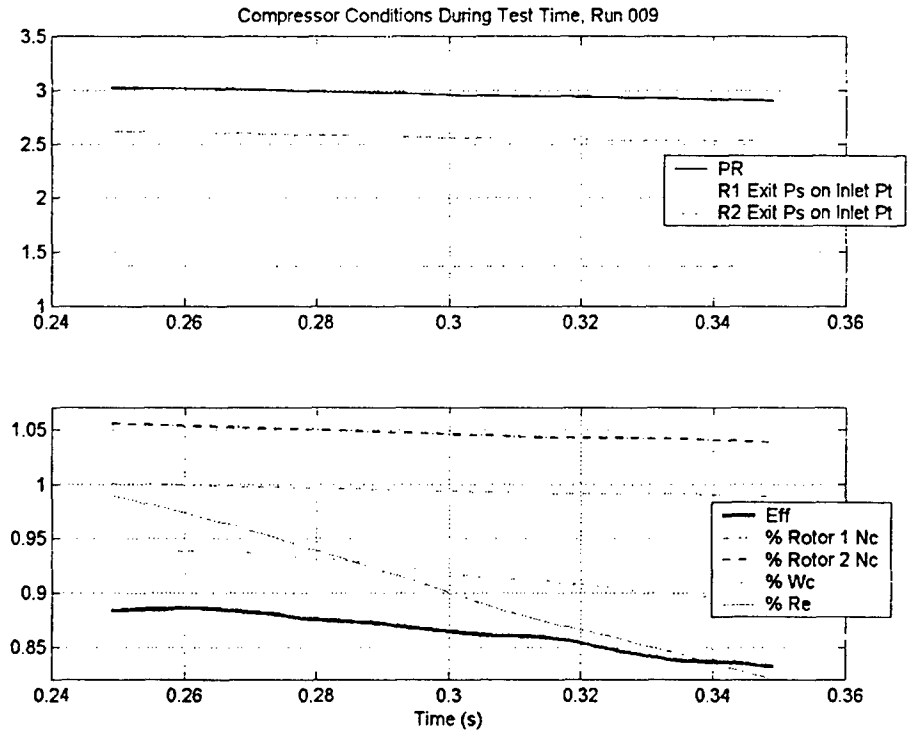


Figure 6.25: Compressor Performance for Run 009

6.5.4 Summary of Performance Results

Table 6.5 lists the results of the CFD and the measured values for two operating points. At the design point the total pressure ratio is 4% lower than the predicted CFD value and the exit static pressure to inlet total pressure ratio is 3% lower than predicted. As can be seen on the map (Figure 6.26) decreasing the throttle area did not increase the pressure ratio. For both cases the measured corrected flow was lower than the CFD prediction. At the 90%-90% run the corrected flow was 2% lower than predicted and at the design point the corrected flow was 6% lower than predicted.

Table 6.6: Comparison of performance parameters for two operating points

	CFD Results [16]				Measured Values					
Corrected Speeds	PsonPt*	PR	Eff	Wc**	PsonPt	PR	Eff	Wc	R1 Nc***	R2 Nc
90%-90%	1.899	2.226	0.810	33.43	2.044	2.329	0.863	34.09	90.4%	90.3%
100%-100%	2.650	3.066	0.884	41.97	2.572	2.934	0.879	39.45	100.7%	100.9%

* PsonPt is the exit static pressure to inlet total pressure ratio

** Wc is the Corrected Flow (lbm/sec/ft^2)

*** Nc is the Corrected Speed as a percent of the design corrected speed

Figure 6.26 is the current compressor map. The values for these points come from an average of the quasi-steady time data during the first three revolutions of Rotor Two after the initial blowdown transient. During three revolutions of rotor two the corrected speeds

are constant to within 0.3% and the inlet correct flow is constant to within 1%. Also, if the axial velocity is assumed constant then the typical through flow time from the upstream instrument window to the downstream instrument window is ~ 0.4 revolutions of Rotor Two. Comparing the predicted CFD line of constant corrected speed, at the design speed, to the measured 100% corrected speed line one can see that the compressor is producing a total pressure ratio 7% lower than predicted. The points on Figure 6.26 with arrows all had the same throttle setting. For the measured 100% corrected speed line the throttle area was changed by 5% from the nominal setting, first more closed, and then more open. At some point the 100% speed line should become vertical. It appears that opening the throttle another 5% will find this vertical section of the speed line. In Figure 6.27 the area-averaged adiabatic core efficiency is plotted vs. corrected flow for each point; along with the CFD predictions. The efficiency of the compressor appears to be better than predicted. Figure 6.28 shows the polytropic core efficiency vs. corrected flow. Error-bars on Figures 6.26-28 indicate the estimated uncertainty for each measurement.

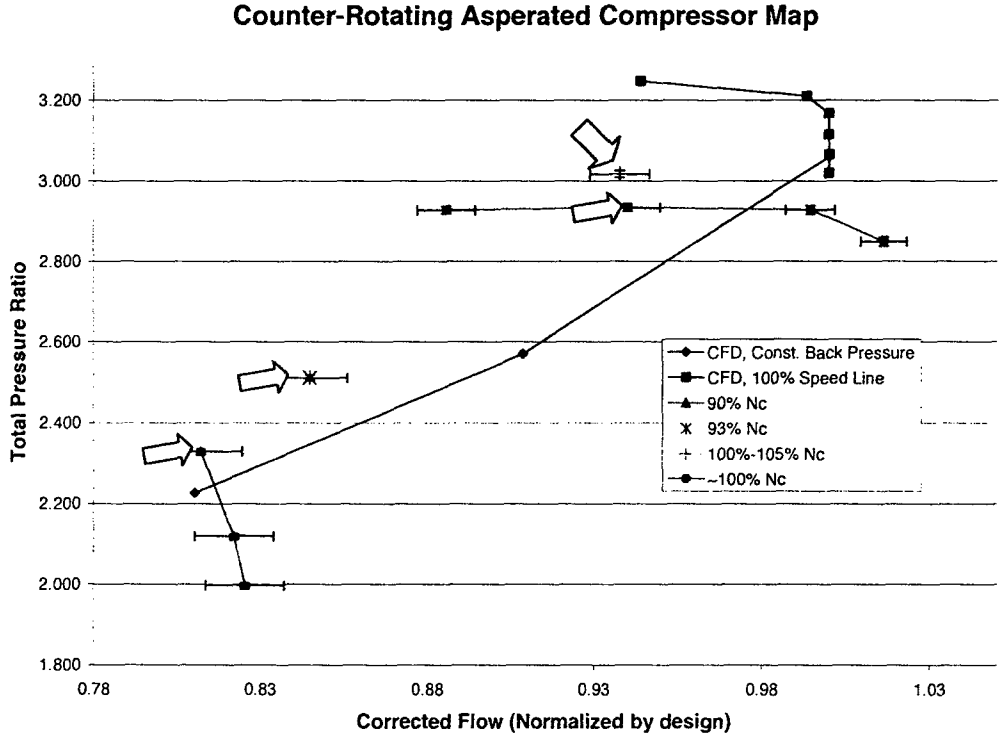


Figure 6.26: Compressor Map, Pressure Ratio vs. Corrected Flow

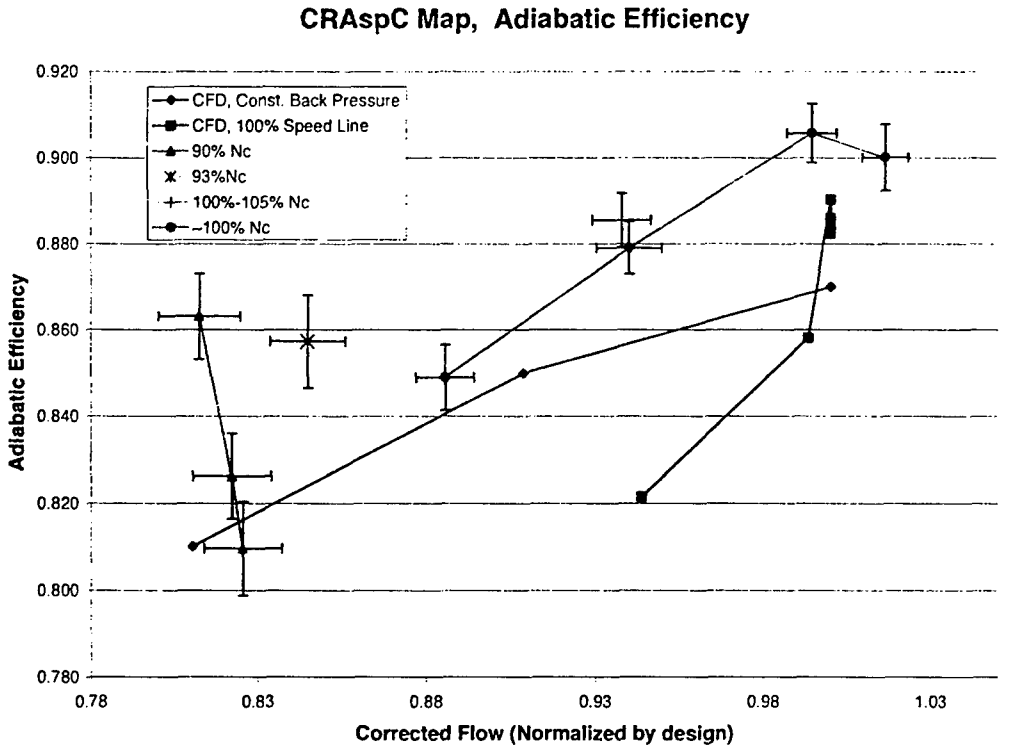


Figure 6.27: Compressor Map, Adiabatic Efficiency vs. Corrected Flow

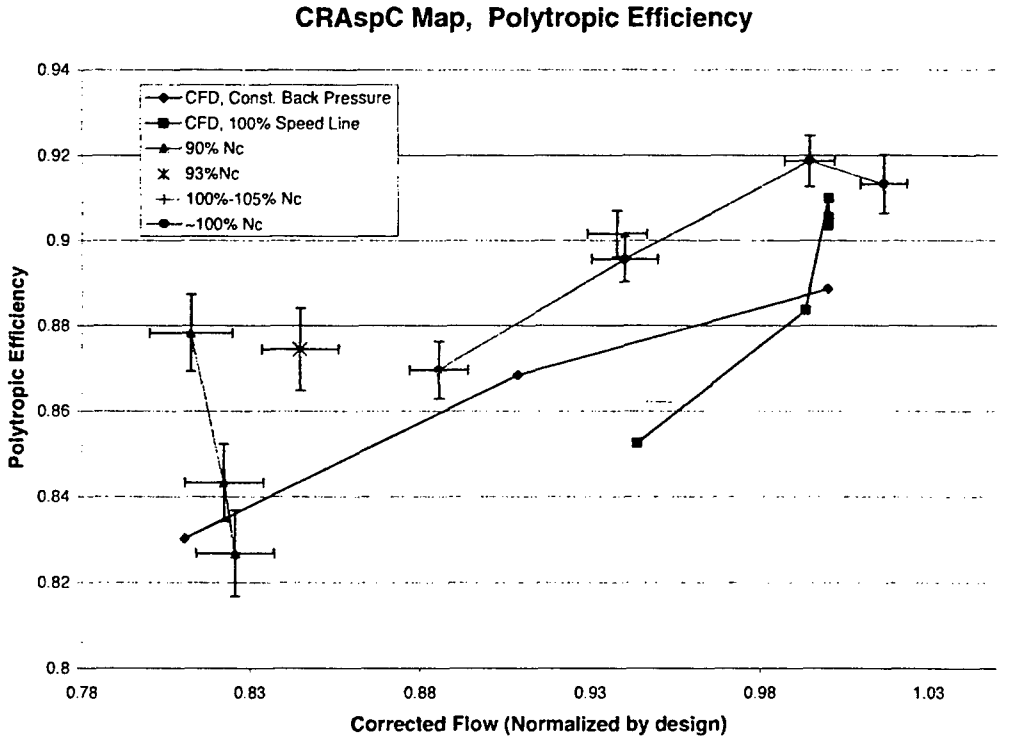


Figure 6.28: Compressor Map, Polytropic Efficiency vs. Corrected Flow

6.5.5 Change in Operating Point during the Test Time

For each run the values that define the operating point of the compressor change from 250 ms to 350 ms. These metrics are the corrected flow entering the compressor, the corrected speeds of the two rotors, the angle of the flow relative to the compressor (this is the angle of a vector made from the inlet velocity and the mid-span wheel speed of Rotor One, shown in Figure 4.1), Reynolds' Number (based on Rotor One chord), and the ratio of the exit static pressure to the inlet total pressure. Table 6.7 lists each of these parameters, how they change, and the average value for each run. A negative 'drop' in Table 6.7 indicates an increase. Corrected flow and corrected speeds are listed as percentages of the design values. The measurement of the exit static pressure to inlet total pressure ratio comes from the high frequency casing static tap. The changes in corrected speeds and Reynolds' agree with the predictions of the lumped parameter model used during the facility design. It was expected that while the pressure ratio across the throttle indicated it was choked, based on 1-D compressible flow theory, the corrected flow across the throttle and into the compressor would remain constant. The change in back pressure ratio seems to indicate that the corrected flow through the throttle is changing and further verify that the 1-D compressible flow model does not hold. A fundamental question that needs to be answered is 'what is the primary source for the changing inlet corrected flow?' If the change in corrected flow is related to something in the facility (i.e. the throttle or the screen) then the data can be treated in a manner where the compressor is considered to be operating in a quasi-steady state through several different operating points. If the source of the change in corrected flow is the compressor then fundamental questions about the compressor must be answered.

Table 6.7: Change in operating conditions during test time

	Wc		Nc Rotor One		Nc Rotor Two		Reynolds' Number		Relative Angle		Back Pressure	
Run	% Drop	Avg.	% Drop	Avg.	% Drop	Avg.	% Drop	Avg.	% Drop	Avg.	% Drop	Avg.
005	2.4%	81.6%	1.2%	89.8%	-0.1%	88.7%	15.4%	8.79E+05	-0.6%	63.6	1.4%	1.69
006	2.3%	81.3%	1.2%	89.6%	0.4%	88.9%	15.4%	8.72E+05	-0.6%	63.7	1.8%	1.82
007	3.6%	79.8%	1.3%	89.8%	1.2%	89.8%	15.3%	8.90E+05	-1.1%	64.2	2.1%	2.02
008	4.0%	82.9%	2.0%	92.9%	2.1%	92.5%	14.3%	9.94E+05	-1.1%	64.0	3.4%	2.17
009	4.9%	91.8%	1.0%	99.4%	1.4%	104.6%	16.9%	8.39E+05	-2.1%	62.5	2.9%	2.57
010	3.8%	92.5%	0.4%	100.5%	0.7%	100.6%	14.9%	6.92E+05	-1.8%	62.4	1.1%	2.55
011	1.9%	87.9%	0.5%	100.4%	0.8%	100.5%	12.7%	6.77E+05	-0.7%	64.0	1.6%	2.55
013	2.8%	98.2%	0.2%	101.5%	0.3%	101.5%	13.6%	7.41E+05	-1.6%	60.6	0.7%	2.53
014	3.0%	100.3%	0.1%	101.7%	0.2%	102.1%	17.0%	7.39E+05	-1.9%	59.9	0.8%	2.45

6.5.5.1 Drop in Efficiency during Test Time

In each test the adiabatic efficiency of the compressor changed during the test time. The drop in adiabatic efficiency was as small as 0.015 and as much as 0.040. For the runs near the design point at 250 ms the compressor was 'good' (based on efficiency) and 'bad' at 350 ms. Thus it is important establish why the efficiency is changing.

An attempt has been made to correlate the change in adiabatic efficiency during test time and the change in inlet Reynolds' number. The inlet Reynolds' number, based on Rotor One chord, varied from run to run and the minimum inlet Reynolds' number for all the runs was ~6 x 10^5. According to Cumpsty a change in adiabatic efficiency can be correlated to a change in Reynolds number by the relationship:

$$(1-\eta) = k \cdot R_e^{-n} \qquad \text{Eqn 6.8 [3]}$$

This relationship has been found to describe hydrodynamically smooth blades with a lower loading coefficient than this compressor. According to Cumpsty up to a Reynolds' number of ~5 x 10^5 n is in the range of 0.10 to 0.13. Above a Reynolds' number of 5 x 10^5 changes in Reynolds' number do not effect the losses of the compressor. Equation 6.6 was manipulated so that k and n could be found by fitting the data, in a least squares manner, for runs 007, 009, and 010. After fitting the model to the data for those runs there is no consistency in the coefficients k and n.. The values for k range from 150 to 1.9 x 10^{12} and the values for n range from 0.53 to 2.24. The values for n are not close to those reported by Cumpsty. This combined with the fact that the Reynolds' number, based on chord, is above the value for which Cumpsty reports that changes in Reynolds' number produce a change in efficiency lead the author to think that the Reynolds' number is not the primary cause for changes in efficiency.

6.5.6 High Frequency Data Analysis

The primary purpose of the two high frequency wall static pressure taps is to assess if the compressors are operating with a rotating stall. The data from these taps was checked after each run and the compressors did not stall during the test time (250 ms to 350 ms). Further analysis of this data demonstrates interesting properties of the compressors, although there is not enough data to make quantitative statements about the phenomenon witnessed. Figure 6.29 shows the exit static pressure to inlet total pressure ratio of the first rotor for 3 revolutions during the test time and the Discrete Fourier Transform of that data. The abscissa of the bottom plot is frequency normalized by the speed of the first rotor. On this scale the frequency of Rotor One is 1 and the Rotor One blade passing frequency is 20. The blade passing frequency of the second rotor is 23. The shock waves that travel upstream from each Rotor Two blade (the peak at 23) have a greater influence in the static pressure measurement than the wakes from Rotor One (the peak at 20). Early in the analysis there were questions about the source of the response peak seen near 3. Kerrebrock suggested that the response could be due to combination tones of the shock waves in Rotor Two; a result of manufacturing variations of the Rotor Two blades. To do ensemble average the time based signal is interpolated so that for each revolution there are N points. For the number of revolutions during the test time (~ 16) the interpolated signal at each of these angular points is averaged. This procedure removes elements of the signal that is not tied to the rotor. Figure 6.30 is the ratio of Rotor One exit static pressure to inlet total pressure ratio ensemble-averaged using the rotor two once-per-revolution signal and its Discrete Fourier Transform. The peak at 3 in Figure 6.30 indicates that the lower frequency peak in Figure 6.29 is tied to Rotor Two.

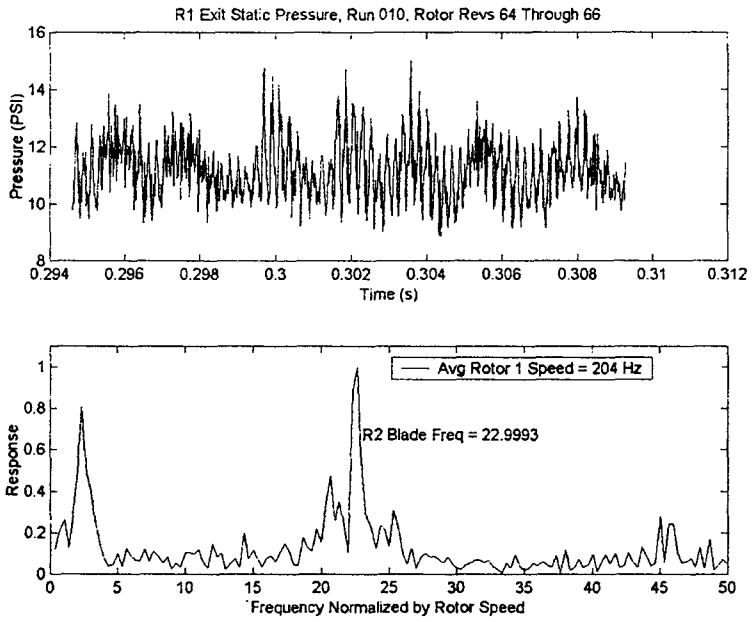


Figure 6.29: High-Frequency wall static pressure measurement between rotors, Run 010

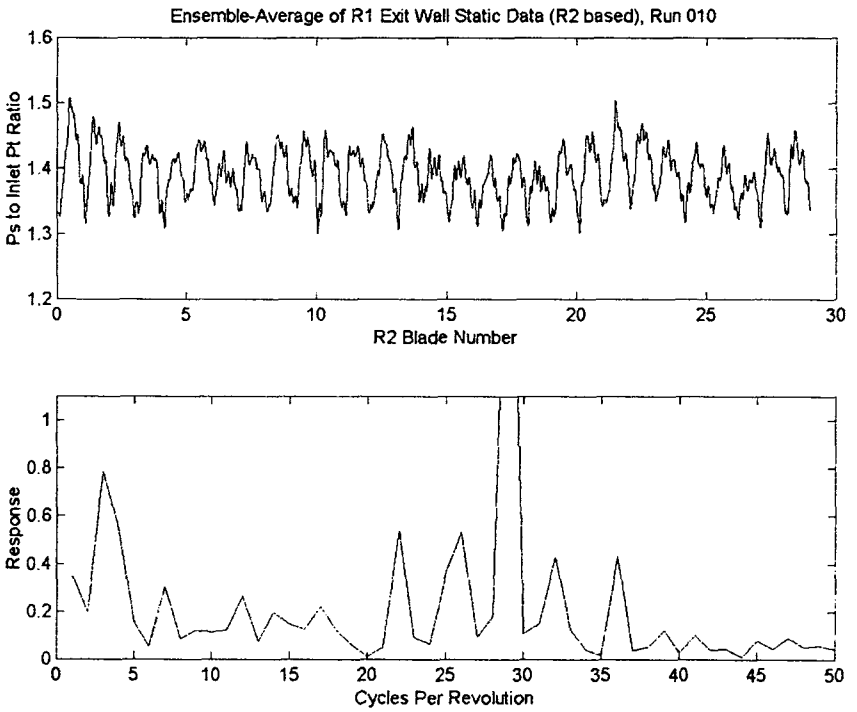


Figure 6.30: High-Frequency wall static pressure, ensemble averaged, Run 010

7 Conclusions and Future Recommendations

7.1 Results

The Counter-Rotating Aspirated Blowdown Compressor Test Facility succeeded in measuring the adiabatic core efficiency of a counter-rotating fan with an uncertainty of ~0.8% by measuring the total temperatures and pressures. The available test time was shorter than desired (~100 ms compared to ~400 ms) because of the drop in supply tank gas temperature but it still exceeded the test time of previous blowdown compressor experiments. Three points were measured on the 90%-90% corrected speed line of the compressor along with 4 points on the 100%-100% corrected speed line. In spite of intentions the compressor was shown to operate with inlet distortions in temperature and pressure. Given the distortion there appeared to be similarities between the CFD and measured performance of the compressor. The measured pressure ratio was ~7% low at the design speed and the adiabatic core efficiency was 1-2% better than predicted.

7.2 Recommendations

The author feels that there is still much that could be learned from this facility. First, it might be of value to industry to finish mapping the compressor. There needs to be more investigation into how varying the corrected speed ratio changes the behavior of the compressor. The compressor has not yet been throttled to stall during the test time so of interest is the corrected flow margin between the design point and the stall point and the stall characteristics of counter-rotating compressor.

7.2.1 Further Analysis

Some of the above questions can be answered through further analysis of the current data. The compressor has entered rotating stall during every run. The high-frequency casing static pressure data during this time could be investigated to learn something about the frequencies of the rotating stall. There is only one circumferential location for this data so there is no information about the number of stall cells. Also caution must be used because typically when the compressor stalls the inlet temperature is so cold that one cannot be certain about the properties of the flow entering the compressor.

The author also feels that improvements need to be made to the lumped parameter model that was used when designing the facility. Improvements would include changing how the compressor is modeled to match what has been observed in tests thus far. This model should also include some estimate of what is occurring in the bleed passage. An improved model has the potential of shedding light on the question of what is causing the change in corrected flow.

7.2.2 Further Measurements

Before another test is run it would be good to replace the pressure screen. This should decrease the inlet distortion. Based on the available data a perforated plate with an open area of 40% provides an adequate loss in total pressure across the screen. In order for the total pressure entering the compressor to be constant to within ±0.5% the open area of the pressure screen must be constant to ±0.5%. In addition to replacing the pressure screen improvements should be made to the bleed flow passage to give a better measurement of the bleed flow. One idea is that an annular sleeve could be inserted into the current bleed flow passage to reduce its volume. This should improve the likelihood of measuring the bleed flow.

In addition to those facility modifications the author would like to see the number of high-frequency pressure measurements increased. High-frequency 4-way pressure probes should be placed behind each rotor [29]. Hopefully the adjustments to the bleed flow passage and the addition of a 4-way probe would allow investigators to find a correlation between the amount of bleed flow and the width of the wake exiting Rotor Two.

Finally, according to the CFD, the aspiration slots set the position of the shock in Rotor Two. Placing several high frequency transducers in an axial pattern above the second rotor would allow for verification of this flow feature. Also adding high frequency wall statics would give insight into rotating stall characteristics.

Works Cited

[1] A.J. Wennestrom, 1990, *Highly Loaded Axial Flow Compressors: History and Current Developments*, Journal of Turbomachinery, Oct 1990, Vol. 112

[2] J.L. Kerrebrock, 2001, *Aircraft Engines and the Gas Turbine;* © Massachusetts Institute of Technology, Cambridge, MA

[3] N.A. Cumpsty, 1989, *Compressor Aerodynamics,* © Longman Scientific & Technical, London U.K.

[4] Dr. Aspi Wadia, Personal Communication

[5] J.F. Onnee, 2005, *Aerodynamic Performance Measurements in a Counter-Rotating Aspirated Compressor;* Masters Thesis, Massachusetts Institute of Technology

[6] J.L. Kerrebrock. *The Prospects for Aspirated Compressors*. MIT – AIAA-2000-2472. 2000

[7] M.A. Saad, 1993, *Compressible Fluid Flow, Second Edition;* © Prentice-Hall Inc, Upper Saddle River, NJ

[8] J.L. Kerrebrock, May 1972, *The M.I.T Blowdown Compressor Facility;* GTL Report No. 108

[9] G.R. Guenette, Jr., 1985, *A Fully Scaled Short Duration Turbine Experiment;* ScD Thesis, Massachusetts Institute of Technology

[10] M. Glynn, Work done under contract October 2003 through January 2004

[11] W.D. Baines & E.G. Peterson, 1951, *An Investigation of Flow through Screens;* Transactions of the ASME

[12] I.E. Idel'chik, 1996, *Handbook of Hydraulic Resistance, Third Edition;* © Begell House Inc., New York, NY

[13] W.C. Young & R.G. Budymas, 2002, *Roark's Formulas for Stress and Strain, Seventh Edition;* © McGraw-Hill, New York, NY

[14] S.S. Rao, 1995, *Mechanical Vibrations 3rd Edition;* © Addison-Wesley Publishing Company, Reading, MA

[15] Personal communication with representatives of Mi-Tech Metals; July, 2004

[16] Ali Merchant, Personal Communication

[17] John Adamczyk, APNASA Solutions

[18] Fritz Neumayer, Personal Communication

[19] M. Glynn, Work done under contract June 2004

[20] May 9, 2005, *TWI Knowledge Summary: Electron-Beam Welding Equipment;* © The Welding Institute, http://www.twi.co.uk/j32k/protected/band_3/ksas001.html

[21] Ultraminiature IS Pressure Transducer, XCQ-062 Series Spec. Sheet; www.kulite.com

[22] National Instruments Product Information, www.ni.com

[23] E. Ower & R.C. Pankhurst, 1977, *The Measurement of Airflow, Fifth Edition;* © Pergamon Press Inc., Elmsford, NY

[24] United Sensor Corporation, www.unitedsensorcorp.com

[25] L.N. Cattafesta, 1988, *An Experimental Investigation of the Effects of Inlet Radial Temperature Profiles on the Aerodynamic Performance of a Transonic Turbine Stage,* Master's Thesis, © Massachusetts Institute Technology

[26] NIST Mixture Property Database Ver. 9.08, 1992, © US Department of Commerce, National Institute of Standards and Technology; Boulder, CO

[27] W.G. Cornell, 1958, *Losses in Flow Normal to Plane Screens;* Transactions of the ASME, May 1958

[28] HW Coleman & WG Steele, 1999, *Experimentation and Uncertainty Analysis for Engineers 2nd Edition,* Wiley-Interscience, New York, NY

[29] B.J. Schuler, 2001, *Experimental Investigation of an Aspirated Fan Stage,* Doctoral Thesis, © Massachusetts Institute Technology

Appendix A: Blowdown Equations

This derivation was first done by Kerrebrock and later expanded by Guenette. We assume an isentropic expansion through the valve, that the flow through the pressure screen is choked, that the supply tank acts as a stagnation plenum, and that properties inside the tank are uniform.

Start with conservation of mass

$$V_S \cdot \left(\frac{d}{dt} \rho_S(t) \right) = \text{mdot}$$

Noting that mass flow out of supply tank equals mass flow through choked screen

$$V_S \cdot \left(\frac{d}{dt} \rho_S(t) \right) = W_{Sc} \cdot \frac{A_{Sc} P_S(t)}{\sqrt{Rg \cdot T_S(t)}}$$

$$V_S \cdot \left(\frac{d}{dt} \rho_S(t) \right) = W_{Sc} \cdot A_{Sc} \rho_S(t) \cdot \sqrt{Rg \cdot T_S(t)}$$

For an Isentropic process:

$$\theta(t) = \frac{\rho(t)}{\rho(0)} = \left(\frac{T(t)}{T(0)} \right)^{\frac{1}{\gamma - 1}} = \left(\frac{P(t)}{P(0)} \right)^{\frac{1}{\gamma}}$$

$$V_S \cdot \rho_S(0) \cdot \left(\frac{d}{dt} \theta(t) \right) = W_{Sc} \cdot A_{Sc} \cdot \rho_S(0) \cdot \sqrt{Rg \cdot T_S(0)} \cdot \theta(t)^{\frac{\gamma+1}{2}}$$

$$\theta(t)^{\frac{-(\gamma+1)}{2}} \cdot \left(\frac{d}{dt} \theta(t) \right) = \frac{W_{Sc} \cdot A_{Sc}}{V_S} \cdot \sqrt{Rg \cdot T_S(0)}$$

Integrate over time:

$$\int_{t=0}^{t=t} \theta(t)^{\frac{-(\gamma+1)}{2}} \cdot \left(\frac{d}{dt} \theta(t) \right) dt = \int_{t=0}^{t=t} \frac{W_{Sc} \cdot A_{Sc}}{V_S} \cdot \sqrt{Rg \cdot T_S(0)}\, dt \qquad \theta(0) = 1$$

$$\frac{2}{1-\gamma} \theta(t)^{\frac{(1-\gamma)}{2}} - \frac{2}{1-\gamma} = \frac{W_{Sc} \cdot A_{Sc}}{V_S} \cdot \sqrt{Rg \cdot T_S(0)}\, t$$

$$\theta(t) = \left(1 + \frac{t}{\tau_b} \right)^{\frac{-2}{\gamma-1}} \qquad \tau_b = \left[\frac{(\gamma - 1) W_{Sc} \cdot A_{Sc}}{2 \cdot V_S} \cdot \sqrt{Rg \cdot T_S(0)} \right]^{-1}$$

Appendix B: Uncertainty Analysis Derivations

Uncertainty Propagation In Corrected Flow Measurement

The through the temperature and pressure range of flow into the compressor the gas mixture used in the facility does not follow the ideal gas law. During the test time the relationship between temperature, pressure, and density vary from the ideal gas law as much as 2%. In order to derive analytical expressions for the impact of measurement uncertainties on the uncertainty of the corrected flow the gas mixture will be assumed to follow the ideal gas law with constant thermodynamic properties such as γ.

The Corrected Flow is:

$$Wc = \frac{\dot{m} \cdot \sqrt{\frac{R_g \cdot T_t}{R_{Air} \cdot T_{t\,Ref}}}}{A_c \cdot \frac{P_t}{P_{t\,Ref}}}$$

$$\dot{m} = f(\gamma, M) \frac{A_C \cdot P_T}{\sqrt{R_g \cdot T_T}}$$

$$f(\gamma, M) = \frac{\sqrt{\gamma} \cdot M}{\left(1 + \frac{\gamma - 1}{2} M^2\right)^{\frac{\gamma+1}{2\cdot(\gamma-1)}}}$$

$$M = \sqrt{\frac{2}{\gamma - 1}\left(\left(\frac{P_t}{P_s}\right)^{\frac{\gamma-1}{\gamma}} - 1\right)}$$

combining these:

$$Wc = \frac{P_{t\,Ref}}{\sqrt{R_{Air} \cdot T_{t\,Ref}}} \frac{\sqrt{\gamma} \cdot M}{\left(1 + \frac{\gamma - 1}{2} M^2\right)^{\frac{\gamma+1}{2\cdot(\gamma-1)}}}$$

The relative uncertainty in the Corrected Flow measurement is:

$$\left(\frac{U_{Wc}}{Wc}\right)^2 = \left(\frac{M}{Wc}\frac{\partial Wc}{\partial M}\right)^2 \cdot \left(\frac{U_M}{M}\right)^2 + \left(\frac{\gamma}{Wc}\frac{\partial Wc}{\partial \gamma}\right)^2 \cdot \left(\frac{U_\gamma}{\gamma}\right)^2$$

$$\frac{M}{Wc}\frac{\partial Wc}{\partial M} = 1 - \frac{(\gamma + 1) \cdot M^2}{2 \cdot \left(1 + \frac{\gamma - 1}{2} M^2\right)}$$

$$\frac{\gamma}{Wc}\frac{\partial Wc}{\partial \gamma}=\frac{1}{2}-\gamma\left[\frac{1}{4}\cdot\frac{\gamma+1}{\gamma-1}\frac{M^2}{(1+\frac{\gamma-1}{\gamma}M^2)}-\frac{\ln(1+\frac{\gamma-1}{2}M^2)}{(\gamma-1)^2}\right]$$

Mach Number Uncertainty:

$$(\frac{U_M}{M})^2=\left(\frac{P_t}{M}\frac{\partial M}{\partial P_t}\right)^2(\frac{U_{Pt}}{P_t})^2+\left(\frac{P_s}{M}\frac{\partial M}{\partial P_s}\right)^2(\frac{U_{Ps}}{P_s})^2$$

$$\frac{P_t}{M}\frac{\partial M}{\partial P_t}=\frac{1}{2}\frac{\gamma-1}{\left(\frac{P_t}{P_s}\right)^{\frac{\gamma-1}{\gamma}}-1}\frac{\left(\frac{P_t}{P_s}\right)^{\frac{\gamma-1}{\gamma}}}{\gamma};\qquad \frac{P_s}{M}\frac{\partial M}{\partial P_s}=\frac{-1}{2}\frac{\gamma-1}{\left(\frac{P_t}{P_s}\right)^{\frac{\gamma-1}{\gamma}}-1}\frac{\left(\frac{P_t}{P_s}\right)^{\frac{\gamma-1}{\gamma}}}{\gamma}$$

$$\frac{\gamma}{M}\frac{\partial M}{\partial \gamma}=\frac{\gamma}{2}\frac{\gamma-1}{\left(\frac{P_t}{P_s}\right)^{\frac{\gamma-1}{\gamma}}-1}\left[\frac{-1}{(\gamma-1)^2}\left(\left(\frac{P_t}{P_s}\right)^{\frac{\gamma-1}{\gamma}}-1\right)+\frac{1}{\gamma^2(\gamma-1)}\left(\frac{P_t}{P_s}\right)^{\frac{\gamma-1}{\gamma}}\ln\left(\frac{P_t}{P_s}\right)\right]$$

Thus, the analytical expression for the uncertainty in the corrected flow measurement is:

$$(\frac{U_{Wc}}{Wc})^2=\left[1-\frac{(\gamma+1)\cdot M^2}{2\cdot(1+\frac{\gamma-1}{2}M^2)}\right]^2\cdot\left[\frac{1}{2}\frac{\gamma-1}{\left(\frac{P_t}{P_s}\right)^{\frac{\gamma-1}{\gamma}}-1}\frac{\left(\frac{P_t}{P_s}\right)^{\frac{\gamma-1}{\gamma}}}{\gamma}\right]^2\left(\frac{U_{Pt}}{P_t}\right)^2+\ldots$$

$$\left[1-\frac{(\gamma+1)\cdot M^2}{2\cdot(1+\frac{\gamma-1}{2}M^2)}\right]^2\cdot\left[-\frac{1}{2}\frac{\gamma-1}{\left(\frac{P_t}{P_s}\right)^{\frac{\gamma-1}{\gamma}}-1}\frac{\left(\frac{P_t}{P_s}\right)^{\frac{\gamma-1}{\gamma}}}{\gamma}\right]^2\left(\frac{U_{Ps}}{P_s}\right)^2+\ldots$$

$$\left[\left(\frac{1}{2}-\gamma\left[\frac{1}{4}\cdot\frac{\gamma+1}{\gamma-1}\frac{M^2}{(1+\frac{\gamma-1}{\gamma}M^2)}-\frac{\ln(1+\frac{\gamma-1}{2}M^2)}{(\gamma-1)^2}\right]\right)^2+\ldots\right.$$

$$\left.\left(1-\frac{(\gamma+1)\cdot M^2}{2\cdot(1+\frac{\gamma-1}{2}M^2)}\right)^2\cdot\left(\frac{\gamma}{2}\frac{\gamma-1}{\left(\frac{P_t}{P_s}\right)^{\frac{\gamma-1}{\gamma}}-1}\left[\frac{-1}{(\gamma-1)^2}\left(\left(\frac{P_t}{P_s}\right)^{\frac{\gamma-1}{\gamma}}-1\right)+\frac{1}{\gamma^2(\gamma-1)}\left(\frac{P_t}{P_s}\right)^{\frac{\gamma-1}{\gamma}}\ln\left(\frac{P_t}{P_s}\right)\right]\right)^2\right]\left(\frac{U_\gamma}{\gamma}\right)^2$$

Uncertainty Propagation in Adiabatic Efficiency

As with the corrected flow uncertainty analysis the fluid is also considered to be an ideal gas for this analysis

The expression for adiabatic efficiency when the flow is an ideal gas, and properties are assumed constant:

$$\eta = \frac{\pi^{\frac{\gamma-1}{\gamma}} - 1}{\tau - 1}$$

η - adiabatic efficiency,
τ - total temperature ratio,
π - total pressure ratio,
γ - ratio of specific heats

The absolute uncertainty in the adiabatic efficiency is:

$$U_\eta^2 = \left(\pi \frac{\partial \eta}{\partial \pi}\right)^2 \left(\frac{U_\pi}{\pi}\right)^2 + \left(\tau \frac{\partial \eta}{\partial \tau}\right)^2 \left(\frac{U_\tau}{\tau}\right)^2 + \left(\gamma \frac{\partial \eta}{\partial \gamma}\right)^2 \left(\frac{U_\gamma}{\gamma}\right)^2$$

Taking the derivatives:

$$\frac{\partial \eta}{\partial \pi} = \frac{\gamma - 1}{\gamma(\tau - 1)} \cdot \pi^{\frac{-1}{\gamma}}, \qquad \frac{\partial \eta}{\partial \tau} = \frac{1 - \pi^{\frac{\gamma-1}{\gamma}}}{(\tau - 1)^2}, \qquad \frac{\partial \eta}{\partial \gamma} = \frac{\pi^{\frac{\gamma-1}{\gamma}} \ln(\pi)}{\gamma^2(\tau - 1)}$$

Relating temperature ratio and pressure ratio to upstream and downstream measurements:

$$\left(\frac{U_\pi}{\pi}\right)^2 = \left(\frac{U_{Pup}}{Pup}\right)^2 + \left(\frac{U_{Pdn}}{Pdn}\right)^2$$

$$\left(\frac{U_\tau}{\tau}\right)^2 = \left(\frac{U_{Tup}}{Tup}\right)^2 + \left(\frac{U_{Tdn}}{Tdn}\right)^2$$

Thus

$$U_\eta^2 = \left(\pi \cdot \frac{\gamma - 1}{\gamma \cdot (\tau - 1)} \cdot \pi^{\frac{-1}{\gamma}}\right)^2 \cdot \left(\left(\frac{U_{PtUp}}{Pt_{Up}}\right)^2 + \left(\frac{U_{PtDn}}{Pt_{Dn}}\right)^2\right) \cdots$$

$$+ \left(\tau \cdot \frac{1 - \pi^{\frac{\gamma-1}{\gamma}}}{(\tau - 1)^2}\right)^2 \cdot \left(\left(\frac{U_{TtUp}}{Tt_{Up}}\right)^2 + \left(\frac{U_{TtDn}}{Tt_{Dn}}\right)^2\right) + \left(\frac{\pi^{\frac{\gamma-1}{\gamma}} \cdot \ln(\pi)}{\gamma \cdot (\tau - 1)}\right)^2 \cdot \left(\frac{U_\gamma}{\gamma}\right)^2$$

Uncertainty Propagation in Corrected Speed

Corrected Speed is defined as:

$$Nc = \frac{N \cdot \pi \cdot D}{\sqrt{R_g \cdot T_t}}$$

Taking the derivatives, and plugging into the equations for Relative Uncertainty yields

$$\left(\frac{U_{Nc}}{Nc}\right)^2 = \left(\frac{U_N}{N}\right)^2 + \frac{1}{4}\left(\frac{U_{Tt}}{T_t}\right)^2 + \frac{1}{4}\left(\frac{U_{Rg}}{R_g}\right)^2$$

The uncertainty in the speed measurement is due to quantization error in the 80 MHz counter cards.

At full speed the relative error in the speed measurement is ~2.7×10^{-6} for Rotor One and ~2.3×10^{-6} for Rotor Two.

Appendix C: Measurement Uncertainties

Pressure Uncertainties that Result form Probe Geometry

Values based on Equations 5.2 and 5.3

Table C.1: Relative uncertainties in pressure measurements due to probe geometry

			Relative Uncertainties		
Run	Inlet Mach	Exit Mach	Up Pt	Up Ps	Down Pt
005	0.535	0.441	0.17%	0.14%	0.26%
006	0.492	0.439	0.17%	0.14%	0.21%
007	0.425	0.429	0.16%	0.13%	0.15%
008	0.424	0.451	0.18%	0.15%	0.15%
009	0.432	0.519	0.24%	0.19%	0.16%
010	0.436	0.521	0.24%	0.19%	0.16%
011	0.433	0.485	0.21%	0.17%	0.16%
013	0.456	0.570	0.30%	0.23%	0.18%
014	0.478	0.593	0.32%	0.25%	0.20%

Pressure Transducer Qualification

After the tests where run the pressure transducers were calibrated to check their linearity. This was done by evacuating the system taking data for 60 seconds at vacuum then venting atmospheric air in. The venting in process was done in steps. The Heise 015 was used as the standard during the calibration, after the indicated Heise 015 pressure was steady to with 0.001 psi for greater than 40 seconds more air was let into the facility to move to the next calibration point. Figure C.1 shows the Heise pressure during the entire qualification test. The range of the qualification was limited to vacuum to 1 atm because 15 psi is the maximum rated pressure difference across the upstream transducers. This meant that although the upstream transducers were qualified over their entire range the downstream transducers were only qualified for 1/3 of their range. The voltage data during the time the Heise reading was constant was averaged to find the transducer non-linearity for that point, the standard deviation of that data, labeled as 'noise' was assumed to be the uncertainty due to noise of the transducer and the signal conditioners. This data is listed in Tables C.2 and C.3.

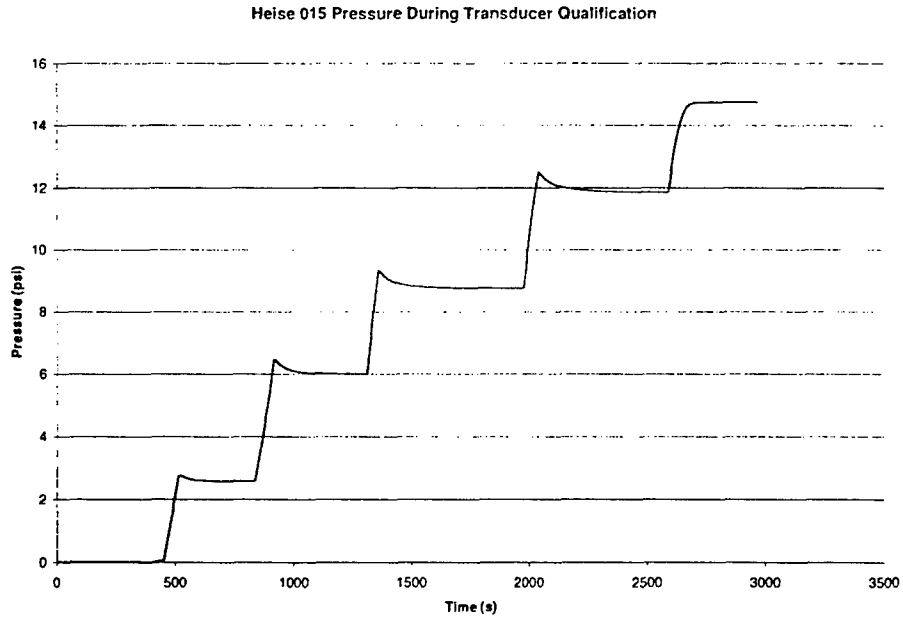


Figure C.1: Pressure history of Heise 015 during transducer qualification

Table C.2: Qualification Data For Upstream Pressure Transducers

Upstream Transducer Uncertainties		
Name	**Linearity**	**Noise**
PT0A	0.12%	0.77%
PT1A	0.10%	0.35%
PDMP	0.50%	0.10%
PT2ZR01	0.12%	0.14%
PT2ZR02	0.16%	0.17%
PPT2C	0.15%	0.20%
PT2ZR04	0.09%	0.17%
PT2ZR05	0.11%	0.15%
PPS2C	0.12%	0.24%
PT2ZR07	0.12%	0.24%
PT2ZR08	0.14%	0.15%
PT2A	0.27%	0.19%
PS2A	0.10%	0.30%
PPT2A	0.14%	0.33%
PPS2A	0.16%	0.28%
PT2B	0.12%	0.13%
PS2B	0.12%	0.33%
PT2C	0.10%	0.15%
PS2C	0.11%	0.11%
PW1	0.09%	0.14%
PPT2B	0.09%	0.15%
PPS2B	0.09%	0.16%
Average	**0.14%**	**0.22%**

Table C.3: Qualification Data for Downstream Pressure Transducers

Down Stream Transducer Uncertainties		
Name	**Linearity**	**Noise**
PT5A	0.05%	0.91%
PPT5A	0.06%	0.16%
PPS5A	0.02%	0.16%
PT5ZR01	0.06%	0.20%
PT5ZR02	0.02%	0.31%
PT5ZR03	0.03%	0.23%
PT5ZR04	0.08%	0.32%
PT5ZR05	0.06%	0.37%
PT5CR01	0.16%	0.19%
PT5CR02	0.13%	0.18%
PT5CR03	1.11%	0.49%
PT5CR04	0.18%	0.14%
PT5CR05	0.10%	0.24%
PS3HS	0.13%	0.47%
PS5AHS	0.09%	0.14%
Average	**0.15%**	**0.30%**

Summary of Pressure Uncertainties

Table C.4: Up Stream Total Pressure Uncertainty

Total Upstream Total Pressure Uncertainty				
Run	**Head Loss**	**Linearity**	**Noise**	**Total**
005	0.17%	0.12%	0.18%	0.28%
006	0.17%	0.12%	0.18%	0.28%
007	0.16%	0.12%	0.18%	0.27%
008	0.18%	0.12%	0.18%	0.28%
009	0.24%	0.12%	0.18%	0.33%
010	0.24%	0.12%	0.18%	0.33%
011	0.21%	0.12%	0.18%	0.30%
013	0.30%	0.12%	0.18%	0.37%
014	0.32%	0.12%	0.18%	0.39%

Table C.5: Down Stream Total Pressure Uncertainty

Total Down Stream Total Pressure Uncertainty				
Run	Head Loss	Linearity	Noise	Total
005	0.26%	0.19%	0.27%	0.42%
006	0.21%	0.19%	0.27%	0.39%
007	0.15%	0.19%	0.27%	0.36%
008	0.15%	0.19%	0.27%	0.36%
009	0.16%	0.19%	0.27%	0.37%
010	0.16%	0.19%	0.27%	0.37%
011	0.16%	0.19%	0.27%	0.37%
013	0.18%	0.19%	0.27%	0.38%
014	0.20%	0.19%	0.27%	0.38%

Table C.6: Up Stream Static Pressure Uncertainty

Total Upstream Static Pressure Uncertainty				
Run	Head Loss	Linearity	Noise	Total
005	0.14%	0.13%	0.21%	0.29%
006	0.14%	0.13%	0.21%	0.28%
007	0.13%	0.13%	0.21%	0.28%
008	0.15%	0.13%	0.21%	0.29%
009	0.19%	0.13%	0.21%	0.32%
010	0.19%	0.13%	0.21%	0.32%
011	0.17%	0.13%	0.21%	0.30%
013	0.23%	0.13%	0.21%	0.34%
014	0.25%	0.13%	0.21%	0.35%

Summary of Temperature Uncertainties

The sources of these uncertainties are discussed in detail in "Aerodynamic Performance Measurements in a Counter-Rotating Aspirated Compressor" [5]

Table C.7: Summary of Absolute Temperature Uncertainty

Sensor Name	Uncertainty (K)				
	Recovery	Conduction	Radiation	Calibration	Total
TCKSU001	0.025	0.005	0.112	0.048	0.124
TCKSU002	0.025	0.005	0.112	0.058	0.129
TCKSU007	0.025	0.005	0.112	0.055	0.127
TCKRU001	0.025	0.073	0.112	0.041	0.142
TCKRU002	0.025	0.073	0.112	0.038	0.141
TCKRU003	0.025	0.073	0.112	0.04	0.142
TCKRU004	0.025	0.073	0.112	0.039	0.141
TCKRU005	0.025	0.073	0.112	0.042	0.142
TCKRU006	0.025	0.073	0.112	0.04	0.142
TCKRU007	0.025	0.073	0.112	0.038	0.141
TCKRU008	0.025	0.073	0.112	0.039	0.141
TCKRU009	0.025	0.073	0.112	0.039	0.141
TCKRU010	0.025	0.073	0.112	0.043	0.143
TCKRU011	0.025	0.073	0.112	0.042	0.142
TCKSD001	0.0065	0.0005	0.299	0.071	0.307
TCKSD002	0.0065	0.0005	0.299	0.036	0.301
TCKSD003	0.0065	0.0005	0.299	0.065	0.306
TCKRD001	0.0065	0.014	0.299	0.033	0.301
TCKRD002	0.0065	0.014	0.299	0.028	0.301
TCKRD003	0.0065	0.014	0.299	0.034	0.301
TCKRD004	0.0065	0.014	0.299	0.034	0.301
TCKRD005	0.0065	0.014	0.299	0.037	0.302
TCKRD006	0.0065	0.014	0.299	0.06	0.305
TCKRD007	0.0065	0.014	0.299	0.326	0.443
TCKRD008	0.0065	0.014	0.299	0.054	0.304
TCKRD009	0.0065	0.014	0.299	0.047	0.303
TCKRD010	0.0065	0.014	0.299	0.062	0.306
TCKRD011	0.0065	0.014	0.299	0.097	0.315

Summary of Gas Mixture Uncertainties

For all the reported performance values the gas tables that are used assume that the gas mixture is the design gas mixture. The gases are mixed in the supply tank by partial pressures. The gases are at room temperature while mixing and pressures do not exceed 2 atm thus the gases are assumed to be ideal and the mole fraction of each gas is the same as its partial pressure in the mixture. The uncertainty in γ and R_g is assumed to be the same as the error in the mole fraction of the mixture compared to the design mole fraction. This uncertainty is summarized in Table C.8

Table C.8: Uncertainty in gas mixture

Run	First gas filled	P 1st (psia)	Final P (psia)	X CO2	X Ar	Absolute Error in Mixture
005	CO2	16.750	34.140	49.06%	50.94%	0.15%
006	CO2	16.820	34.280	49.07%	50.93%	0.16%
007	CO2	16.820	34.230	49.14%	50.86%	0.23%
008	Ar	19.910	38.750	48.62%	51.38%	0.29%
009	CO2	16.840	34.410	48.94%	51.06%	0.03%
010	CO2	14.280	29.110	49.06%	50.94%	0.15%
011	CO2	14.320	29.270	48.92%	51.08%	0.01%
013	CO2	14.380	29.370	48.96%	51.04%	0.05%
014	CO2	14.300	29.180	49.01%	50.99%	0.10%

Appendix D: Blowdown Test Details

Sequence of Test Operations

1. Check Facility
   1.1. Verify that everything is sealed, instruments in place, throttle set correctly
2. Pull Vacuum
   2.1. Verify that the cooling water for the pump is on.
   2.2. Verify that the facility is approaching vacuum at the appropriate rate and there are no leaks.
   2.3. Turn on reference vacuum pump
      2.3.1. verify that pressure transducers respond when back pressure is swapped from vacuum to atmosphere
      2.3.2. verify that all transducers operate within the voltage range of the A/D
3. Perform Pre-Fill Calibrations
   3.1. Details of calibration procedures follow
4. Turn on water and heaters for gas fill system heat exchangers
   4.1. Ensure that the drive motors and water heaters are not on at the same time
5. Open appropriate valves on the CO_2 and the Ar bottle farms
6. Use pressure from an Ar bottle to hold the fast-acting valve closed with ~200 psi
7. Fill the supply tank to a value greater than the desired initial pressure
   7.1. Fill first with CO_2, after reaching desired pressure wait until the output of the Heise 150 is constant for at least 1 minute
      7.1.1. Record the supply tank pressure and temperature
   7.2. Fill with Ar to a value that is calculated based on the filled CO_2 pressure
      7.2.1. Record pressure after the Heise 150 is constant for at least 1 minute, multiple fills might be required to get the design mixture ratio
8. Perform Post-Fill Calibrations
9. Open the A/D program and the motor control program
   9.1. Input and double check appropriate variables for each
10. Arm the fast-acting valve with ~600 psi of pressure
    10.1. If there is a problem while accelerating the rotors firing the valve will decelerate the rotors faster than the motor drives can brake them
11. Begin accelerating the rotors
12. With the A/D program begin logging 'pre-test data'
13. While the rotors are spinning vent the supply tank until it is at the desired initial pressure and record ambient temperatures and pressures
14. Once both rotors are at the set speed set them both to 'coast' and immediately fire the valve
15. After ~5 seconds use the motor drives to brake the rotors
16. ~5 minutes after the rotors have stopped spinning perform the Post-Test Calibrations
17. "Safe" the facility
    17.1. Vent system to atm or begin pulling vacuum for next test
    17.2. Close all valves on the bottle farms
    17.3. Depressurize the fast-acting valve
    17.4. Turn off power to motor drives

Calibration Method

Two point calibrations of each pressure transducer occur three times during each test. The calibrations occur before the supply tank is filled (Pre-Fill Cal), with the entire tunnel in vacuum; after the supply tank is filled (Post-Fill Cal), with every transducer except for the supply tank transducers in vacuum; and several minutes after the test (Post-Test Cal), with the entire tunnel at one pressure level somewhere between vacuum and atmospheric. During all of these calibrations the pressure in the dump tank and the supply tank is measured with Heise absolute pressure transducers that were calibrated to be accurate to 0.15% of their range. The two pressure difference points are created by opening a valve that switches the reference pressure from vacuum to atmosphere. The reference vacuum pressure is measured using a Varian Type 053 Vacuum Gauge and atmospheric pressure in the lab is measured right before the calibration by switching the dump tank Heise from the dump tank to atmospheric.

In addition to the Heise absolute transducers two SensoTec absolute pressure transducers are supply and dump tanks and attached to the same A/D card as the other pressure transducers. There are 100 ms between when the A/D system starts logging data and when the valve begins opening. Data from the SensoTecs is averaged during this time to establish the initial pressures in the facility. This information is then used with the scales calculated from the two points in the calibrations to establish a zero for each transducer.

Of the three calibrations only the Post-Test Cal calibrates the transducers in a manner similar to the operation range. During the Pre and Post-Fill Cals the calibration range is from zero to negative one atmosphere. These calibrations are used to check the stability of the transducers and as an extra check that all the transducers are responding before the test. When the data is reduced the scale and zero calculated from the Post-Test Cal are used.

Appendix E: Raw Data Documentation

This appendix documents the raw data for Run 013. Also documented are metrics for what is happening within the facility, more details on data reduction, and what happens after the test time.

Raw Data

Figure E.1 is the pressures of the supply tank (PT0A, STEC 150) and the total pressure in the valve (PT1A).

Figure E.2 is the mid-stream upstream single total pressure measurements.

Figure E.3 is the upstream static pressure measurements; wall taps and pitot.

Figure E.4 is the upstream total pressure rake measurements, for all rakes the probe numbered '1' is at the hub.

Figure E.5 is the upstream total temperature single measurements, the thermocouples are not calibrated below 212° K.

Figure E.6 is the upstream total temperature rake measurements, the thermocouples are not calibrated below 212° K.

Figure E.7 is the casing static pressure measurements. PS3HS is between the rotors and PS5AHS is behind Rotor Two.

Figure E.8 is the pitot probe in the middle of the downstream span.

Figure E.9 is the down stream total pressure measurements.

Figure E.10 is the downstream total temperature measurements.

Figure E.11 is the pressures in the dump tank, the STEC050 transducer is in a different location than PDMP, which explains the variation.

Figure E.12 is the pressure in the bleed flow.

Figure E.13 is the speeds of each rotor.

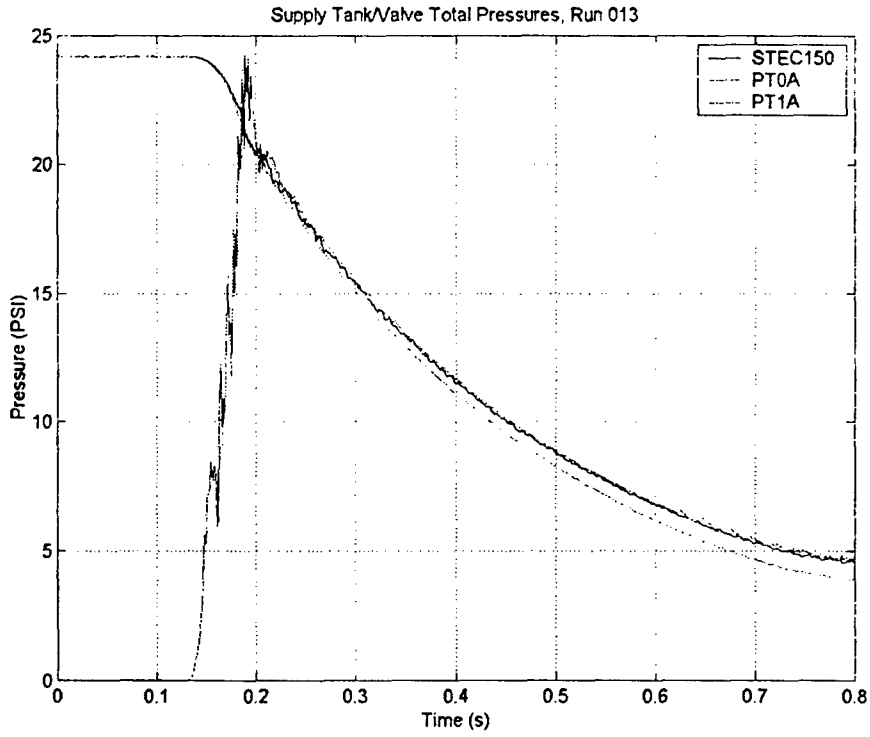


Figure E.1: Supply Tank Pressures, Run 013

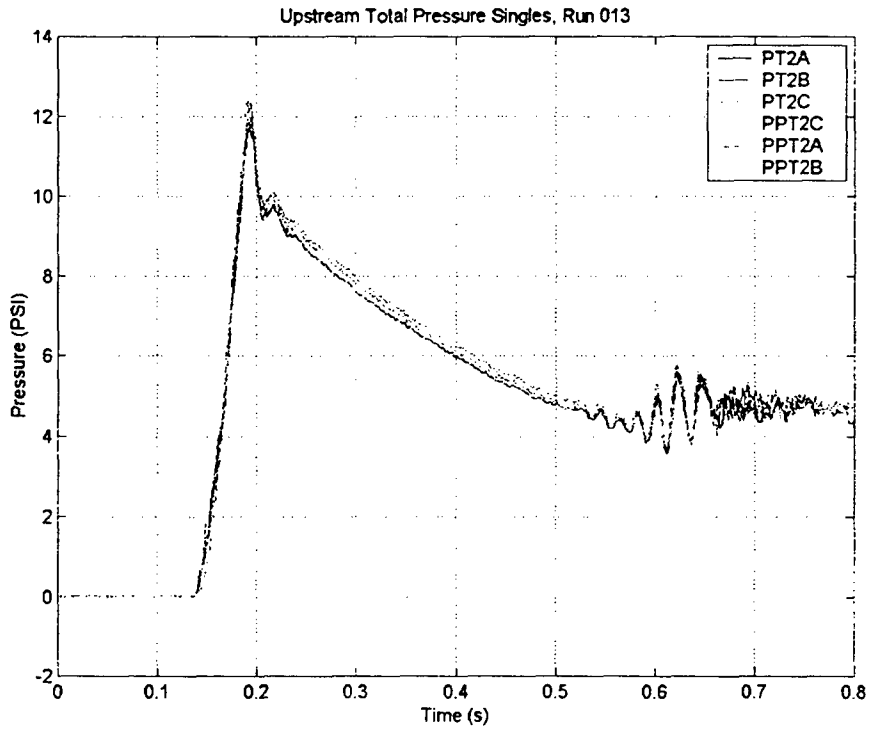


Figure E.2: Upstream Total Pressure Singles, Run 013

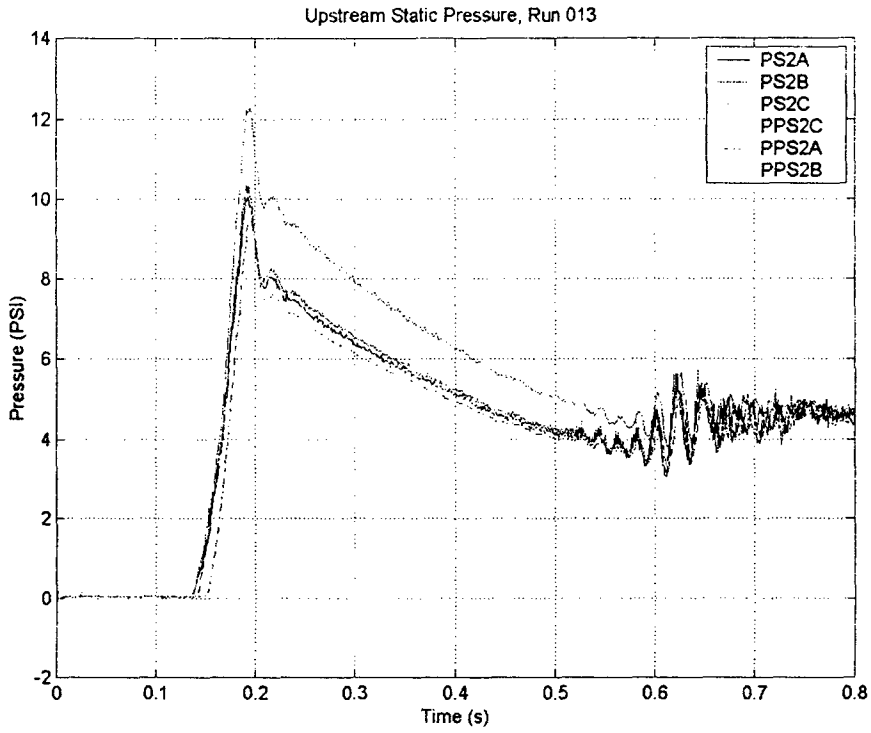


Figure E.3: Upstream Static Pressures, Run 013

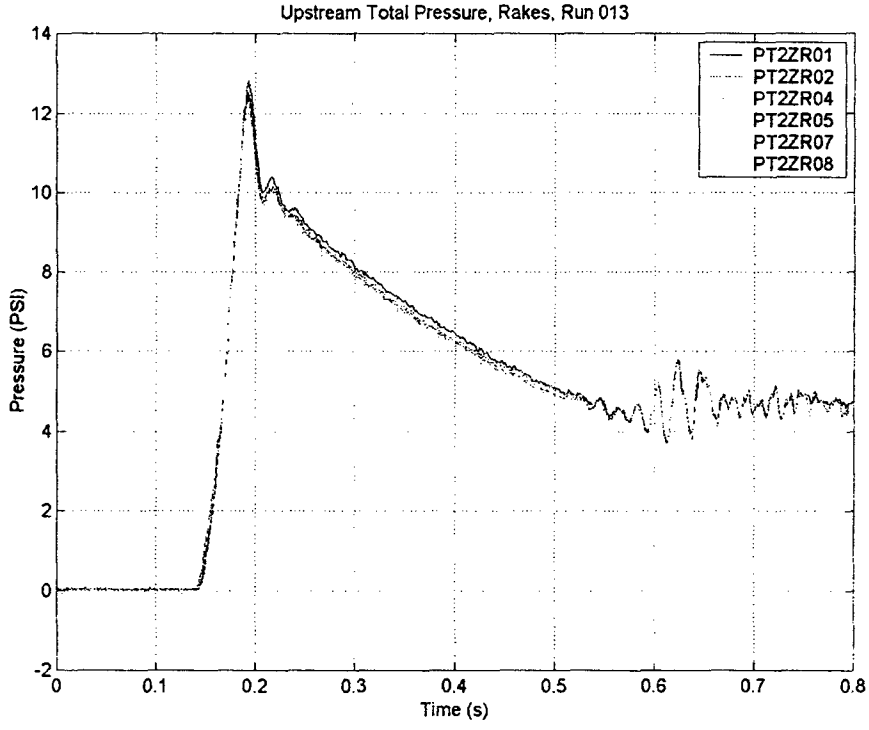


Figure E.4: Upstream Total Pressure, Rakes Run 013

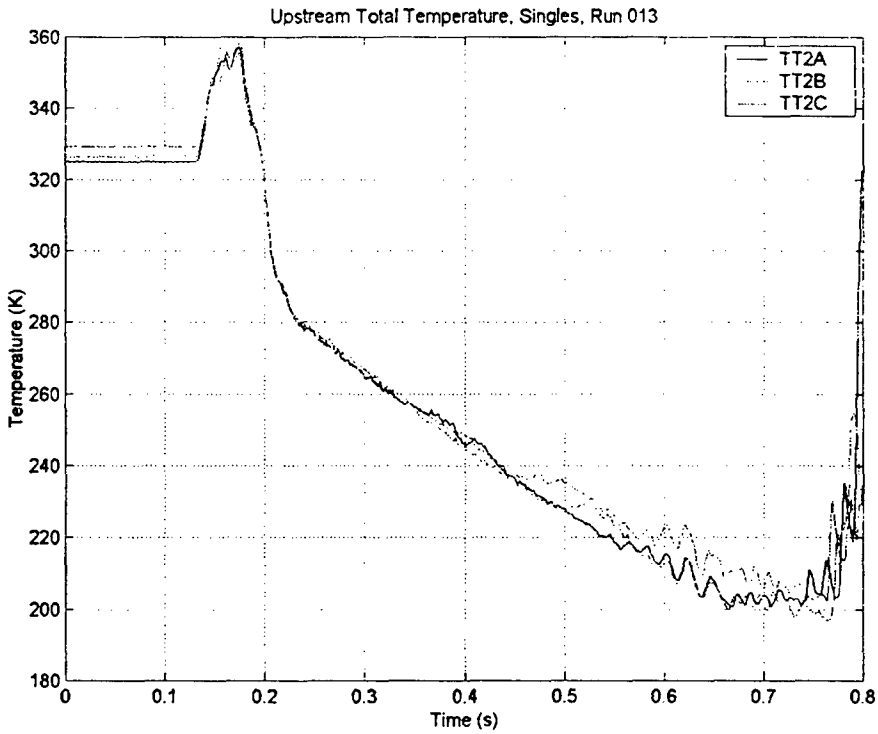


Figure E.5: Upstream Total Temperature Singles, Run 013

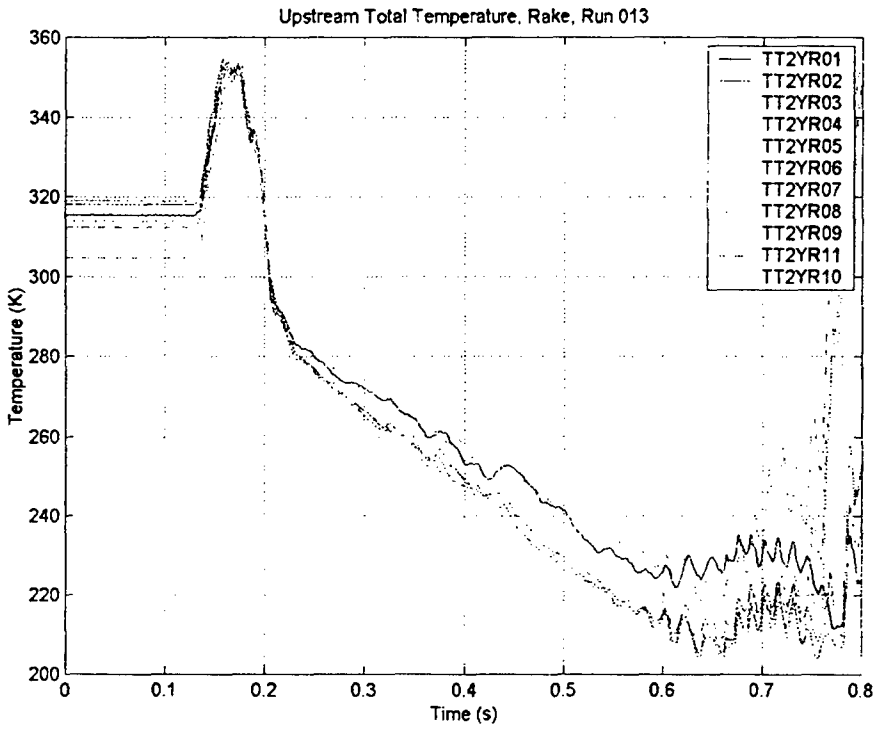


Figure E.6: Upstream Total Temperature Rake Measurements, Run 013

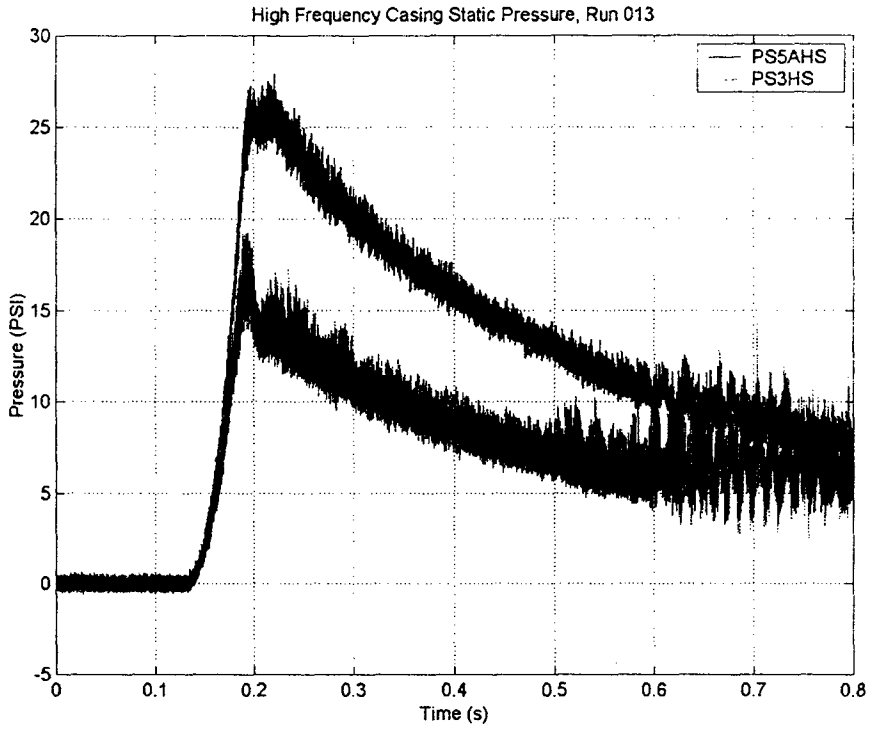


Figure E.7:High frequency casing static pressure measurements, Run 013

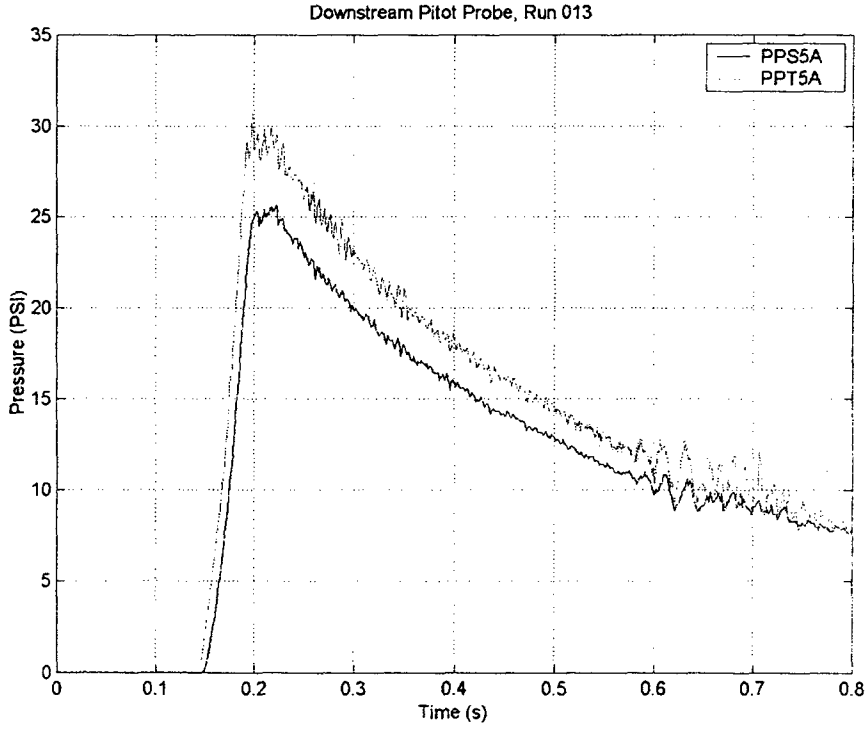


Figure E.8: Downstream mid-stream Pitot Probe, Run 013

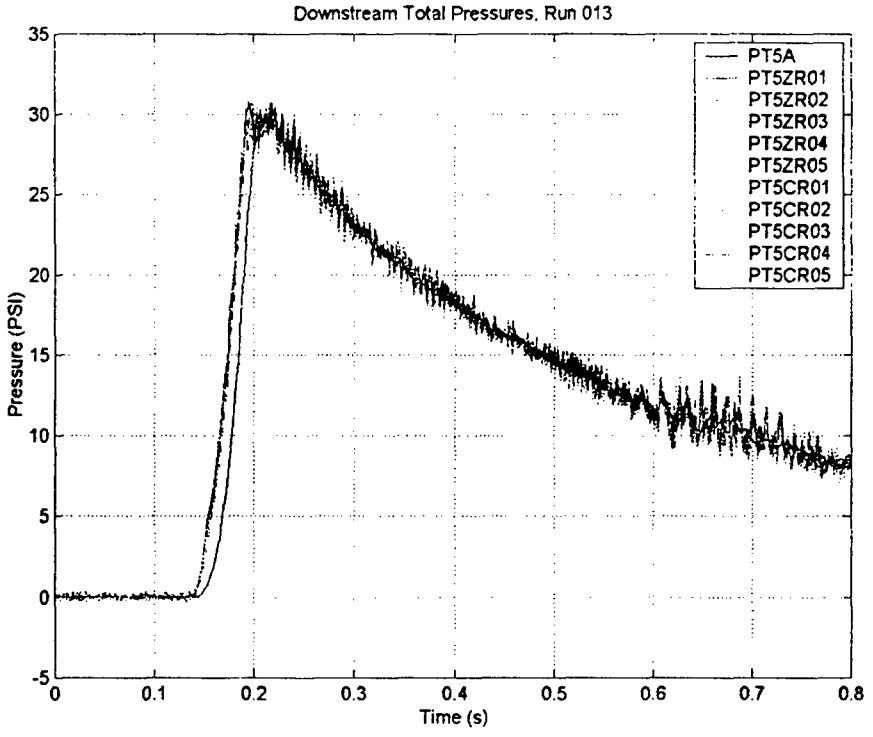


Figure E.9: Downstream Total Pressures, Run 013

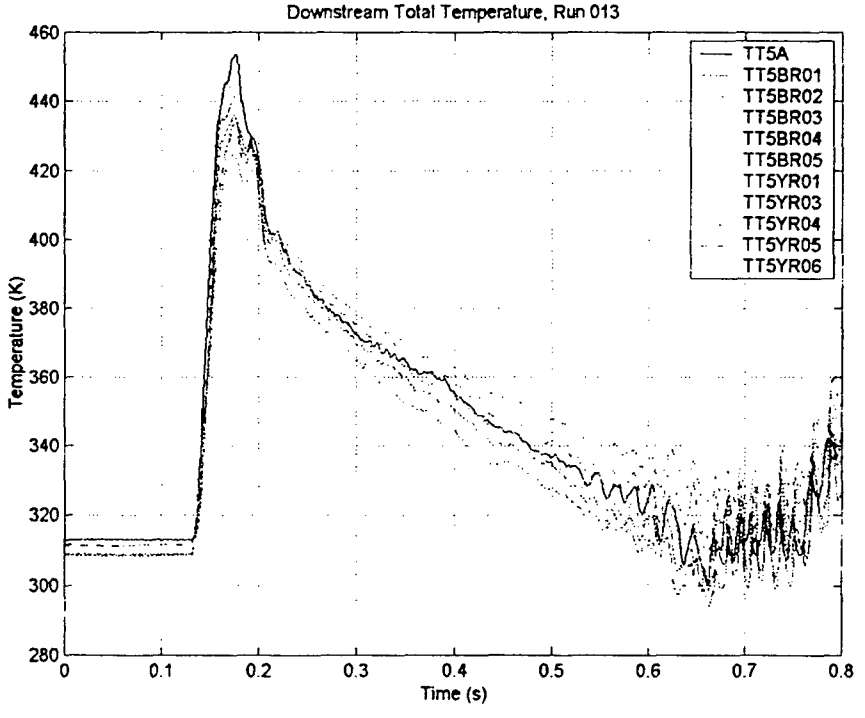


Figure E.10: Downstream Total Temperatures, Run 013

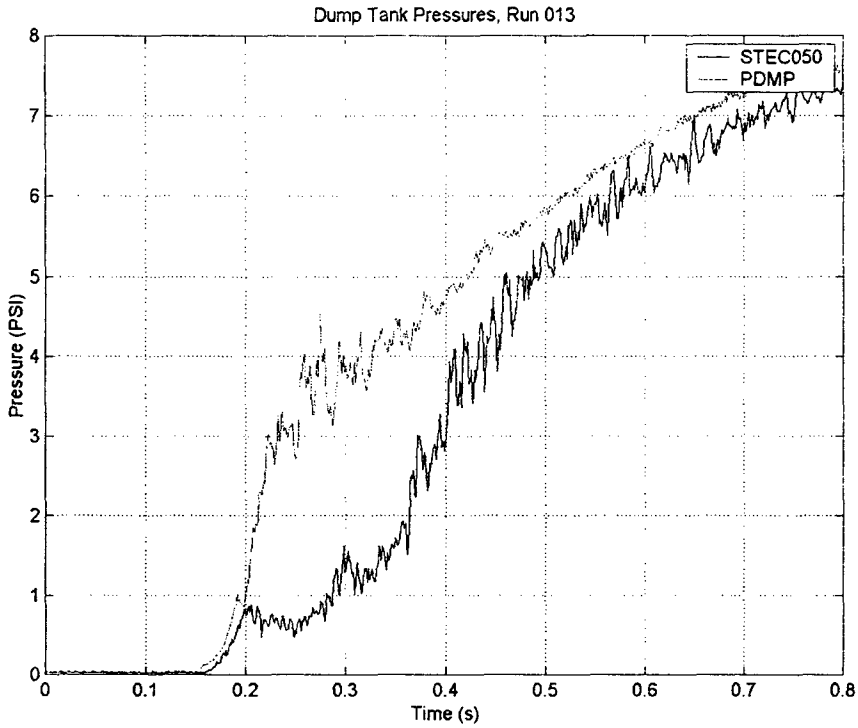


Figure E.11: Dump Tank Pressures, Run 013

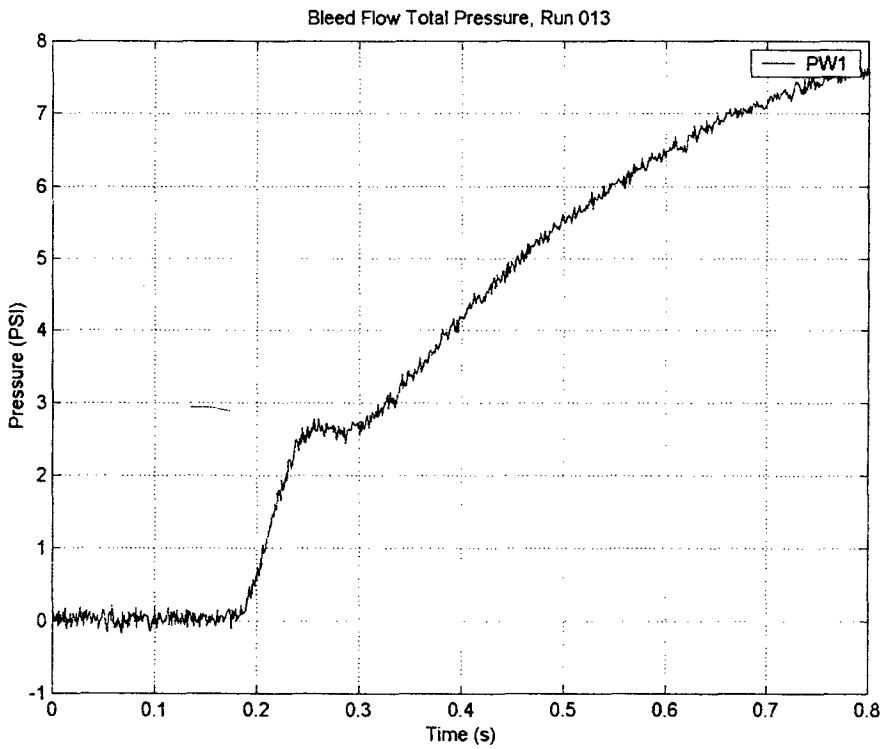


Figure E.12: Bleed Flow Total Pressure, Run 013

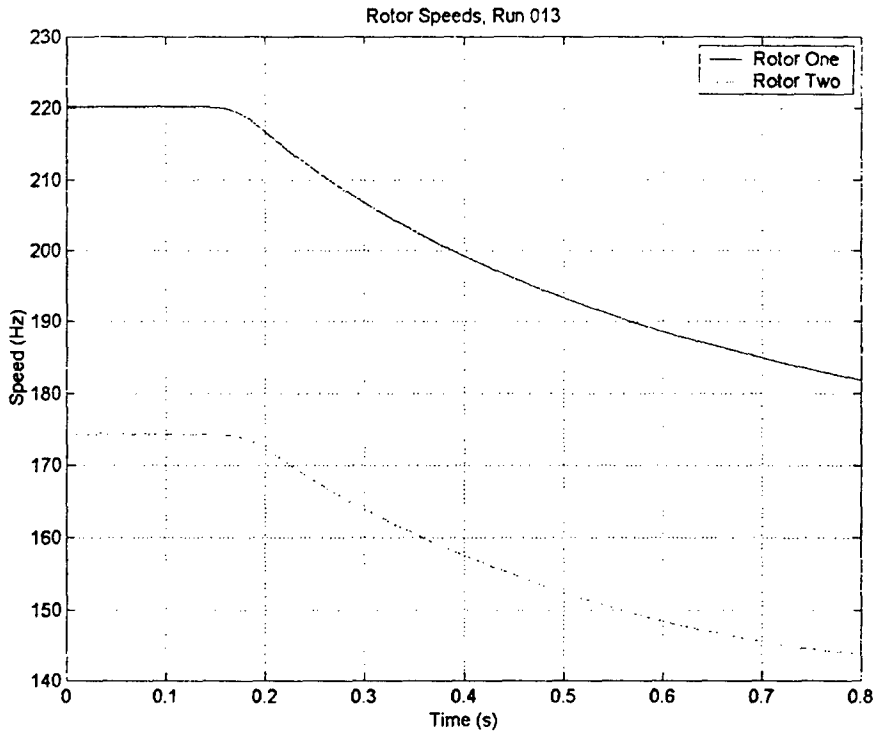


Figure E.13: Rotor speeds during Run 013

Facility Conditions & Test Time Selection

Figure E.14 is the corrected speeds of each rotor, normalized by the design corrected speeds. Figure E.15 is the corrected speeds during the test time. Between 250 ms and 350 ms the corrected speeds vary by less than 0.5% for Run 013. Constant corrected speed is one criteria when deciding what the test time is.

Figure E.16 is the pressure ratios across the screen, the pressure ratio across the screen, and the pressure ratio across the bleed flow passage (Rotor Two exit total pressure divided by the bleed passage total pressure). The horizontal line is the approximate minimum pressure ratio for choked flow. It was thought that while the throttle and screen were choked the corrected flow into the compressor would be constant. The pressure ratio across the bleed passage is currently the only way to make any statement about the bleed flow. As long as this passage is choked the corrected bleed flow should be constant. Figure E.17 is the entropy entering the compressor normalized by entropy at 250 ms. This plot verifies that the blowdown is occurring isentropically, as the model assumes, and that the instruments are well calibrated.

Selecting the 'test time' is arbitrary. The throttle must be choked, the corrected speeds must be constant to within some value (1% of the design was used), the initial compression wave must have passed and the upstream temperature of the gas must be

greater than 225° K. 250 ms to 350 ms was selected as a test time for each run because these parameters were met and using the same test time for each run simplified reduction and comparisons from one run to another.

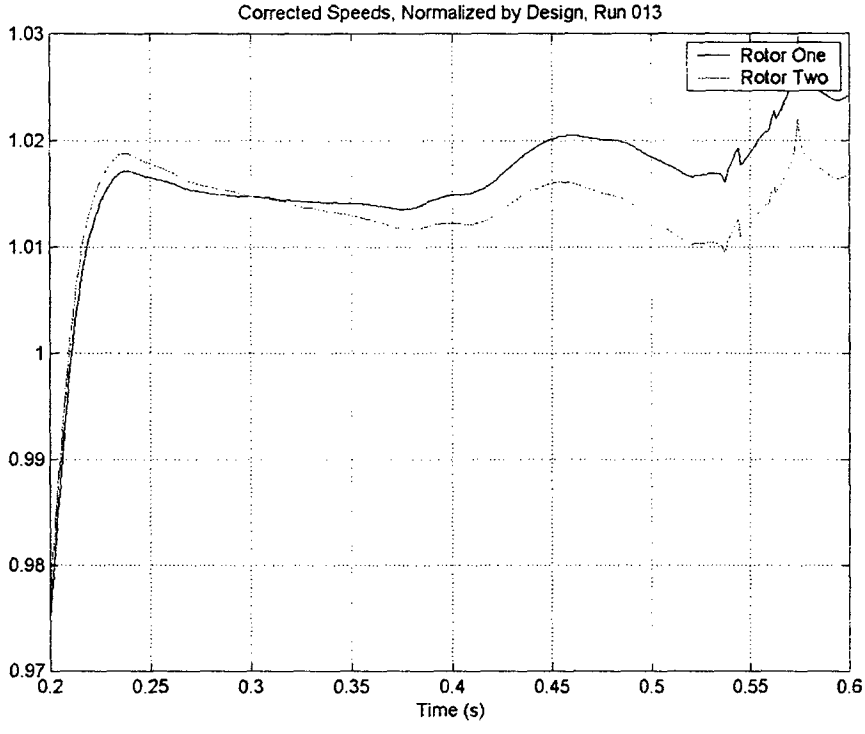


Figure E.14: Corrected Speeds During Run 013

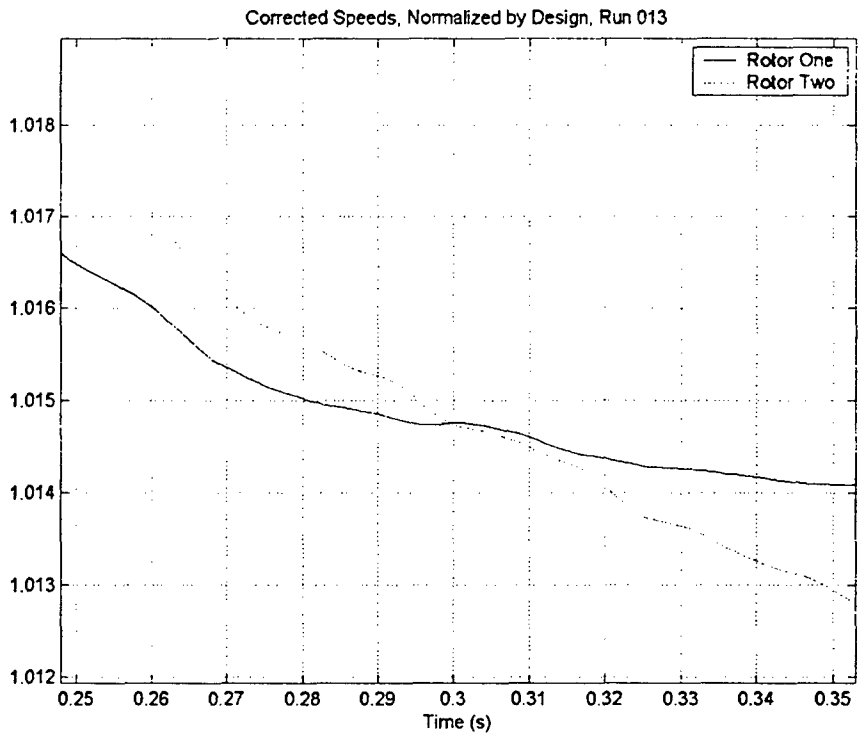


Figure E.15: Corrected speeds between 250 ms and 350 ms for Run 013

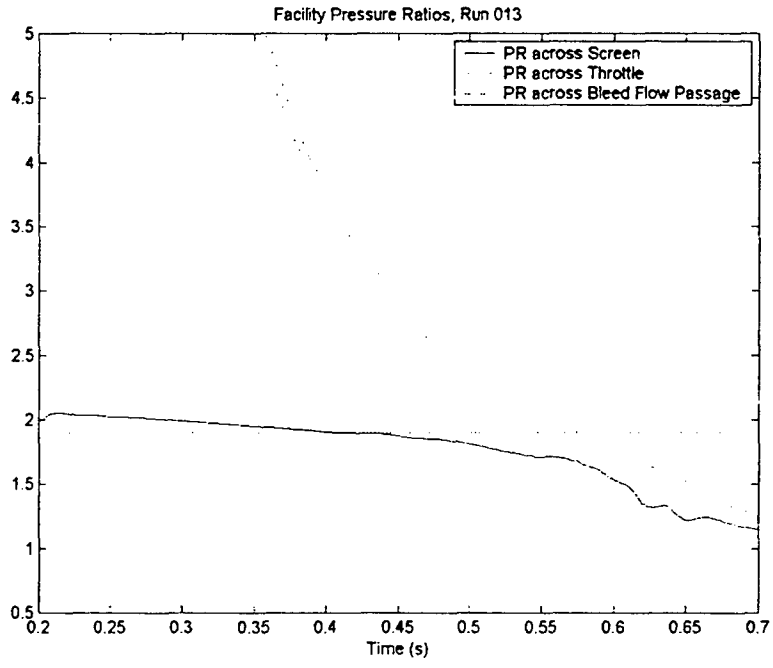


Figure E.16: Important pressure ratios in the facility for Run 013

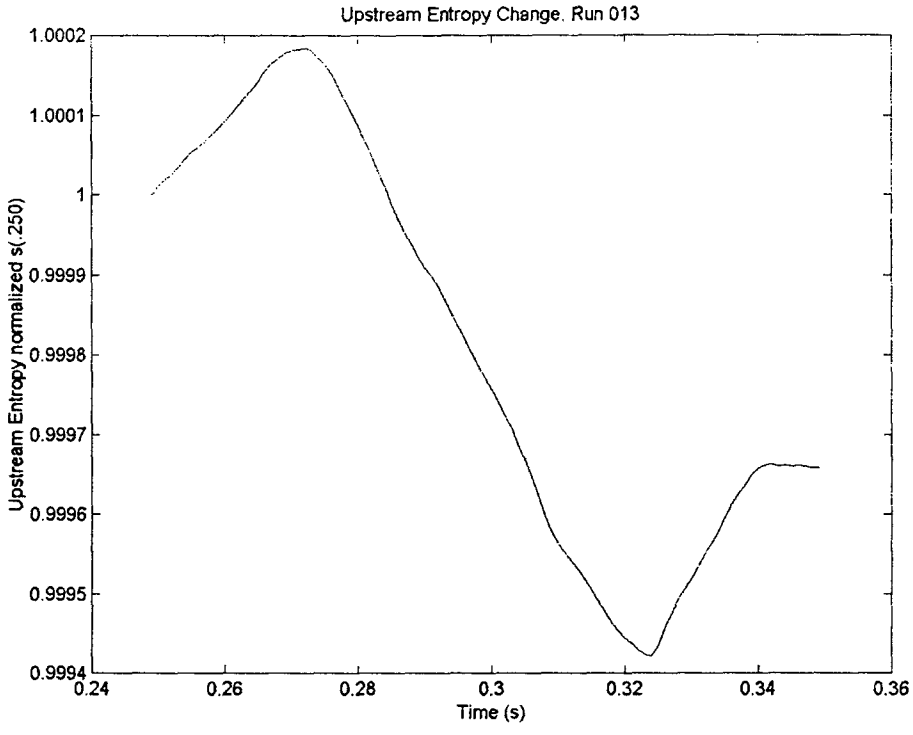


Figure E.17: Entropy entering Compressor, normalized by *s*(0.250), Run 013

Corrected Flow

When available the three upstream pitot probes are used to determine the corrected flow in each window in the manner described in Section 6.2.2. For each window the total temperature and total pressure are assumed to be constant radially and circumferentially. The average upstream conditions are determined by a mass flow weighted average of each of the window measurements. Figure E.18 through E.20 are the mass flow, corrected flow, and Mach number for each window during the test time. Also plotted is the mass flow weighted average value.

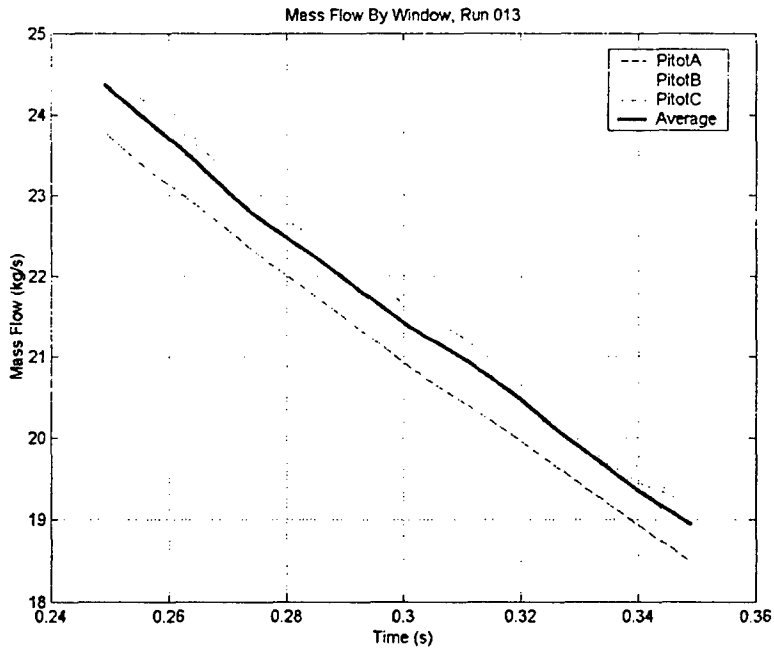


Figure E.18: Mass flow at each measurement location, Run 013

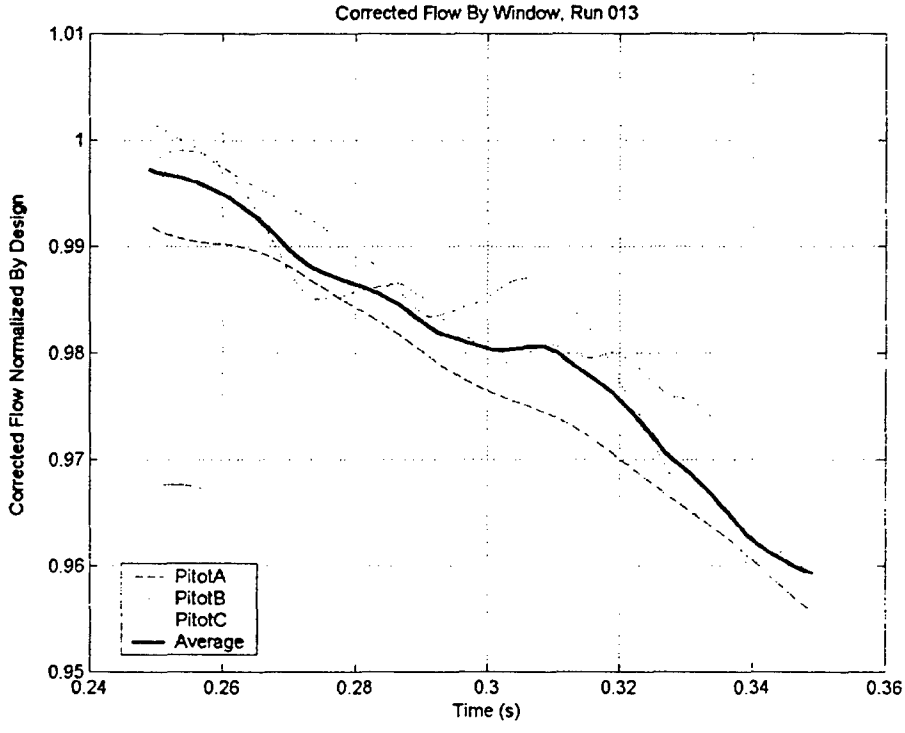


Figure E.19: Corrected flow normalized by the design value at each measurement location, Run 013

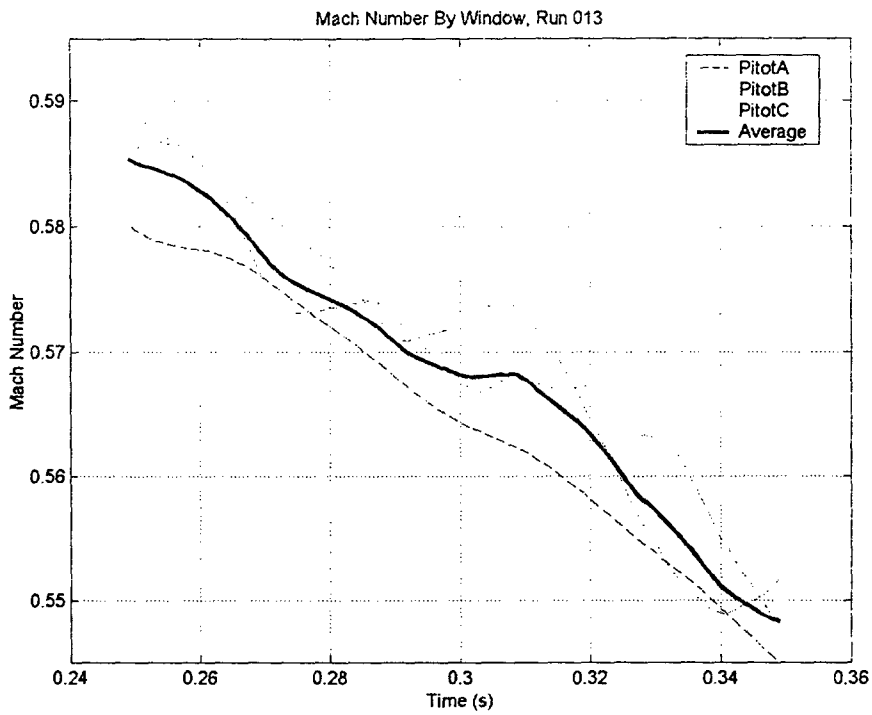


Figure E.20: Mach Number at each measurement location, Run 013

Pressure Ratio & Temperature Ratio

Figure E.21 is the pressure ratio and temperature ratio for Run 013 between 150 ms and 700 ms. After the initial transient the pressure ratio has a flat parabolic profile and around 500 ms the compressor begins to stall (the stall can be seen in Figure E.12).

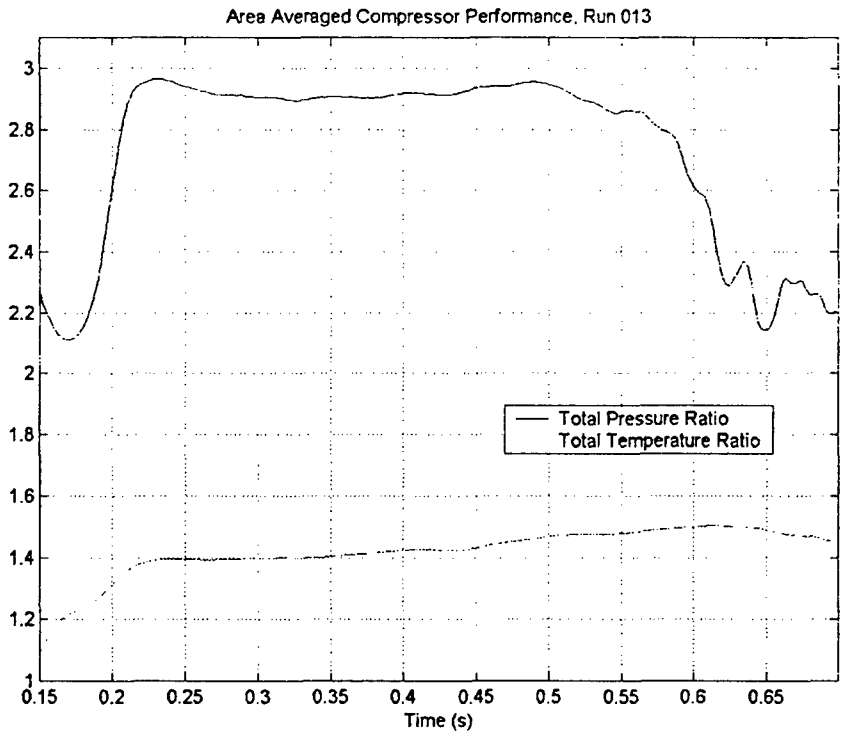


Figure E.21: Pressure Ratio and Temperature Ratio during Run 013

Figure E.22 shows the adiabatic efficiency, corrected flow normalized by the design value, and Reynolds' number normalized by the Reynolds' number used for analysis. The time range for the plotted data is shorter than that of Figure E.20 because below the lowest temperature of the NIST table is 250° K.

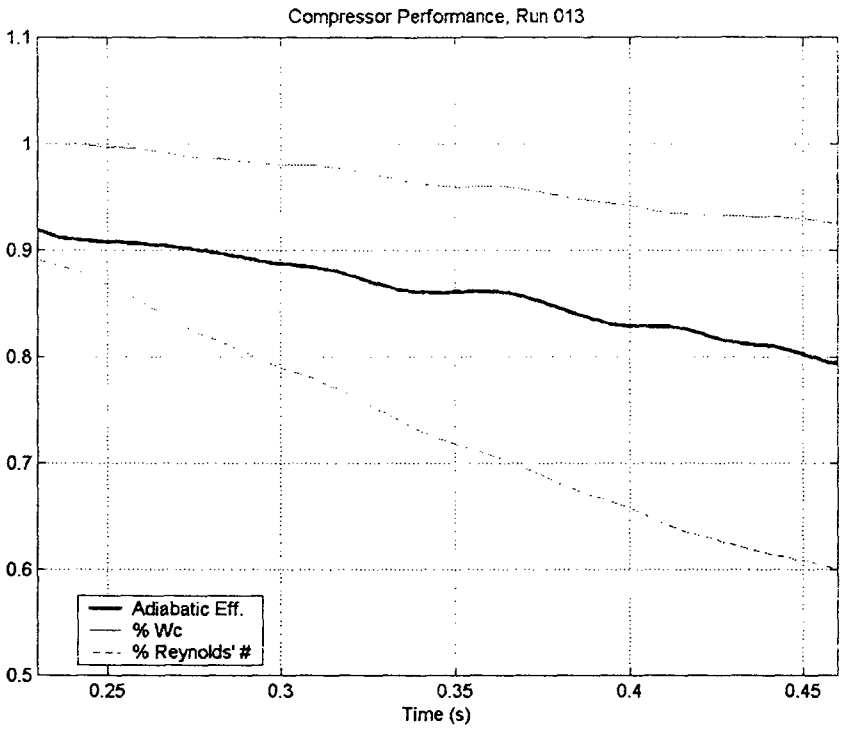


Figure E.22: Adiabatic efficiency, average inlet corrected flow, and inlet Reynolds' number for Run 013

This document was created with Win2PDF available at http://www.daneprairie.com.
The unregistered version of Win2PDF is for evaluation or non-commercial use only.

Aerodynamic Performance Measurements in a Counter-Rotating Aspirated Compressor

by

Jean-François Onnée

Ingénieur des Arts et Manufactures (2003)

Ecole Centrale Paris (Châtenay-Malabry, France)

Submitted to the Department of Aeronautics and Astronautics
in Partial Fulfillment of the Requirements for the Degree of

Master of Science in Aeronautics and Astronautics

at the

Massachusetts Institute of Technology

June 2005

© 2005 Massachusetts Institute of Technology
All rights reserved

Author.....
Department of Aeronautics and Astronautics
May 20, 2005

Certified by.....
Professor Alan H. Epstein
R.C. Maclaurin Professor
Department of Aeronautics and Astronautics
Thesis Supervisor

Accepted by.....
Professor Jaime Peraire
Department of Aeronautics and Astronautics
Chairman, Department Committee on Graduate Students

Aerodynamic Performance Measurements in a Counter-Rotating Aspirated Compressor

by

Jean-François Onnée

Submitted to the Department of Aeronautics and Astronautics
on May 20, 2005, in partial fulfillment of the
requirements for the Degree of
Master of Science in Aeronautics and Astronautics

Abstract

This thesis is an experimental investigation of the aerodynamic performances of a counter-rotating aspirated compressor. This compressor is implemented in a blow-down facility, which gives rigorous simulation of the characteristic aerodynamic parameters in which a compressor operates in steady state conditions. To measure the efficiency of this unique machine, the total temperature as well as the total and the static pressures at the inlet and the outlet of the compressor are measured.

Due to the short test time (~100 ms) and unsteady nature of the blow-down environment, performance measurements in a short-duration test facility place especially demanding requirements on the accuracy and the response of the temperature and pressure sensors. For the total temperature probes, 0.0005-inch-diameter type-K thermocouple gage wires were assembled in specially designed casings allowing to perform measurements at determined span and circumferential locations. As for pressure probes, ultraminiature piezo-resistive transducers were used. The uncertainties related to their performances is estimated.

These results are then processed to obtain an estimation of the uncertainties in the efficiency measurement. The error related to the time-resolution as well as the discrete spatial sampling pattern are also assessed. The blow-down test facility provides a quasi-isothermal environment. The non-adiabatic effects lead to a biased efficiency measurement. A corresponding correction to estimate the adiabatic efficiency of the compressor is detailed. Finally, results from the first compressor test runs are provided.

Thesis Supervisor: Alan H. Epstein
Title: R.C. Maclaurin Professor of Aeronautics and Astronautics
Director of the Gas Turbine Laboratory

Acknowledgments

I would like to thank Professor Alan H. Epstein and Dr. Gerald R. Guenette for having given me the opportunity to work on this innovative project. I am very grateful for their guidance, support and kindness during the course of this experimental work.

I would like to thank all the members of the blow-down counter-rotating aspirated compressor team, namely Professor Jack L. Kerrebrock, Dr. Ali Merchant, Dr. Fritz Neumayer and my fellow research student David V. Parker, for their teachings, support and precious help.

Many thanks to Jack Costa, Viktor Dubrowski and James Letendre for their help, patience and skills in turning my drawings into actual probes. I am also grateful to the entire GTL staff for their kindness.

I cannot express enough gratitude to my parents and my sister, whose love and support gave me the opportunity to earn this degree. I would like to address a special thought to my regretted grand-mother Mamama, for her love and supporting prayers throughout my studies.

Finally, I would like to thank all my friends, overseas, for their support, and here in the United States, for making these two years in New England a great experience.

This work was supported by the Defense Advanced Research Projects Agency, Dr. S. Walker, Manager.

Contents

1. Introduction 19
   1.1. Motivation 19
   1.2. Objective and Approach 21
   1.3. Thesis Outline 23
2. Experimental Facility 25
   2.1. The Counter-Rotating Aspirated Compressor 25
   2.2. The MIT Blow-Down Counter-Rotating Compressor Facility 28
   2.3. Operation of the MIT Blow-Down Counter-Rotating Compressor 31
   2.4. Instrumentation and Data Acquisition 32
      2.4.1. Instrumentation used on the Facility 32
      2.4.2. Data Acquisition Devices 35
3. Total Temperature Measurement 37
   3.1. Introduction 37
   3.2. Requirements for Total Temperature Probe in a Blow-Down Facility 38
   3.3. Basic Theory of Thermocouple Technology 39
   3.4. Total Temperature Probe Design 42
      3.4.1. Probe Head Design and Model 42
      3.4.2. Upstream and Downstream Total Temperature Single Probes 47
      3.4.3. Upstream and Downstream Total Temperature Rakes 48
      3.4.4. Mechanical Integrity within the Flow Conditions 50
      3.4.5. Signal Conditioning 55
   3.5. Static Calibration of Total Temperature Probes 56
      3.5.1. Calibration Equipment 56
      3.5.2. Calibration of Thermocouples 57
   3.6. Uncertainty Estimation of Total Temperature Measurement 60
      3.6.1. Recovery Error and Response Time 60
      3.6.2. Conduction Error 62
      3.6.3. Radiation Error 64

3.6.4. Overall Uncertainty of Total Temperature Measurement 65
4. Total Pressure Measurement 67
4.1. Introduction 67
4.2. Requirements for Total Pressure Probe in a Blow-Down Facility 68
4.3. Total Pressure Design 69
4.3.1. Isolated Pressure Measurement probes 69
4.3.2. Total Pressure Rakes 69
4.3.3. Signal Conditioning 70
4.4. Probe Calibration 71
4.5. Uncertainty Estimation of Pressure Measurement 71
5. Aerodynamic Performance Measurement 77
5.1. Introduction 77
5.2. Uncertainty of Adiabatic Efficiency Measurement 79
5.2.1. Uncertainty due to Instrumentation Imperfections 79
5.2.2. Uncertainty Due to Discrete Spatial Sampling 81
5.2.3. Uncertainty Due To Time Sampling 84
5.3. Non-Adiabatic Effects in a Blow-Down Test Environment 84
5.3.1. Difference Between Blow-Down Efficiency and Adiabatic Efficiency ... 85
5.3.2. Correction to provide to Measured Efficiency 87
6. Experimental Results 91
6.1. Introduction 91
6.2. Test Data 91
6.2.1. Preliminary Tests 91
6.2.2. Matched Corrected Speed Run Results 93
6.2.3. Preliminary Compressor Map 106
7. Conclusion 107
7.1. Summary 107
7.2. Future Work 109
8. Appendix A: Detailed Calculation of the Correction Between Indicated and Adiabatic Efficiencies in a Blow-Down Test Facility. 111

9. Appendix B: Detailed calculation of the Total Temperature Probe Errors. 135
10. Appendix C: Total Temperature Probes Drawings..... 145
11. Appendix D: Total Pressure Probes Drawings 153
12. Appendix E: Detailed Type-K Thermocouple Manufacturing Description 157

List of Figures

Figure 1.1 - Effect of suction on boundary layer growth..... 20
Figure 2.1 – Inlet Guide Vane Mounted on Forward Section..... 25
Figure 2.2 – Rotor 1..... 26
Figure 2.3 – Rotor 2..... 27
Figure 2.4 - Bleed Flow Passage in a Rotor 2 Blade..... 27
Figure 2.5 – The MIT Blow-Down Compressor Facility..... 29
Figure 2.6 – Forward Test Section..... 30
Figure 2.7 – Aft Test Section..... 31
Figure 2.8 – Instrumentation Positions on Test Stand..... 34
Figure 3.1 – Thermocouple Circuit with External Reference Junction..... 41
Figure 3.2 – Ice Point Reference Chambers..... 41
Figure 3.3 – Thermocouple Head Design..... 43
Figure 3.4 – Infinite Cylinder with Initial Uniform Temperature Subjected to Sudden Convection Conditions..... 44
Figure 3.5 – Compressional Heating in the Blow-Down Seen by the Upstream Probes.. 47
Figure 3.6 – Downstream Temperature Probe Mounted on Brass Plug..... 48
Figure 3.7 – Fully assembled upstream total temperature rake..... 50
Figure 3.8 – Schematic of Free Jet Resistance Test..... 51
Figure 3.9 – Picture of 0.0005-inch Thermocouple Gage..... 52
Figure 3.10 – Gage Wire Shapes Tested in the Free Jet Stand..... 52
Figure 3.11 – Wire response-time in (s) versus the Percentage of Load Reduction for ¼" heads by Decreasing the Vent Hole Size..... 54
Figure 3.12 – Evolution of the Recovery Error versus the Percentage of Load Reduction for ¼" heads, by Decreasing the Vent Hole Size..... 54
Figure 3.13 – Evolution in Conduction Error versus the Percentage of Load reduction by Decreasing the Inlet Area of a ¼" head..... 55
Figure 3.14 – Schematic of One-Dimensional Conduction-Convection Model for Thermocouple Wire..... 64

Figure 3.15 – Conduction Error Percentage, Predicted by a Steady State One-Dimensional Conduction-Convection Model..... 64
Figure 4.1 – Fully-Assembled Upstream Total Pressure Rake..... 70
Figure 5.1 – Inlet and Outlet Relative Entropy Variations..... 83
Figure 5.2 – Enthalpy – Entropy Diagram for the Compression Processes in Compressors..... 85
Figure 5. 3 – Difference Between Adiabatic and Indicated Efficiency Over the Test Time..... 89
Figure 6.1 – Corrected Speeds During Test Time Normalized by Full Design Speed – Run 003..... 93
Figure 6.2 – Upstream Total Temperatures of Run 010..... 96
Figure 6.3 – Downstream Total Temperatures of Run 010..... 96
Figure 6.4 – Upstream and Downstream Radial Total Temperature Distribution at 250 ms, 300 ms and 350 ms for Run 010..... 97
Figure 6.5 – Area-Averaged Pressure History in the Supply Tank, the Valve, Upstream and Downstream of the Compressor, in the Bleed Flow and in the Dump Tank for Run 010..... 97
Figure 6.6 – Upstream Total Pressure at Three Midspan Locations for Run 010..... 98
Figure 6.7 – Upstream Static Pressure Distribution for Run 010..... 98
Figure 6.8 – Upstream Pitot Total and Static Pressures for Run 010..... 99
Figure 6.9 – Downstream Pitot Total and Static Pressures for Run 010..... 99
Figure 6.10 – Upstream Total Pressure Rake Measurements for Run 010..... 100
Figure 6.11 – Downstream Total Pressure Rake Measurements for Run 010..... 100
Figure 6.12 - Upstream and Downstream Radial Total Pressure Distribution at 250 ms, 300 ms and 350 ms for Run 010..... 101
Figure 6.13 – Pressure Ratio, Temperature Ratio and Efficiency Radial Distributions at 250 ms, 300 ms and 350 ms for Run 010..... 101

Figure 6.14 – High Speed Static Pressures Behind Rotor 1 (Blue) and Rotor 2 (Green) for Run 010..... 102
Figure 6.15 - High Speed Static Pressures Behind Rotor 1 (Blue) and Rotor 2 (Green) for Run 010 between 250 ms and 255 ms.....102
Figure 6.16 – Upstream and Downstream Mach Numbers for Run 010..... 103
Figure 6.17 – Rotor 1 and 2 Normalized Corrected Speeds for Run 010..... 103
Figure 6.18 – Compressor Conditions During Test Time for Run 010..... 104
Figure 6.19 – Compressor Performance During Test Time for Run 010..... 104
Figure 6.20 – Preliminary Counter-Rotating Aspirated Compressor Map for Corrected Speeds Between 88% and 102%.....106
Figure A.1. - Temperature Profile vs. η Inside Rotor 1 at Various Time Points..... 117
Figure A.2. - Temperature Profile vs. η Inside Rotor 2 at Various Time Points..... 118
Figure A.3. - Temperature Evolution at the Surface of the Leading Edge of Rotor 1 over 1s..... 118
Figure A.4. - Temperature Evolution at the Surface of the Leading Edge of Rotor 2 over 1s..... 119
Figure A.5. – Biot Number at Leading Edge (a) and Trailing Edge (b) of Rotor 1 over 1s..... 120
Figure A.6. - Biot Number at Leading Edge (a) and Trailing Edge (b) of Rotor 2 over 1s..... 121
Figure A.7. – Temperature Evolution at the Surface of the Leading Edge of Rotor 1 Over 1s..... 123
Figure A.8. - Temperature Evolution at the Surface of the Trailing Edge of Rotor 1 Over 1s..... 124
Figure A.9. - Temperature Evolution at the Surface of the Leading Edge of Rotor 2 Over 1s..... 124
Figure A.10. - Temperature Evolution at the Surface of the Trailing Edge of Rotor 2 Over 1s..... 125
Figure A.11. - Temperature Evolution at the Surface of the IGV Over 1s..... 125

Figure A.12. – Temperature Evolution of Rotor 2 Hub vs. Depth for Different Time Points (a) and vs. Time at the Surface (b)..... 126
Figure A.13. - Temperature Evolution of Rotor 1 Hub vs. Depth for Different Time Points (a) and vs. Time at the Surface (b)..... 127
Figure A.14. - Temperature Evolution of the Leading Edge Parts of Rotor 1 Blades vs. Depth for Different Time Points (a) and vs. Time at the Surface (b)..... 128
Figure A.15. - Temperature Evolution of the Trailing Edge Parts of Rotor 1 Blades vs. Depth for Different Time Points (a) and vs. Time at the Surface (b)..... 129
Figure A.16. - Temperature Evolution of the Leading Edge Parts of Rotor 2 Blades vs. Depth for Different Time Points (a) and vs. Time at the Surface (b)..... 130
Figure A.17. - Temperature Evolution of the Trailing Edge Parts of Rotor 2 Blades vs. Depth for Different Time Points (a) and vs. Time at the Surface (b)..... 131
Figure A.18. - Difference Between Adiabatic and Indicated Efficiency Over the Test Time..... 134
Figure B.1. – Radiation Error Evolution for the Upstream Probes, Over 1s..... 142
Figure B.2. - Radiation Error Evolution for the Downstream Probes, Over 1s..... 143
Figure C.1. – Upstream Rake Total Temperature Measurement Head..... 147
Figure C.2. – Downstream Rake Total Temperature Measurement Head..... 148
Figure C.3. – Upstream Total Temperature Measurement Probe..... 149
Figure C.4. - Downstream Total Temperature Measurement Probe..... 150
Figure C.5. – Upstream Total Temperature Measurement Rake Assembly..... 151
Figure C.6. – Downstream Total Temperature Measurement Rake Assembly (5 Head Model)..... 152
Figure D.1. – Upstream Total Pressure Measurement Rake Assembly..... 155
Figure D.2. – Downstream Total Pressure Measurement Rake Assembly..... 156
Figure E.1. – Close-Up View of the Thermocouple Gage Wire Epoxied to the Ceramic Stem..... 160
Figure E.2. – View of the Thermocouple Extension Cables Laced Together in the Rake Airfoil Cavity..... 163

List of Tables

Table 2.1 – Individual performances of each rotor predicted by CFD calculation..... 28

Table 2.2 – Overall compressor performances and back pressure setting predicted by CFD calculation..... 28

Table 3.1 – Specifications for the Rosemount Standard Platinum Resistance thermometer model 162N..... 57

Table 3.2 – Summary of Probes Geometries, Inner Mach Numbers, Recovery Errors and Time Responses..... 62

Table 3.3 – Detailed Summary of Thermocouple Probes' Errors..... 66

Table 4.1 – Pressure Sensor Name Nomenclature..... 70

Table 4.2 – Upstream Total Pressure Uncertainty..... 74

Table 4.3 – Downstream Total Pressure Uncertainty..... 74

Table 4.4 – Total Upstream Static Pressure Error..... 74

Table 4.5 – Upstream Transducer Uncertainty..... 75

Table 4.6 – Downstream Transducer Uncertainty..... 76

Table 5.1 – Radial Sampling Uncertainty..... 82

Table 5.2. – Absolute and Relative Uncertainties in Total Temperature and Pressure Measurements for Runs 005 to 014..... 90

Table 5.3. – Scaling Coefficients, Scaled Uncertainties in Temperature, Pressure and Specific Heat Ratio and Efficiency Uncertainty for Runs 005 to 014..... 90

Table 6.1. - Compressor Initial Operating Conditions, Performances and State at 250 ms for Runs 005 to 014..... 105

Table B.1. – Casing Mach Number, Wire and Bead Response Times for the Upstream Probes at t = 250 ms and t = 500 ms..... 139

Table B.2. - Casing Mach Number, Wire and Bead Response Times for the Downstream Probes at t = 250 ms and t = 500 ms..... 140

Nomenclature

a	Sound velocity, m/s
A_c	Thermocouple wire cross-sectional surface area
Bi	Biot number
C_p	Specific heat at constant pressure
E_{rec}	Recovery Error
F_0	Fourier number
h	Heat transfer coefficient, W/m^2K – Enthalpy, J/kg
h_{01}	Inlet total enthalpy, J/kg
$h_{02,ad}$	Outlet total enthalpy for an adiabatic compression, J/kg
$h_{02,ind}$	Indicated outlet total enthalpy, J/kg
$h_{02,is}$	Outlet total enthalpy for an isentropic compression
k	Thermal conductivity, W/mK
L	Thermocouple wire length exposed to the flow, m
m	Characteristic spatial frequency of the heat equation ofr one-dimensional steady state conduction-convection transfer, $1/m^2$
M	Mach number
$\dot{m}$	Mass-flow rate, kg/s
p	Static pressure, Pa
P	Thermocouple perimeter, m
P_s	Static pressure, Pa
P_t	Total pressure, Pa
P_{01}	Inlet total pressure, Pa
P_{02}	Outlet total pressure, Pa
r	Thermocouple radius variable, m – Recovery factor
r_0	Thermocouple nominal radius, m
r^*	Thermocouple non-dimensional radius
t^*	Dimensionless time
T	Thermocouple temperature pattern, K

T_i	Thermocouple initial temperature, K
T_s	Static temperature, K
T_t	Total temperature, K
$T_{t,ind}$	Indicated total temperature, K
$T_{t,j}$	Junction total temperature, K
T_{surr}	Thermocouple casing temperature, K
T_{wall}	Wall temperature, K
T_{01}	Inlet total temperature, K
$T_{02,ad}$	Outlet total temperature for an adiabatic compression, K
$T_{02,ind}$	Indicated outlel total temperature, K
$T_{02,is}$	Otlet total temperature ofr an isentropic compression, K
T_∞	Free flow temperature, K
V	Flow velocity, m/s
W_a	Actual work provided to the compression, W
W_{ideal}	Ideal compressor work, W
x	Thermocouple gage length variable, m

Greek Symbols

γ	Specific heat ratio
ε	Emittance
η_c	Compressor efficiency
η_{ind}	Indicated efficiency obtained from direct measurements
θ	Difference between thermocouple and gas temperatures, K
ν^*	Dimensionless temperature
π_c	Compressor pressure ratio
ρ	Flow density, kg/m^3
σ	Stefan-Boltzmann constant, W/m^2K^4
τ	Temperature ratio

1. Introduction

1.1. Motivation

Over the past 40 years, the aerodynamic performances of conventional compressors have increased enormously, thanks to the development of several enhancing design methodologies. But beyond those methods, the idea of developing compressors capable of achieving higher pressure ratios thanks to higher rotating velocities continued to make its way. The idea of a counter-rotating compressor is a case in point in that matter. Replacing the traditional stator by a rotor rotating in the opposite direction of the preceding rotor is a technique that would allow higher relative velocities and hence higher pressure ratio. But this technique alone is not efficient as high turning flows result in separation of the flow from the blades' surface on the second rotor. It is in this context that the concept of aspiration comes to play a role.

For the past 10 years, the prospects for aspirated compressors have become a center of focus for research laboratories. Studies have been able to prove the benefits of this technique. It allows one to reduce the amount of low energy fluid around the blades, which is tantamount to decreasing in the boundary layer thickness, as shown in Figure 1.1. The work available at a given tip speed can hence be increased, which expands the design space for compressor stages. The related benefits is either a higher pressure ratio

per stage, or a lower blade speed for a given pressure ratio, or a compromise between the two. More information can be found in [1]. This breakthrough technique has enabled to create blades capable of remaining efficient when submitted to high turning flows, perfectly suitable for a counter-rotating assembly. The envisioned benefits of this breakthrough technique include high pressure ratios per stage and shorter and lighter machines. The synergy with counter-rotating turbines can be underlined in this context.

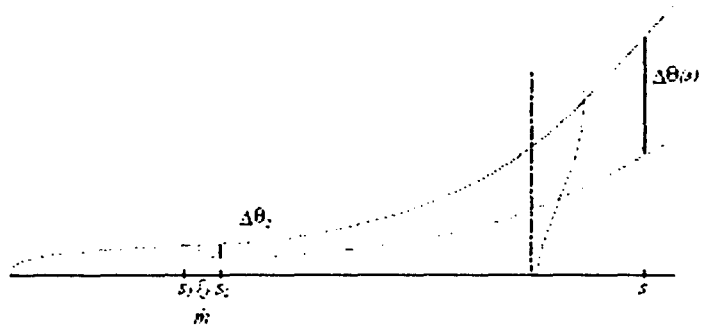


Figure 1.1 - Effect of suction on boundary layer growth

Since the early 1970's, MIT has performed and developed many short-duration blow-down tests on turbines and compressors. The technology is based on transient testing techniques that are able to provide highly accurate data at a relatively low cost. Using proper scaling of the facility, it is possible to reproduce and measure the flow's non-dimensional parameters that characterize the compressor in a steady operating mode. The actual testing time of the compressor is hence quite short, on the order of 400-500ms. This allows the total energy consumption to be kept at a low level. Meanwhile, the building and maintenance costs of the short-duration rig are greatly reduced in comparison to a traditional test stand.

These are the justifications that fostered the conception, design and operation of a counter-rotating aspirated compressor in a blow-down testing facility at the Gas Turbine Laboratory. This thesis deals with the aerodynamic performance measurements of this compressor. We can already state here that high frequency response instrumentation is a

key requirement for this testing configuration. A detailed description of the design and the characteristics of these instruments will be provided in the next chapters. The associated error analysis will be provided as well. Testing in transient conditions implies a certain number of consequences in the interpretation of the measured efficiency. The difference between steady state test measured efficiencies and transient test measured efficiencies will be addressed.

1.2. Objective and Approach

The objective of the experiment is to determine the efficiency of a one-stage counter-rotating aspirated compressor. From thermodynamic considerations, for a given total pressure ratio π_c the efficiency of a compressor is defined as:

$$\eta_c = \frac{W_{ideal}}{W_a} \tag{1.1}$$

where W_{ideal} is the ideal work of compression for that given π_c in isentropic conditions and W_a is the actual work of compression applied to achieve the same total pressure ratio.

Assuming the gas is ideal and the mass-flow as well as the specific heat ratio are constant through the compressor, the ideal work of compression can be calculated as:

$$W_{ideal} = \dot{m} C_p T_{01} \left(\left(\frac{P_{02}}{P_{01}} \right)^{\frac{\gamma-1}{\gamma}} - 1 \right) \tag{1.2}$$

where $\dot{m}$ is the mass flow rate, C_p is the constant pressure heat coefficient, T_{01} and P_{01} are the total temperature and total pressure of gas at the inlet of the compressor, P_{02} is the total pressure of gas at the exit, γ is the specific heat ratio.

Defining the actual way for a compressor is a more intricate problem. In steady state, a compressor runs under adiabatic conditions and its work can be written as:

$$W_a = \dot{m} C_p \left(T_{02.ad} - T_{01} \right) \tag{1.3}$$

where $T_{02,ad}$ is the total temperature of gas at the exit of a compressor in an adiabatic process. This expression is valid under the same conditions stated for equation (1.2).

Following those definitions, the latter process-defined actual work (1.3) leads to the most commonly used definition of adiabatic compressor efficiency. It can be written as:

$$\eta_{ad} = \frac{\pi_c^{\frac{\gamma-1}{\gamma}} - 1}{\tau - 1} \tag{1.4}$$

where:

$$\pi_c = \frac{P_{02}}{P_{01}} \tag{1.5}$$

$$\tau = \frac{T_{02}}{T_{01}} \tag{1.6}$$

Equation number (1.4) tells us that in order to make an efficiency measurement, it is sufficient to know the aerodynamic parameters at the inlet and the outlet of a compressor and to know the thermodynamic properties of the gas. So measuring the inlet and outlet total temperatures and total pressures would give the answer for the adiabatic efficiency of a compressor.

It is however very important to recall here that a blow-down facility does not provide the testing conditions for the previous efficiency calculation to be led in a straightforward manner. A blow-down compressor works in non-adiabatic conditions and in unsteady or quasi-steady conditions both in terms of aerodynamic parameters of the flow and in terms of thermodynamic properties of the gas. The efficiency was thus computed by calculating the isentropic enthalpy rise and the actual enthalpy rise of the gas mixture, based on the measured data:

$$\eta_{ind} = \frac{h_{02,is} - h_{01}}{h_{02,ind} - h_{01}} \tag{1.7}$$

The common approach to describing compressor performance is to quote their adiabatic efficiency. As explained earlier, a blow-down test facility cannot directly yield this information. It is then also mandatory to try and assess the amount of difference

between the indicated efficiency, and the efficiency the compressor would have had for the same operating point, had it been tested in adiabatic and steady state conditions. This subject will be analyzed in chapter 5 and 6.

1.3. Thesis Outline

The remainder of the thesis is organized into the following chapters.

Chapter 2 describes the experimental facility. A description of the Counter-Rotating Aspirated Compressor is given along with a brief explanation of the blow-down compressor test rig operations. The accuracy requirements for temperature measurement along with the temperature sensors development, design and calibration processes and the assessment of their performances are covered in chapter 3. Chapter 4 focuses on the pressure measurements. The total pressure probe design and calibration are shown along with the uncertainty associated to their data measurements. The following chapter deals with efficiency computation and more precisely with the evaluation of the difference of efficiency measurements between a short-duration test and a steady state test. Experimental results are provided in chapter 6 and they are followed by a final summary and conclusion in chapter 7. Further detailed information related to the error analysis of the temperature probes and efficiency measurements are given in appendix, along with detailed instructions and drawings of the manufacturing process of those probes.

2. Experimental Facility

This chapter provides a description of the Counter-Rotating Aspirated Compressor and the experimental facility used to measure its aerodynamic performances. The configuration and operation during a typical run are described, along with the instrumentation probes and the data acquisition systems.

2.1. The Counter-Rotating Aspirated Compressor

The counter-rotating aspirated compressor consists of 3 rotating parts, namely an IGV, rotor 1 and rotor 2.

The IGV is made of 35 blades, bound together by a one-piece annular shroud.

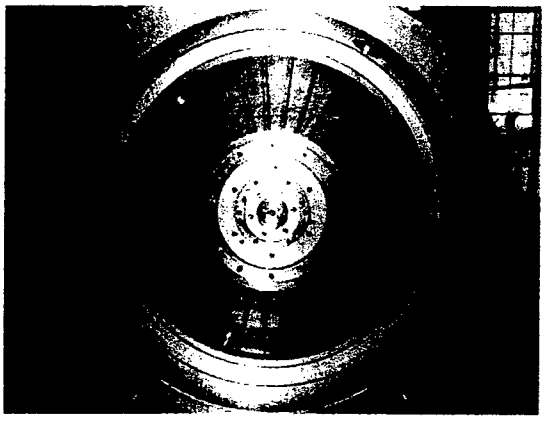


Figure 2.1 – Inlet Guide Vane Mounted on Forward Section.

Rotor 1 consists of 20 un-shrouded blades.



Figure 2.2 – Rotor 1.

Rotor 2 is the aspirated feature of this compressor. It is indeed counter-rotating with respect to rotor one. It is confronted by a high turning flow and must hence accommodate the aspiration system that will remove the bulk of the low energy part of the flow on the suction surface, by aspirating the boundary layer. Rotor 2 consists of 29 blades designed with aspiration slots on their suction side and a channel to drive the flow out of the core flow, towards the bleed flow (Figure 2.3 and Figure 2.4). In the blow-down facility, the rotating parts are placed in vacuum. The flow is than rapidly released in the rig. Suction relies on the pressure difference between the incoming flow and the rest of the facility sitting in vacuum.

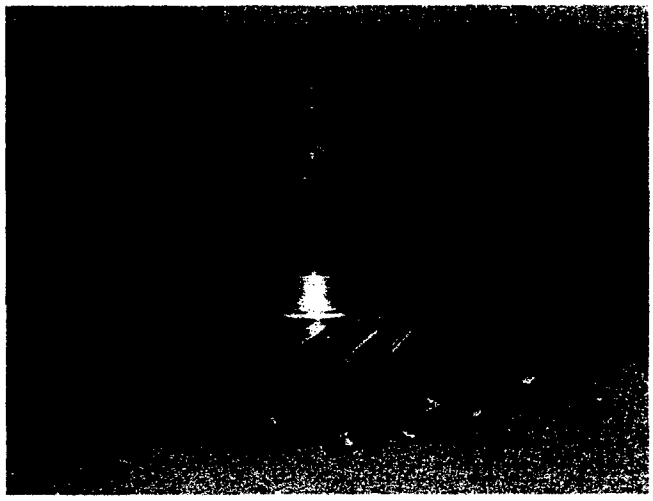


Figure 2.3 – Rotor 2.

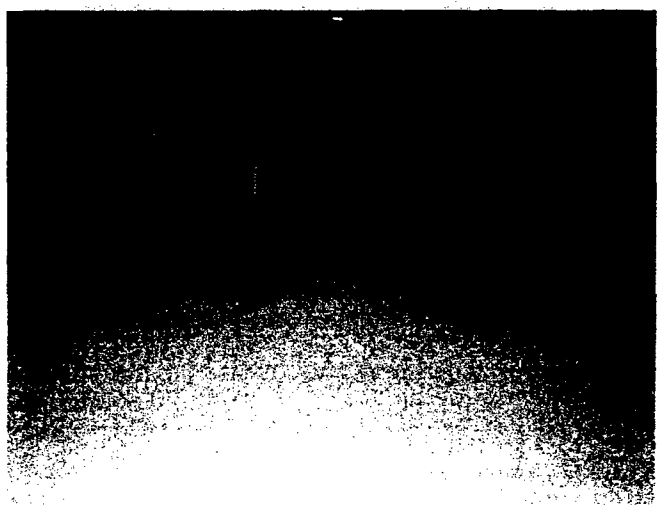


Figure 2.4 - Bleed Flow Passage in a Rotor 2 Blade.

Table 2.1 and Table 2.2 summarize the predicted performance of each rotor as well as the entire compressor at for different operating points. These results are based on CFD calculations performed by Ali Merchant at MIT and engineers at APNASA. assuming the throttle opening length ensure the appropriate back pressure. The goal of this experiment is to try to verify experimentally these predictions.

	Rotor 1			Rotor 2		
Speeds	PR 1	TR 1	Eff 1 (%)	PR 2	TR 2	Eff 2 (%)
100-100	1.91	1.23	89	1.60	1.16	89
95-95	1.78	1.21	87	1.44	1.12	89
90-90	1.68	1.18	85	1.37	1.13	74
85-85	1.60	1.17	84	1.36	1.12	76
80-80	1.50	1.15	81	1.29	1.10	78

Table 2.1 – Individual performances of each rotor predicted by CFD calculation.

	Both			
Speeds	PR	TR	Eff (%)	Throttle Length (in)
100-100	3.06	1.43	87	3.53
95-95	2.57	1.36	85	3.50
90-90	2.30	1.33	82	3.50
85-85	2.17	1.31	81	3.60
80-80	1.93	1.26	80	3.75

Table 2.2 – Overall compressor performances and back pressure setting predicted by CFD calculation.

2.2. The MIT Blow-Down Counter-Rotating Compressor Facility

The tests to investigate the aerodynamic performance of the counter-rotating aspirated compressor were performed on a blow-down compressor test rig. The non-dimensional equations of continuity, motion and energy show that it is the ratio of forces, fluxes and states that determine the flow field. Hence, only the non-dimensional parameters characterizing the steady state running conditions need to be reproduced to simulate the engine operation. Those parameters are the corrected mass flow, the corrected speed, the ratio of specific heat, the Mach number at the inlet and the outlet of the compressor, and, to a lesser extent, the Reynolds number. The blow-down test rig has been designed and dimensioned so as to maintain these non-dimensional parameters approximately constant over the test period, matching the values these parameters would have in steady state. This section only purports to give a brief description of the blow-down compressor facility. Details of the rig design and operations can be found in [2].

Several design requirements and constraints applied to the design of the testing facility. One of them is the urban location of MIT, which required keeping all operating stresses within safe limits. This aspect accounted partly for the type of gas used in the

tunnel. A mixture of Argon and CO_2 was chosen. The mixture ratio is set by the desired specific heat ratio γ. This choice presented several advantages over a classic air mix. The Argon-CO_2 mixture has a larger density, which allows the compressor rotors' physical speeds to be lower for a given corrected speed than if the test gas had been air. The facility can hence be operated at a lower level of stress in the blades, the disks, the blisks and the flywheel and other rotating parts.

Figure 2.5. shows the blow-down compressor facility. It breaks down into five major components: the supply tank, the fast-acting valve, the forward test section, the aft test section and the dump tank.

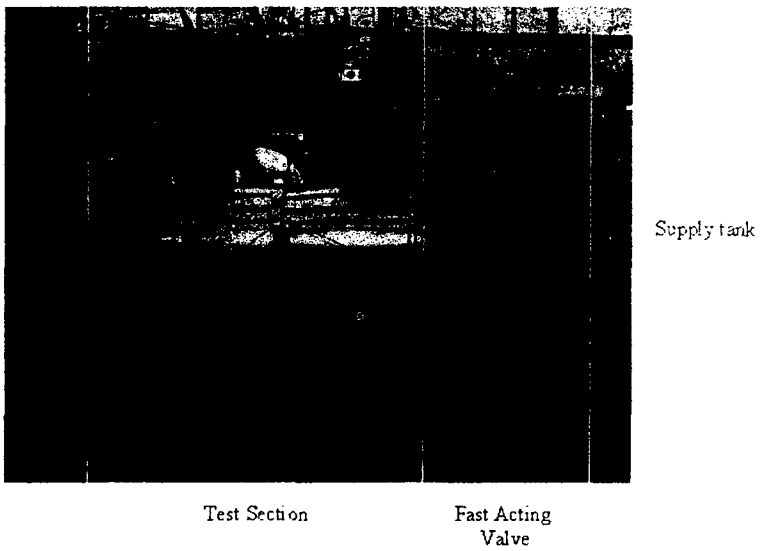


Figure 2.5 -- The MIT Blow-Down Compressor Facility.

The supply tank has a volume of 157 ft^3 and can safely hold pressures up to 100 psia. It sits on wheels.

The fast acting valve separates the supply tank filled with gas, from the test sections and the dump tank sitting in vacuum. It was designed to open in less than 50 ms and provide a smooth expansion path for the gas exiting the tank. It is followed by a screen designed to set the appropriate pressure and mass-flow, as well as uniform inlet conditions in the inlet plane of the compressor.

The forward test section houses the IGV and the first rotor, as well as its drive motor and flywheel. It also houses a pressure screen aimed at imposing the correct pressure and mass flow upstream of the rotors. The motor and the flywheel are mounted on the same shaft as rotor 1, which imposed tight requirements in the design of those parts and their fitting in the inner diameter of the flow-path section. The flywheel is aimed at providing the rotor with the necessary inertia during its coasting phase to match the required corrected speed. Figure 2.6 shows a cross-sectional view of the forward test section.

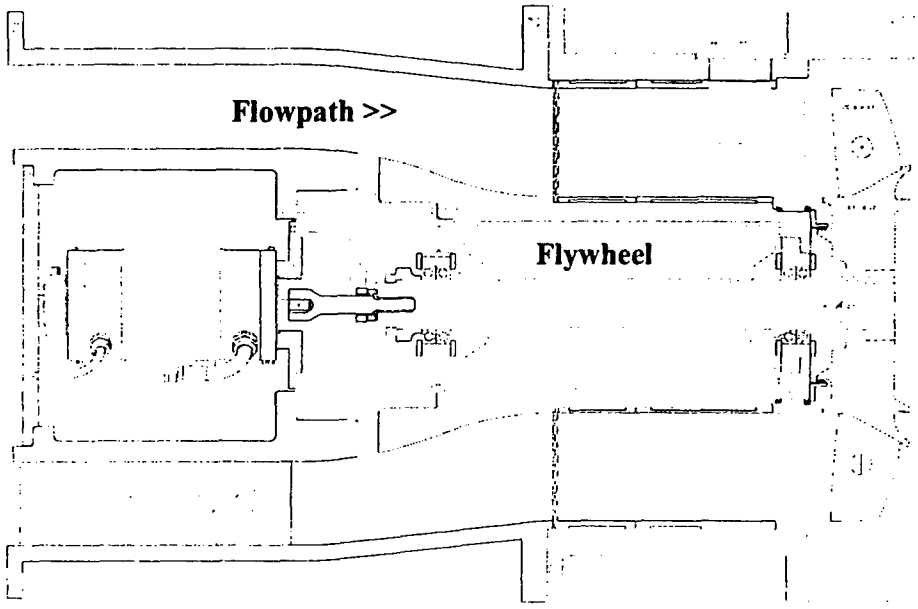


Figure 2.6 – Forward Test Section.

The aft test section houses the counter-rotating aspirated rotor with its rotating system and the throttle. Here again, the rotating system is mounted inside the inner diameter of the flow-path, which splits into two parts, the main path and a bleed flow passage. The flow path ends in the throttle, which sets the corrected flow. Figure 2.7 shows a cross-sectional view of the aft test section

Finally the dump tank is a 570 ft^3 tank bolted to the ground.

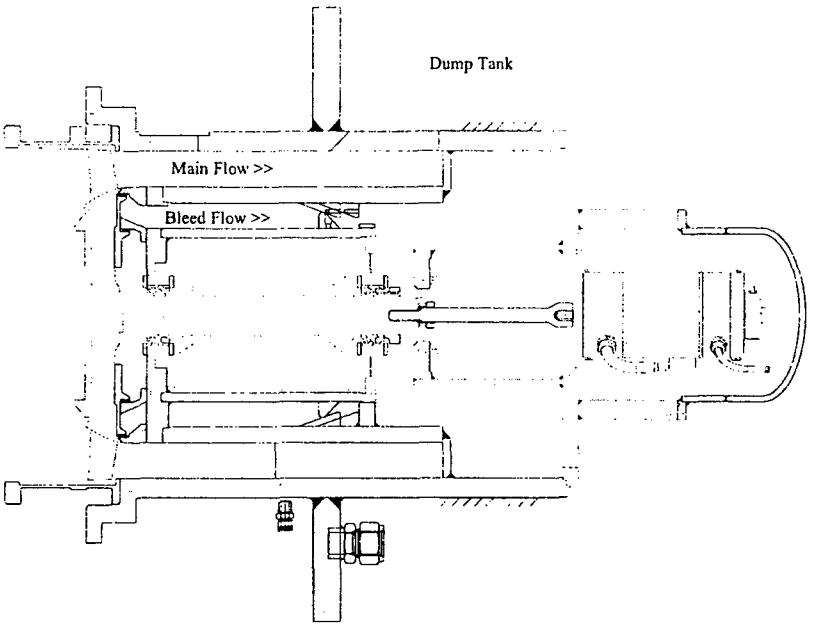


Figure 2.7 – Aft Test Section.

In the forward test section, as well as in the aft one, there are seven instrumentation window ports for access to the flow field. Each set consists of 2 sets of three windows equally spaced 120degrees apart. These two sets of three windows are rotated 20 degrees away from one another. The last windows are located on the bottom of the test cross-section. These windows are used to hold the total and static pressure probes as well as the total temperatures probes. Additional pressure sensors are placed further upstream and further downstream of the rotors.

2.3. Operation of the MIT Blow-Down Counter-Rotating Compressor

A brief description of the operation of the blow-down compressor is given in this paragraph. First, the tunnel is evacuated by an external vacuum system. Pressure probes then undergo a first calibration procedure. Once this calibration is done, the fast acting valve is closed. CO_2 is then loaded in the supply tank. Argon is later added to get the appropriate mole fractions and pressure. The pressure transducers are calibrated a second time. The two rotors are then spun up to the desired speeds. The A/D system is armed. The two rotors are then set to coast and the firing circuitry is triggered immediately after.

The fast-acting valve opens and releases the gas mixture in the tunnel. At the same time, the A/D system starts acquiring data. Both rotors are decelerated under the gas friction. After a transient mode of 200 milliseconds, the non-dimensional parameters characterizing the flow are maintained in a quasi-steady state for 300 milliseconds. The throttle un-chokes 700 milliseconds after the firing circuitry has been triggered, which marks the end of the test. The data acquisition system keeps on recording data for 1,300 milliseconds more. The rotors are finally braked and the pressure transducers are calibrated for a third and last time. The entire tunnel is eventually vented to atmosphere.

2.4. Instrumentation and Data Acquisition

2.4.1. Instrumentation used on the Facility

The MIT blow-down compressor is instrumented with many advanced flow sensors.

The supply tank is fitted with a total pressure transducer and a Sensotec 150psig gage. A pressure transducer records the total pressure between the valve and the screen.

Upstream from the IGV, 5 of the 7 pressure plugs are fitted with instrumentation. The A, B and C windows, which are 120 degrees apart, are each fitted with a static and a total pressure probe as well as Pitot probes. Each probe is hooked to pizeoresistive differential Kulite transducer. These window plugs all carry a total temperature probe. These probe heads shelter 0.0005-inch-diameter type-K thermocouples, which have sufficient response time to be able to record the compressional heating of the start-up transient of the blow-down tests. A detailed description of the design, the calibration and the uncertainties linked to the probes is given in chapters 3 and 4. An 8-probe total pressure probe rake is mounted one the windows, while an 11-probe total temperature probe rake is mounted at the same axial location but 120 degrees apart from the pressure rake. All these probes are oriented in a straight direction to face the incoming flow.

Downstream of the compressor, there is only one plug used to carry the single pressure and total temperature probes. The reduction in flow passage lead to the design of two rakes for both the temperature and the pressure measurements instead of one

upstream. The temperature rakes have 5 and 6 heads while the pressure rakes carry 5 impact heads each. For each type of measurement, the two rakes are located within the same angular sector. These rakes as well as the other total measurement probes can be rotated to account for the swirl coming out of the second rotor.

In order to detect any stall on the rotors, a high-speed static pressure probes have been set up behind each rotor.

A three-way wedge probe is mounted in the bleed flow passage, while a static sensor records the pressure in the dump tank, along with a Sensotec 050 device.

Figure 2.8 gives detailed view of the instrumentation display on the rig.

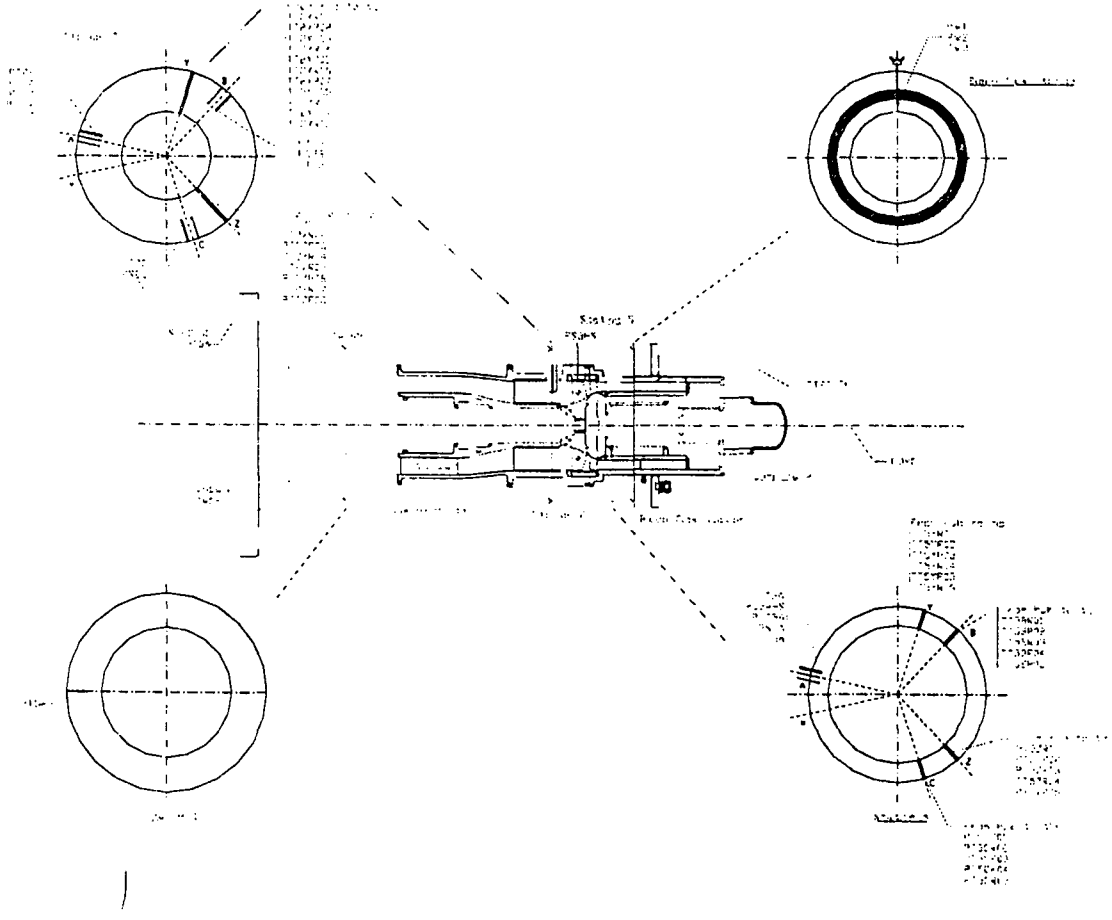


Figure 2.8 – Instrumentation Positions on Test Stand.

2.4.2. Data Acquisition Devices

Though a blow-down test lasts only 1 second, an impressive amount of test data is sampled and taken into computer memories. For sampling purpose, a central data acquisition system in employed on the test facility. This system is fitted with two types of A/D cards:

1. Two National Instruments PCI-6031E 64-analog-channel 16-bit-analog cards were used for the thermocouple and the pressure sensors. The sampling frequency of these systems was set to 1,000 Hz over 2 seconds.[18]

2. A National Instruments PCI-6143 8-analog-channel 16-bit A/D card with a 100 kHz sampling frequency per channel. This card is used to record high speed data from static pressure located behind each rotor. [19]

A National Instruments PCI-6602 8-channel 32-bit counter card with an 80 MHz maximum sampling rate was installed on the data acquisition computer to record the speeds of the two rotors. [20]

These cards were mounted on a Dell x86 computer, equipped with a 260 MHz processor and offering 332 kB of RAM.

High sampling Data acquisition is a delicate process that can cause buffer saturation. In order to avoid any risk of losing control on the rotors which could results in serious accidents, the motor drive monitoring system was installed on a completely independent computer. This computer was a Dell x86 with a 65 MHz processor and 60 kB RAM. An RS-422 interface card was mounted on this computer to communicate with the Yaskawa GPD 515/G5 controlling the operating mode and settings of the drive motors.

3. Total Temperature Measurement

3.1. Introduction

The purpose of this experiment is to determine the aerodynamic performances of the counter-rotating aspirated compressor. This approach requires the determination of the total temperature and the total pressures of the compressor. The transient testing conditions impose these instrument pieces to have an extremely short time-response so to be able to capture and record the entire data during the one second test time. The total temperature measurements rely on type-K thermocouples. The design and the manufacturing of those elements are based on the probe concept developed for the MIT Blow-down Turbine and described in [3].

This chapter first lists the requirements for the design of the total temperature measurement probes in a blow-down facility. A brief description of the basic theory of thermocouple technology is detailed, followed by a thorough description of the thermal model used to design the different probes. The manufacturing and robustness test processes are then detailed, followed by a description of the static calibration experiments. Finally, uncertainties involved in the probe data measurements are addressed.

3.2. Requirements for Total Temperature Probe in a Blow-Down Facility

In a traditional steady state test, the inlet and outlet total temperatures remain constant over the testing time, which is very long compared to the frequency response of the probes. But in the case of a blow-down test rig, the experiment aims at analyzing the behavior of the rotating assembly during a very short transient state, where the non-dimensional parameters characterizing the flow conditions are maintained constant. In that purpose, the type and requirements imposed on the instrumentation characteristics differs widely from a conventional testing environment. There is a strong requirement for very fast response total temperature probes. In the present case, the fast-acting valve opens within 50 ms, a compressional heating occurs for the next 200 ms before the set of data starts recording useful values where the quasi-steady test conditions are simulated. So the total temperature probes are supposed to reach to the gas temperature before the quasi-steady period starts and they are required to be fast responsive so that it can record the real-time changes in flow temperature.

As will be discussed in chapter 5, the uncertainty of temperature measurement plays a key role in the estimation of the efficiency measurement uncertainty. The influence coefficient due to the temperature measurement error weighs approximately three times more than that due to pressure measurement error. The goal of this work is to measure total temperature with less than 0.180 K upstream and 0.352 K downstream.

It is also very important that the design of the probes allows recording the total temperature of the flow. The design of the casing, the rakes and the plugs should allow the orientation of the heads to ensure that they face the flow and record the total parameters. This is less of an issue for the upstream probes, as the flow is filtered by a pressure screen which is here to guarantee the uniformity of the incoming flow. The downstream conditions are however different, as the counter-rotating nature of the compressor is bound to trigger vortices and swirls in the facility.

3.3. Basic Theory of Thermocouple Technology

The theory behind thermocouple technology was discovered and developed by Thomas Johann Seebeck in 1821. He carried an experiment joining two wires of dissimilar metals (a copper wire and a bismuth wire) and noticed that the temperature difference between the two junctions led to the generation of an electromotive force in the closed loop, resulting in a continuous electric current. This experiment was then verified with a set of dissimilar metals that form the thermoelectric series. Research showed that a bijective relation exists between the voltage inside the closed circuit made of any pair of thermoelectric metals and the temperature gradient between the two junctions binding them. The detailed theory of thermocouple can be found in [4]. Here, we present three fundamental laws of thermoelectric circuits:

1. A thermoelectric current cannot be sustained in a circuit of a single homogeneous material, however varying in cross section, by application of heat alone. This law implies that two different metals are required at least to form a thermocouple circuit.
2. The algebraic sum of the thermo-electromotive forces in a circuit composed of any number of dissimilar materials is zero if all the circuit is at a uniform temperature. A direct consequence to this law is that a third homogeneous material can be added inside the loop without modifying the net electromotive force as long as its extremities are maintained at the same temperature.
3. If two dissimilar homogeneous metals produce a thermal electromotive force of E_1, when the junctions are at T1 and T2, and a thermal e.m.f. of E2, when the junctions are at T2 and T3, the e.m.f. generated when the junctions are at T1 and T3 will be E1+E2.

Two consequences can be induced from this last law. First, a thermocouple can be calibrated for a particular reference temperature and used with any other temperature reference provided an adequate correction is applied. Second, extension wires can be added to the thermocouple circuit without affecting the net e.m.f., provided they are of

similar nature, i.e. bear the same thermoelectric characteristics as the wires forming the thermocouples.

Standard thermocouple tables are provided for 0°C reference temperatures, that is when the reference junction is maintained at 0°C. In the case an external reference junction cannot be used, a proper use of the last two laws along with the standard thermocouple tables for the adequate thermoelectric metal pair, allows to compute the absolute temperature of the measuring junction. The details are given in [3]. It is very important to notice that, during a measurement or a set of measurements, the temperature of the reference junction must be maintained as constant as possible. When an external 0°C reference junction is used, the voltage reading can directly be input in the standard thermocouple tables to determine the corresponding temperature of the measuring junction. For this experiment, five Ice Point Reference Junction Omega TRCIII capable of accommodating six thermocouple reference points each, are used (Figure 3.2). These devices are designed, calibrated and certified to maintain 0°C at an accuracy of ±0.1°C and a stability of ±0.04°C for constant ambient [15].

When a filter or an amplifier are used to enhance the signal output, it is necessary to proceed to the calibration of the thermocouple probe and the corresponding reference cell, so as to account for the imperfections in the signal treatment and also the imperfections and impurities associated with the thermocouple manufacturing.

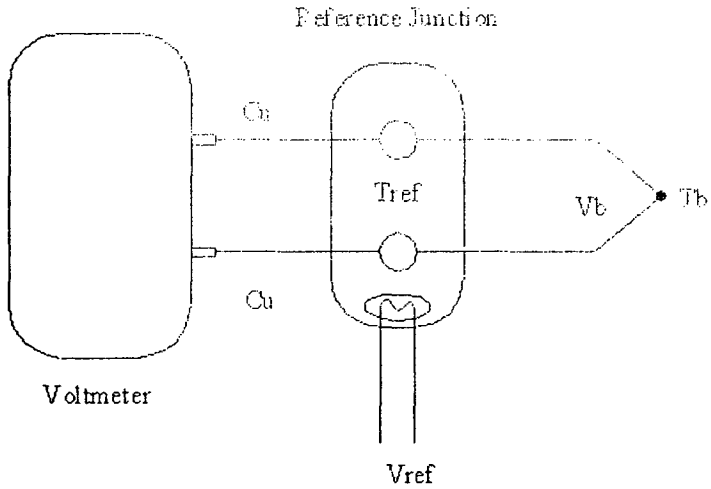


Figure 3.1 – Thermocouple Circuit with External Reference Junction.

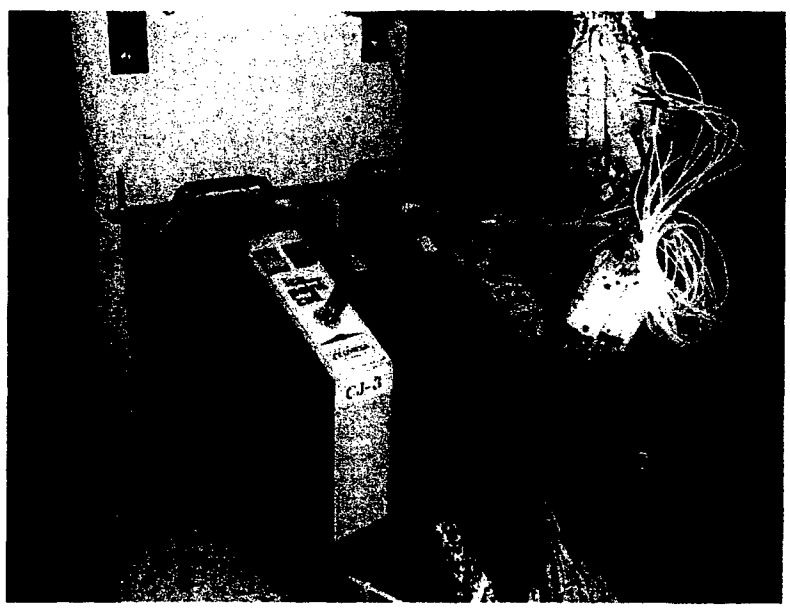


Figure 3.2 - Ice Point Reference Chambers.

3.4. Total Temperature Probe Design

3.4.1. Probe Head Design and Model

The probe head design and model are directly inspired from the endeavors and researches done over fast response thermocouple probes on the MIT blow-down turbine project. As is detailed in [3], thermocouple probes are subject to a number of error sources. These sources stem from the heat conduction from the wire and the supporting ceramic stems, the radiation of the casing, the recovery aspects and the calibration procedures. The response time is also an aspect which shall not be neglected in a short duration testing facility.

As was the case on the blow-down turbine project, type-K thermocouple gages were chosen for this project, because of their enduring stability and linearity. In order to reduce the response time of each probe, 0.0005 inch diameter thermocouple wires were chosen. This type of wire happens to be the smallest thermocouple wire size available on the market. As shown on Figure 3.3, the thermocouple bead is located in the middle of the probe. The wire is held straight between two ceramic stems to which it is epoxied. This assembly is inserted into a protecting casing regulating the flow speed around the gage. The sensor wires are soldered to thicker thermocouple extension wires at the other end of the insert. This design encompasses several advantages. First and foremost, exposing a significant length of the thermocouple gage allows significant reduction in the conduction error. The thermocouple wires are subjected to the same flow and temperature conditions as the junction, which reduces the temperature gradient on either side of the bead. A more detailed calculation of that phenomenon will be given in section 3.6.2. A second aspect is related to the structural resistance of the probe to the jet flow. As has been observed on previous MIT blow-down experiments as well as on the mechanical integrity probe tests conducted for this project (see section 3.4.4.), hanging the thermocouple gage in a straight and softly stretched manner between the two stems prevents the wires from being damaged by the turbulence enticed by the flow inside the casing. These flow disturbances can lead to the gage rupture near the bead, where the

strongest stress conditions are applied. Finally, the casing ensures not only a protection of the thermocouple gage from hazardous manipulations, but thanks to a vent hole system, it allows to significantly reduce the speed of the flow around the gage.

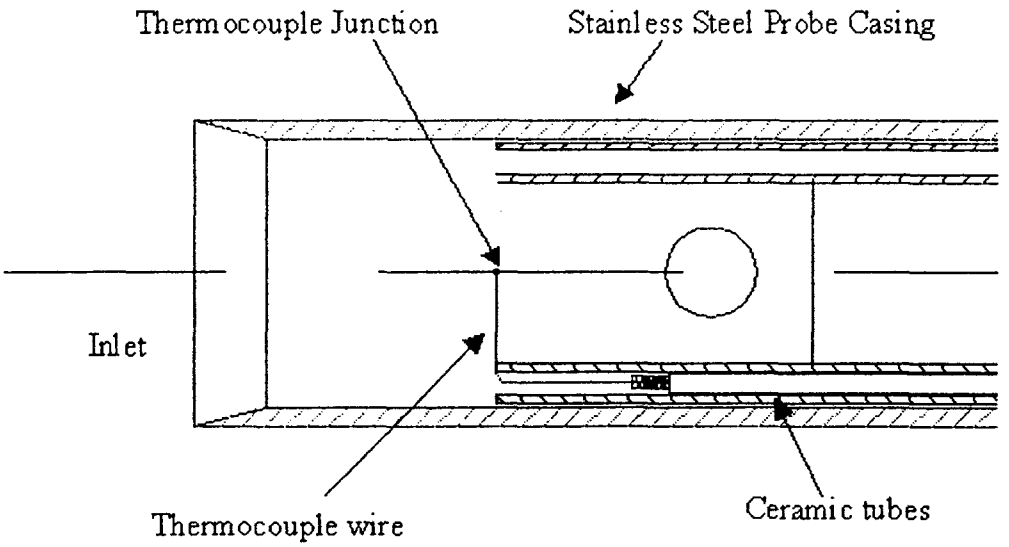


Figure 3.3 – Thermocouple Head Design.

In the case of a short duration blow-down test, determining the time response of the probe is equivalent to determining how quickly the center of the thermocouple gage wire reaches the temperature imposed by the test gas surrounding it. Practically, we try to determine the time required for that centerline point temperature to be within 1% of the flow temperature.

As a secondary consequence of the choices made to reduce the conduction error of the probe, the length of the gage exposed to the flow is much larger than the wire diameter. This geometrical consideration validates the infinite cylinder heat transfer theory as an appropriate model to compute the cross-sectional transient conduction inside the gage wires. References for that model can be found in [7].

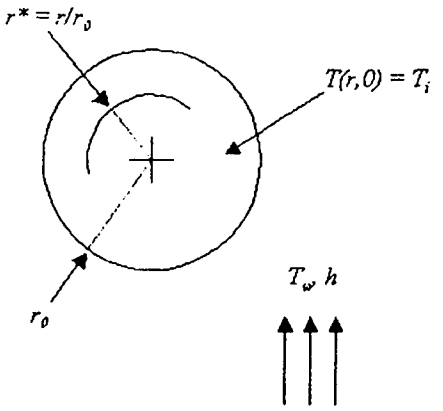


Figure 3.4 – Infinite Cylinder with Initial Uniform Temperature Subjected to Sudden Convection Conditions.

For an infinite cylinder, only one spatial coordinate is needed to describe the internal temperature distribution. The heat equation is reduced to:

$$\frac{\partial^2 T}{\partial r^2} = \frac{1}{\alpha} \cdot \frac{\partial T}{\partial t} \tag{3.1}$$

In order to solve this equation, it is necessary to specify one initial and two boundary conditions. The initial condition is:

$$T(r,0) = T_i \tag{3.2}$$

and the boundary conditions are:

$$\left.\frac{\partial T}{\partial r}\right|_{r=0} = 0 \tag{3.3}$$

and

$$-k \left.\frac{\partial T}{\partial r}\right|_{r=0} = h\left[T(r_0,t) - T_\infty\right] \tag{3.4}$$

where h is the convection heat transfer coefficient and k is the thermal conductivity of the thermocouple wire.

Equation (3.2) supposes that the temperature distribution inside the wire is uniform. Equation (3.3) defines the radial symmetry of the problem and equation (3.4) describes the convectional heat exchange at the surface of the gage wire for any $t>0$.

A practical way of solving this problem is to define the equation involving the non-dimensional forms of the dependent variables. These dimensionless variables are:

$$\upsilon^* \equiv \frac{T - T_\infty}{T_i - T_\infty} \tag{3.5}$$

The dimensionless form of the spatial coordinate is:

$$r^* \equiv \frac{r}{r_0} \tag{3.6}$$

As for the time variable, it is replaced by the Fourier number:

$$t^* \equiv \frac{\alpha \cdot t}{r_0^2} \equiv F_0 \tag{3.7}$$

The problem hence becomes:

$$\frac{\partial^2 \upsilon^*}{\partial r^{*2}} = \frac{\partial \upsilon^*}{\partial F_0} \tag{3.8}$$

with the initial condition:

$$\upsilon^*(r^*, 0) = 1 \tag{3.9}$$

and the boundary conditions:

$$\left.\frac{\partial \upsilon^*}{\partial r^*}\right|_{r^*=0} = 0 \tag{3.10}$$

$$\left.\frac{\partial \upsilon^*}{\partial r^*}\right|_{r^*} = 1 = -Bi \cdot \upsilon^*(1, t^*) \tag{3.11}$$

where Bi is the Biot number, defined as:

$$Bi \equiv \frac{h \cdot r_0}{k} \tag{3.12}$$

The exact solution to this dimensionless problem is a linear superposition of particular solution involving Bessel functions of the first kind:

$$\upsilon^*(r^*, t^*) = \sum_{n=1}^{\infty} C_n \exp(-\varsigma_n^2 \cdot F_0) \cdot J_0(\varsigma_n \cdot r^*) \tag{3.13}$$

where

$$C_n = \frac{2}{\varsigma_n} \cdot \frac{J_1(\varsigma_n)}{J_0^2(\varsigma_n) + J_1^2(\varsigma_n)} \tag{3.14}$$

and the discrete values of ς_n are the positive roots of the transcendental equation:

$$\varsigma_n \cdot \frac{J_1(\varsigma_n)}{J_0(\varsigma_n)} = B_i \tag{3.15}$$

J_0 and J_1 are Bessel functions of the 0^{th} and 1^{st} order of the first kind.

The Biot number is determined by the geometry and the nature of the wire, as well as by the convection heat transfer coefficient, which is determined by a first order modeling of the flow temperature, that will be detailed in the error modeling section in section 3.6. Theory lets us know that for values of the Biot number below 0.01, the first term of the response series needs to be retained for a 2% accuracy. Solving equations (3.14) and (3.15) gives the values of C_1 and ς_1 which can than be substituted in equation (3.13) to find the corresponding Fourier number. The corresponding time can then be deduced from this result. Accordingly, the calculations, which are detailed in Appendix B, give the following results: it takes 30 ms for the center line of the infinite-long type K thermocouple wire to be within 1% of the boundary flow temperature, at the upstream locations, and 19 ms at the downstream locations. A similar calculation has been done for the bead, which has the shape of a sphere with four times the radius of the wire. It takes 57 ms for the center of the junction bead to reach 99% of the external temperature for the upstream probes and 36 ms for the downstream located probes. This model allows the theoretical validation of the choice of 0.0005-inch thermocouple gages to satisfy the design requirement for very fast response probes.

As in all blow-down facilities, a phenomenon known as compressional heating can be observed at the early stage of the startup transient. The high pressure in the supply tank coupled with the initial vacuum in the test section has the effect of compressing the gas and, therefore, heating it, as explained in [5]. This phenomenon is very short in time and its duration is directly linked to the speed with which the valve opens. So far, only

fast response probes have been able to detect it. Hence, the capacity of a probe to record this phenomenon, which translates into a temperature spike, as shown in Figure 3.5, is an experimental criterion for a probe response qualification.

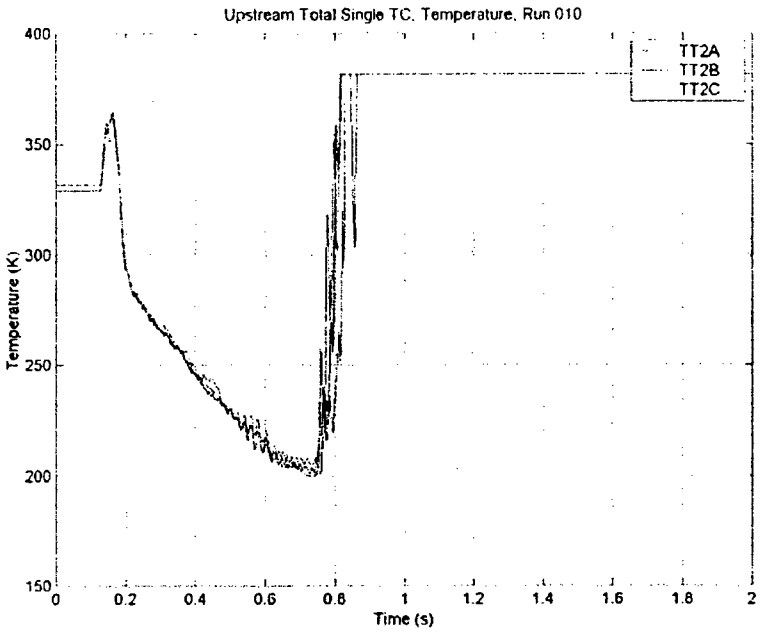


Figure 3.5 – Compressional Heating in the Blow-Down Seen by the Upstream Probes.

3.4.2. Upstream and Downstream Total Temperature Single Probes

As is explained in section 3.6.2, an efficient way to reduce the conduction error for a given probe is to expose significant length of wire to the flow, on either side of the junction bead. But this length should also allow the gage wire to sustain the dynamic pressure of the blow-down flow. In these circumstances, it was decided to manufacture ¼-inch single thermocouple heads.

For these heads, the gage is inserted in a ¼-inch OD casing with a 0.016-inch thick wall. These casings are each vented with two holes diametrically opposed, whose dimensions have been determined by the surrounding flow conditions and the recovery error, as explained in section 3.6.1. The gage wire is hung between two half-inch-long ceramic stems epoxied on a stainless steel spacer whose diameter matches the inner diameter of the casing. The epoxy used can endure temperatures up to 500 F. The gage

wire ends are soldered to 0.010-inch diameter thermocouple extension wires, inside the ceramic tubes. These extension parts run through a 3/16-inch stem tube, filled with epoxy to seal the probe. These single probes are mounted via Swagelock fitting on brass plugs located at the inlet and outlet stations of the compressor. These extension wires connect to thicker thermocouple extension wires to the external ice point reference chambers were they mate with temperature reference junctions maintained at 0°C. The signal is caught there and led to special conditioning instruments that will be described in section 3.4.5.

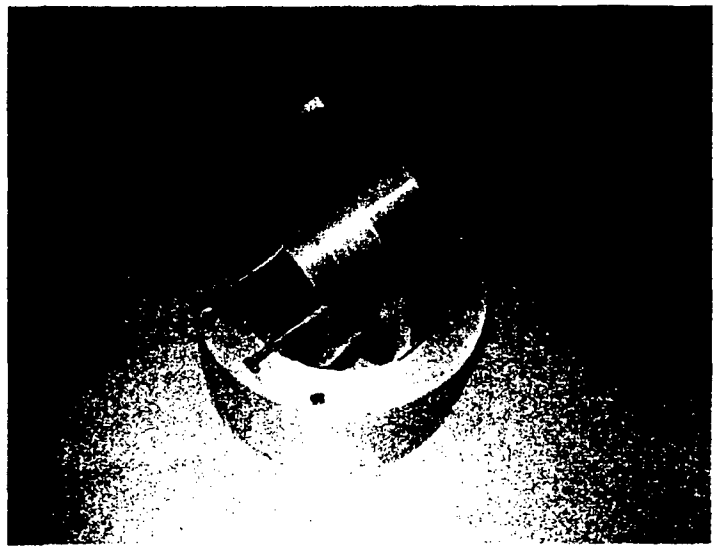


Figure 3.6 – Downstream Temperature Probe Mounted on Brass Plug.

3.4.3. Upstream and Downstream Total Temperature Rakes

In order to determine the radial distribution of the temperature at the inlet and the outlet of the compressor, total temperature rakes have been designed. They consist of specially designed airfoils fitted with thermocouple heads on their leading edges. One rake is located upstream of the compressor, it supports 11 heads, spaced in such a manner that they will record temperature figures for similar annular areas. The reduction in the flow duct radius led to the design of two downstream rakes, one with 5 probes and the other with 6 probes. The arrangement of these heads is again organized in a way that all probes will cover identical annular flow areas. However, we should underscore the

exception of the tip probes on the 6-head rake, that had to be shifted towards the mid-radius of the duct, due to their casing diameter.

These airfoils have been designed so as to disturb as little as possible the flow pattern. On the one hand, this implies that the airfoils should have the smallest thickness possible. But on the other hand, the thermocouple probe performances are still subjected to conduction error, which require, to be overcome, a larger head diameter. In these circumstances, a consensual approach was found with 3/16-inch head probes. These heads have the same length and share the same layout as their single counterparts, only with a smaller inner casing diameter and a different vent hole size. Each airfoil actually consists of a main body encompassing the leading and trailing edges, with a cavity in the middle, and a cover side sliding in the airfoil span direction. It has a circular base through which it is screwed to an aluminum canister. For manufacturing reasons, each canister consists of two mating parts. The extension wires are laced together at the back of the probe heads and run down the canister to a sealed multi-pin connector where these wires are soldered to thicker thermocouple extension wires crimped to thermocouple grade sockets. The sealing of the connector is ensured by an O-ring placed between the connector part and the aft canister, and by epoxy potting, poured between the sockets. Each of these assemblies fit on machined brass plugs, which mount on the test rig. The downstream rakes have the ability to be rotated with respect to the brass plug, in order for the probes to face the flow and record the total parameters. These orientations are dependent on the speed regime the compressor is tested at. Cables have been made to be mate with the multi-pin connector and connect the thermocouple heads to their external reference junctions, as in the case of the single probe heads. From there on, the information is led to special signal conditioning devices before being recorded by the A/D devices.

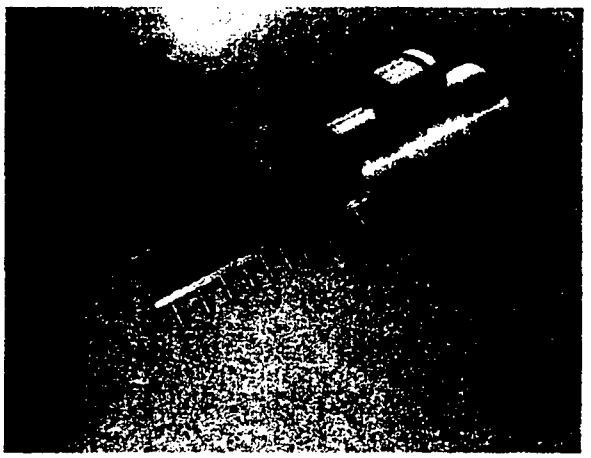


Figure 3.7 – Fully assembled upstream total temperature rake.

Each probe is given an instrument name, according to a certain logic pattern. These names all start by the letters 'TCK', which stand for type-K thermocouples. The following letter can either be an 'R', for the heads mounted on rakes, or an 'S', for the single probes. These letters are followed by a 'U', for the upstream probes or a 'D' the downstream probes. Finally, a three-digit number is added. This information is stored in an electronic instrument database, where each probe is recorded, with the references and names of all the cables and the devices that are active in their functioning. This is not only important for archiving purposes, but also and above all, for calibration purposes, as will be explained in section 3.5.

3.4.4. Mechanical Integrity within the Flow Conditions

After having determined a design capable of satisfying the requirements for the blow-down testing thermal conditions, it was necessary to set up a test that would validate this design in terms of structural integrity of the probes when they are submitted to the dynamic pressure of the flow. In this purpose, a free-jet stand was used. This facility consists of a plenum tube with a circular opening at one end and a connection to a pressurized air system at the other. The gas expands isentropically through the open exit of the plenum. The total pressure of the gas is hence conserved. Inside the plenum, the speed of the gas is close to zero. It is hence possible to monitor the dynamic pressure

coming out of the plenum tube by setting its inner pressure to a certain value through a feeding valve.

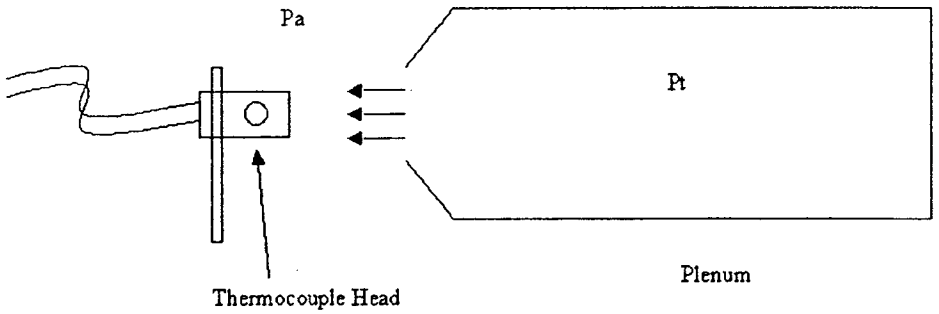


Figure 3.8 – Schematic of Free Jet Resistance Test.

To gather the best efficiency out of this validation test, the simulation aimed at reproducing the strongest dynamic pressure the probes were likely to encounter in the compressor. These conditions occur for the design speed test, at the downstream locations, at the starting of the transient blow-down. The dynamic pressure reaches almost 6 psi in such conditions. The pressure inside the plenum had to be brought to 20.7 psi to reproduce these conditions, and to achieve a safety factor of one. The probes were than exposed to this dynamic pressure in different ways. The first way tried to systematically search for the pressure leading to the gage break. A given probe would be submitted to any total pressure values between the ambient pressure and the limit value of 22 psi, in steps of 0.5 psi. Several tests showed that the downstream probes were unable to sustain the level of dynamic pressure required. Many broke just around 21 psi, which was perfectly suitable for the upstream probes, which would only be submitted to total pressures of 18 psi at most. Digital camera pictures showed that the breaking points were systematically located at the nearest proximity of the bead junction. The manufacturing process requires the two thermoelectric metal wires to be at a 60° angle from one another, at the location where the bead is machined. Our probe manufacturing process required stretching this gage, creating elbows in the immediate vicinity of the bead. Kinking the gage wire in this location turned out to render it more fragile.

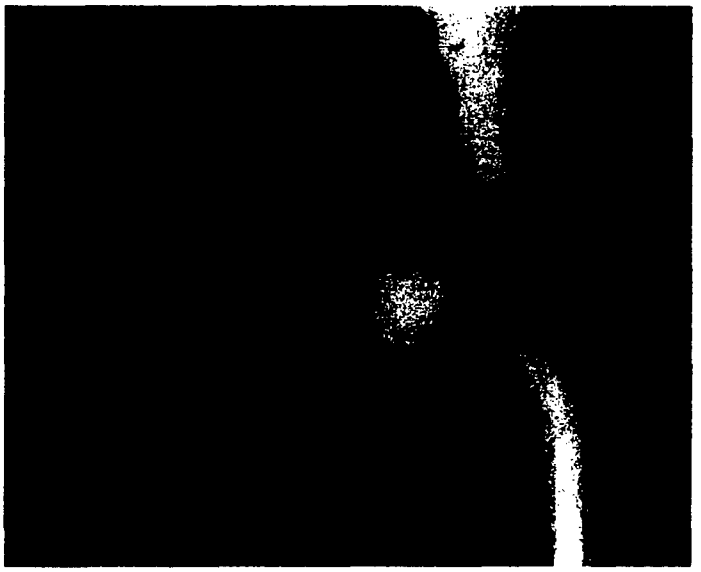


Figure 3.9 – Picture of 0.0005-inch Thermocouple Gage.

Consequently, several solutions were examined. The first one consisted in trying to manufacture the heads without stretching the gage wire between the two ceramic stems, so as to release the level of stress in this wire and avoid the kinks creating fragile areas on either side of the bead junction. Several gage wire shapes and assembling processes were made, but they all turned out to be either to hard to realize, or totally inefficient to improve the probe design in terms of structural integrity to the tests. Releasing the stress led to the gage wire [illegible] to the drawbacks of the turbulent flow inside the head casing.

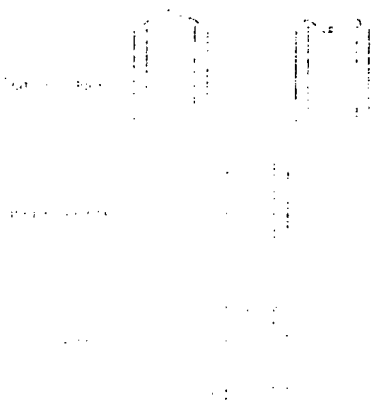


Figure 3.10 – Gage Wire Shapes Tested in the Free Jet Stand

Another option consisted of changing the vent hole sizes on the head casings. As will be explained in section 3.6.1., the vent hole size sets the recovery error of the thermocouple probe, by regulating the flow of air inside the casing. Decreasing the vent hole size would result in a smaller flow speed and hence a smaller dynamic pressure on the gage wire. But reducing the Mach number inside the head had other consequences as well. Although it allows reduced recovery error, it increases the response time of the gage, by reducing the convection heat transfer coefficient around the wire. Another option was to reduce the casing diameter, to reduce the length of wire exposed to the flow. This reduction would entail an increase in conduction error of the probe. In order to achieve the best decision, a comparative study was conducted to assess the modifications any given load reduction on the wire would have on the recovery and the conduction error as well as the response time of the probe, which are all affected by the different options detailed above. These modifications are summarized in Figure 3.11, Figure 3.12 and Figure 3.13.

This study showed that the best consensus, entailing the lesser losses in design requirements as well as manufacturing procedures, would consist in reducing the vent hole size of the downstream probes to achieve a 30% reduction in load on the gage wire. This solution imposed an increase of 3 ms in response time, which corresponds to a 10% increase, but granted a 35% decrease in recovery error. The exponential changes in conduction error with the reduction in load showed the higher impact on the quality of the measurements a reduction in casing diameter would have had.

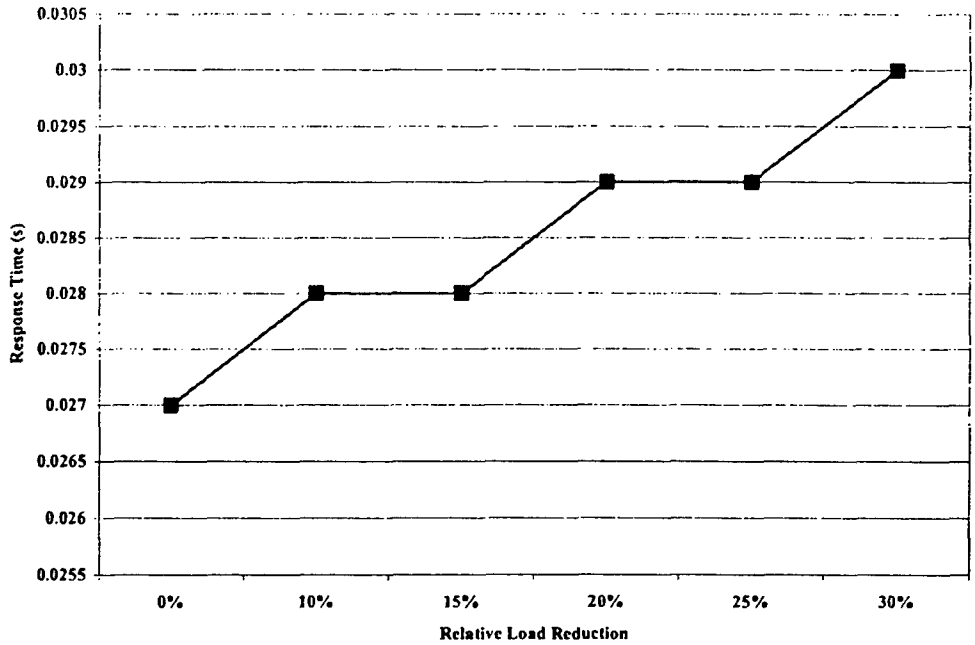


Figure 3.11 – Wire response-time in (s) versus the Percentage of Load Reduction for ¼" heads by Decreasing the Vent Hole Size.

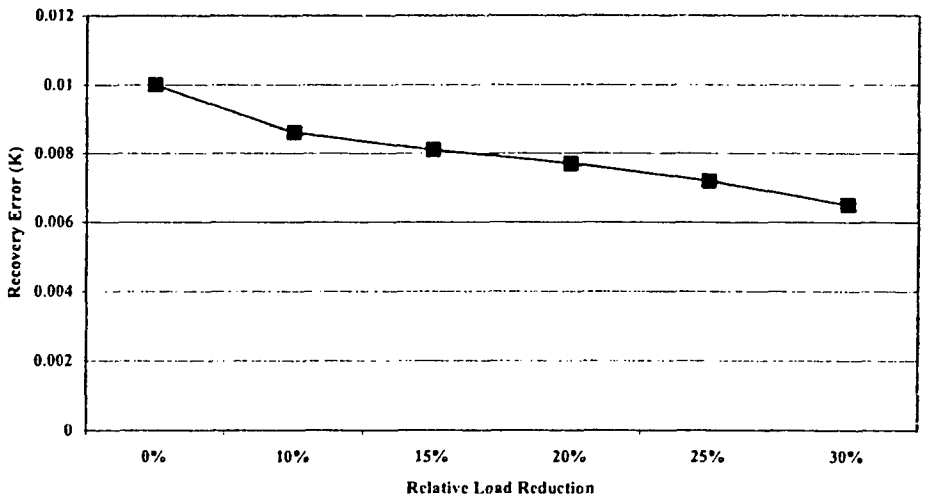


Figure 3.12 – Evolution of the Recovery Error versus the Percentage of Load Reduction for ¼" heads, by Decreasing the Vent Hole Size.

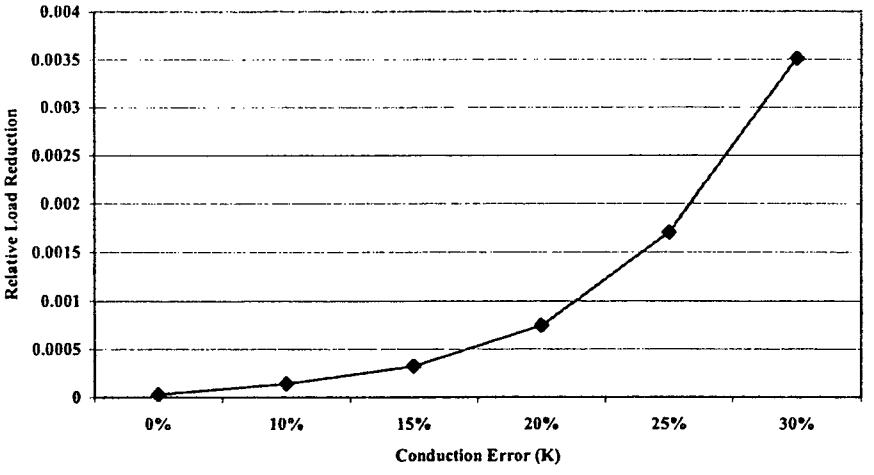


Figure 3.13 – Evolution in Conduction Error versus the Percentage of Load reduction by Decreasing the Inlet Area of a ¼" head.

Following the same protocol, the new probes were tested to find the pressure causing the gage wire to break. They proved to be much more resistant and broke under a total pressure of 26 psi, which corresponds to a safety factor of 2 in terms of dynamic pressure.

To finally validate the assembly process, it was decided to submit all the different probes to a test simulating the pressure pulse they would see in the test rig. This protocol consisted in reproducing the pressure pulse consecutive to the firing of the fast acting valve. Each head would be placed in the flow path but would remain protected from it by a bar of angled iron. The pressure in the plenum would be brought to 22 psi, and the angle iron would be removed quickly. The air flow in the plenum would be shut right after.

3.4.5. Signal Conditioning

Output signals from the total temperature probes are filtered and amplified by 2B31L analog device signal conditioners. After amplification, the signals are fed into multiplexer A/D systems, which are described in section 2.4.2. This type of signal conditioner module has small offset drift with temperature and time (0.6 μV/°C and 3 μV/month from

specifications) and low gain non-linearity (0.025% max from specifications). Experiments indicate offset variation of less than 0.0006 mV (corresponding to 0.001 K at gain 1000) during a typical day. The conditioner module provides an adjustable-gain amplifier, a three-pole low pass filter and also an adjustable transducer excitation. All thermocouple signals are low-pass filtered at 500 Hz.

3.5. Static Calibration of Total Temperature Probes

As has been explained in section 3.3, using signal enhancing and conditioning devices on thermocouple probes require the probes to be calibrated, as each device introduces some error and drift from the standard thermocouple tables. In this chapter, the calibration equipment used is described, as well as the calibration procedures of the thermocouple probes.

3.5.1. Calibration Equipment

The calibration of the thermocouple probes aims at determining and creating a file associating each voltage output of the instrumentation to the corresponding temperature of the probe. For that purpose, the probes are placed in a medium that is thermally conductive and electrically non-conductive, so as to render the calibration independent of the medium the probe is in. The thermocouple probes of the counter-rotating aspirated compressors are submitted to temperatures that range from -60°C to 170°C. This range cannot be covered by a single calibration fluid. It was hence necessary to acquire two different calibration baths. For the lower part of the temperature range, a calibration bath of the type 7381 from Hart Scientific was used. This device offers an 18-inch deep cavity and is fitted with a cooling system that allows it to reach temperatures ranging from -80°C to 110°C [8]. The fluid used in that bath is Hart Scientific HFE 7500, which can be used between -75°C and 100°C. This fluid was chosen for its reasonable price and its probe cleaning simplicity. The upper temperature calibration was handled by a Hart Scientific 6330 calibration bath. This device covers temperatures from 35°C to 300°C. The cavity is 9.25 inches deep. The fluid used was Silicon oil 200.20 that can cover temperatures from 10°C to 230°C. Each bath is fitted with an automatic stirring system

that guarantee a flow temperature uniformity of less than 0.02°C at 200°C for the 6330 model and 0.007°C at 0°C for the 7381 model. Each bath can be monitored either manually or automatically via an RS-232 connection.

To optimize the quality of the calibration files, the calibration bath's temperature is recorded in two ways. The first way is a built-in system that is used to monitor the bath. The second one relies on a NIST-traceable Rosemount Standard Platinum Resistance Thermometer model 162N. The specifications are given in Table 3.1. This device is used to establish the calibration file. The resistance of the Rosemount thermometer is measured by a Fluke 8520A digital multimeter. This multimeter can be operated remotely via an integral IEEE-488 interface, allowing triggering from the data acquisition computer.

Temperature range	-200°C to 400°C
Stability	0.10°C/year
Self-Heating	28 mW/°C
Time Constant	1.0 sec
Max. Calibration Uncertainty (below 200°C)	0.025°C

Table 3.1 – Specifications for the Rosemount Standard Platinum Resistance thermometer model 162N.

A Labview data acquisition program, named TCCalMain, is run on a DELL x86 computer. This program reads and records the voltage output of each thermocouple amplifier through the A/D and the resistance of the Rosemount thermometer through the Fluke digital multimeter. The program displays the temperature reading of the calibration bath. A setting file where the starting temperature set-point, the number of set-points, the temperature increment, the sampling rate, the sampling count as well as the bath conditions to start recording a set-point, must be specified to operate the baths through the Labview program. The end product is a text file gathering the calibration conditions, the probe name, as well as the set-point recordings.

3.5.2. Calibration of Thermocouples

To perform a calibration, the thermocouple probes are mounted on a metallic plate. In the case of the single probes, the plate is fitted with 6 Swagelock fittings. The length of stem is set to ensure the heads remain in the calibration fluid over the entire

calibration process and despite the fluid's changes in volume. An extra hole was drilled to accommodate the Rosemount thermometer as close to the heads as possible. The plate is used as a lid for the bath, so as to reduce convection from its surface and to protect the fluid from dust or other particles. As for the rakes, the metallic plate is fitted with a 3.2"inch hole to support a Teflon jig onto which the rake mounts. The rakes' canisters are designed with a flange to ease the assembly of the rake onto the brass piece. This flange is a convenient way of holding the rake in the bath. But the forward canisters are not long enough to guarantee that the probes are immersed in the fluid at all times. In the meantime, the flange was too large to be inserted in the bath. It was hence necessary to unscrew the two parts of the rakes' canisters and to design a jig that would allow to hold the front part in the fluid while keeping the aft part of the canister outside the cavity.

Once mounted, the probes are then hooked to their assigned extensions wires to their cold junction thermometers. The signal is then carried to the A/D device through the amplifier cards. For the accuracy and quality of the calibration, it is mandatory to hold the external reference junction cells to the stable temperature of 0°C. This requires the cells to be switched on at least 24 hours prior to the calibration. It is also mandatory to name, identify and record thoroughly each wire and device linking each probe to the data acquisition system, as the calibration and the signal is strongly dependent on the physical properties of these accessories. To ensure a proper use of the probes, the thermocouple have to be linked to the same wires, cold cells and amplifying cards as they were during their calibration to validate the information they provide. This information is stored in a LabView database named "InstrumentDataBase".

The calibration setting file is used to set up each calibration. For this experiment, each probe is calibrated from –60°C to 60°C on the cold bath and from 50°C to 170°C on the hot bath, by increments of 10°C. This gives two overlapping points for each probe, which allows a partial check for the validity of a calibration measurement. The bath temperature setting is monitored from the computer. The computer records the bath temperature every five seconds and computes the associated average value over the last 3 minutes, along with the corresponding standard deviation. These parameters play a key role in determining the right moment for the computer to make a calibration

measurement. It appears mandatory to guarantee the stability and the homogeneity of the fluid temperature to make an accurate and sensible recording. The average of the last 3-minute bath temperature recordings must be within 1 K from the set-point value while the standard deviation must be less than 0.1 K. When these criteria are met, the computer records 500 samples of data from the Rosemount thermometer and from the A/D device at the rate of 50 Hz. The corresponding averages are stored in a separate text file for each probe.

As mentioned earlier, the two calibration baths are operated with different fluids. To transfer the probes from one bath to the other, the thermocouples are cleaned with ethanol, which very efficiently dissolves the fluids and evaporates. This procedure prevents any mixing of the two fluids and contributes to the quality of the calibrations.

The calibrations are used to determine probe drifts with time. Several calibrations are hence necessary to determine this aspect and to obtain the proper calibration files. A Matlab program was written to check the validity and the quality of the calibration of the thermocouple probes. For each thermocouple probe, this program treats their calibration file in a chronological order. It first performs a 9^{th}-order polynomial regression on the data of all but the latest calibration file. It than computes and plots the difference in temperature between the data points of the last calibration file and the temperature the polynomial fit gives for the same voltage output, for each of the previous calibration files. Another comparison is done between those calibration curves and a 9^{th}-order polynomial fit for the last file. An average error is also plotted. The choice for a 9^{th}-order polynomial regression is based on the fact that the ideal law linking the voltage output of a type-K thermocouple and its corresponding temperature is a 9^{th}-order polynomial. This choice was hence made in a conservative perspective.

This program has been able to show that the thermocouple probes age at the higher range of temperatures. Calibration after calibration, the difference plotted by the Matlab program was a brought down to a level less than 0.1 K. This latter value was chosen to determine whether the thermocouple probes were still subjected to drifts or whether they could be used with the corresponding calibration file. Closer attention was also paid to the overlapping temperature range between the two baths. Here again, a

difference of less than 0.1 K was set as an acceptance criterion. Once a calibration file is judged acceptable, it is stored as a Matlab file that is automatically used in the data processing.

To further check the drifts in calibration, the single probes were recalibrated after the first three runs. Again, difference of less than 0.1 K was recorded between this calibration and the last one used for the first tests, which showed the absence of drift for these probes.

3.6. Uncertainty Estimation of Total Temperature Measurement

The property of thermocouple material slightly varies due to imprecision in fabrication. This error can be reduced through proper calibration of each individual thermocouple. The related uncertainty is than totally dependent on the calibration method and the quality of the calibration equipment. But there are three other factors or sources of uncertainty in the temperature measurement of fluid flow. These sources are the recovery error, the conduction error and the radiation error. In this following chapter, we will discuss those three sources and quantitatively evaluate them.

3.6.1. Recovery Error and Response Time

Total temperature can be measured only when the fluid flow is brought to rest isentropically. Unfortunately, temperature probes cannot satisfy this requirement. How close the measured temperature is to the true total temperature can be evaluated by the recovery factor r.

$$r \equiv \frac{T_{t,ind} - T_s}{T_t - T_s} \tag{3.16}$$

where $T_{t,ind}$ is the measured total temperature, T_t is the true total temperature, and T_s is the static temperature. If for a certain probe, r is equal to 1, then this probe stagnates the fluid flow isentropically without any loss.

A reasonable assumption for the evaluation of recovery loss is that all the measurement error is caused by recovery effect. In [5], the recovery error is estimated as:

$$E_{rec} = \frac{(1-r)\cdot\frac{\gamma-1}{2}\cdot M^2}{1+\frac{\gamma-1}{2}M^2} T_t \tag{3.17}$$

where M is the Mach number, and T_t can be calculated with the known parameters of the compressor.

[6] shows that the recovery factor is highly dependent on the geometry of the probe as well as the operating conditions and the material constituting the thermocouple gage. Consequently, it can only be determined experimentally and no a priori law encompassing those parameters has been established yet. Hence, the best estimation available is still the ideal concept linked to the Prandtl number of the fluid flow. In these circumstances, the recovery factor is set by the flow and is an external factor in the computation of the recovery error. The Mach number is the only parameter that can be set by the design of the probes to determine the recovery error. This Mach number is determined by the ratio of the casing inlet surface area to the vent hole surface area. For a subsonic flow, a reduction in Mach number entails a reduction in the recovery error, all other parameters being equal. The goal is to reduce the recovery error as much as possible, but a reduction in the Mach number around the thermocouple junction implies an increase in the time response of the probe, as has been explained earlier. The recovery error helps determine a Mach number that leads to the computation of the probe time response. For the upstream probes, the best compromise was found for a recovery error of 0.025 K, which lead to a time response of 30 ms. The associated vent hole have a diameter of 0.096 inches for the single probes and 0.076 inches for the rake probes. As

for the downstream probes, the recovery error was contained even more, at 0.0065 K, with a time response of 19 ms, and vent holes of 0.074 inches for the single probes and 0.060 inches on the rake probes.

Probes	Inlet diameter (in)	Vent hole diameter (in)	Mach number	Recovery Error (K)	Time response (s)
3/16 upstream	0.174	0.076	0.059	0.0250	0.030
1/4 upstream	0.219	0.096	0.059	0.0250	0.030
3/16 downstream	0.174	0.060	0.030	0.0065	0.019
1/4 downstream	0.219	0.074	0.030	0.0065	0.019

Table 3.2 – Summary of Probes Geometries, Inner Mach Numbers, Recovery Errors and Time Responses.

3.6.2. Conduction Error

As mentioned earlier, the conduction loss was the biggest error source that made the previously designed total temperature probes unsuitable to the blow-down type tests. In this design, the 0.0005-inch type-K thermocouple is stretched across the inner diameter of the stainless steel shield. The wire is supported by two ceramic tubes. While the flow comes into the probes, heat is convected from the test gas to the wires. It is also conducted from the wires to the supporting ceramic tubes. Previously, we have shown that the time response at upstream test condition amounts to 30 ms and 19 ms at downstream conditions. With such fast time response, we can assume a one-dimensional steady state conduction-convection model to calculate the conduction error.

The heat equation for one-dimensional steady state conduction-convection of a fin with uniform cross-sectional area can be written as:

$$\frac{d^2T}{dx^2} - \frac{hP}{kA_c}(T - T_\infty) = 0 \tag{3.18}$$

where T is the temperature of the fin, x is the coordinate along the fin, h is the convection heat transfer coefficient, k is the thermal conductivity of the thermocouple, P is the perimeter of the thermocouple, A_c is the constant cross-sectional area, and T_∞ is the gas temperature.

If we define the difference between the thermocouple temperature and the gas temperature as

$$\theta(x) \equiv T(x) - T_\infty \tag{3.19}$$

then, we can rewrite equation (3.18) as

$$\frac{d^2\theta}{dx^2} - m^2\theta = 0 \tag{3.20}$$

where

$$m^2 \equiv \frac{hP}{kA_c} \tag{3.21}$$

Equation (3.20) is a linear, homogeneous, second-order differential equation with constant coefficients. Its general solution is of the form

$$\theta(x) = C_1 e^{mx} + C_2 e^{-mx} \tag{3.22}$$

To evaluate the constants C_1 and C_2, it is necessary to specify boundary conditions. In our case, the two boundary conditions are the same. Figure 3.14 shows the schematic of the one-dimensional convection-conduction model of the thermocouple. The temperature difference between the gas and wall at the two ends of the thermocouple is the same as

$$\theta(0) = \theta(L) = T_{wall} - T_\infty \equiv \theta_{wall} \tag{3.23}$$

The solution to equation (3.20) is

$$\theta(x) = \theta_{wall} \frac{\sinh(mx) + \sinh(m(L-x))}{\sinh(mL)} \tag{3.24}$$

The flow parameters different and the gas properties change through the compressor. This results in different conduction losses. Figure 3.15 shows the difference between the gas temperature and the thermocouple wire temperature divided by the difference between the wall temperature and the gas temperature, which is the relative measurement error, for the upstream ¼-inch temperature probes. Qualitatively, the errors are small. For the upstream conditions, the rake probes show a conduction error of 0.073 K, while the single probes one of 0.005 K. For the downstream conditions, the rake probes show a conduction error of 0.014 K and the singles 0.0005 K. Such low values are due to the small size of the thermocouple wires and the great length exposed to the gas. The fact that the conduction loss does not penetrate from the inner wall of the probe shield to the middle of the thermocouple wire resulted from these two positive factors.

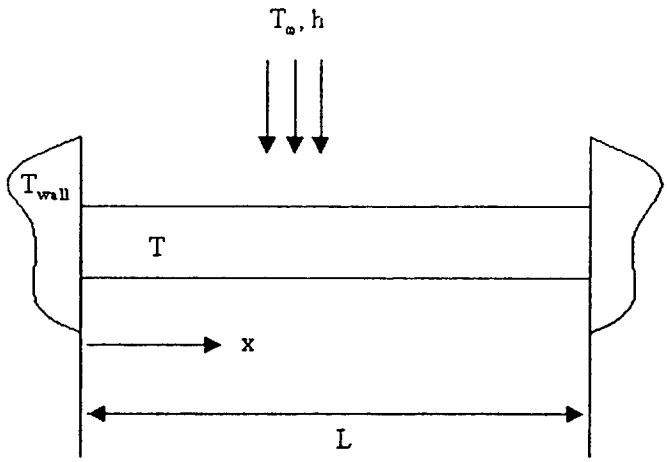


Figure 3.14 – Schematic of One-Dimensional Conduction-Convection Model for Thermocouple Wire.

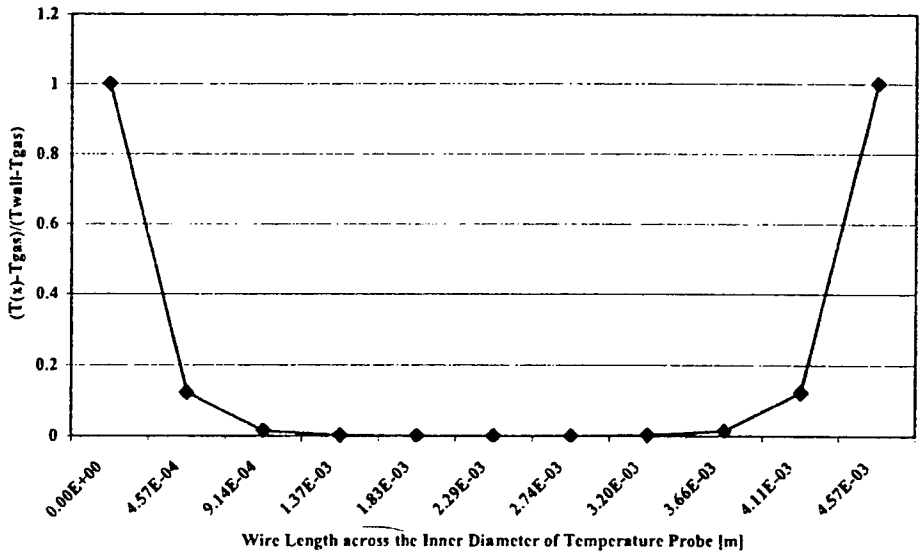


Figure 3.15 – Conduction Error Percentage, Predicted by a Steady State One-Dimensional Conduction-Convection Model.

3.6.3. Radiation Error

Radiation of the thermocouple wires is also an important error source in temperature measurement. As in [5], the radiation error is evaluated at steady state

conditions, and the assumption is that all the heat convected from the gas to the thermocouple is radiated to the surrounding body, i.e. the probe stainless steel shield. The error can be expressed as

$$E_{rad} = \frac{\sigma\varepsilon(T_{t,j}^4 - T_{surr}^4)}{h} \tag{3.25}$$

where σ is the Stefan-Boltzman constant and ε is the emissivity of the junction. A value of 0.4 is used for chromel-alumel material [9]. h is the convection heat transfer coefficient. $T_{t,j}$ is the temperature of the thermocouple junction. T_{surr} is the temperature of the surrounding shield. Since the upstream and downstream total temperature probes are sitting in the test section of the tunnel, their temperature is room temperature prior to the test. The probes are essentially a part of the tunnel, thus they are a comparatively large heat sink. A heat transfer calculation performed on the blades show that the probe shield temperature will not change significantly during the test time. Therefore, the radiation shielding for the thermocouple sensors in short-duration experiment has little effectiveness. During a test upstream and downstream temperature sensors see different gas temperatures, and h is also different. The error due to radiation loss for upstream temperature probes is 0.112 K and that for the downstream probes is 0.299 K. The latter value is obtained for the highest temperature the probe sees. Detailed calculation is given in Appendix B.

3.6.4. Overall Uncertainty of Total Temperature Measurement

The four major sources of uncertainty have been discussed in the previous paragraphs. The following table summarizes the quantitative estimates of those errors. These errors stem from independent sources. The total absolute error is hence computed as the square root of the sum of the squares of each source. The percent uncertainty is calculated with upstream and downstream flow conditions.

Sensor Name	Error (K)				
	Recovery	Conduction	Radiation	Calibration	Total
TCKSU001	0.025	0.005	0.112	0.048	**0.124**
TCKSU002	0.025	0.005	0.112	0.058	**0.129**
TCKSU007	0.025	0.005	0.112	0.055	**0.127**
TCKRU001	0.025	0.073	0.112	0.041	**0.142**
TCKRU002	0.025	0.073	0.112	0.038	**0.141**
TCKRU003	0.025	0.073	0.112	0.040	**0.142**
TCKRU004	0.025	0.073	0.112	0.039	**0.141**
TCKRU005	0.025	0.073	0.112	0.042	**0.142**
TCKRU006	0.025	0.073	0.112	0.040	**0.142**
TCKRU007	0.025	0.073	0.112	0.038	**0.141**
TCKRU008	0.025	0.073	0.112	0.039	**0.141**
TCKRU009	0.025	0.073	0.112	0.039	**0.141**
TCKRU010	0.025	0.073	0.112	0.043	**0.143**
TCKRU011	0.025	0.073	0.112	0.042	**0.142**
TCKSD001	0.0065	0.0005	0.299	0.071	**0.307**
TCKSD002	0.0065	0.0005	0.299	0.036	**0.301**
TCKSD003	0.0065	0.0005	0.299	0.065	**0.306**
TCKRD001	0.0065	0.014	0.299	0.033	**0.301**
TCKRD002	0.0065	0.014	0.299	0.028	**0.301**
TCKRD003	0.0065	0.014	0.299	0.034	**0.301**
TCKRD004	0.0065	0.014	0.299	0.034	**0.301**
TCKRD005	0.0065	0.014	0.299	0.037	**0.302**
TCKRD006	0.0065	0.014	0.299	0.060	**0.305**
TCKRD007	0.0065	0.014	0.299	0.326	**0.443**
TCKRD008	0.0065	0.014	0.299	0.054	**0.304**
TCKRD009	0.0065	0.014	0.299	0.047	**0.303**
TCKRD010	0.0065	0.014	0.299	0.062	**0.306**
TCKRD011	0.0065	0.014	0.299	0.097	**0.315**

Table 3.3 – Detailed Summary of Thermocouple Probes' Errors.

4. Total Pressure Measurement

4.1. Introduction

The measurement of the pressures at the inlet and the outlet of the compressor is required to the aerodynamic performance study. As mentioned in section 2.4.1, the blow-down compressor employs one 8-head impact total pressure probe rake upstream of the IGV and two 5-head impact total pressure probe rakes. In addition, upstream of the compressor are located three sets of pressure sensors encompassing each a Kiel head total pressure probe, a static pressure point and a Pitot probe. One comparable set is mounted downstream of the compressor, where the static sensor window is fitted with a high-speed pressure sensor. Along with the total temperature measurement, these probes allow the mass-flow and the Mach number at different locations in the flow to be estimated. Several other pressure sensors are mounted on the rig, namely a high-speed static tap between the two rotors, and a 3-way wedge probe in the bleed flow passage. Both the supply and the dump tanks have been fitted with a redundant static pressure measurement system.

In this chapter, the requirements for the total pressure measurement are outlined. The design of the total pressure probe rakes is described. The online calibration

procedure is detailed and lastly, an uncertainty estimation of the total pressure measurement is presented.

4.2. Requirements for Total Pressure Probe in a Blow-Down Facility

The purpose of the total pressure probe is to record the stagnation pressure in the flow field. In this perspective, the probe should be designed to stop the flow isentropically and add dynamic pressure to static pressure. The probes must hence be adaptable to the flow direction so as to record the total parameters. The single total pressure measurement points are achieved using both Kiel-head and Pitot probes, which are fitted on brass plugs via Swagelock fittings, gripping their stems. This allows an easy rotation of the probes towards the flow direction. As for the radial total pressure distribution, it is measured through special airfoil-shaped rakes accommodating impact heads on their leading edges. This choice was made so as to minimize the blockage effect caused by the introduction of rakes in the flow. Impact heads present the advantage of being relatively small in comparison to other total pressure measurement devices. But the direct consequence of the small inlet section area of these impact heads is their relatively strong sensitivity to misalignment. Consequently, the rakes they are mounted on have to be easily adjustable.

The main type of pressure transducer used in the counter rotating aspirated compressor is a piezoresistive strain gage. A piezoresistive transducer is essentially a variable resistor that changes its resistance under different mechanical strains. This type of transducer is very sensitive to pressure change and has good response frequency, which is a prevailing critical factor in a blow-down facility. But in the case of ultraminiature gauges, this technology shows some instability caused by non-linearity and hysteresis effects. To overcome these particularities, these Kulite sensors are calibrated against two high precision Heise transducers prior to filling the supply tank, once the supply tank is filled and immediately after a test. A Heise DXD 150 psia is located in the supply tank and a HEISE model DXD 15 psia is recording the pressure in the dump tank. These two transducers are also piezoresistive strain gauges.

For further accuracy, two absolute strain gage transducers were mounted on the supply and the dumps tanks. The model implemented upstream from the compressor is a Sensotec SuperTJE – 150 psia and the one on the rear is a Sensotec TJE – 50 psia.

4.3. Total Pressure Design

4.3.1. Isolated Pressure Measurement probes

The isolated pressure probes encompass the Kiel heads, the Pitot probes as well as the flush mount static pressure tubes. The first two types are commercially available devices. Their geometry has been certified and calibrated by their manufacturer. More information can be found in [13] and [14].

The Kiel head total pressure probes are of type KCD and KCC. The inner side of the sensing head is shaped as a Venturi. Kiel heads show a noticeable insensivity to flow angle, which ranges to ±54° in yaw and ±49° in pitch. Pitot probes show a lot more sensitivity in that respect. Yaw and pitch affect the reading the same way and result in relative static and total pressure measurement errors of 3% and 1% respectively for yaw/pitch angle of ±10°.

4.3.2. Total Pressure Rakes

The stationary upstream low-frequency total pressure rake has eight impact heads. The eight heads are radially arranged on the leading edge of the supporting airfoil. Each head has sharp leading edge, which is effective in reducing the sensitivity to misalignment. A 15° bevel angle was chosen for these impact heads. This angle provides ±27.5% insensivity. [10]. They are connected to fine aluminum tubes and Tygon tubes which transfer the pressure outside of the rig and onto which pressure transducers are mounted. An efficient use of epoxy guarantees the integrity and the sealing of the rake. This device does not have the ability to rotate, as the flow is supposed to enter the compressor deprived of any swirl. The pressure sensors used are Kulite XCQ-062-15, which can sustain a pressure of 15 psig. Back reference pressure is provided to the transducers via Tygon tubing which is connected to an external vacuum pump. A Lemo

connector cable is mounted on the back of the transducer and carries the information to an amplifier box.

The two downstream rakes are identical to the upstream one, except that they only carry five impact heads each. The Kulite transducers are capable of sustaining higher pressures, namely 50 psig. These rakes have been designed to be rotated around the span direction, so as to face the swirl of the flow coming out of the compressor.

The naming convention used for these probes is summarized in the Table 4.1.

Sensor Name	Location
PT2ZRxx	Upstream of NGV
PT5CRxx	Downstream of rotor 2
PT5ZRxx	Downstream of rotor 2

Table 4.1 – Pressure Sensor Name Nomenclature.

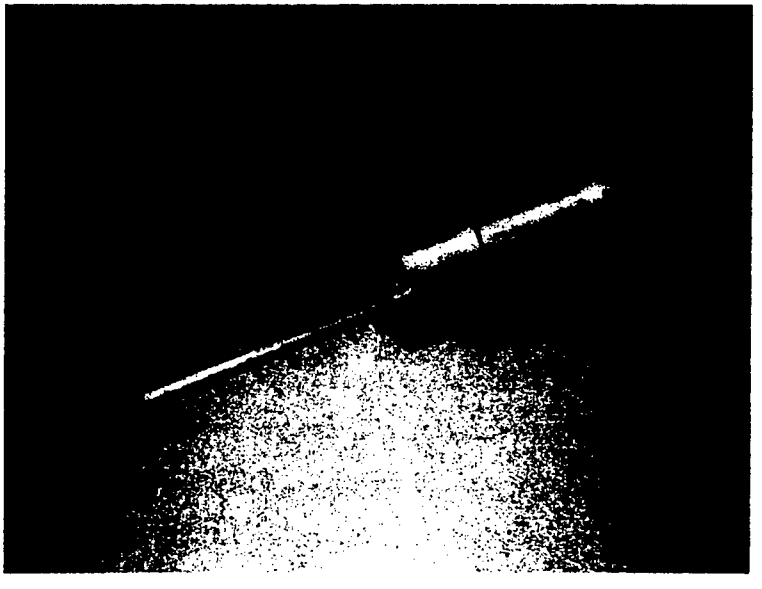


Figure 4.1 – Fully-Assembled Upstream Total Pressure Rake.

4.3.3. Signal Conditioning

Output signals from the total pressure probes are filtered and amplified by AD521IC analog device signal conditioners. After amplification, the signals are also fed into multiplexer A/D systems, described in section 2.4.2. The conditioner module provides an adjustable-gain amplifier, a three-pole low pass filter and also an adjustable transducer excitation. All pressure transducer signals are low-pass filtered at 500 Hz.

4.4. Probe Calibration

For most pressure transducers, the relation between pressure and voltage is linear. Therefore, we need to know the sensitivity and zero offset of each transducer. In order to minimize the offset drift of the pressure transducers due to time, run-time calibration method is applied in a blow-down test. Pre-fill calibration is done when the tunnel is in vacuum, post-fill calibration is done once the supply tank has been filled and the post-test calibration is done after the tunnel pressure has reached steady state conditions. The two differential pressure states are recorded by alternately switching the transducer reference pressure to atmosphere and vacuum. The three calibrations are compared to see how much the transducers drift.

To determine the scale and the zero of each transducer, a Matlab program called AutoCal was written. It first starts by determining the scales by associating the voltages recorded by each transducer to two differential pressures. The first one corresponds to the case when the back pressure system is in vacuum while the second one corresponds to the case when it is sitting at atmosphere. The associated pressures are then the difference between the pressure read by the Heise transducer sitting in the same condition as the transducer in the process of calibration and the back pressure.

Determining the voltage that corresponds to a pressure of zero is done based on data recorded right before the blow-down, as Kulite transducers show a tendency to drift. This zero is computed as the difference between the voltage read by each transducer and the pressure read by the Sensotec probe, in the corresponding condition, divided by the scale established earlier. We should point out that the Sensotec probes are calibrated against the Heise transducers during the pre-fill and the post-test calibrations.

4.5. Uncertainty Estimation of Pressure Measurement

The total uncertainty in both upstream and downstream pressure measurements will be considered to consist of three parts: the probe error, the signal noise and the transducer error. Since these errors are not correlated, the root mean square will be taken.

The probe error results from the aerodynamic interference of the probe. This error is reduced by using an airfoil probe body shape. An error is introduced when the probe is misaligned with the flow direction. The impact head with 15° bevel angle provides ±27.5° insensitivity to the flow angle. Within this ±27.5°, the measurement error is less than 1% of the dynamic head. It is of interest to determine the probe error caused by misalignment upstream and downstream of the compressor stage. Following the approach taken in [11] gives:

$$\frac{1}{2}\rho V^2 = \frac{1}{2}\rho M^2 a^2 = \frac{\gamma}{2} M^2 p \tag{4.1}$$

The non-dimensional form of the dynamic pressure becomes:

$$\frac{\frac{1}{2}\rho V^2}{P_t} = \frac{\gamma M^2}{2(1+\frac{\gamma-1}{2}M^2)^{\gamma/\gamma-1}} \tag{4.2}$$

The maximum non-dimensional error, then, should be 1% of the value given by equation (4.2). Using the recorded upstream and downstream time-averaged Mach numbers and average specific heat ratio, we have been able to compute the total probe error for each run. The results are summarized in Table 4.2 and Table 4.3.

For the static measurement points on the Pitot heads, the non-dimensional form of the dynamic pressure over the static pressure becomes:

$$\frac{\frac{1}{2}\rho V^2}{P_s} = \frac{\gamma M^2}{2} \tag{4.3}$$

The maximum non-dimensional error, then, should be 1% of the value given by equation (4.3). Using again the results of each test run, the static Pitot probe errors have been computed. They are summarized in Table 4.4.

The transducer error mainly comes from non-linear behavior of the transducer and the drift of zero-offset. Often times, these two error sources work together, and it is not easy to separate them. To measure the error on each probe, the following process is followed. The tunnel is first brought to vacuum. A calibration is performed. Air is than injected in the tunnel to a pressure of 2.65 psi. Once this pressure has settled, data are

sampled from all pressure measurement probes over 30 sec. More air is let inside the tunnel and these steps are repeated 6 times at the intermediate pressures of 6.05, 8.85, 12 psi and atmosphere pressure of 14.85 psi. After the final set of data is recorded, another calibration is performed. For each step, the probes measurements are computed using the 2 calibrations. The results are than compared to the Heise readings of the pressure in the tunnel. Hence, for each pressure level, an average relative error is calculated, along with a standard deviation. The final transducer error is taken as the mean value of the individual relative errors. As for the mean standard deviation, knowing the data have been recorded on a time scale that is much larger than the inverse of the sampling rate, it represents the noise associated to each pressure instrument signal. The results are gathered in Table 4.5 and Table 4.6. They correspond to calculation made with the last calibration file, which was performed under conditions closer to the blow-down test conditions. We were able to detect a difference of 0.05% with the results obtained with the first calibration.

Another important source of error is linked to the effects of temperature on the transducer sensitivity. This phenomenon was thoroughly studied in [5]. Transducer sensitivities can vary from 1% to 2.5% over the compensated temperature range, which corresponds to 25°C to 80°C. It is therefore important to determine the temperature that the transducer "sees" during a test. The pressure sensors are mounted outside of the tunnel, so that their operating temperature is that of the room. Each transducer is submitted to the gas that has traveled along the 3"-long stainless steel tubes, which are initially at room temperature. The tubing hence modifies the gas temperature. In addition, heat must diffuse through the gas present in the tubes once their initial filling is complete. The time required for this transfer is on the order of the diffusive time scale L^2/α, where L is equal to 3" and α is the gas diffusivity, equal to $18.8\text{x}10^{-6}\ m^2/s$. This yields a characteristic time of 5 minutes, which is very large compared to the test duration. Alternatively heat can be conducted along the tube length. In that case, the characteristic time-scale for this process is 27 minutes. All this shows that the transducer temperature remains unchanged during the blow-down test and that the effects of temperature on the transducer output are negligible in this application. More information can be found in [5].

Upstream Total Pressure Total Error						
Run ID	**gamma**	**Mach #**	**Head Loss**	**Transducer**	**Noise**	**Total**
005	1,429	0,441	0,17%	0,12%	0,18%	0,28%
006	1,430	0,439	0,17%	0,12%	0,18%	0,28%
007	1,430	0,429	0,16%	0,12%	0,18%	0,27%
008	1,431	0,451	0,18%	0,12%	0,18%	0,28%
009	1,432	0,519	0,24%	0,12%	0,18%	0,33%
010	1,431	0,521	0,24%	0,12%	0,18%	0,33%
011	1,431	0,485	0,21%	0,12%	0,18%	0,30%
013	1,433	0,570	0,30%	0,12%	0,18%	0,37%
014	1,434	0,593	0,32%	0,12%	0,18%	0,39%

Table 4.2 – Upstream Total Pressure Uncertainty.

Downstream Total Pressure Total Error						
Run ID	**gamma**	**Mach #**	**Head Loss**	**Transducer**	**Noise**	**Total**
005	1,399	0,535	0,26%	0,19%	0,27%	0,42%
006	1,397	0,492	0,21%	0,19%	0,27%	0,39%
007	1,394	0,425	0,15%	0,19%	0,27%	0,36%
008	1,391	0,424	0,15%	0,19%	0,27%	0,36%
009	1,385	0,432	0,16%	0,19%	0,27%	0,37%
010	1,385	0,436	0,16%	0,19%	0,27%	0,37%
011	1,384	0,433	0,16%	0,19%	0,27%	0,37%
013	1,385	0,456	0,18%	0,19%	0,27%	0,38%
014	1,387	0,478	0,20%	0,19%	0,27%	0,38%

Table 4.3 – Downstream Total Pressure Uncertainty.

Total Upstream Static Pressure Error						
Run ID	**gamma**	**Mach #**	**Head Loss**	**Transducer**	**Noise**	**Total**
005	1.429	0.441	0.14%	0.13%	0.21%	0.29%
006	1.430	0.439	0.14%	0.13%	0.21%	0.28%
007	1.430	0.429	0.13%	0.13%	0.21%	0.28%
008	1.431	0.451	0.15%	0.13%	0.21%	0.29%
009	1.432	0.519	0.19%	0.13%	0.21%	0.32%
010	1.431	0.521	0.19%	0.13%	0.21%	0.32%
011	1.431	0.485	0.17%	0.13%	0.21%	0.30%
013	1.433	0.570	0.23%	0.13%	0.21%	0.34%
014	1.434	0.593	0.25%	0.13%	0.21%	0.35%

Table 4.4 – Total Upstream Static Pressure Error.

Upstream Transducer Uncertainties		
Name	**Transducer**	**Noise**
PT0A	0,12%	0,77%
PT1A	0,10%	0,35%
PDMP	0,50%	0,10%
PT2ZR01	0,12%	0,14%
PT2ZR02	0,16%	0,17%
PPT2C	0,15%	0,20%
PT2ZR04	0,09%	0,17%
PT2ZR05	0,11%	0,15%
PPS2C	0,12%	0,24%
PT2ZR07	0,12%	0,24%
PT2ZR08	0,14%	0,15%
PT2A	0,27%	0,19%
PS2A	0,10%	0,30%
PPT2A	0,14%	0,33%
PPS2A	0,16%	0,28%
PT2B	0,12%	0,13%
PS2B	0,12%	0,33%
PT2C	0,10%	0,15%
PS2C	0,11%	0,11%
PW1	0,09%	0,14%
PPT2B	0,09%	0,15%
PPS2B	0,09%	0,16%
Average	**0,14%**	**0,22%**

Table 4.5 – Upstream Transducer Uncertainty.

Downstream Transducer Uncertainties		
Name	**Transducer**	**Noise**
PT5A	0,05%	0,91%
PPT5A	0,06%	0,16%
PPS5A	0,02%	0,16%
PT5ZR01	0,06%	0,20%
PT5ZR02	0,02%	0,31%
PT5ZR03	0,03%	0,23%
PT5ZR04	0,08%	0,32%
PT5ZR05	0,06%	0,37%
PT5CR01	0,16%	0,19%
PT5CR02	0,13%	0,18%
PT5CR03	1,11%	0,49%
PT5CR04	0,18%	0,14%
PT5CR05	0,10%	0,24%
PS3HS	0,13%	0,47%
PS5AHS	0,09%	0,14%
Average	**0,15%**	**0,30%**

Table 4.6 – Downstream Transducer Uncertainty.

5. Aerodynamic Performance Measurement

5.1. Introduction

The two previous chapters discussed the uncertainties related to the instruments used in the tunnel. The purpose of the experiment is to determine the aerodynamic efficiency of the compressor. The most accurate way to compute the efficiency of the compressor is to resort to NIST tabulated values of the thermodynamic properties of the gas mixture used in the tunnel. The facility runs in non-adiabatic conditions, the specific heat ratio changes across the compressor and the mass-flow is not constant because of the aspiration process on rotor 2. Consequently, we cannot rely on the traditional equations to compute the efficiency. Here is how the process followed in this case unfolds:

- A gas table is created out of the NIST tables for the gas mixture used.
- The raw voltage data are converted to engineering units, using the AutoCal.m program for the pressure transducers and the individual Matlab calibration files for the thermocouples. This data is than processed through a first order low-pass filter with a lowpass frequency of 12 Hz, to eliminate the noise.
- The total upstream rake pressures and temperatures are area-averaged. The gas tables allow determination of the corresponding total upstream enthalpy.

- The static temperature is computed using the total temperature and pressure as well as the measured static pressure in the gas table on a constant entropy line.
- The inlet velocity of the fluid is then derived from the difference between the total and the static enthalpy of the incoming gas. The gas tables help determine the gas density and the sound velocity for these parameters. An inlet Mach number is derived accordingly.
- The downstream total pressure, along with the upstream total parameters help compute what the isentropic total downstream temperature would be. This allows to determine the downstream total isentropic enthalpy.
- The efficiency is then computed:

$$\eta = \frac{h_{0-Dn-Isen} - h_{0-Up}}{h_{0-Dn-ind} - h_{0-Up}}$$

where $h_{0-Dn-Isen}$ is the downstream total isentropic enthalpy of the gas, h_{0-Up} is the upstream total enthalpy and $h_{0-Dn-ind}$ is the indicated downstream total enthalpy. Further information can be obtained in [2].

We now want to estimate the uncertainty in the measurement of the efficiency. Two ways are possible to reach this goal. The first way consists in perturbing the inputs to the efficiency calculation program described previously by the amount of error computed for each type of instruments. These perturbations can be added or subtracted to the recorded signals. Several combinations are hence possible. The uncertainty will than be given by the difference between the efficiency computed without any perturbations and the one computed with perturbations yielding the largest difference. A second way to calculate the impact instrument errors have on the efficiency uncertainty is to reinforce the assumptions about the thermodynamic process the gas is undergoing in the tunnel so as to be able to derive an analytical equation of the uncertainty. In this respect, we have to assume that the compressor is working adiabatically, that the gas mixture is ideal, that the mass-flow through the compressor is constant (no aspiration) and that the specific heat ratio remains unchanged in the compression. Under these circumstances, we can derive a first order approximation of the uncertainty associated to the efficiency calculation.

Recording data in discrete and limited locations in the tunnel triggers further uncertainty. We will address this question, along with the issues set by the time sampling of the parameters.

Finally in this chapter, we will explain the difference between the measured efficiency and the adiabatic efficiency and assess the amplitude of correction needed to be provided to obtain an equivalent adiabatic efficiency from our measurements.

5.2. Uncertainty of Adiabatic Efficiency Measurement

5.2.1. Uncertainty due to Instrumentation Imperfections

The first method was applied for the results of run 010. The maximum difference between a perturbed signal efficiency calculation and the direct calculation amounts to 0.131 points of efficiency.

The analytical method requires starting from the definition of the adiabatic efficiency for a compressor operated with an ideal gas, for a constant mass flow and specific heat ratio. It is given by

$$\eta = \frac{\pi^{\frac{\gamma-1}{\gamma}} - 1}{\tau - 1} \tag{5.1}$$

The efficiency η is a function of the pressure ratio π, the temperature ratio τ and the specific heat ratio γ. Knowing that these parameters are independent from one another, the absolute error in efficiency as a function of the absolute uncertainty in pressure ratio, temperature ratio and specific heat ratio is given by the following equation [12]:

$$U_\eta^2 = \left(\frac{\partial \eta}{\partial \pi}\right)^2 U_\pi^2 + \left(\frac{\partial \eta}{\partial \tau}\right)^2 U_\tau^2 + \left(\frac{\partial \eta}{\partial \gamma}\right)^2 U_\gamma^2 \tag{5.2}$$

where U_X is the absolute uncertainty in X.

A more useful expression is that using the relative uncertainties in the pressure, temperature and specific heat ratios:

$$U_\eta^2 = \left(\pi \frac{\partial \eta}{\partial \pi}\right)^2 \left(\frac{U_\pi}{\pi}\right)^2 + \left(\tau \frac{\partial \eta}{\partial \tau}\right)^2 \left(\frac{U_\tau}{\tau}\right)^2 + \left(\gamma \frac{\partial \eta}{\partial \gamma}\right)^2 \left(\frac{U_\gamma}{\gamma}\right)^2 \tag{5.3}$$

From the definition of the pressure ratio and the temperature ratio, we can derive expressions of uncertainties of these parameters as a function of the relative uncertainties in upstream and downstream temperatures and pressures:

$$\left(\frac{U_\pi}{\pi}\right)^2 = \left(\frac{U_{Pup}}{Pup}\right)^2 + \left(\frac{U_{Pdn}}{Pdn}\right)^2 \tag{5.4}$$

$$\left(\frac{U_\tau}{\tau}\right)^2 = \left(\frac{U_{Tup}}{Tup}\right)^2 + \left(\frac{U_{Tdn}}{Tdn}\right)^2 \tag{5.5}$$

The uncertainty equation (5.2) shows that each error is multiplied by a coefficient obtained from the differentiation, which defines the impact a variation in one parameter will have over the sought uncertainty. From equations (5.4) and (5.5), we can see that the upstream and downstream parameters are multiplied by the same magnification factors. These are:

$$\frac{\partial \eta}{\partial \pi} = \frac{\gamma - 1}{\gamma(\tau - 1)} \cdot \pi^{\frac{-1}{\gamma}} \tag{5.6}$$

$$\frac{\partial \eta}{\partial \tau} = \frac{1 - \pi^{\frac{\gamma-1}{\gamma}}}{(\tau - 1)^2} \tag{5.7}$$

$$\frac{\partial \eta}{\partial \gamma} = \frac{\pi^{\frac{\gamma-1}{\gamma}} \ln(\pi)}{\gamma^2(\tau - 1)} \tag{5.8}$$

Using the results from each of the runs, we are able to compute the first order uncertainty for each efficiency measurement. The results are presented in Table 5.2 and Table 5.3. We can notice that the magnification coefficient for the temperature is three times larger than that of the pressure and that the influence of the specific heat ratio is not to be minimized. The relative uncertainty of the specific heat ratio is approximated to the first order by the error in gas mixture computed for each run.

Using these equations and the results from the error analysis from the previous chapters, we can compute a first order approximation of the adiabatic efficiency

uncertainty. The error is systematically smaller than one point of efficiency for each of the runs performed.

The first method yields much better results than the analytical method. For run 010, the second method gives an uncertainty of 0.660 points of efficiency compared to 0.131 points for the empirical method, which corresponds to an approximate ratio of 5.

5.2.2. Uncertainty Due to Discrete Spatial Sampling

For practical reasons, the MIT Blow-Down compressor facility allows only a discrete spatial data sampling. As was explained in section 2.4.1, single instrumentation probes are scattered circumferentially in three equally spaced sectors. Similarly, the pressure and temperature rakes only allow a discrete sampling of the radial distribution of the aerodynamic parameters of the flow. Assessing the amount of uncertainty linked to these aspects appears as an issue of interest.

In terms of radial distribution, the dimensions of the pressure impact heads and total temperature heads did not allow to adequately sample data in the end wall boundary layer. To assess a level of uncertainty in that respect, calculations were made using the 100% - 100% CFD simulation results. The radial area averaged values of the compressor's pressure and temperature ratios and efficiency were computed in two different ways based on the same set of CFD calculations. The first way consisted in using the complete spanwise set of data. The second consisted in only using the values corresponding to the same span locations as the actual probes on the rakes. These values were scaled by the adequate surface area associated with their location. The results of these calculations are presented in Table 5.1. Under sampling of the end wall conditions seems to have a significant impact on the efficiency calculation.

	Complete sampling	Actual Sampling	Uncertainty
Pressure Ratio	2.97	3.00	0.96
Temperature Ratio	1.43	1.42	0.25
Efficiency	86.07%	87.55%	1.73

Table 5.1 – Radial Sampling Uncertainty.

Circumferentially, the total and static pressure measurements have recorded a pressure distortion in the inlet plane of the compressor. A thorough examination of the pressure screen has proved that the screen hole pattern is not uniform, which would tend to explain this phenomenon. More explanations are given in [2]. Assuming the total pressure in front of the screen is uniform, these hole measurements permit a determination of a total pressure value in each 20° section of the inlet area. Run measurements showed that distortions were only limited to pressure and did not involve temperature. An uncertainty is directly related to this pressure distribution. To assess the impact on the overall compressor measurements, the concept of parallel compressors is used. Each section sees the same compressor, with the same characteristic. Similarly, each outlet section is associated to the inlet section with the same azimuthal position. But its corresponding corrected mass-flow differs from the average corrected mass-flow computed from the actual runs by a factor equal to the ratio of the average inlet total pressure to the total pressure in the section. Using the compressor map established from the full speed runs 010, 011, 013 and 014, we are able to establish a pressure and a temperature ratio for each section and to compute the corresponding outlet values. These calculations permit one see the circumferential entropy structure of the flow, both upstream and downstream of the compressor. The relative entropy variation is plotted in Figure 5.1.

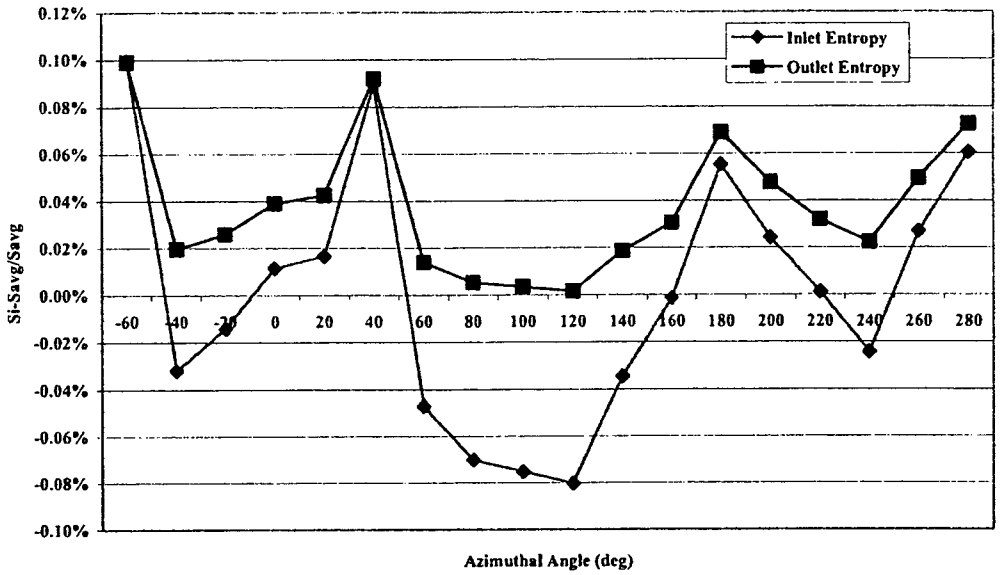


Figure 5.1 – Inlet and Outlet Relative Entropy Variations.

The compressor seems to have increased the average relative entropy variation from section to section from 0.0003% to 0.0381%, but reduced the corresponding standard deviation. The concept of parallel compressors is responsible for the similar shapes of the variation curves upstream and downstream of the compressor. The maximum variation points are located in the sections where the inlet total pressure is smaller than the average pressure, which is caused by a smaller number of holes in these locations.

Beyond this first calculation, an area averaged value of the total temperature and pressure can be computed for each section, upstream and downstream of the compressor. These values can be compared to the temperature and pressure values used in the effective calculation of the efficiency, which yields the relative circumferential uncertainty in pressure and temperature. Using the same uncertainty measurement technique as in section 5.2.2, the spatial efficiency uncertainty can be estimated. Calculations showed an absolute uncertainty of 0.95%. These changes are first order estimations of how the compressor reacts to variations in corrected mass-flow. We should

underscore the fact that the compressor map used to compute the downstream parameters comes from a manual extrapolation of test runs.

5.2.3. Uncertainty Due To Time Sampling

As pointed out in section 4.5, noise coming from the electrical environment is part of the signals recorded of the various instrument channels. This noise can account for a relative error of 0.2% to 0.30% on the pressure probes for instance. To adequately remove the perturbation linked to this phenomenon, a low pass filter is used in the data processing. To implement this filter in the case of a discrete set of data, a running average method is used. It is very important that the filter does not entail any phase distortion in the signal. The filter used first processes in the forward direction, then reverses the filtered sequence and runs it back in the filter. Although the cutting frequency was originally set at 60 Hz, it proved to be around 12 Hz, attenuating all signals with a higher frequency at the rate of 20 dB/decade. This technique does not add any uncertainty to the measurements.

5.3. Non-Adiabatic Effects in a Blow-Down Test Environment

In a steady state test rig, a compressor operates virtually adiabatically – there is very little heat transfer between the working gas and the walls. This is why the efficiency of a compressor is always referred to as the adiabatic efficiency. In a short-duration test facility, the tunnel will stay at near room temperature, the characteristic test time scale remains very short compared to the time needed for the tunnel to reach the fluid temperature. Calculations show that in a short-duration test facility, the walls are isothermal but the blades see a small variation in temperature. Hence, a certain amount of heat is transferred from the test gas to the walls of the facility as well as the compressor blades and hub casing.

In this chapter, we will first focus on the implications this phenomenon has on the compression process. We will then discuss how to correct the measured efficiency to estimate the equivalent adiabatic efficiency.

5.3.1. Difference Between Blow-Down Efficiency and Adiabatic Efficiency

The difference between an adiabatic compression and the compression in a blow-down environment is illustrated in Figure 5.2. All state parameters are stagnation quantities. Subscript "1" represents the compressor inlet conditions and subscript "2" the outlet conditions. Three compression processes are plotted on the figure. They represent three thermodynamic paths to raise the gas pressure from P_{01} to P_{02}.

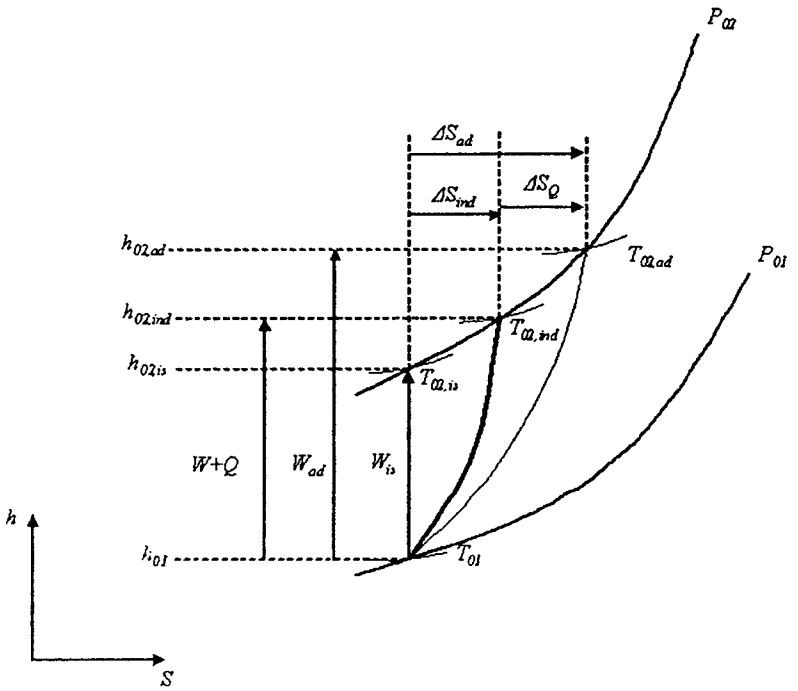


Figure 5.2 – Enthalpy – Entropy Diagram for the Compression Processes in Compressors.

For an ideal compression, the entropy rise across the compressor is equal to zero. The exit enthalpy $h_{02,is}$ can be computed from the isentropic relations for an ideal gas with constant specific heat ratio γ.

$$\frac{T_{02,is}}{T_{01}} = \left(\frac{P_{02}}{P_{01}}\right)^{\frac{\gamma-1}{\gamma}} \tag{5.9}$$

The ideal work corresponds to the case where the compressor would work without any loss.

$$W_{is} = h_{02,is} - h_{01} \tag{5.10}$$

Real compressors operate with losses. The actual compression work to achieve the same pressure ratio is hence larger. Under adiabatic conditions, we define the adiabatic work W_{ad} as the difference between the adiabatic exit enthalpy $h_{02,ad}$ (actually measured in steady state test rigs), for state conditions P_{02} and $T_{02,ad}$, and the inlet total enthalpy h_{01}:

$$W_{ad} = h_{02,ad} - h_{01} \tag{5.11}$$

Consequently, the adiabatic efficiency yields as the ratio of these two thermodynamic transformations:

$$\eta_{ad} = \frac{h_{02,is} - h_{01}}{h_{02,ad} - h_{01}} \tag{5.12}$$

As explained above, the blow-down compressor does not allow the measurement of an adiabatic compression. It only yields indicated values. The exit temperature is an indicated value $T_{02,ind}$ which corresponds to an indicated exit total enthalpy $h_{02,ind}$. The enthalpy rise in the flow stems hence from two exchange sources: work W and the wall heat transfer Q.

$$h_{02,ind} - h_{01} = W + Q \tag{5.13}$$

We can define the corresponding indicated efficiency that comes out of the post processing of the data recorded during the tests:

$$\eta_{ind} = \frac{h_{02,is} - h_{01}}{h_{02,ind} - h_{01}} \tag{5.14}$$

We can easily derive a relation between the indicated and the adiabatic efficiencies:

$$\frac{1}{\eta_{ind}} = \frac{h_{02,ind} - h_{01}}{h_{02,is} - h_{01}} = \frac{h_{02,ad} - h_{01}}{h_{02,is} - h_{01}} + \frac{h_{02,ind} - h_{02,ad}}{h_{02,is} - h_{01}} \tag{5.15}$$

$$\frac{1}{\eta_{ind}} = \frac{1}{\eta_{ad}} + \frac{h_{02,ind} - h_{02,ad}}{h_{02,is} - h_{01}} \tag{5.16}$$

Assessing the correction to provide to the indicated efficiency comes down to estimating the adiabatic exit total enthalpy.

5.3.2. Correction to provide to Measured Efficiency

Equation (5.16) shows that it is necessary to estimate the exit adiabatic total temperature to assess the correction to provide. According to Figure 5.2, the loss difference in enthalpy rise is due to the heat exchange between the flow and the facility walls. The problem comes down to estimating this exchange as well as its impact on the efficiency. To do so, we first estimate the heat exchange between the fluid and the walls using a one-dimensional compressible flow analysis. The surface heat transfer coefficient is computed from an estimation of the Stanton number. The lump capacity model is used to calculate the heat transfer with the blades while the semi-infinite body model is used for the transfers with the compressor's tip and hub casings. More details are given in Appendix A. Second, we derive an equation linked to the properties of entropy. Entropy is a thermodynamic state quantity. It hence only depends on the initial and final state conditions of the fluid. Therefore, the entropy generated in an adiabatic compressor can be viewed as the sum of two parts: the entropy generated in a blow-down facility and the entropy change due to the heat transfer:

$$\Delta S_{ad} = \Delta S_{ind} + \Delta S_{Q} \tag{5.17}$$

where ΔS_Q for a reversible heat transfer can be quantified as

$$\Delta S_{Q} = \int_{1}^{2} \left(\frac{\delta Q}{T} \right)_{rev} = \frac{Q}{T^*} \tag{5.18}$$

The temperature T^* is the equivalent temperature at which the heat transfer takes place in the compressor.

For an ideal gas, the entropy change can be written as

$$\Delta S = S_2 - S_1 = C_p \cdot \ln\left(\frac{T_{02}}{T_{01}} \right) - R \cdot \ln\left(\frac{P_{02}}{P_{01}} \right) \tag{5.19}$$

This expression can be modified in the following form:

$$\frac{P_{02}}{P_{01}} = \left[\frac{T_{02}}{T_{01}} \cdot \exp\left(-\frac{\Delta S}{C_p}\right)\right]^{\frac{\gamma}{\gamma-1}} \tag{5.20}$$

The two thermodynamic paths of interest correspond to the same pressure ratio. So, using equation (5.20), we can assert that:

$$\frac{T_{02,ad}}{T_{01}} \cdot \exp\left(-\frac{\Delta S_{ad}}{C_p}\right) = \frac{T_{02,ad}}{T_{01}} \cdot \exp\left(-\frac{\Delta S_{ind} + \Delta S_Q}{C_p}\right) = \frac{T_{02,ind}}{T_{01}} \cdot \exp\left(-\frac{\Delta S_{ind}}{C_p}\right) \tag{5.21}$$

This equation unveils the following relation:

$$T_{02,ad} = T_{02,ind} \cdot \exp\left(\frac{\Delta S_Q}{C_p}\right) \tag{5.22}$$

We presume that the difference in entropy due to heat exchange is very limited in amplitude. We thus decide to apply a first order Taylor series around zero to get an simpler expression.

$$T_{02,ad} = T_{02,ind} \cdot \left(1 + \frac{\Delta S_Q}{C_p}\right) \tag{5.23}$$

or

$$T_{02,ad} = T_{02,ind} \cdot \left(1 + \frac{Q}{C_p T^*}\right) \tag{5.24}$$

Hence, the sought difference between the exit adiabatic total enthalpy and the indicated value can be approximated as follows:

$$h_{02,ad} - h_{02,ind} = Q\frac{T_{02,ind}}{T^*} \tag{5.25}$$

and finally:

$$\frac{1}{\eta_{ind}} = \frac{1}{\eta_{ad}} - \frac{Q}{h_{02,is} - h_{01}}\frac{T_{02,ind}}{T^*} \tag{5.26}$$

This equation shows the impact the heat transfer has on the correction to be provided to the indicated efficiency. The difference between the inverse of both the indicated and the adiabatic efficiencies is proportional to the heat transfer, scaled by a

temperature ratio that needs to be further assessed. The temperature T^* defined in equation (5.18) is the equivalent temperature at which the heat transfer would occur in the compressor. In reality, this heat transfer takes place at the various locations that are at different temperatures. The upper bound is the indicated exit temperature and the lower bound is the inlet temperature. A larger and hence more reliable correction is obtained with the latter bound. The scaling coefficient is than equal to the temperature ratio across the compressor. A model based on the blow-down time constant yields a difference between the indicated and the adiabatic efficiencies of about 0.1% for an indicated value of 87%, which corresponds to the value obtained at a 100% speed (Figure 5. 3). The correction is hence very small.

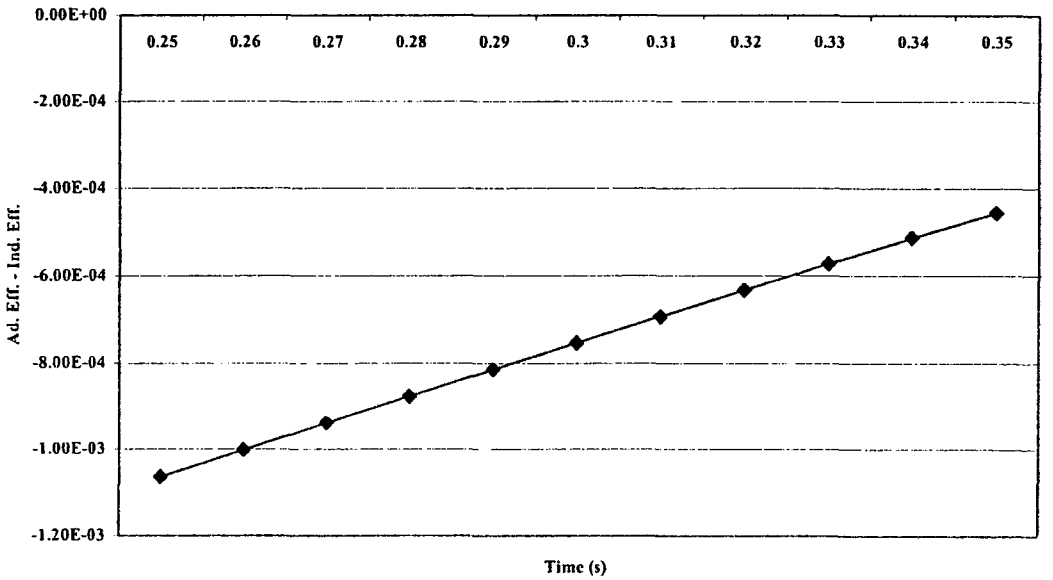


Figure 5. 3 – Difference Between Adiabatic and Indicated Efficiency Over the Test Time.

				Abs Tt Uncertianty		Relative Uncertainty				
Run ID	Avg PR	Avg TR	Meas. Eff	Up (K)	Dn	Up Pt	Dn Pt	Up Tt	Dn Tt	gamma
005	1.983	1.266	0.792	0.142	0.327	0.31%	0.42%	0.05%	0.10%	0.15%
006	2.103	1.287	0.811	0.142	0.327	0.31%	0.39%	0.05%	0.09%	0.16%
007	2.303	1.315	0.842	0.142	0.327	0.31%	0.36%	0.05%	0.09%	0.23%
008	2.468	1.351	0.840	0.142	0.327	0.32%	0.36%	0.05%	0.09%	0.29%
009	2.973	1.415	0.868	0.142	0.327	0.36%	0.37%	0.05%	0.09%	0.03%
010	2.915	1.406	0.873	0.142	0.327	0.36%	0.37%	0.05%	0.09%	0.15%
011	2.899	1.422	0.836	0.142	0.327	0.34%	0.37%	0.05%	0.09%	0.01%
013	2.910	1.398	0.888	0.142	0.327	0.40%	0.38%	0.05%	0.09%	0.05%
014	2.836	1.382	0.885	0.142	0.327	0.42%	0.38%	0.05%	0.09%	0.10%

Table 5.2. – Absolute and Relative Uncertainties in Total Temperature and Pressure Measurements for Runs 005 to 014.

	Error Coefficients			Uncertainty Per Measurement					
Run ID	Eff*UMF P	Eff*UMF T	Eff*UMF Gamma	Up Pt	Dn Pt	Up Tt	Dn Tt	gamma	Efficency Uncertainty
005	1.347	-3.142	2.225	0.42%	0.56%	-0.16%	-0.30%	0.34%	0.85%
006	1.267	-2.952	2.280	0.40%	0.50%	-0.16%	-0.28%	0.36%	0.80%
007	1.182	-2.780	2.393	0.36%	0.43%	-0.15%	-0.26%	0.55%	0.84%
008	1.080	-2.446	2.375	0.34%	0.39%	-0.13%	-0.22%	0.69%	0.90%
009	0.959	-2.159	2.558	0.34%	0.35%	-0.11%	-0.19%	0.07%	0.54%
010	0.973	-2.205	2.552	0.35%	0.36%	-0.12%	-0.19%	0.37%	0.66%
011	0.935	-2.032	2.442	0.31%	0.34%	-0.11%	-0.18%	0.03%	0.51%
013	0.995	-2.297	2.598	0.39%	0.37%	-0.12%	-0.20%	0.13%	0.61%
014	1.033	-2.433	2.622	0.43%	0.40%	-0.13%	-0.22%	0.25%	0.69%

Table 5.3. – Scaling Coefficients, Scaled Uncertainties in Temperature, Pressure and Specific Heat Ratio and Efficiency Uncertainty for Runs 005 to 014.

6. Experimental Results

6.1. Introduction

Fourteen runs of the blow-down counter-rotating aspirated compressor were performed, with rotor speeds of 90%-90%, 95%-95% and 100%-100%. This chapter presents the preliminary test runs performed to check the integrity of the compressor as well as the setting adjustments. Attention is then focused on the following runs, where the two rotor corrected speeds are matched. Finally, a tentative compressor map is presented.

6.2. Test Data

6.2.1. Preliminary Tests

Six preliminary tests were necessary to verify the operation of the compressor, ensuring its mechanical integrity and learning to match the two rotor corrected speeds. During the four first tests, the compressor's mechanical speed was set to have the rotors' corrected speeds reach 85% of their design values. Data showed that the facility behaved without any mechanical problems and that it was able to deliver a quasi-steady operating state between 200 ms and 600 ms after the firing of the fast acting valve. The entire set of instruments survived the physical constraints imposed by the dynamic pressure of the

flow as well as the facility vibrations. However, some additional setting adjustments appeared necessary. While rotor 1 behaved properly and as expected, rotor 2 corrected speed did not match rotor 1's. It actually reached values above 90% at the end of the quasi-steady state, as shown in Figure 6.1. This phenomenon revealed that rotor 2 was not putting out enough work, due to too low a back pressure. This parameter is set by a throttle located at the rear of the aft section, separating the compressor flow passage from the dump tank. Closing this throttle too much causes the rotor to stall. To avoid that, a safety margin on the calculation of the adequate opening of the throttle was implemented. Reducing progressively this margin allowed the two rotor corrected speeds to match. Meanwhile, the upstream instrumentation pointed out a pressure and a temperature distortion in the inlet plane of the compressor. Adding two electrical fans in the supply tank to improve the mixing of the argon with the carbon dioxide helped get rid of the temperature gradient in the inlet plane, while improving the filling time of the supply tank. As for the pressure distortion, it persisted both for the total and the static values. The source of this phenomenon was investigated and results showed that non-uniformity in the pressure screen hole pattern may account for these discrepancies. More information can be found in [2].

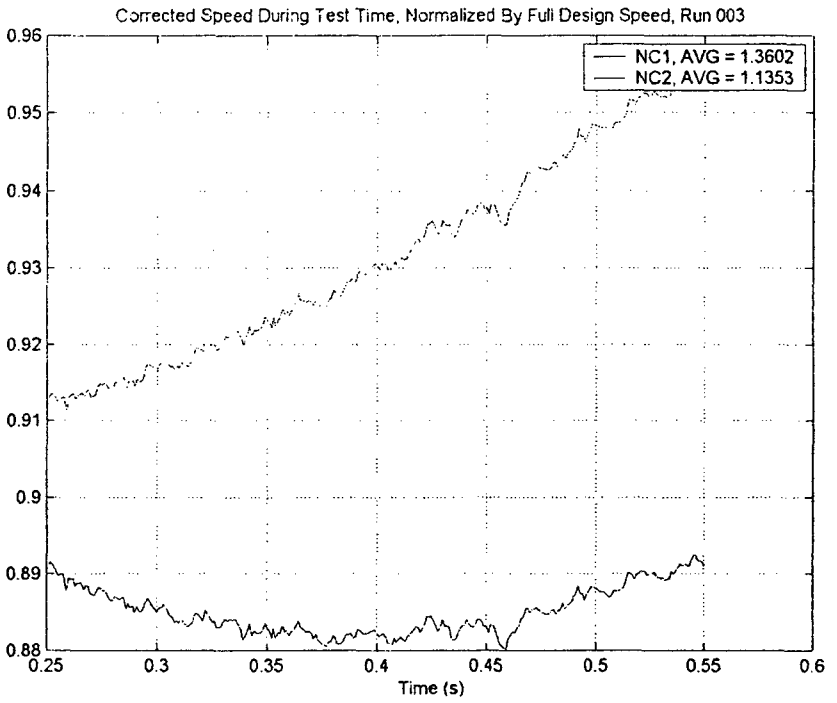


Figure 6.1 – Corrected Speeds During Test Time Normalized by Full Design Speed – Run 003.

6.2.2. Matched Corrected Speed Run Results

The two rotor corrected speeds were matched from run 007 to run 014. In this section, we will only comment on the results from run 010, which correspond to a 100% - 100% speed run.

The histories of the inlet and exit total temperatures are shown in Figure 6.2 and Figure 6.3. Three upstream and one downstream single total temperature probes placed at mid-span were used for this test along with the upstream and the two downstream rakes. A first remark is that all probes are able to observe the compressional heating mentioned in section 3.4.1. Figure 6.2 shows that between 220 ms and 500 ms, the temperature decreases almost linearly. This interval corresponds to the quasi-steady state of the compressor. To improve the study of the compressor and the better assess its performances, the time window considered for the post processing steps was limited to the interval between 250 ms and 350 ms. This corresponds to the early part of the quasi-

steady state period. Data proved to be more linear and undergoing less variation in that time window. Besides, the end of the quasi-steady state proved to be difficult to determine accurately from run to run. 350 ms turned out to be a safe value in that respect. The total temperature rakes give a radial profile of the temperature distribution upstream and downstream of the compressor (cf. Figure 6.4). The upstream rake tends to show a classic temperature pattern with higher temperatures near the end walls. The downstream rake showed however a more original distribution, with a quasi-linear spanwise growth in temperature. A drop was nonetheless recorded near the outer end-wall where heat exchanges are taking place.

The history of the area-averaged pressures in each section of the tunnel is pictured in Figure 6.5. In both the upstream and the downstream sections of the compressor, it takes 750 ms after the opening of the fast-acting valve for the pressures to become homogeneous inside each section. The front and the aft pressures then converge asymptotically. The upstream total and static pressure measurements show a persistent distortion in the inlet plane of the compressor on the order of 2% from window to window (Figure 6.6 and Figure 6.7). We remind the reader that the single pressure measurement probes are located in windows located 120° apart from one another. The upstream and downstream Pitot probe measurements are presented in Figure 6.8 and Figure 6.9. They allow a first order estimation of the flow Mach numbers. Their measurements are associated to the other total and static pressure measurements and used as input data to the NIST gas tables that yields the flow speeds, the sound velocities and hence the Mach number at the various stages of the machine for non-ideal gases. As for the upstream and downstream total pressure rakes, their measurements over the test-time are gathered in Figure 6.10 and Figure 6.11. The radial pressure patterns are presented in Figure 6.12. While the upstream rake is recording a uniform span distribution, the downstream rakes show a significant drop in the outer casing region. The rotors tip clearance could account for this fact.

The rake measurements can be converted into radial performance distribution, as plotted in Figure 6.13. The most striking aspect of this representation is the efficiency greater than 1 in the hub region of the compressor. Studies have shown that this

phenomenon is due to radial convection of losses around that region. This uncovers a limit to the assumption which associates the flow parameters of each downstream relative radial position to the flow parameters for the same upstream relative radial position.

A high speed static pressure probe was placed behind each rotor to better observe any stall of the compressor. A Fourier analysis permitted determination of the frequencies content. Theoretically, when rotor 2 is not stalled, its high static signal should mostly consist of rotor 2 and rotor 1 blade passage frequencies as well as a coupling phenomenon between the two rotors. Once other frequencies start growing in amplitude, the rotor is considered stalled. However, the limit between the two states for rotor 2 did not prove to be very obvious. Some stall is feared to have taken place during the time window of interest for runs 007 to 009. The pressure in the supply tank was lowered to overcome this issue.

The Mach numbers are plotted in Figure 6.16. The downstream value turned out to remain constant over the period of interest, but a significant decrease affected the upstream value.

Figure 6.17 show the rotor's normalized corrected speeds. Between 250 ms and 350 ms, the two speeds matched to less the 0.1% of the design speed. Such an achievement is made possible by an appropriate setting of the back pressure via the throttle opening and the matching of the inertias of the two rotors to the work ratio across the compressor. The curved shape of the speed variations during the quasi-steady state time recall the second order polynomial predicted by the programs used to scale the tunnel. Positioning the minimum value of the corrected speed in the appropriate time window is depending on the supply tank pressure.

The compressor performances are summarized in Figure 6.19 and Figure 6.20, which display very promising results. A pressure ratio of 2.95 and a temperature ratio of 1.41 for an efficiency of 0.886 were recorded on average between 250 ms and 350 ms. For the full design speed runs, the CFD simulated a pressure ratio of 3.06 and a temperature ratio of 1.43 for an efficiency of 87% (table 2.2).

The initial operating conditions, as well as the performance results at 250 ms for each run are summarized in Table 6.1.

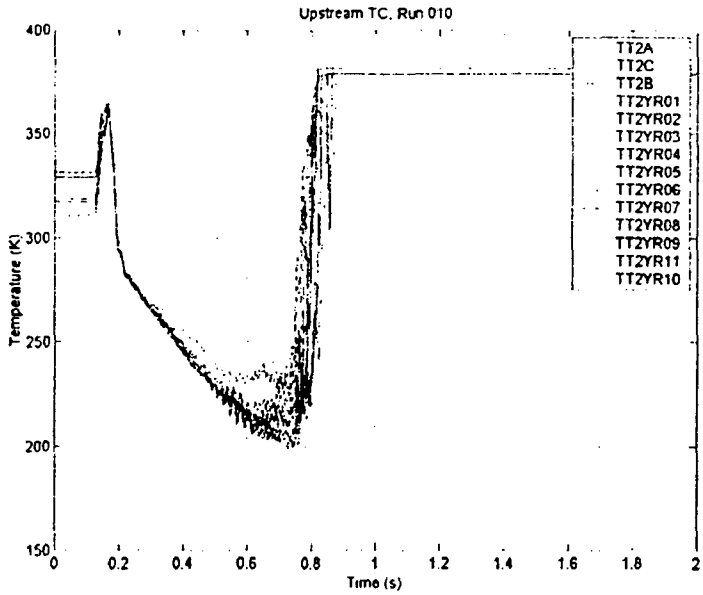


Figure 6.2 – Upstream Total Temperatures of Run 010.

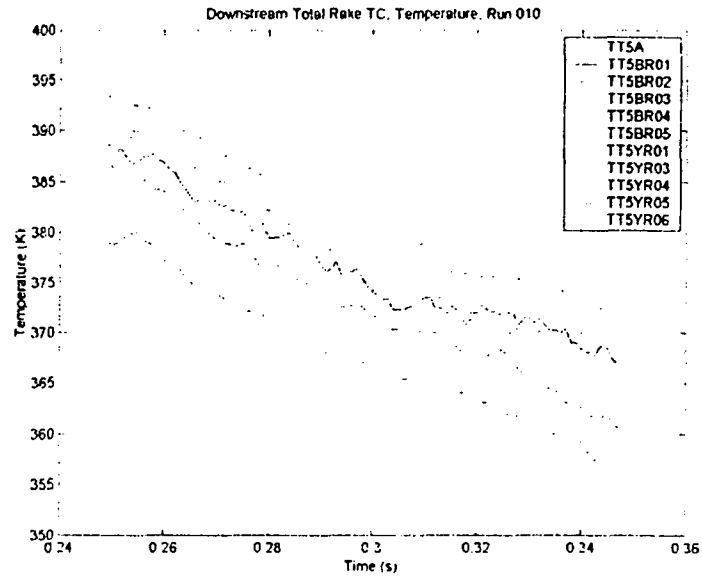


Figure 6.3 – Downstream Total Temperatures of Run 010.

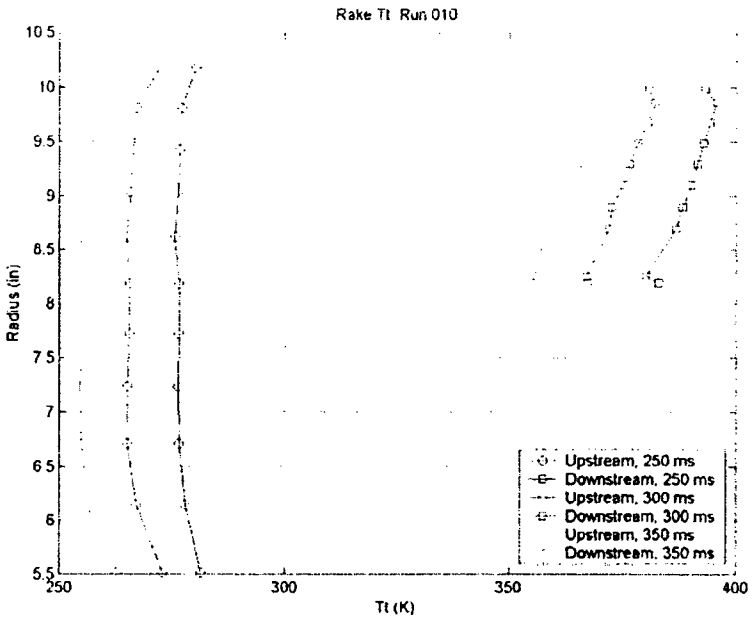


Figure 6.4 – Upstream and Downstream Radial Total Temperature Distribution at 250 ms, 300 ms and 350 ms for Run 010.

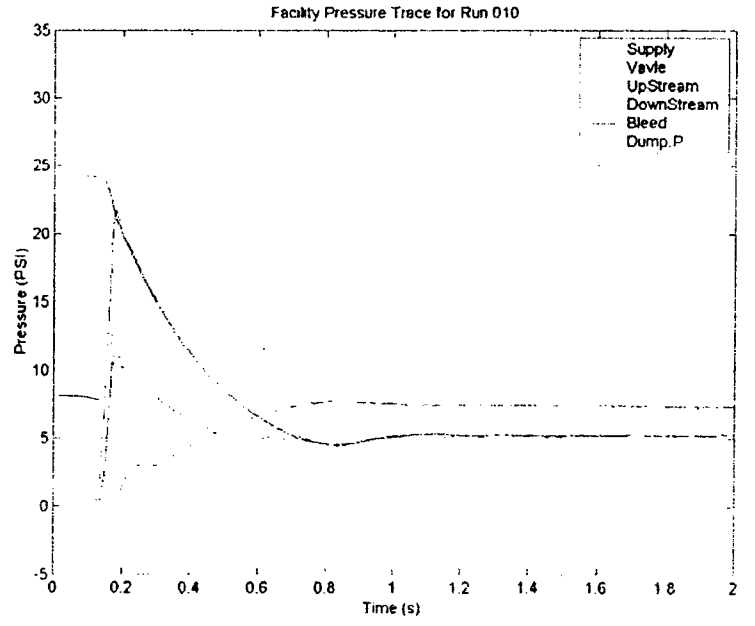


Figure 6.5 – Area-Averaged Pressure History in the Supply Tank, the Valve, Upstream and Downstream of the Compressor, in the Bleed Flow and in the Dump Tank for Run 010.

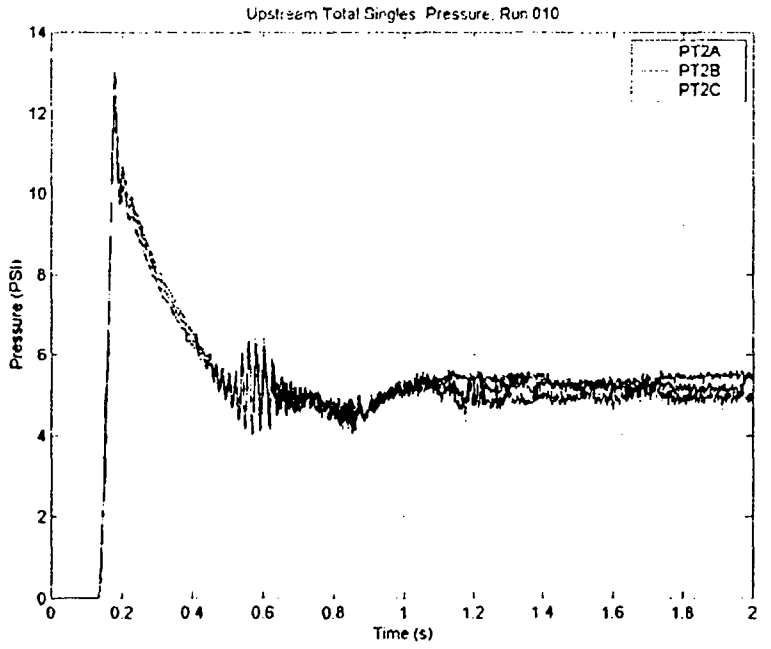


Figure 6.6 – Upstream Total Pressure at Three Midspan Locations for Run 010.

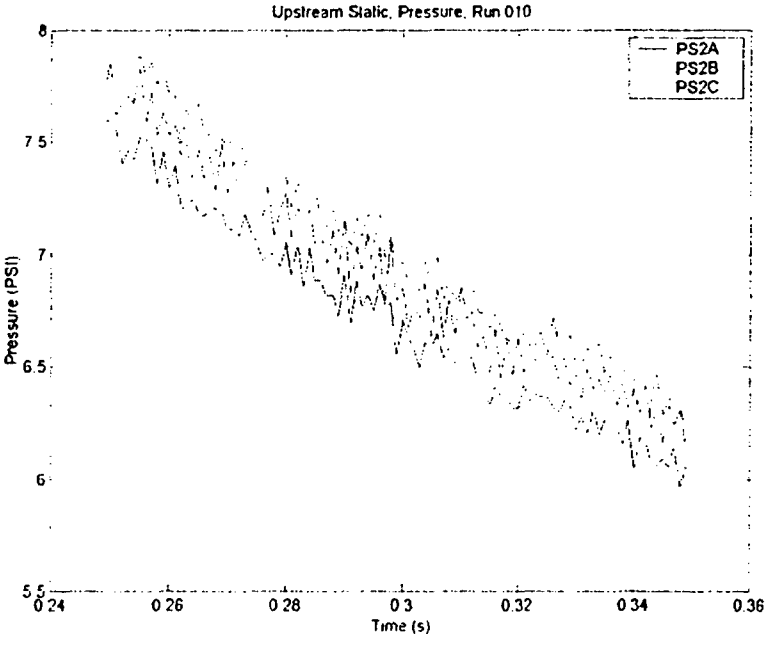


Figure 6.7 – Upstream Static Pressure Distribution for Run 010.

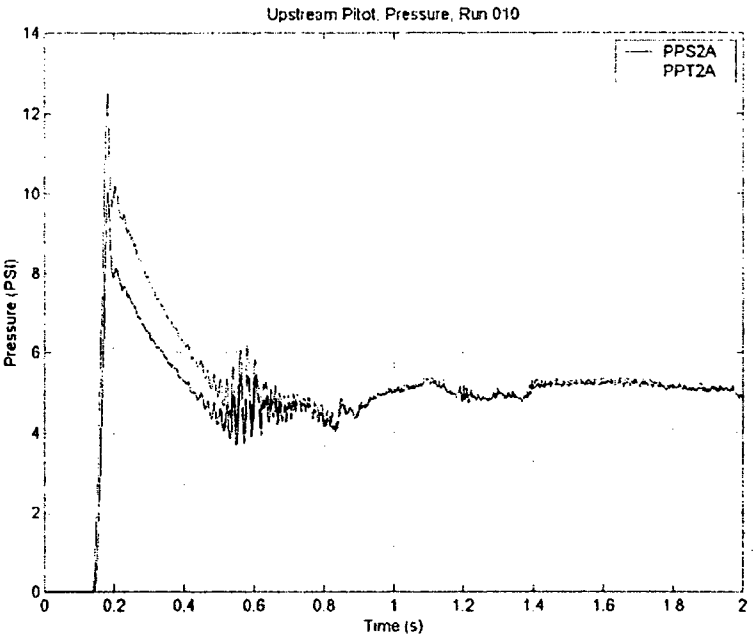


Figure 6.8 – Upstream Pitot Total and Static Pressures for Run 010.

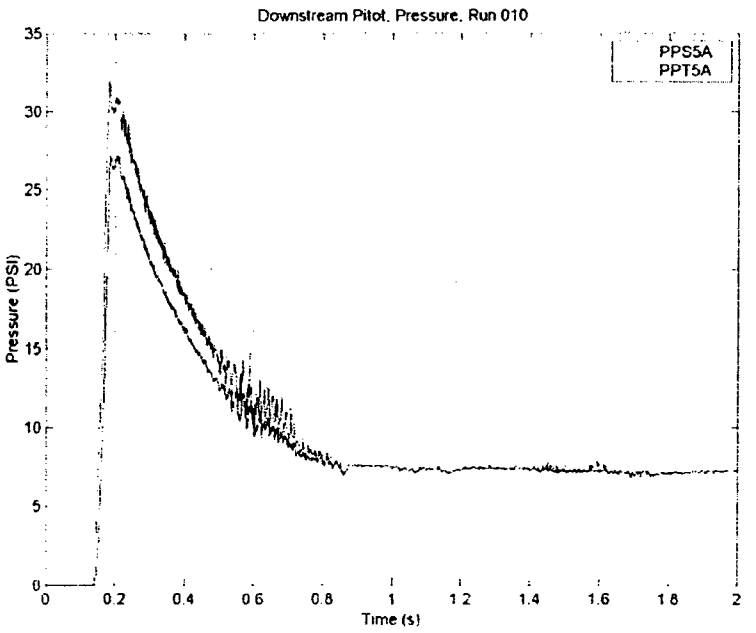


Figure 6.9 – Downstream Pitot Total and Static Pressures for Run 010.

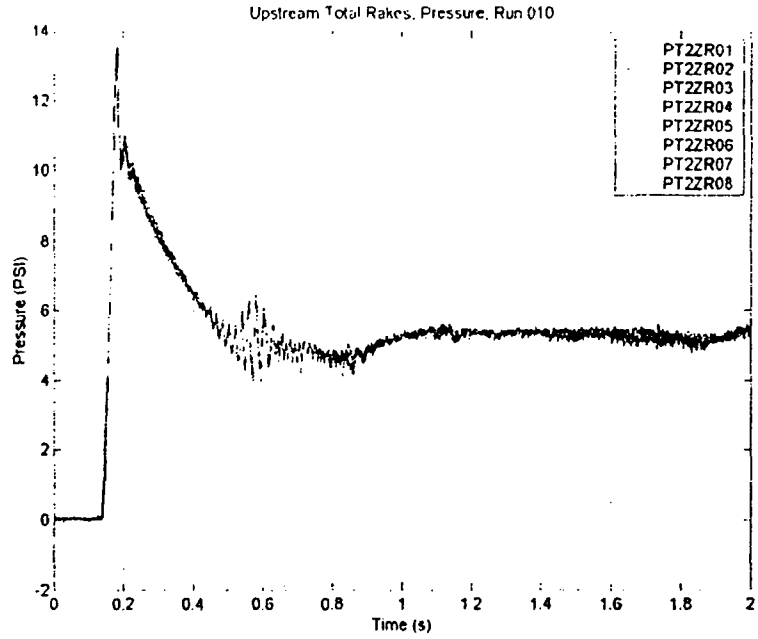


Figure 6.10 – Upstream Total Pressure Rake Measurements for Run 010.

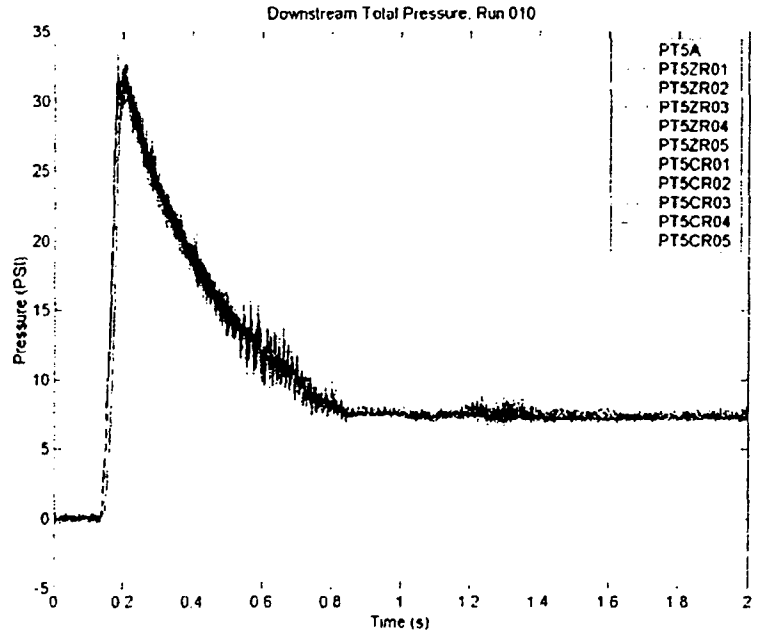


Figure 6.11 – Downstream Total Pressure Rake Measurements for Run 010.

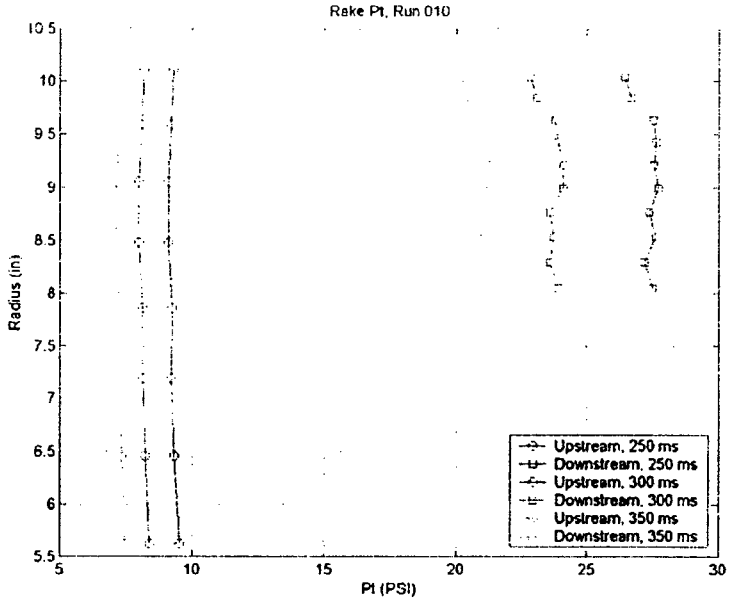


Figure 6.12 - Upstream and Downstream Radial Total Pressure Distribution at 250 ms, 300 ms and 350 ms for Run 010.

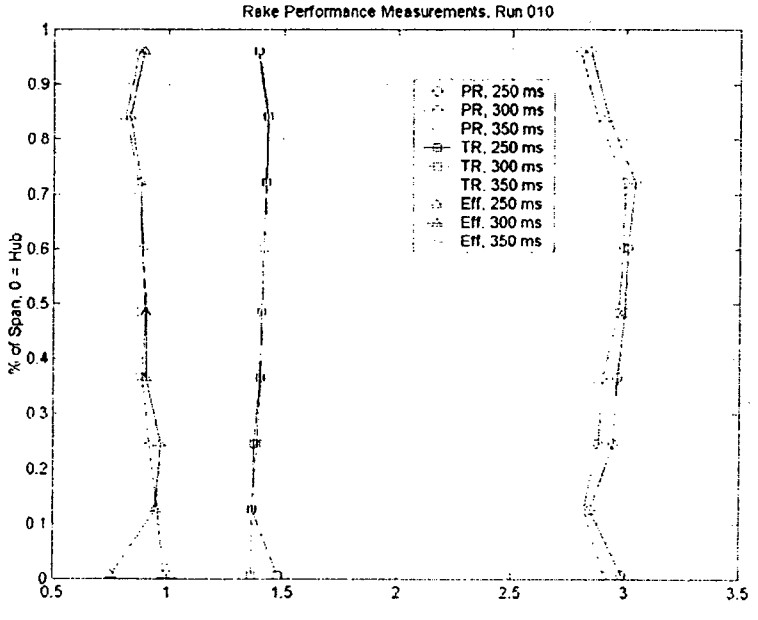


Figure 6.13 – Pressure Ratio, Temperature Ratio and Efficiency Radial Distributions at 250 ms, 300 ms and 350 ms for Run 010.

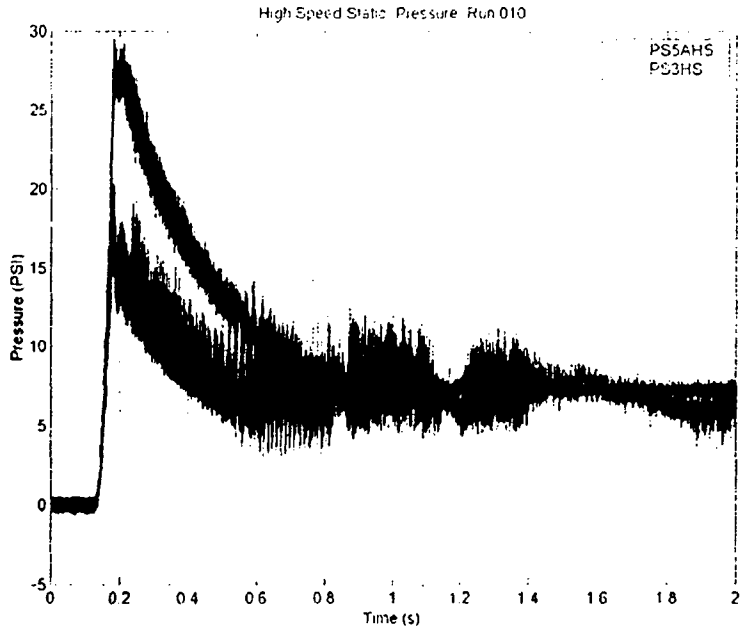


Figure 6.14 – High Speed Static Pressures Behind Rotor 1 (Blue) and Rotor 2 (Green) for Run 010.

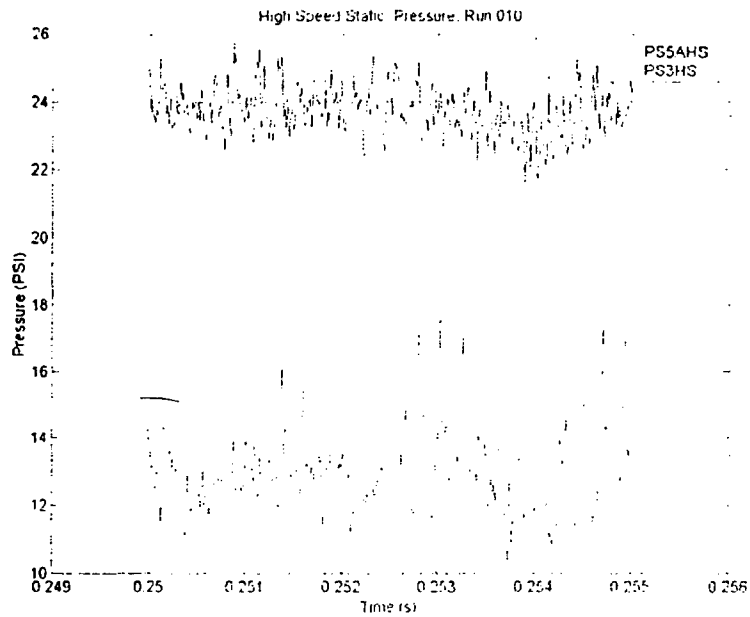


Figure 6.15 - High Speed Static Pressures Behind Rotor 1 (Blue) and Rotor 2 (Green) for Run 010 between 250 ms and 255 ms.

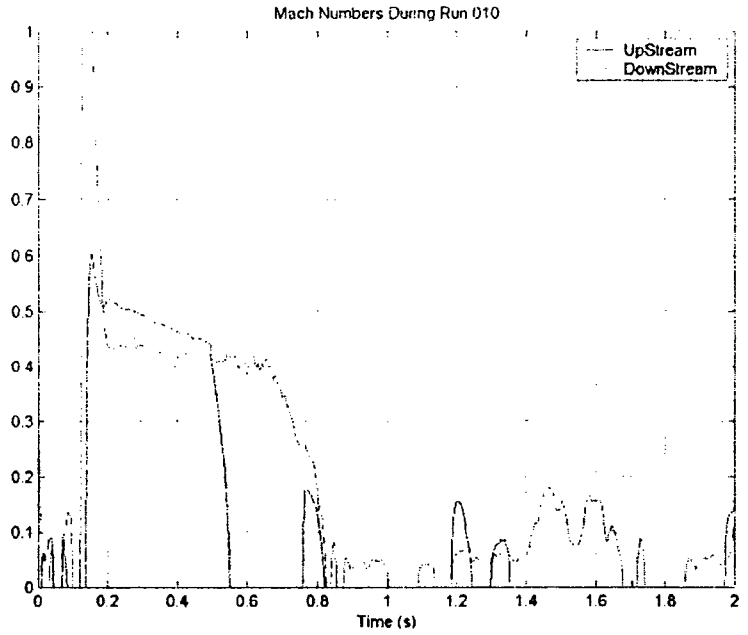


Figure 6.16 – Upstream and Downstream Mach Numbers for Run 010.

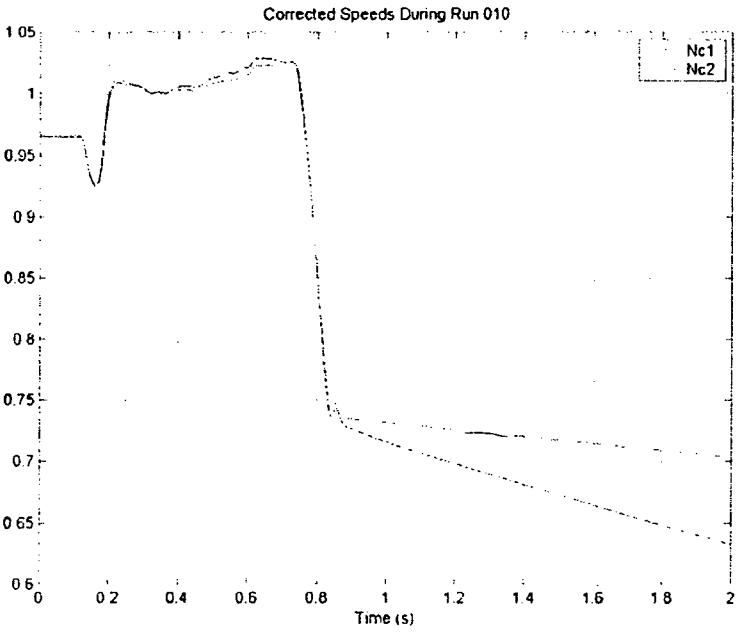


Figure 6.17 – Rotor 1 and 2 Normalized Corrected Speeds for Run 010.

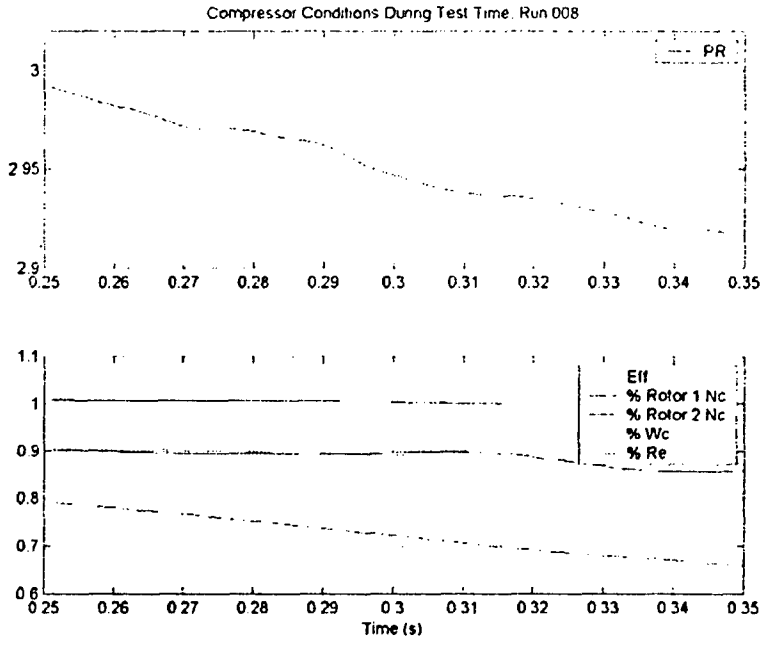


Figure 6.18 – Compressor Conditions During Test Time for Run 010.

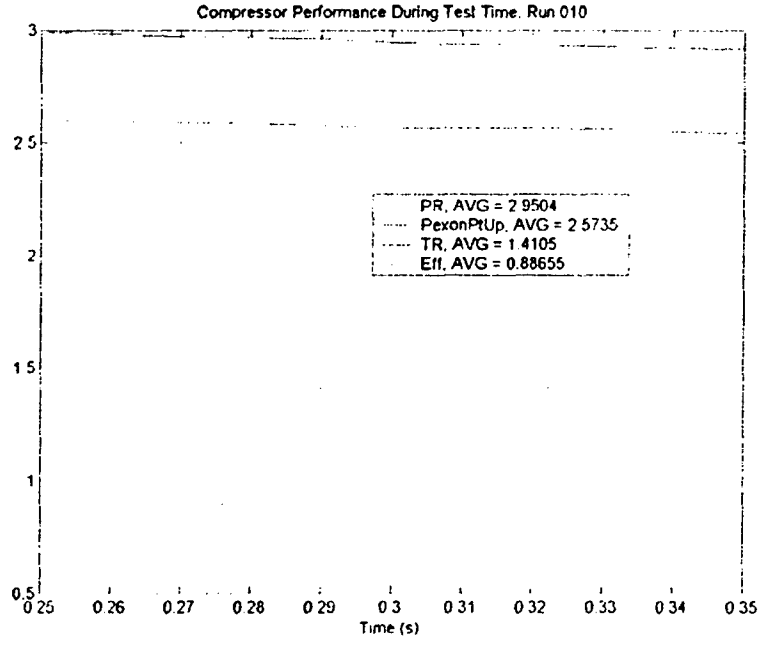


Figure 6.19 – Compressor Performance During Test Time for Run 010.

	RUN ID	005	006	007	008	009	010	011	013	014
Initial Conditions	**Tank Pressure (PSI)**	30.05	30.13	30.24	34.86	29.82	24.21	23.95	24.21	24.19
	R1 Speed (Hz)	198.44	198.45	198.35	209.54	220.04	219.25	219.42	220.26	220.15
	setting	198.7	198.7	198.7	209.8	220.4	220.4	220.4	220.4	220.4
	R2 Speed (Hz)	151.14	153.03	155.91	164.53	183.82	174.08	174.22	174.35	174.38
	setting	151.3	153.2	156	164.8	184	174.6	174.6	174.6	174.6
	Throttle (in^2)	98.15	88.88	82.44	82.44	82.44	82.44	78.44	86.58	90.68
At 260 ms	**Rotor 1 NC**	0.903	0.901	0.904	0.938	1.000	1.007	1.006	1.016	1.018
	Rotor 2 NC	0.886	0.89	0.903	0.934	1.054	1.009	1.008	1.017	1.022
	Wc/WcDes	0.825	0.822	0.812	0.845	0.938	0.94	0.886	0.994	1.016
	Entrance Mach	0.446	0.444	0.437	0.46	0.532	0.534	0.49	0.582	0.603
	PR	1.997	2.119	2.329	2.511	3.017	2.934	2.928	2.928	2.849
	TR	1.264	1.286	1.314	1.351	1.414	1.403	1.417	1.395	1.377
	Eff	0.81	0.826	0.863	0.857	0.885	0.879	0.849	0.906	0.9
	Inlet Gamma	1.426	1.426	1.427	1.428	1.428	1.428	1.427	1.429	1.431
	Exit Gamma	1.396	1.394	1.391	1.388	1.382	1.382	1.381	1.383	1.384
	Eff Throt Area (in^2)	98.15	88.88	82.44	82.44	82.44	82.44	78.435	86.58	90.675
	Discharge Coef	0.981	1.026	1.007	0.979	0.911	0.938	0.943	0.966	0.967

Table 6.1. - Compressor Initial Operating Conditions, Performances and State at 250 ms for Runs 005 to 014.

6.2.3. Preliminary Compressor Map

As explained previously, the compressor operates quasi-steadily between 250 ms and 300 ms. Over this period of time, the corrected speeds of the two rotors are maintained constant to 1%. Data have shown that the inlet corrected mass-flow, which was originally meant to remain constant during the quasi-steady phase, decreases by 3% to 4% over the same range. Thanks to these aspects, a preliminary compressor map can be drawn for each of the test runs, by plotting the compressor pressure ratio versus the normalized inlet corrected mass-flow for constant corrected speed lines. The results encompassing runs 005 to 014 is presented in Figure 6.20. The main particularity of this map is that for each speed line, the pressure ratio of the machine increases with the inlet corrected flow. The operating conditions have not allowed to record the steep drop in pressure ratio as the corrected flow starts significantly overcoming the design inlet corrected flow value. We should mention that this trend was not scheduled by the CFD calculations, which prediction for the design speed line is presented in superposition Figure 6.20. More information can be found in [16] and [17].

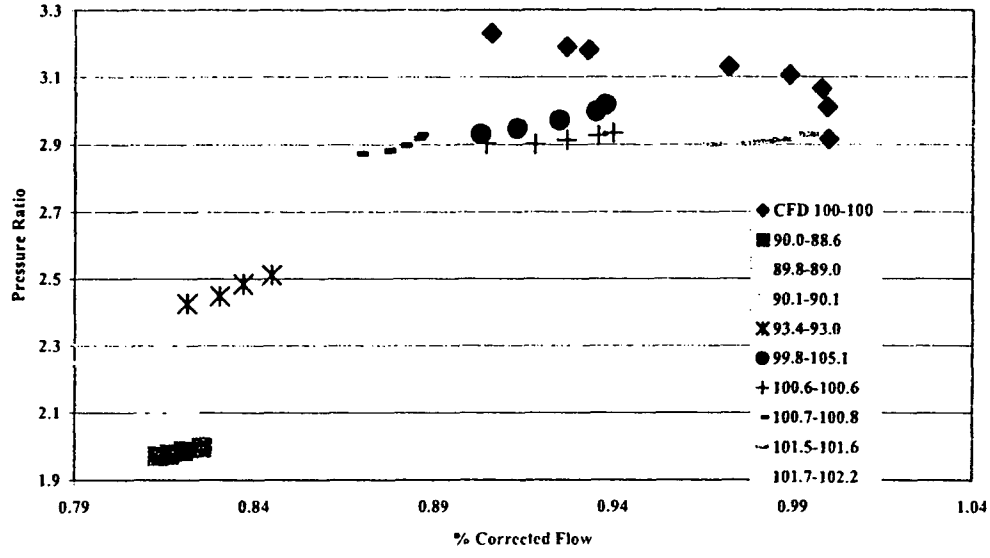


Figure 6.20 – Preliminary Counter-Rotating Aspirated Compressor Map for Corrected Speeds Between 88% and 102% Compared to CFD Full-Speed Line Predictions.

7. Conclusion

7.1. Summary

In order to measure the aerodynamic performances of a counter-rotating aspirated compressor in a short duration facility, total temperature and pressure measurement probes have been designed.

The total temperature measurement sensors have been manufactured using 0.0005-inch diameter type-K thermocouple gage wires, hung across the inner diameter of the probe head. An infinite cylinder transient conduction-convection heat transfer model was used to predict the response time. The model showed that it takes 30 ms for the upstream probes and 19 ms for the downstream probes to read the fluid temperatures in the facility, which satisfies the response-time problem for transient testing conditions. These thermocouples were inserted in single measurement probes, with a ¼-inch casing diameter, as well as in radial measurement probes, with a 3/16-inch casing diameter, mounted on airfoil-shaped rakes. Thanks to extensive procedures, their calibration errors was contained to less than 0.1 K. Vent holes were designed in the casings of these heads to optimize the tradeoff between the response time of the sensors, the recovery error associated to the non-isentropic stagnation of the flow by the probes and the mechanical resistance of the thermocouple wires to the flow's dynamic pressure. The conduction

error of the sensors was reduced to a minimum of 0.073 K for the upstream rake probes, 0.014 K for the downstream rake probes, 0.005 K for the upstream single probes and 0.0005 K for the downstream single probes, thanks to larger casing diameters. The radiation error appeared to be the black sheep in the error analysis of the temperature probes. Due to the short duration of the test, the probe casings behave quasi-isothermally while the thermocouple wires is following the flow temperature. Consequently, the radiation error averaged 0.112 K for the upstream probes and 0.299 K for the downstream probes. The overall uncertainties of the temperature probes for this project amounted to an average of 0.14 K for the upstream probes and 0.30K for the downstream probes.

The pressure measurements were performed using mainly ultraminiature Kulite piezoresistive strain gauge differential transducers. This type of transducer has very high frequency response. These sensors show scale non-linearities as well as zero drifts, which require several in situ calibrations of each transducer. This helped bring down the corresponding relative probe error to 0.15%, which is on the order of the error imposed by the geometry of the sensing tubes on which the transducers were mounted. Signal noise remains the main error source for the pressure probes. The corresponding average relative error is equal to 0.30%, which is twice as much as the transducer error alone. Overall, the relative pressure measurement error amounted to 0.30% to 0.40%.

These errors have been compiled to compute the uncertainty in the efficiency measurement. Two methods were presented, one consisting in perturbing the inputs of the data reduction programs and recording the amount of change obtained in the efficiency, the other consisting in considering the test rig as an adiabatic compressor operating with an ideal gas at constant mass-flow and specific heat ratio, and deriving an analytical equation of the efficiency uncertainty. The first method gave much better results, forecasting an uncertainty of 0.131 points of efficiency, compared to 0.500 to 0.900 points of efficiency for the approximated model. The errors related to the discrete time and spatial samplings of the flow have been addressed. While the time treatment of the signal settled the first concern, the inlet pressure distortion entailed an uncertainty of 0.95% on the efficiency, due to the discrete spatial repartition of the measurement probes. The impact of the non-adiabatic effects of the short-duration testing environment have

also been estimated. The correction between the efficiency computed from direct measurements on the test rig and the corresponding adiabatic efficiency is proportional to the amount of heat transferred between the fluid and the facility walls, scaled by the temperature ratio of the compressor. Calculations showed that this correction term is smaller than 0.1 point of efficiency. The behavior of each probe and the results of the data reduction process during Run 010 have been presented. A preliminary compressor has been established and compared to the CFD predictions. The positive slopes of the empirical speed lines are a peculiar feature of this compressor.

7.2. Future Work

Many thrilling challenges remain in the measurement of the aerodynamic performances of the blow-down counter-rotating aspirated compressor.

A first group of challenges are linked to the performances of the measurement probes themselves. While all other errors have been brought to a minimum level, the thermocouple probes are submitted to a persisting radiation error, linked to the constant temperature of the head casings. Further study must be undertaken to allow the casings' temperature to better follow the flow temperature. As for the pressure transducers, the noise error can be reduced to the same level as the other sources by improving the electrical installation of the facility.

The second group concerns the facility. The operation of the tunnel has shown an inlet pressure distortion, which could be due to imperfections in the inlet pressure screen [2]. This phenomenon requires further studies. More instrumentation is needed in the bleed flow passage, to better assess the change in mass-flow over the test time. The preliminary compressor map has also unveiled an unexpected feature, namely that the pressure ratio grows with the corrected mass-flow. More instrumentation might help clear this point and better understand the way a blow-down counter-rotating aspirated compressor operates.

8. Appendix A: Detailed Calculation of the Correction Between Indicated and Adiabatic Efficiencies in a Blow-Down Test Facility.

GOAL: We want to determine the evolution of the blade temperature during a one second test.

Method: We compute the heat flux in each rotor and plot the corresponding response of the blade temperature

Blade thermal properties:

	Rotor 1 (17-4PH)	Rotor 2 (Al 2046)
Thermal diffusivity:	$\alpha 1 := 5.1 \cdot 10^{-6} \cdot \frac{m^2}{s}$	$\alpha 2 := 73 \cdot 10^{-6} \cdot \frac{m^2}{s}$
Thermal conductivity:	$k1 := 18.3 \cdot \frac{W}{m \cdot K}$	$k2 := 177 \cdot \frac{W}{m \cdot K}$
Density:	$\rho 1 := 7800 kg \cdot m^{-3}$	$\rho 2 := 2770 kg \cdot m^{-3}$
Heat coefficient	$c1 := 460 J \cdot K^{-1} \cdot kg^{-1}$	$c2 := 875 J \cdot K^{-1} \cdot kg^{-1}$

Initial temperature: T0 = 300K

Gas properties:

$Cp := 691.5 \cdot J \cdot kg^{-1} \cdot K^{-1}$

$\gamma := 1.40$

$Rg := 198.27 J \cdot kg^{-1} \cdot K^{-1}$

Flow characteristics:

Before Rotor 1	Absolute Inlet Mach Number	M0 = 0.65
	Total Inlet Temperature	Tt0 = 300K
	Total Inlet Pressure	Pt0 = 83789Pa
Rotor 1	Relative Inlet Mach number	M0b = 1.27
	Relative outlet Mach Number	M1b = .69
Rotor 2	Relative Inlet Mach number	M2b = 1.33
	Relative Outlet Mach number	M3b = 0.73

These conditions change with time according to the blowdown time constant and model:

$\tau bd := 2.373 \cdot s$

$$Tt0(t) := T0 \cdot \frac{1}{\left(1 + \frac{t}{\tau bd}\right)^2} \qquad (A.1)$$

$$pt0(t) := pt00 \cdot \left(1 + \frac{t}{\tau bd}\right)^{\frac{-2\cdot\gamma}{\gamma-1}} \qquad (A.2)$$

Assumptions:

Computation is done assuming unsteady inlet conditions at rotor 1. At each time t, we are able to determine the heat flux imposed by the airflow to the blades of the compressor, this assuming that there is no delay in the propagation of the information about the changes in the inlet conditions of rotor 1.

The adiabatic recovery coefficient is computed in the case of a turbulent boundary layer.

The static temperature of the gas is supposed to remain constant between the 2 rotors.

Critical assumption: The Prandtl number is assumed to be 0.774.

The temperature evolution in the blade is computed assuming the blades are semi-infinite solids submitted to a time variable surface heat flux. Then the blades are supposed to be isothermal in the thickness direction.

We assume for the test that the gas mixture we use has a Prandtl number of Pr = 0.774

We also know the friction coefficient of the each blade, from the flow path computation.

For rotor 1: Cf1 = 0.002

For rotor 2: Cf2= 0.0013

Then, according [21], in a turbulent boundary layer, the Stanton number is:

$$St1 := \frac{\frac{Cf1}{2}}{1 + 13 \cdot \left(Pr^{\frac{2}{3}} - 1\right) \cdot \sqrt{\frac{Cf1}{2}}} \qquad (A.4)$$

$$St2 := \frac{\frac{Cf2}{2}}{1 + 13 \cdot \left(Pr^{\frac{2}{3}} - 1\right) \cdot \sqrt{\frac{Cf2}{2}}} \qquad (A.5)$$

We can compute the turbulent recovery coefficient:

The turbulent Prandtl number is Prt = 0.9

Hence, according to[21]:

$$r := Prt + (Pr - Prt) \cdot \left(\frac{11.5}{20}\right)^2 \tag{A.6}$$

$r = 0.858$

Computation:

- At the inlet of rotor 1:

$$\rho a0(t) := \frac{pt0(t)}{Rg \cdot Tt0(t)} \cdot \left[1 + \frac{(\gamma - 1) \cdot M0^2}{2}\right]^{\frac{1}{1-\gamma}} \tag{A.7}$$

$$Ts0(t) := \frac{Tt0(t)}{1 + \frac{(\gamma - 1) \cdot M0^2}{2}} \tag{A.8}$$

$$a0(t) := \sqrt{\gamma \cdot Rg \cdot Ts0(t)} \tag{A.9}$$

$$Tt0b(t) := Ts0(t) \cdot \left(1 + \frac{\gamma - 1}{2} \cdot M0b^2\right) \tag{A.10}$$

$$qs0(t) := -St1 \cdot \rho a0(t) \cdot Cp \cdot \left(Tt0b(t) \cdot \frac{1 + r \cdot \frac{\gamma - 1}{2} \cdot M0b^2}{1 + \frac{\gamma - 1}{2} \cdot M0b^2} - T0\right) \cdot M0b \cdot a0(t) \tag{A.11}$$

- At the outlet of rotor 1:

The total temperature inside the blade remains constant from the rotating frame point of view.

$$Tt1b(t) := Tt0b(t) \tag{A.12}$$

$$Ts1(t) := \frac{Tt1b(t)}{1 + \frac{(\gamma - 1) \cdot M1b^2}{2}} \tag{A.13}$$

$$Pt0b(t) := \frac{pt0(t)}{\left[1 + \frac{(\gamma - 1) \cdot M0^2}{2}\right]^{\frac{\gamma}{\gamma - 1}}} \cdot \left[1 + \frac{(\gamma - 1) \cdot M0b^2}{2}\right]^{\frac{\gamma}{\gamma - 1}} \tag{A.14}$$

$$Pt1b(t) := Pt0b(t) \tag{A.15}$$

$$\rho a1(t) := \frac{Pt1b(t)}{\left[1 + \frac{(\gamma - 1) \cdot M1b^2}{2}\right]^{\frac{\gamma}{\gamma - 1}}} \cdot \frac{1}{Rg \cdot Ts1(t)} \tag{A.16}$$

$$a1(t) := \sqrt{\gamma \cdot Rg \cdot Ts1(t)} \tag{A.17}$$

$$qs1(t) := -St1 \cdot \rho a1(t) \cdot Cp \cdot \left(Tt1b(t) \cdot \frac{1 + r \cdot \frac{\gamma - 1}{2} \cdot M1b^2}{1 + \frac{\gamma - 1}{2} \cdot M1b^2} - T0 \right) \cdot M1b \cdot a1(t) \tag{A.18}$$

- At the inlet of rotor 2: we assume that the static temperature is not changed between the outlet of rotor 1 and the inlet of rotor 2.

$$Tt3b := Tt2b \tag{A.19}$$

$$Tt2b(t) := Ts2(t) \cdot \left(1 + \frac{\gamma - 1}{2} \cdot M2b^2\right) \tag{A.20}$$

$$\rho a2(t) := \rho a1(t) \tag{A.21}$$

$$a2(t) := \sqrt{\gamma \cdot Rg \cdot Ts2(t)} \tag{A.22}$$

$$qs2(t) := -St2 \cdot \rho a2(t) \cdot Cp \cdot \left(Tt2b(t) \cdot \frac{1 + r \cdot \frac{\gamma - 1}{2} \cdot M2b^2}{1 + \frac{\gamma - 1}{2} \cdot M2b^2} - T0\right) \cdot M2b \cdot a2(t) \tag{A.23}$$

- At the outlet of rotor 2:

$$Tt3b := Tt2b \tag{A.24}$$

$$Pt3b(t) := \frac{Pt1b(t)}{\left[1 + \frac{(\gamma - 1) \cdot M1b^2}{2}\right]^{\frac{\gamma}{\gamma - 1}}} \cdot \left[1 + \frac{(\gamma - 1) \cdot M2b^2}{2}\right]^{\frac{\gamma}{\gamma - 1}} \tag{A.25}$$

$$\rho a3(t) := \frac{Pt3b(t)}{\left[1 + \frac{(\gamma - 1) \cdot M3b^2}{2}\right]^{\frac{\gamma}{\gamma - 1}}} \cdot \frac{1}{Rg \cdot \frac{Tt3b(t)}{1 + \frac{(\gamma - 1) \cdot M3b^2}{2}}} \tag{A.26}$$

$$Ts3(t) := \frac{Tt3b(t)}{1 + \frac{(\gamma - 1) \cdot M3b^2}{2}} \tag{A.27}$$

$$a3(t) := \sqrt{\gamma \cdot Rg \cdot Ts3(t)} \tag{A.28}$$

$$qs3(t) := -St2 \cdot \rho a3(t) \cdot Cp \cdot \left(Tt3b(t) \cdot \frac{1 + r \cdot \frac{\gamma - 1}{2} \cdot M3b^2}{1 + \frac{\gamma - 1}{2} \cdot M3b^2} - T0\right) \cdot M3b \cdot a3(t) \tag{A.29}$$

According to [22], the leading edges temperatures for each rotor are given by:

$$Te1(\eta,t) := T0 + \frac{\sqrt{\alpha 1}}{k1\cdot\sqrt{\pi}}\cdot\int_0^t -qs0(t-\tau)\cdot e^{-\eta^2}\cdot\frac{1}{\sqrt{\tau}}\,d\tau \tag{A.30}$$

$$Te2(\eta,t) := T0 + \frac{\sqrt{\alpha 2}}{k2\cdot\sqrt{\pi}}\cdot\int_0^t -qs2(t-\tau)\cdot e^{-\eta^2}\cdot\frac{1}{\sqrt{\tau}}\,d\tau \tag{A.31}$$

$x1(\eta,t) := \eta\cdot 2\cdot\sqrt{\alpha 1\cdot t}$

$x1(2,1s) = 9.033\times 10^{-3}\,m$

$x1(2,0.5\cdot s) = 6.387\times 10^{-3}\,m$

$x2(\eta,t) := \eta\cdot 2\cdot\sqrt{\alpha 2\cdot t}$

$x2(2,1s) = 0.034m$

$x2(2,0.5\cdot s) = 0.024m$

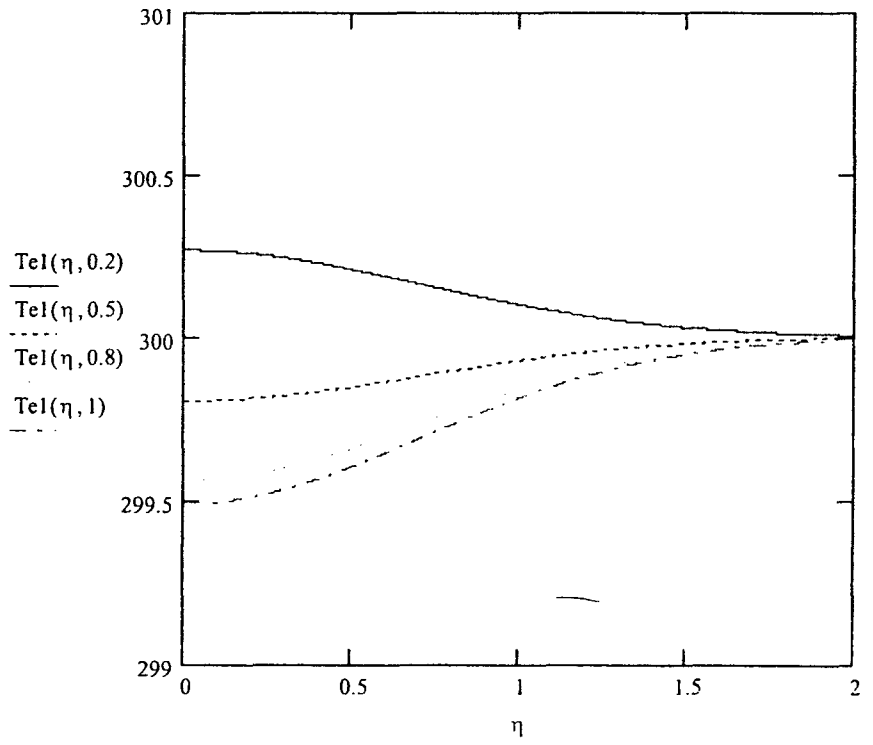


Figure A.1. - Temperature Profile vs. η Inside Rotor 1 at Various Time Points.

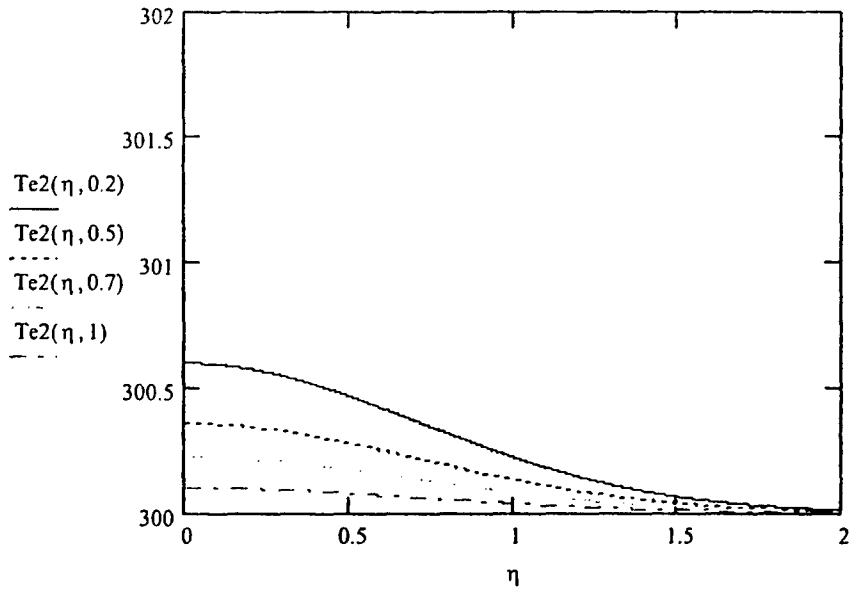


Figure A.2. - Temperature Profile vs. η Inside Rotor 2 at Various Time Points.

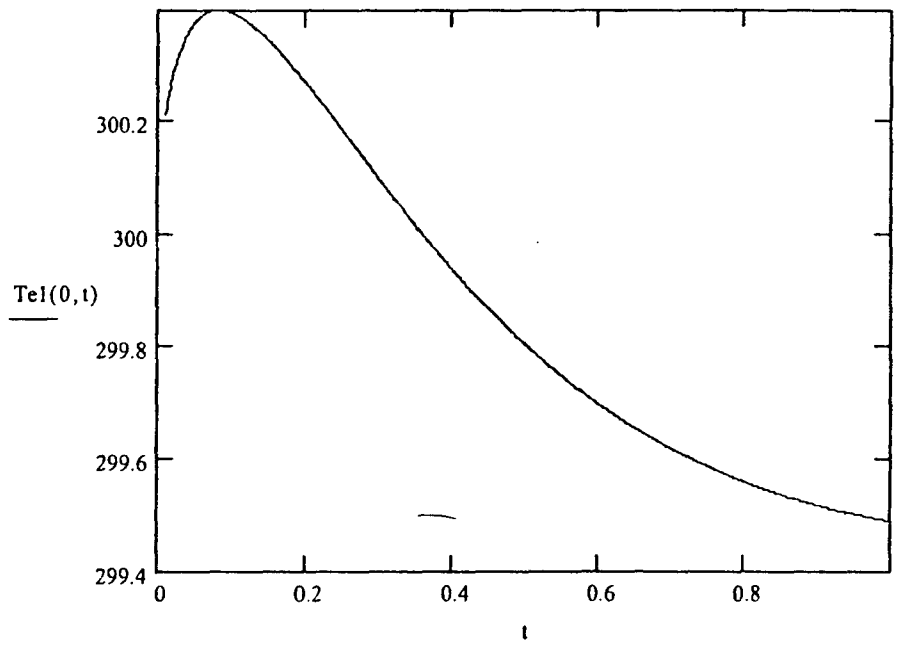


Figure A.3. - Temperature Evolution at the Surface of the Leading Edge of Rotor 1 over 1s

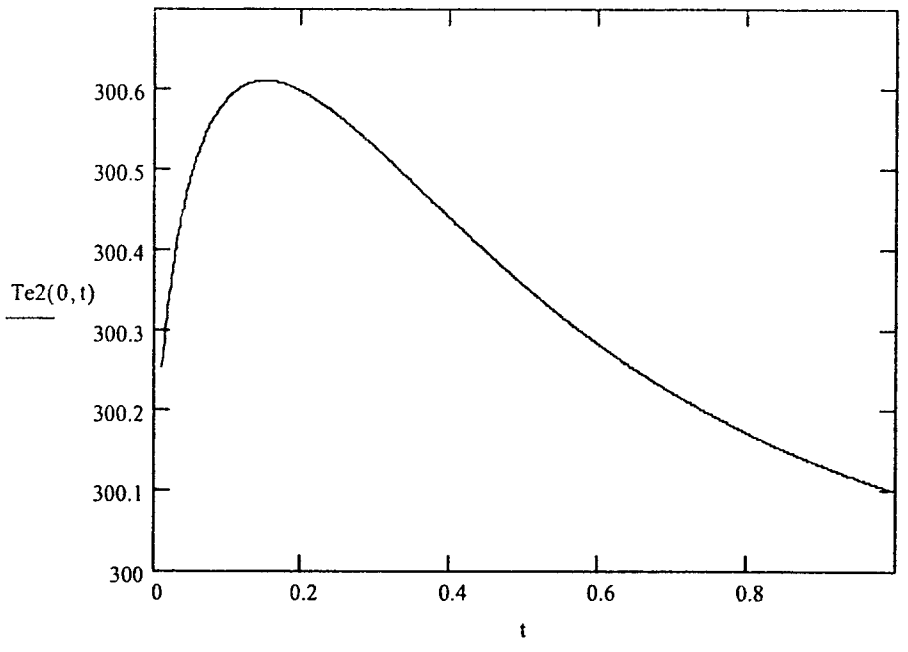


Figure A.4. - Temperature Evolution at the Surface of the Leading Edge of Rotor 2 over 1s.

The non-dimensional length of this problem seems relatively large compared to the thickness of the blades. Over 1 second, the length beyond which the blade is not affected by the temperature change is:

For rotor 1 $x1(2, 1s) = 9.033 \times 10^{-3} m$

For rotor 2 $x2(2, 1s) = 0.034m$

We shall notice here that the heat flux has been calculated assuming the blade temperature to be constant, and from this result the corresponding temperature evolution of the blade temperature has been plotted. The small variation observed show the consistency of the way we proceeded, although this model does not represent correctly what happens in the blades.

We might have to consider the lumped thermal capacity model. We can compute the Biot number for each stage:

For rotor 1:

$$hc0(t) := St1 \cdot \rho a0(t) \cdot Cp \cdot M0b \cdot a0(t) \quad \text{(A.32)}$$

$$hc1(t) := St1 \cdot \rho a1(t) \cdot Cp \cdot M1b \cdot a1(t) \quad \text{(A.33)}$$

$L1 = 0.0023m$

$$Bi0(t) := \frac{hc0(t) \cdot L1}{k1} \quad \text{(A.34)} \qquad Bi1(t) := \frac{hc1(t) \cdot L1}{k1} \quad \text{(A.35)}$$

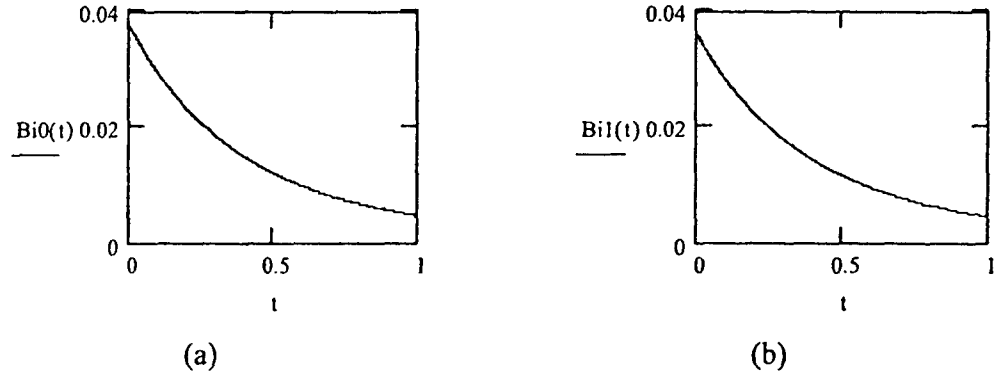


Figure A.5. – Biot Number at Leading Edge (a) and Trailing Edge (b) of Rotor 1 over 1s.

For rotor 2:

$$hc2(t) := St2 \cdot \rho a2(t) \cdot Cp \cdot M2b \cdot a2(t) \quad \text{(A.36)}$$

$$hc3(t) := St2 \cdot \rho a3(t) \cdot Cp \cdot M3b \cdot a3(t) \quad \text{(A.37)}$$

$L2 = 0.0017m$

$$Bi2(t) := \frac{hc2(t) \cdot L2}{k2} \quad \text{(A.37)} \qquad Bi3(t) := \frac{hc3(t) \cdot L2}{k2} \quad \text{(A.38)}$$

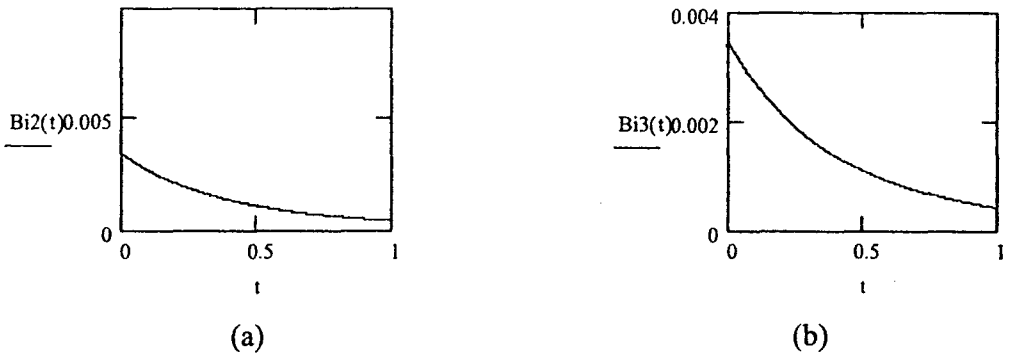


Figure A.6. - Biot Number at Leading Edge (a) and Trailing Edge (b) of Rotor 2 over 1s.

We get Biot numbers on the order of 0.1, which justifies the use of the lumped capacity models.

Cross section surface areas:

For the IGV $AcIGV := 0.067 \cdot in^2$

For rotor 1 $Ac1 := 0.54in^2$

For rotor 2 $Ac2 := 0.28in^2$

We can estimate the surface area of the blades, from the cross section view, assuming the blades to be trapezoidal and dividing the measures by the cosine of the average relative angle.

For the IGV $AIGV := (0.0055m \cdot 5 \cdot 0.026 \cdot m \cdot 5)$ $AIGV = 3.575 \times 10^{-3} m^2$

For rotor 1 $A1 := \frac{[(0.026m + 0.02m) \cdot 5 \cdot 0.0115m \cdot 5]}{\cos\left(\frac{60deg + 46.4deg}{2}\right)}$ $A1 = 0.022m^2$

Foro rotor 2 $A2 := \frac{[(0.016m + 0.012m) \cdot 5 \cdot 0.0075m \cdot 5]}{\cos\left(\frac{62deg + 50.3deg}{2}\right)}$ $A2 = 9.425 \times 10^{-3} m^2$

We can also estimate the volume of each blade:

For the IGV $VIGV := AcIGV \cdot 0.026m \cdot 5$ $VIGV = 5.619 \times 10^{-6} m^3$

For rotor 1 $V1 := Ac1 \cdot \left[0.02m \cdot 5 + \frac{(0.026m - 0.02m) \cdot 5}{2}\right]$ $V1 = 4.006 \times 10^{-5} m^3$

For rotor 2 $V2 := Ac2 \cdot \left[0.012m \cdot 5 + \frac{(0.016m - 0.012m) \cdot 5}{2}\right]$ $V2 = 1.265 \times 10^{-5} m^3$

Let T1 be the temperature of the blades of rotor 1 and T2 the temperature of the blades of rotor 2, in this lump thermal capacity model. For each rotor, we can compute the evolution of the temperature using the heat transfer computed at the leading edge or at the trailing edge of the blade. Letter 'l' will refer to the temperature at the leading edge and letter 't' to that at the trailing edge.

T1l must satisfy the following differential equation:

$$\frac{d}{dt}T = -hc0(t) \cdot \frac{\frac{A1}{2}}{\left(\rho 1 \cdot c1 \cdot \frac{V1}{2}\right)} \cdot T(t) + hc0(t) \cdot \frac{\frac{A1}{2}}{\left(\rho 1 \cdot c1 \cdot \frac{V1}{2}\right)} \cdot Tt0b(t) \cdot \frac{1 + r \cdot \frac{\gamma - 1}{2} \cdot M0b^2}{1 + \frac{\gamma - 1}{2} \cdot M0b^2} \quad (A.39)$$

Using the constant variation method, we are able to compute the solution:

$$\lambda 1l(t) := 1 + \int_0^t \frac{hc0(u) \cdot \frac{A1}{2} \cdot Tt0b(u) \cdot \frac{1 + r \cdot \frac{\gamma - 1}{2} \cdot M0b^2}{1 + \frac{\gamma - 1}{2} \cdot M0b^2}}{\rho 1 \cdot \frac{V1}{2} \cdot c1 \cdot T0 \cdot e^{\int_0^u \frac{\frac{-A1}{2}}{\rho 1 \cdot \frac{V1}{2} \cdot c1} hc0(\tau)\, d\tau}} du \tag{A.40}$$

$$T1l(t) := \lambda 1l(t) \cdot T0 \cdot e^{\int_0^t \frac{\frac{-A1}{2}}{\rho 1 \cdot \frac{V1}{2} \cdot c1} hc0(\tau)\, d\tau} \tag{A.41}$$

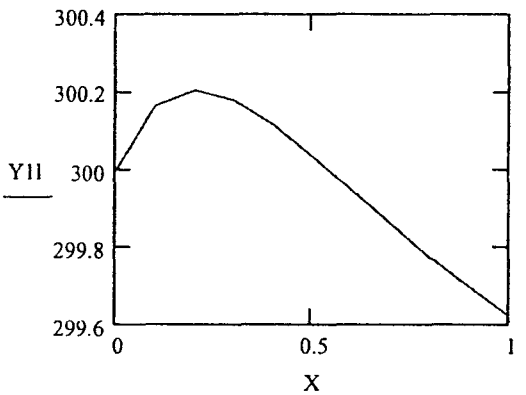


Figure A.7. – Temperature Evolution at the Surface of the Leading Edge of Rotor 1 Over 1s.

Similarly, at the trailing edge of rotor 1:

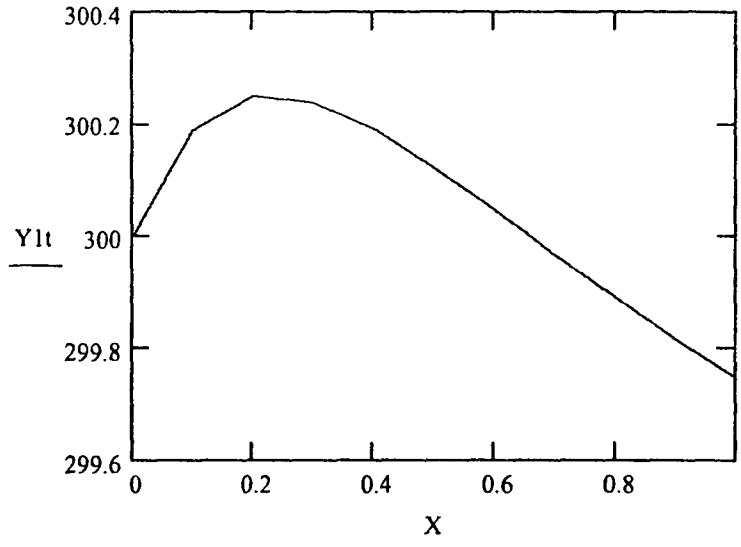


Figure A.8. - Temperature Evolution at the Surface of the Trailing Edge of Rotor 1 Over 1s.

At the leading edge of rotor 2:

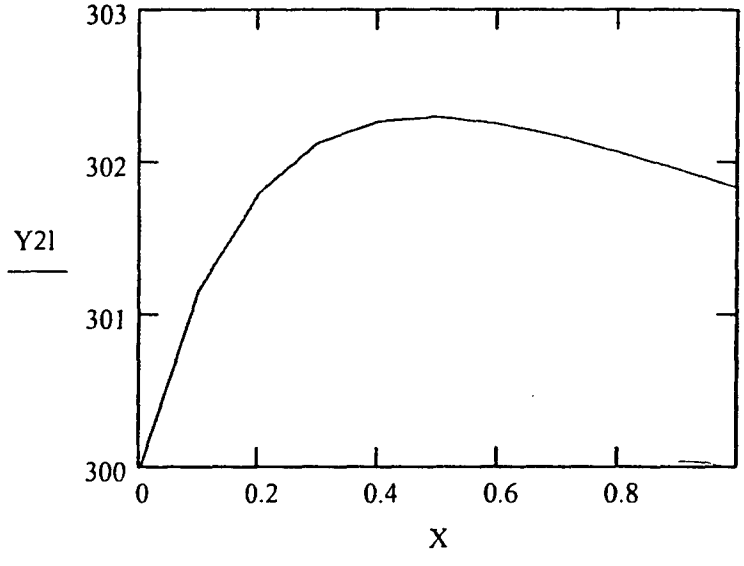


Figure A.9. - Temperature Evolution at the Surface of the Leading Edge of Rotor 2 Over 1s.

At the trailing edge of rotor 2:

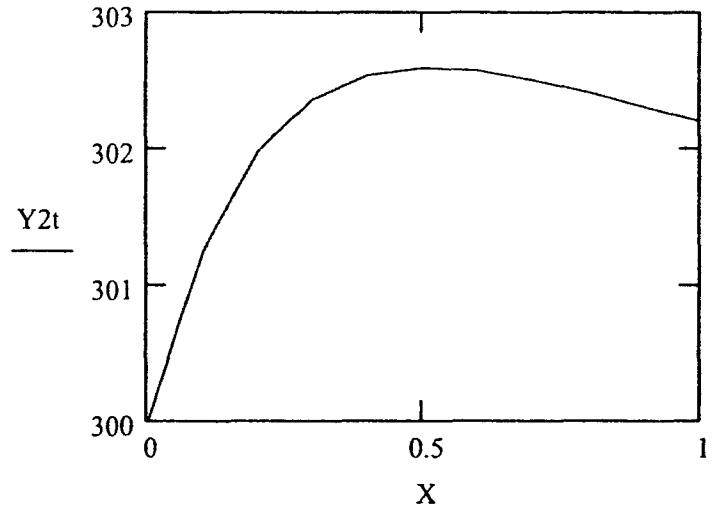


Figure A.10. - Temperature Evolution at the Surface of the Trailing Edge of Rotor 2 Over 1s.

As for the IGV:

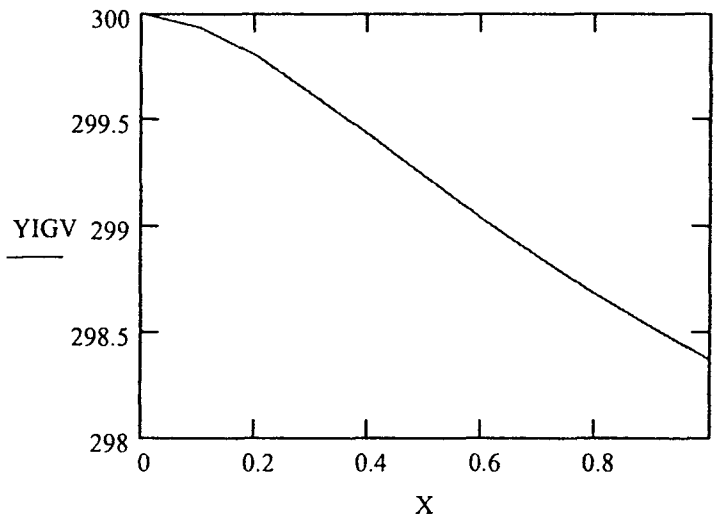


Figure A.11. - Temperature Evolution at the Surface of the IGV Over 1s.

The results concerning the heat transfer at the level of the hub of the rotors are similar to the time unsteady results computed for the blades as semi-infinite bodies. We do not take into account the thermal boundary layer. Rotor 2 hub is however made of steel 17-4PH contrary to the corresponding blades, which are in aluminum.

For rotor 2 hub, the result is:

$$Te3(\eta,t) := T0 + \frac{\sqrt{\alpha 1}}{k1\cdot\sqrt{\pi}}\cdot\int_0^t -qs2(t-\tau)\cdot e^{-\eta^2}\cdot\frac{1}{\sqrt{\tau}}\,d\tau \qquad (A.42)$$

Over the test time, the temperature profiles in the hub for various time dates are:

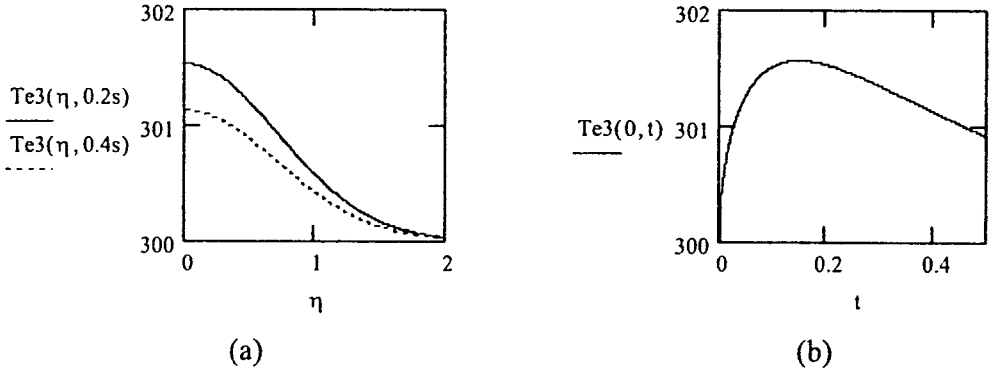


Figure A.12. – Temperature Evolution of Rotor 2 Hub vs. Depth for Different Time Points (a) and vs. Time at the Surface (b).

The walls of the duct are assumed to be made of carbon steel AISI 1010.

Thermal diffusivity $\alpha 3 := 18.8\cdot 10^{-6}\cdot\frac{m^2}{s}$

Density $\rho 3 := 7830\frac{kg}{m^3}$

Constant Heat capacity $c3 := 434\frac{J}{K\cdot kg}$

Thermal conductivity $k3 := \alpha 3\cdot\rho 3\cdot c3$

$k3 = 63.887 kg\,m\,s^{-3}K^{-1}$

For the walls that are located in front of rotor 1, the heat transfer flux is

$$qs00(t) := -St1 \cdot \rho a0(t) \cdot Cp \cdot \left(Tt0(t) \cdot \frac{1 + r \cdot \frac{\gamma - 1}{2} \cdot M0^2}{1 + \frac{\gamma - 1}{2} \cdot M0^2} - T0 \right) \cdot M0 \cdot a0(t) \qquad \text{(A.43)}$$

The corresponding temperature is:

$$Te0(\eta, t) := T0 + \frac{\sqrt{\alpha 3}}{k3 \cdot \sqrt{\pi}} \cdot \int_0^t -qs00(t - \tau) \cdot e^{-\eta^2} \cdot \frac{1}{\sqrt{\tau}} \, d\tau \qquad \text{(A.44)}$$

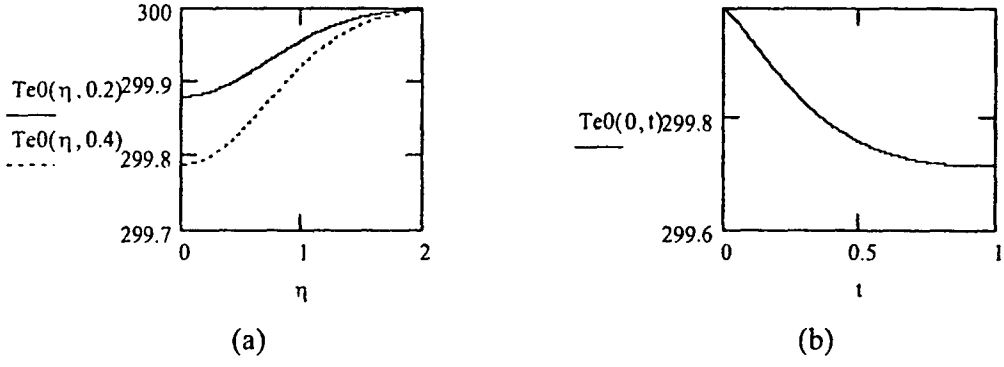


Figure A.13. - Temperature Evolution of Rotor 1 Hub vs. Depth for Different Time Points (a) and vs. Time at the Surface (b).

For the rotor casing:

$$qs0e(t) := -St1 \cdot \rho a0(t) \cdot Cp \cdot \left(Tt0(t) \cdot \frac{1 + r \cdot \frac{\gamma - 1}{2} \cdot M0^2}{1 + \frac{\gamma - 1}{2} \cdot M0^2} - T0 \right) \cdot M0 \cdot a0(t) \qquad \text{(A.45)}$$

$$Tee0(\eta, t) := T0 + \frac{\sqrt{\alpha 3}}{k3 \cdot \sqrt{\pi}} \cdot \int_0^t -qs0e(t - \tau) \cdot e^{-\eta^2} \cdot \frac{1}{\sqrt{\tau}} \, d\tau \qquad \text{(A.46)}$$

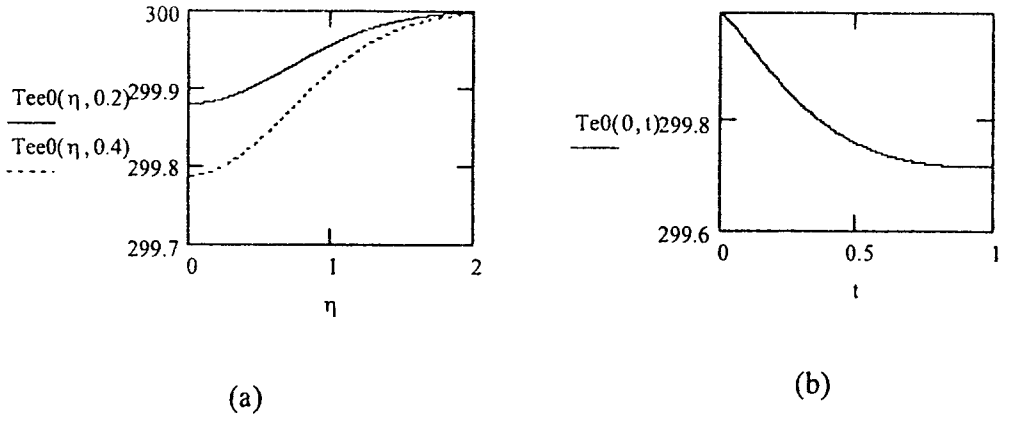


Figure A.14. - Temperature Evolution of the Leading Edge Parts of Rotor 1 Blades vs. Depth for Different Time Points (a) and vs. Time at the Surface (b).

- At station 1:

Let M1 be the total Mach number at mid-span.

M1x – axial Mach number at station 1 $M1x := 0.48$

Rotor 1 tip rotating speed $Vr1 := 1450\frac{ft}{s}$

Corresponding Mach number $Mr1(t) := \frac{Vr1}{a1(t)}$

Thus:

$$M1(t) := \sqrt{M1x^2 + \left(Mr1(t) - \sqrt{M1b^2 - M1x^2}\right)^2} \tag{A.47}$$

$$qs1e(t) := -St1 \cdot \rho a1(t) \cdot Cp \cdot \left[Ts1(t) \cdot \left(1 + r \cdot \frac{\gamma - 1}{2} \cdot M1(t)^2\right) - T0\right] \cdot M1(t) \cdot a1(t) \tag{A.48}$$

$$Tee1(\eta, t) := T0 + \frac{\sqrt{\alpha 3}}{k3 \cdot \sqrt{\pi}} \cdot \int_0^t -qs1e(t - \tau) \cdot e^{-\eta^2} \cdot \frac{1}{\sqrt{\tau}}\, d\tau \tag{A.49}$$

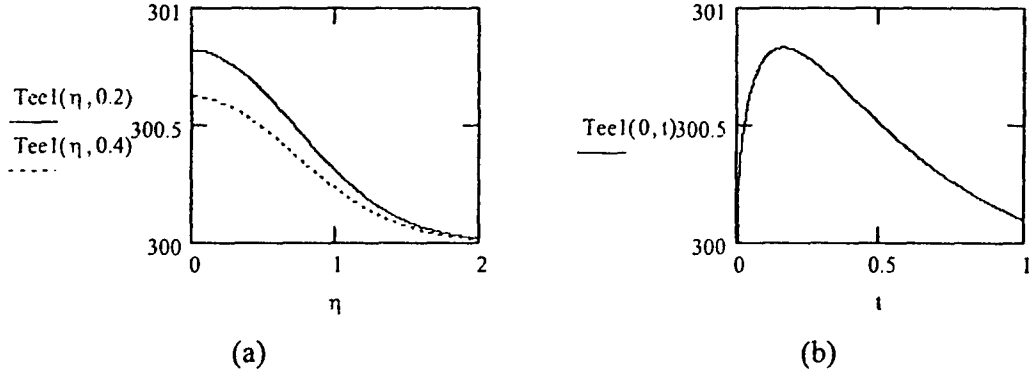


Figure A.15. - Temperature Evolution of the Trailing Edge Parts of Rotor 1 Blades vs. Depth for Different Time Points (a) and vs. Time at the Surface (b).

- At station 2:

Let M2 be the total Mach number at mid-span.

M2x – axial Mach number at station 2 $M2x := 0.6$

Rotor 2 tip rotating speed $Vr2 := 1100\frac{ft}{s}$

Corresponding Mach number $Mr2(t) := \frac{Vr2}{a2(t)}$

Thus:

$$M2(t) := \sqrt{M2x^2 + \left(Mr2(t) - \sqrt{M2b^2 - M2x^2}\right)^2} \tag{A.50}$$

$$qs2e(t) := -St2 \cdot \rho a2(t) \cdot Cp \cdot \left[Ts2(t) \cdot \left(1 + \frac{\gamma - 1}{2} \cdot r \cdot M2(t)^2\right) - T0\right] \cdot M2(t) \cdot a2(t) \tag{A.51}$$

$$Tee2(\eta, t) := T0 + \frac{\sqrt{\alpha 3}}{k3 \cdot \sqrt{\pi}} \cdot \int_0^t -qs2e(t - \tau) \cdot e^{-\eta^2} \cdot \frac{1}{\sqrt{\tau}}\, d\tau \tag{A.52}$$

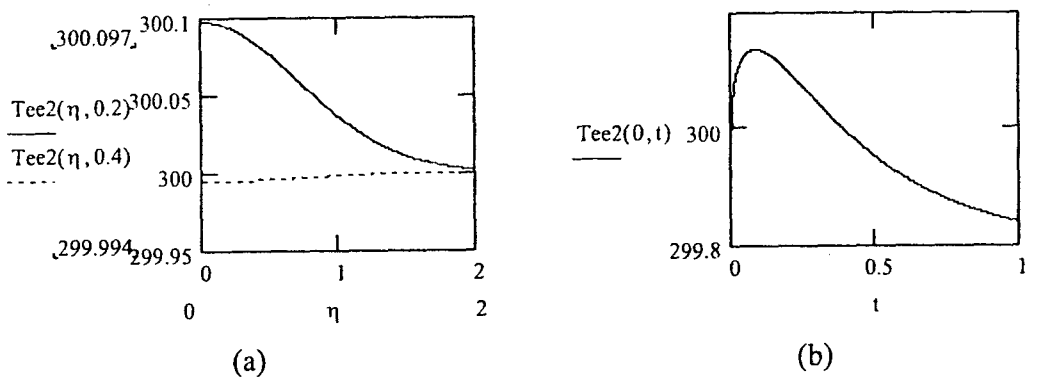


Figure A.16. - Temperature Evolution of the Leading Edge Parts of Rotor 2 Blades vs. Depth for Different Time Points (a) and vs. Time at the Surface (b).

- At station 3:

Let M3 be the total Mach number at mid-span:

M3x – axial Mach number at station 3 $M3x := 0.47$

Corresponding Mach number $Mr3(t) := \frac{Vr2}{a3(t)}$

Thus:

$$M3(t) := \sqrt{M3x^2 + \left(Mr3(t) - \sqrt{M3b^2 - M3x^2}\right)^2} \tag{A.53}$$

The total temperature in the annulus behind rotor 2 is given by:

$$Tt3(t) := Ts3(t) \cdot \left(1 + \frac{\gamma - 1}{2} \cdot M3(t)^2\right) \tag{A.54}$$

The corresponding heat transfer is

$$qs3e(t) := -St2 \cdot \rho a3(t) \cdot Cp \cdot \left(Tt3(t) \cdot \frac{1 + r \cdot \frac{\gamma - 1}{2} \cdot M3(t)^2}{1 + \frac{\gamma - 1}{2} \cdot M3(t)^2} - T0 \right| \cdot M3(t) \cdot a3(t) \tag{A.55}$$

Here again, we assume the walls to be a semi-infinite body. The temperature variation is given by:

$$Tee3(\eta, t) := T0 + \frac{\sqrt{\alpha 3}}{k3 \cdot \sqrt{\pi}} \cdot \int_0^t -qs3e(t - \tau) \cdot e^{-\eta^2} \cdot \frac{1}{\sqrt{\tau}} d\tau \tag{A.56}$$

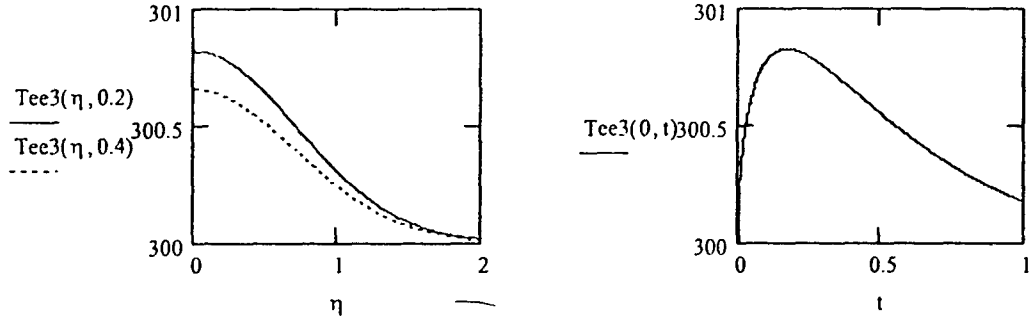


Figure A.17. - Temperature Evolution of the Trailing Edge Parts of Rotor 2 Blades vs. Depth for Different Time Points (a) and vs. Time at the Surface (b).

We will now compute the heat transfer in the walls behind rotor 2

M3ex := 0.48

$$qs4(t) := -St2 \cdot \rho a3(t) \cdot Cp \cdot \left(Tt3(t) \cdot \frac{1 + r \cdot \frac{\gamma - 1}{2} \cdot M3ex^2}{1 + \frac{\gamma - 1}{2} \cdot M3ex^2} - T0 \right) \cdot M3ex \cdot a3(t) \qquad \text{(A.57)}$$

Let us compute the overall heat transfer:

For rotor 1:
$$Qr1(t) := \frac{A1}{2} qs0(t) \cdot 20 + \frac{A1}{2} qs1(t) \cdot 20 \qquad \text{(A.58)}$$

For rotor 2:
$$Qr2(t) := \frac{A2}{2} \cdot qs2(t) \cdot 29 + \frac{A2}{2} \cdot qs3(t) \cdot 29 \qquad \text{(A.59)}$$

For the IGV:
$$QIGV(t) := 35 \cdot hcIGV(0s) \cdot AIGV \cdot \left(Tt0(t) \cdot \frac{1 + r \cdot \frac{\gamma - 1}{2} \cdot M0^2}{1 + \frac{\gamma - 1}{2} \cdot M0^2} - T0 \right) \qquad \text{(A.60)}$$

For the front duct:
$$Qfront(t) := 0.0427m^2 \cdot qs00(t) \qquad \text{(A.61)}$$

For the aft duct:
$$Qaft(t) := 0.0353m^2 \cdot qs4(t) \qquad \text{(A.62)}$$

For rotor 1 hub:
$$Qcone1(t) := 0.0045m^2 \cdot \left(\frac{qs0(t) + qs1(t)}{2} \right) \qquad \text{(A.63)}$$

For rotor 2 hub:
$$Qcone2(t) := 0.008m^2 \cdot \left(\frac{qs2(t) + qs3(t)}{2} \right) \qquad \text{(A.64)}$$

For the casing around rotor 1:
$$Qring1(t) := 0.015m^2 \cdot \left(\frac{qs0e(t) + qs1e(t)}{2} \right)$$

For the casing around rotor 2:
$$Qring2(t) := 0.014m^2 \cdot \left(\frac{qs2e(t) + qs3e(t)}{2} \right)$$

The total heat transfer is equal to:

$$Qw(t) := Qr1(t) + Qr2(t) + QIGV(t) + Qfront(t) + Qaft(t) + Qcone1(t) + Qcone2(t) + Qring1(t) + Qring2(t) \qquad \text{(A.66)}$$

From there on, we want to compute the correction to provide to the indicated efficiency to find the adiabatic efficiency. This correction is based on the difference between the total enthalpy measured at the outlet of rotor 2 and the total adiabatic enthalpy at this same station. The computation of this difference is based on the assumption on the remarks detailed in section 5.3. So the difference between the 2 enthalpies is equal to the heat exchanged in the compression (The justification of this assumption will be given later):

$$1/\eta_{ad}=1/\eta_{ind}+Q_w*\tau/(h_{o2is}-h_{01}) \qquad \text{(A.67)}$$

Let 'Corr' be the correction term. Than, using the blow-down model:

$Wc := 0.586$ $Pis := 0.4$ $Pic := 1.9 \cdot 1.6$

$Ac := 252.40\,in^2$ $P0 := 30.403\,psi$ $\tau := 1.43$

$$Corr(t) := \frac{\tau \cdot Qw(t)}{\frac{Pis \cdot P0 \cdot \left(1 + \frac{t}{\tau bd}\right)^{\frac{-2\gamma}{\gamma-1}} \cdot Ac \cdot Wc}{\sqrt{Rg \cdot T0 \cdot \left(1 + \frac{t}{\tau bd}\right)^{-2}}} \cdot Cp \cdot Tt0(t) \cdot Pic^{\frac{\gamma-1}{\gamma}}} \qquad \text{(A.68)}$$

$$\eta ad(\eta ind, t) := \frac{1}{\frac{1}{\eta ind} - Corr(t)} \qquad \text{(A.69)}$$

$$Errmes(\eta ind, t) := \eta ad(\eta ind, t) - \eta ind \qquad \text{(A.70)}$$

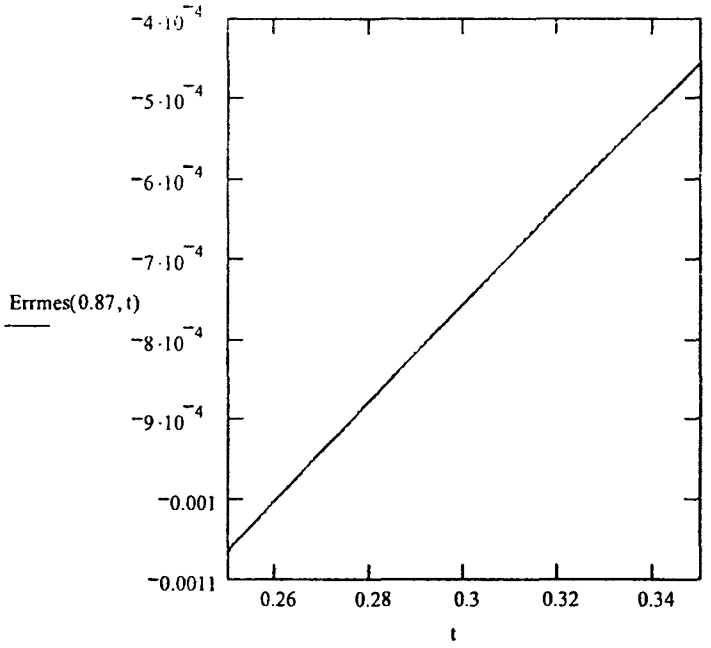


Figure A.18. - Difference Between Adiabatic and Indicated Efficiency Over the Test Time.

9. Appendix B: Detailed calculation of the Total Temperature Probe Errors.

For the upstream rake temperature probes, we can compute the Biot number around the wire to determine the response time of this wire.

For an error of 0.025K due to the recovery error, with a recovery factor in the laminar case equal to the square root of the Prandtl number, we can compute the necessary Mach number in the shield:

- At t = 0s:

$Tt0(0s) = 300K$

$\mu i1 := 1.838 \cdot 10^{-5} \cdot \frac{kg}{m \cdot s}$

$Pri1 := 0.77$

$\gamma i1 := 1.40$

$kgi1 := 1.641 \cdot 10^{-2} \cdot \frac{W}{m \cdot K}$

$$Mvi1 := \sqrt{\frac{0.025K}{\left[\left(1 - \sqrt{Pri1}\right) \cdot T0 - 0.025K\right] \cdot \frac{\gamma i1 - 1}{2}}} \qquad \text{(B.1)}$$

Which yields a Mach number of:

$$Mvi1 = 0.059$$

Let us compute the vent hole area that will give us this Mach number around the thermocouple. We need to account for the compressibility effects in the flow:

$$Ainlet := \pi \cdot \left(\frac{4.4069}{2} \cdot 10^{-3} m\right)^2$$

$Cd := 0.6$

$$Yi1(Aventi1) := 1 - \left[0.41 + 0.35 \cdot \left(\frac{Aventi1}{Ainlet}\right)^2\right] \cdot \frac{1}{\gamma i1} \cdot \left[1 - \left(1 + \frac{\gamma i1 - 1}{2} \cdot M0^2\right)^{\frac{-\gamma i1}{\gamma i1 - 1}}\right] \qquad \text{(B.2)}$$

$$Mvi1 \cdot \sqrt{\gamma i1 \cdot Rg \cdot \frac{Tt0(0s)}{1 + \frac{\gamma i1 - 1}{2} \cdot Mvi1^2}} - Yi1(\lambda) \cdot Cd \cdot \left(1 + \frac{\gamma i1 - 1}{2} \cdot M0^2\right)^{\frac{-1}{\gamma i1 - 1}} \cdot \frac{\lambda}{Ainlet} \cdot M0 \cdot a0(0s) = 0$$

(B.3)

$\lambda i1 := \text{Find}(\lambda)$

$\lambda i1 = 2.923 \times 10^{-6}\, m^2$

$$Dventi1 := \sqrt{\frac{\lambda i1}{\pi}} \cdot 2$$

(B.4)

$$Dventi1 = 1.929 \times 10^{-3}\, m$$

For the single probes, this calculation gives a vent hole size of:

$$Dventisin1 = 2.424 \times 10^{-3}\, m$$

Now, the corresponding heat transfer coefficient and Biot number are:

$$hcprobei1(t,R) := \frac{0.664 \cdot \sqrt{\rho a0(t) \cdot \left(Mvi1 \cdot \sqrt{\gamma i1 \cdot Rg \cdot \frac{Tt0(t)}{1 + \frac{\gamma i1 - 1}{2} \cdot Mvi1^2}}\right) \cdot \frac{2 \cdot R}{\mu i1}} \cdot Pri1^{\frac{1}{3}} \cdot kgi1}{2 \cdot R}$$

(B.5)

$$Bioti1(R,t) := hcprobei1(t,R) \cdot \frac{R}{19.2 \frac{W}{m \cdot K}}$$

(B.6)

$$Bioti1\left(\frac{12.7}{2} \cdot 10^{-6} m, 0s\right) = 9.564 \times 10^{-4}$$

With such a low value of the Biot number, only the first coefficient of the series given the temperature response of the thermocouple is representative of the behavior of the thermocouple. The time response is given by the following calculation:

$x := 0.1$

Given

$$x \cdot J1(x) - Biot1\left(\frac{12.7}{2} \cdot 10^{-6}\,m, 0s\right) \cdot J0(x) = 0 \qquad \text{(B.7)}$$

$xi1 := Find(x)$

$xi1 = 0.044$

$$\frac{2}{xi1} \cdot \frac{J1(xi1)}{(J0(xi1))^2 + (J1(xi1))^2} = 1 \qquad \text{(B.8)}$$

$$ti1 := \frac{-1}{xi1^2} \cdot \ln(0.01) \cdot \frac{\left[\frac{\left(12.7 \cdot 10^{-6}\,m\right)}{2}\right]^2}{\frac{19.2\frac{W}{m \cdot K}}{8730\frac{kg}{m^3} \cdot 448\frac{J}{kgK}}}$$

$ti1 = 0.02s$

Let us do the computation of the time-response for the bead, which has the shape of a sphere with a diameter of 3*0.0005 in. From [7], we can use the following equations:

$$x \cdot \cos(x) + \left(\text{Bioti1}\left(\frac{2 \cdot 12.7}{2} \cdot 10^{-6}\text{m}, 0\text{s} \right) - 1 \right) \cdot \sin(x) = 0 \tag{B.9}$$

$xib1 := \text{Find}(x)$

$xib1 = 0.064$

$$2 \cdot \frac{\sin(xib1) - xib1 \cdot \cos(xib1)}{xib1 - \sin(xib1) \cdot \cos(xib1)} = 1 \tag{B.10}$$

$$tib1 := \frac{-1}{xib1^2} \cdot \ln(0.01) \cdot \frac{\left[\frac{\left(2 \cdot 12.7 \cdot 10^{-6} \cdot \text{m} \right)}{2} \right]^2}{\frac{19.2 \cdot \frac{\text{W}}{\text{m} \cdot \text{K}}}{8730 \cdot \frac{\text{kg}}{\text{m}^3} \cdot 448 \cdot \frac{\text{J}}{\text{kg} \cdot \text{K}}}}$$

$tib1 = 0.037\text{s}$

This process can be repeated for t = 0.250 s and t = 0.500 s. The results are:

Time (s)	Casing Mach Number	Wire Response Time (s)	Bead Response Time(s)
0.250	0.058	0.03	0.057
0.500	0.059	0.045	0.084

Table B.1. – Casing Mach Number, Wire and Bead Response Times for the Upstream Probes at t = 250 ms and t = 500 ms.

Similarly, for the downstream rake probes, a similar calculation gives a vent hole size of:

$$Dventel = 1.502 \times 10^{-3} m$$

As for the Mach number in the head casing and the response times:

Time (s)	Casing Mach number	Wire response time (s)	Bead response time(s)
0.000	0.03	0.012	0.023
0.250	0.03	0.019	0.036
0.500	0.03	0.028	0.053

Table B.2. - Casing Mach Number, Wire and Bead Response Times for the Downstream Probes at t = 250 ms and t = 500 ms.

The downstream single probes must have a vent hole size of:

$$Dventesinl = 1.878 \times 10^{-3} m$$

Let us focus in the conduction error for the upstream probes:

The characteristic spatial frequency of the phenomenon is equal to:

$$mi(t,R) := \sqrt{\frac{hcprobei3(t,R)\cdot 2\cdot \pi \cdot R}{19.2\frac{W}{m\cdot K}\cdot \pi \cdot R^2}} \qquad \text{(B.11)}$$

For the 3/16 probes, the conduction error is equal to:

L0 := 0.135in

$$\frac{2\cdot \sinh\left(\frac{mi\left(0.5s, 12.7\cdot \frac{10^{-6}}{2}\cdot m\right)\cdot L0}{2}\right)\cdot (T0 - Tt0(0.5s))}{\sinh\left(mi\left(0.5\cdot s, 12.7\cdot \frac{10^{-6}}{2}\cdot m\right)\cdot L0\right)} = 0.073K$$

For the 1/4 probes, the conduction error is equal to:

L14 := .180in

$$\frac{2\cdot \sinh\left(\frac{mi\left(0.5s, 12.7\cdot \frac{10^{-6}}{2}\cdot m\right)\cdot L14}{2}\right)\cdot (T0 - Tt0(0.5s))}{\sinh\left(mi\left(0.5\cdot s, 12.7\cdot \frac{10^{-6}}{2}\cdot m\right)\cdot L14\right)} = 5.27\times 10^{-3}K$$

As for the conduction error of the downstream probes:

$$me(t,R) := \sqrt{\frac{hcprobee3(t,R)\cdot 2\cdot \pi \cdot R}{19.2\frac{W}{m\cdot K}\cdot \pi \cdot R^2}} \qquad \text{(B.12)}$$

For the 3/16 probes:

$$\frac{2\cdot \sinh\left(\frac{me\left(0.5s, 12.7\cdot \frac{10^{-6}}{2}\cdot m\right)\cdot L0}{2}\right)\cdot \tau\cdot (T0 - Tt0(0.5s))}{\sinh\left(me\left(0.5\cdot s, 12.7\cdot \frac{10^{-6}}{2}\cdot m\right)\cdot L0\right)} = 0.014K$$

For the ¼ probes:

$$\frac{2\cdot\sinh\left(\frac{me\left(0.5s,12.7\cdot\frac{10^{-6}}{2}\cdot m\right)\cdot L14}{2}\right)\cdot\tau\cdot(T0-Tt0(0.5s))}{\sinh\left(me\left(0.5\cdot s,12.7\cdot\frac{10^{-6}}{2}\cdot m\right)\cdot L14\right)}=4.979\times 10^{-4}K$$

Last concern is the radiation error:

Upstream, we compute that:

$$\sigma := 5.67\cdot 10^{-8}\frac{W}{m^2K^4}$$

$\varepsilon m := 0.4$

$$Eradi(t,R) := \frac{\sigma\cdot\varepsilon m\cdot\left(Tt0(t)^4-T0^4\right)}{hcprobei3(t,R)} \qquad \text{(B.13)}$$

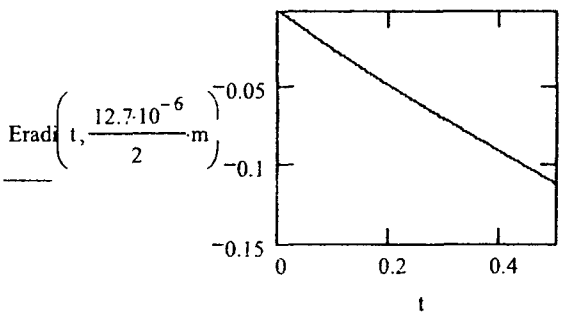


Figure B.1. – Radiation Error Evolution for the Upstream Probes, Over 1s.

Downstream:

$$\text{Erade}(t, R) := \frac{\sigma \cdot \varepsilon m \cdot \tau^4 \cdot \left(Tt0(t)^4 - T0^4\right)}{\text{hcprobee3}(t, R)} \tag{B.14}$$

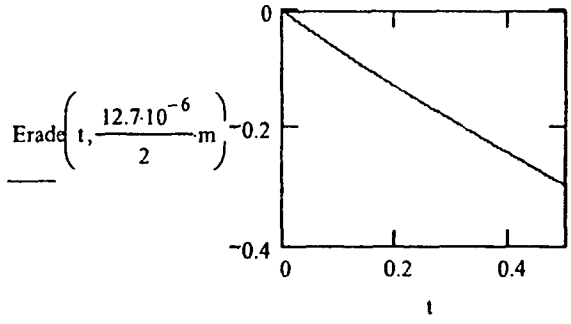


Figure B.2. - Radiation Error Evolution for the Downstream Probes, Over 1s.

10. Appendix C: Total Temperature Probes Drawings

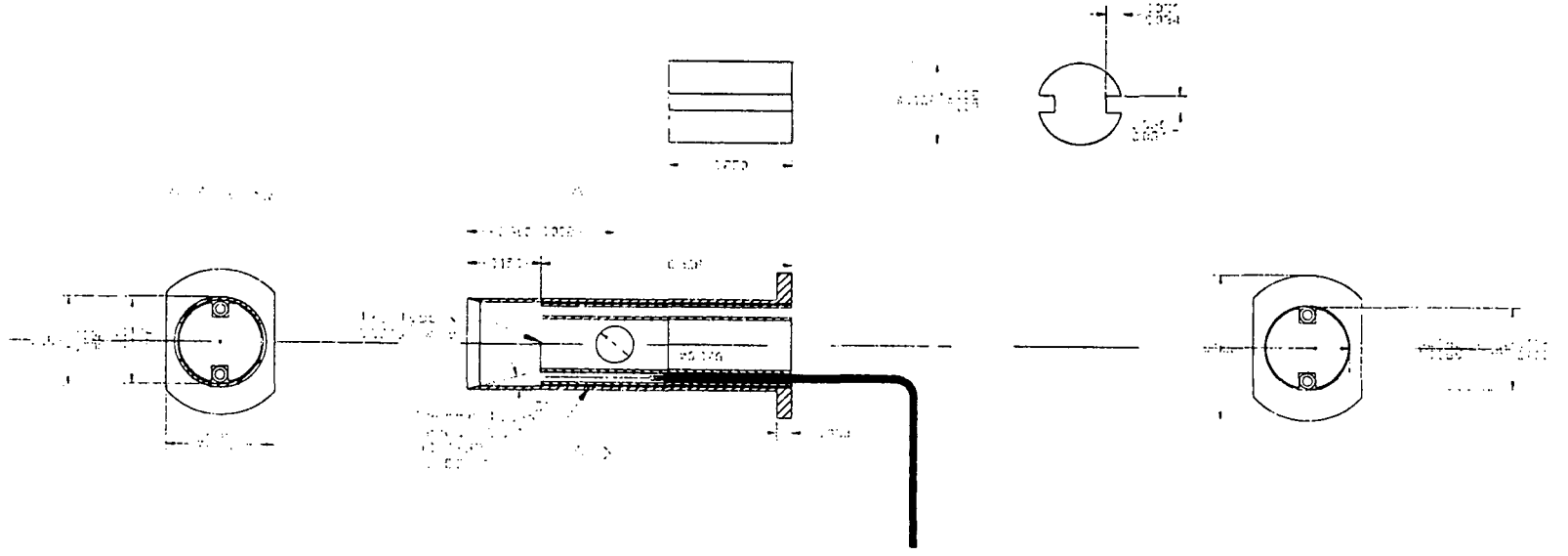


Figure C.1. – Upstream Rake Total Temperature Measurement Head.

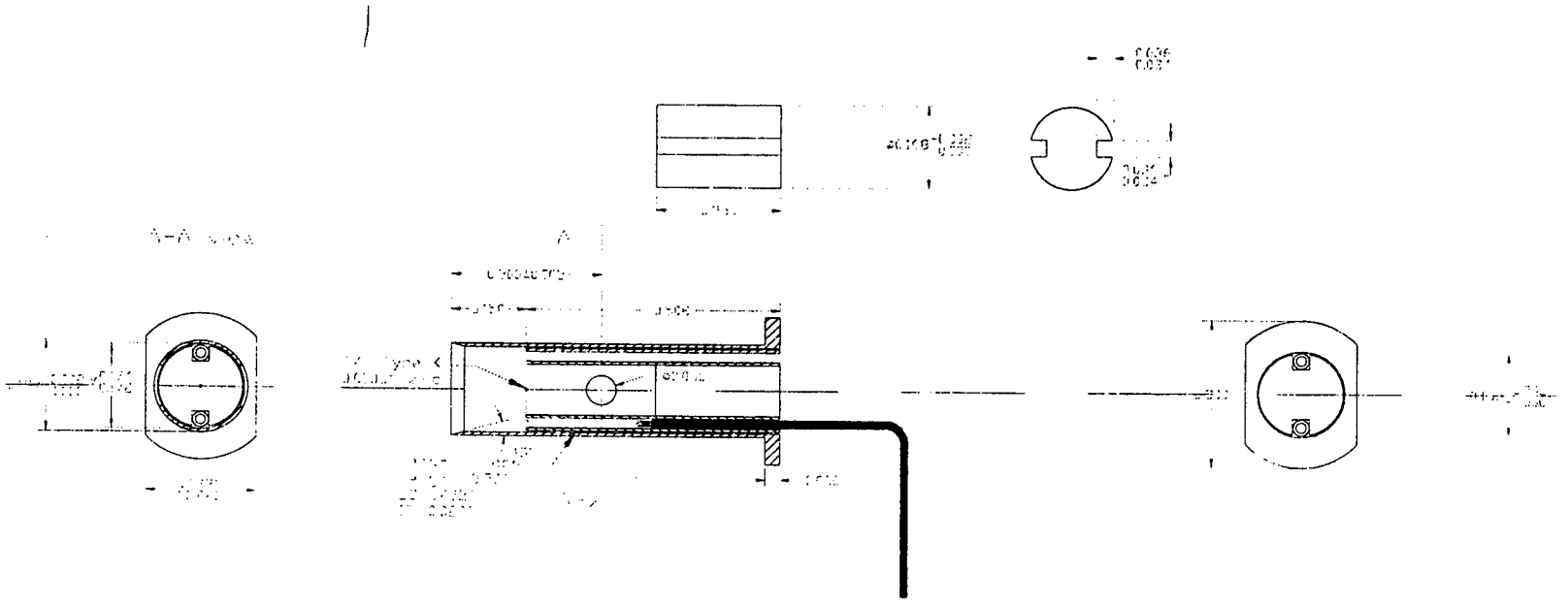


Figure C.2. – Downstream Rake Total Temperature Measurement Head.

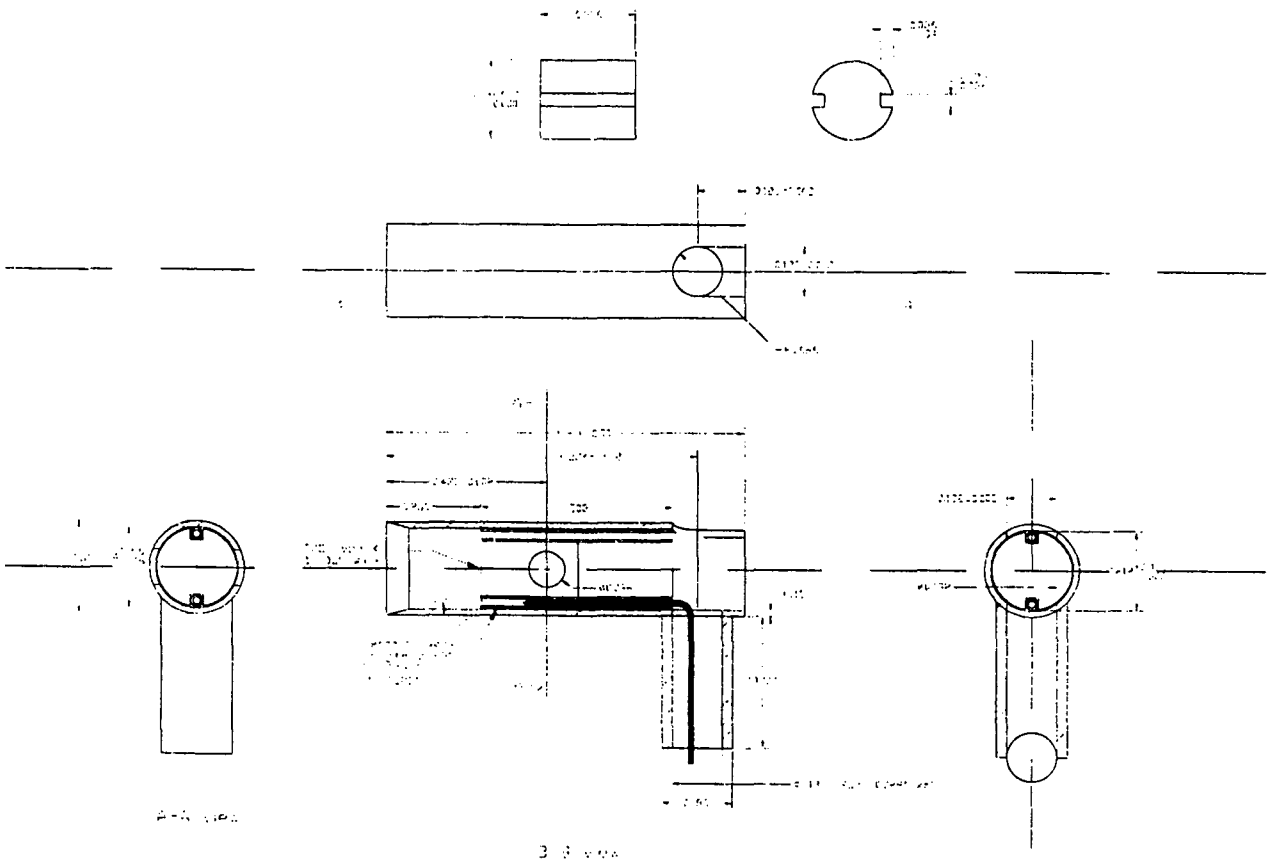


Figure C.3. – Upstream Total Temperature Measurement Probe.

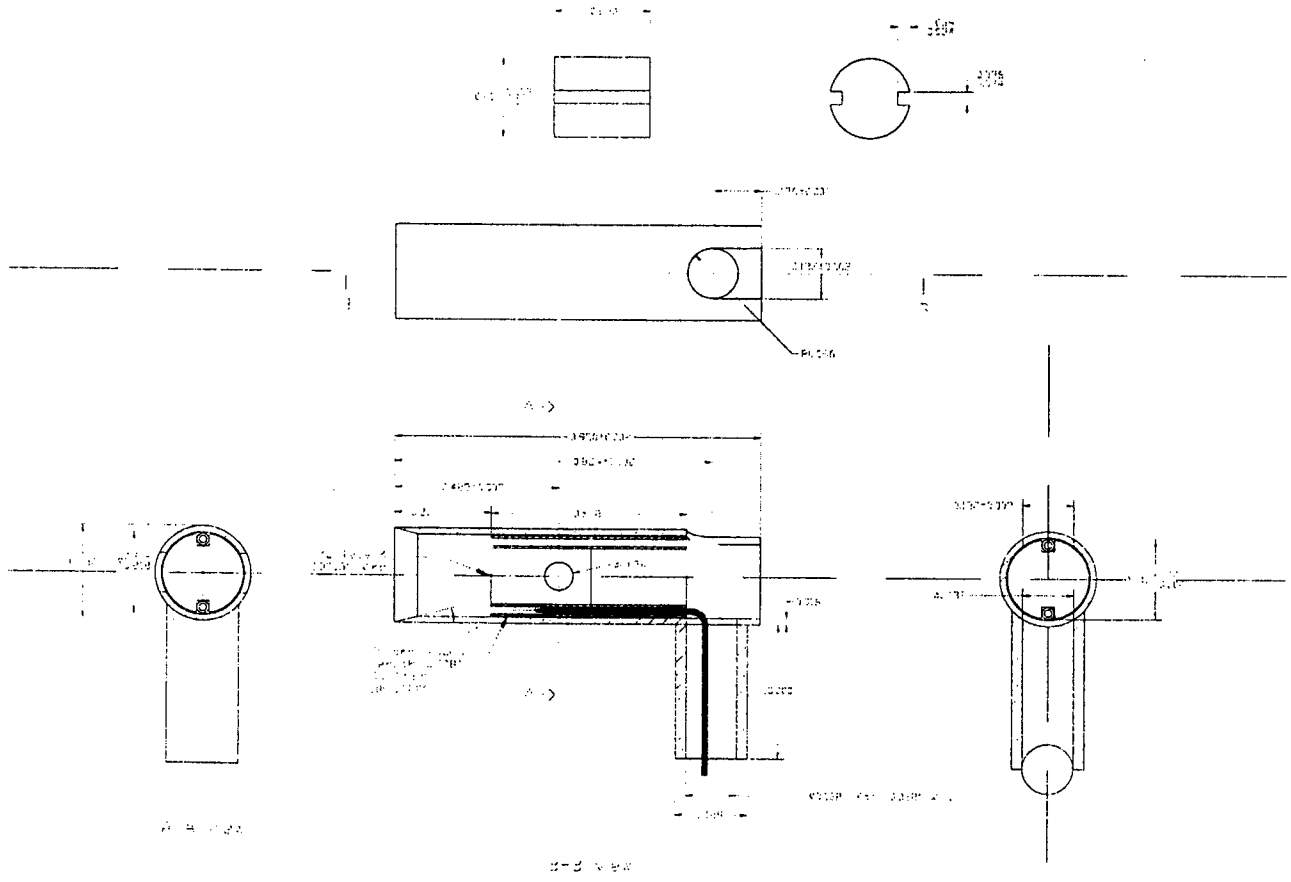


Figure C.4. - Downstream Total Temperature Measurement Probe.

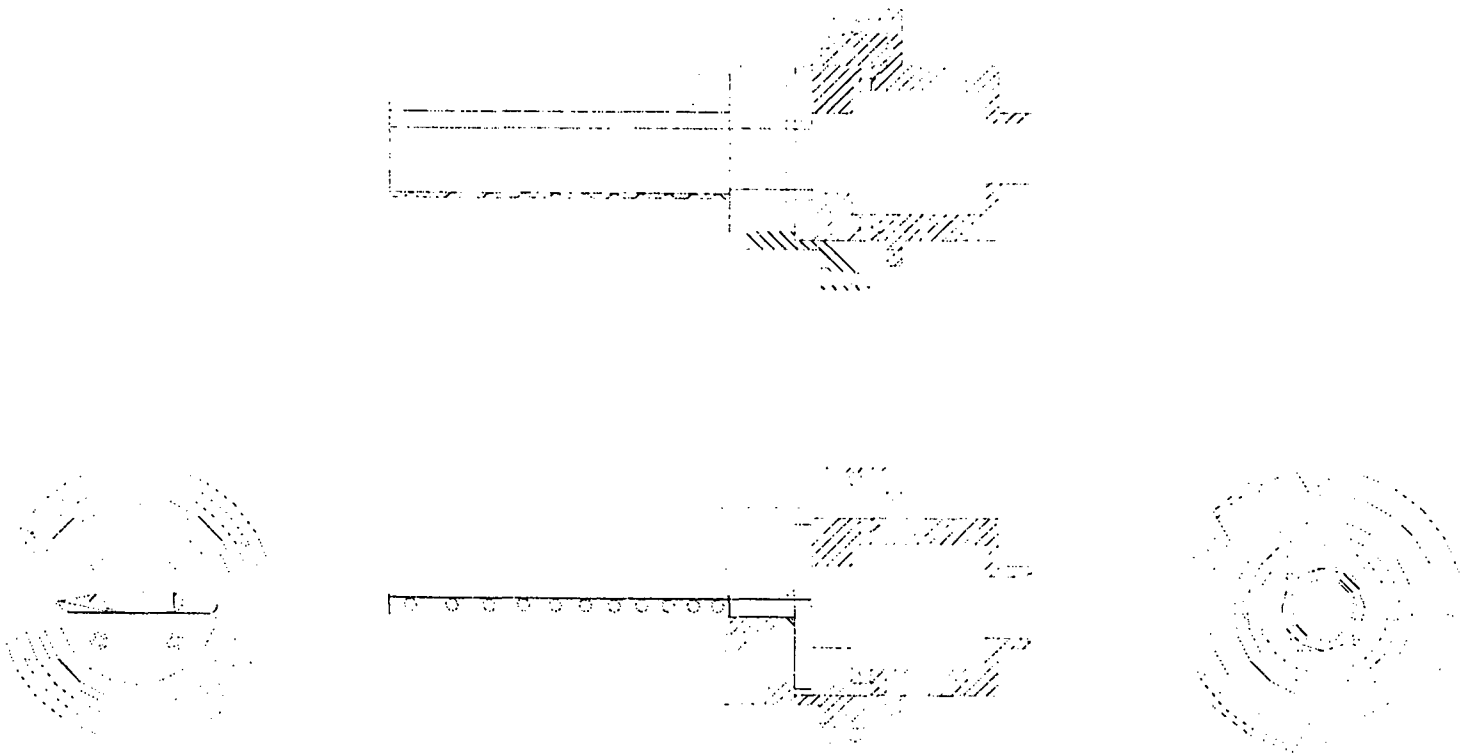


Figure C.5. – Upstream Total Temperature Measurement Rake Assembly.

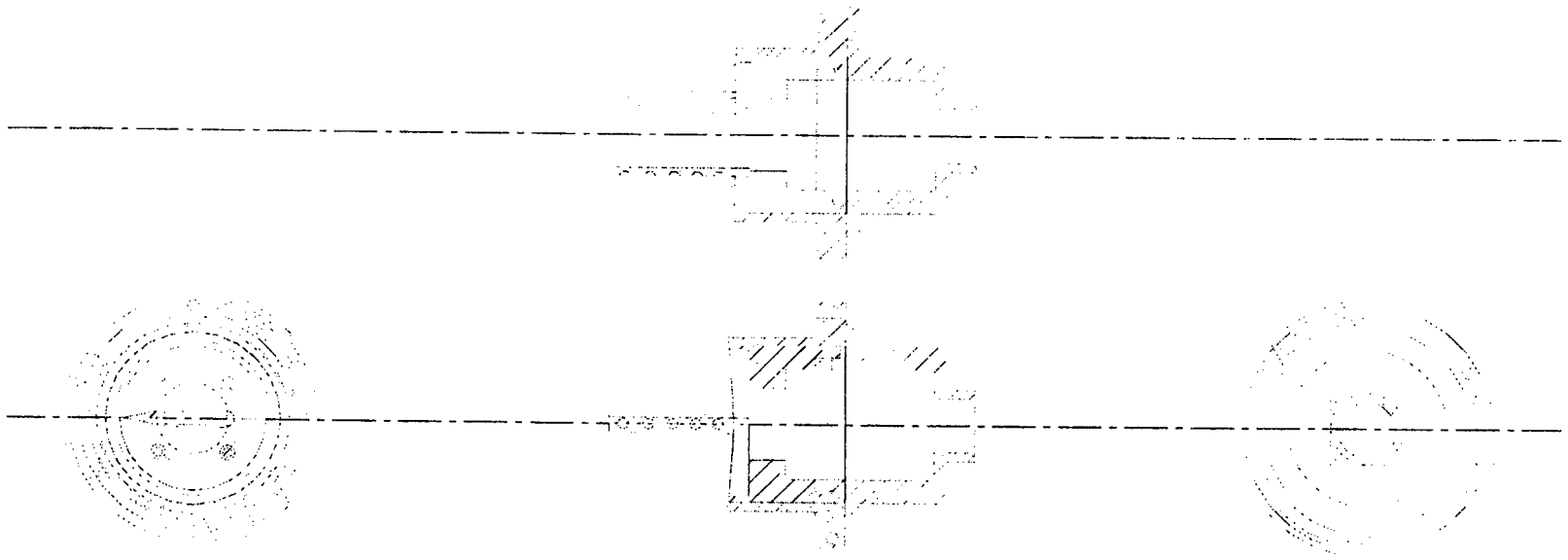


Figure C.6. – Downstream Total Temperature Measurement Rake Assembly (5 Head Model).

11. Appendix D: Total Pressure Probes Drawings

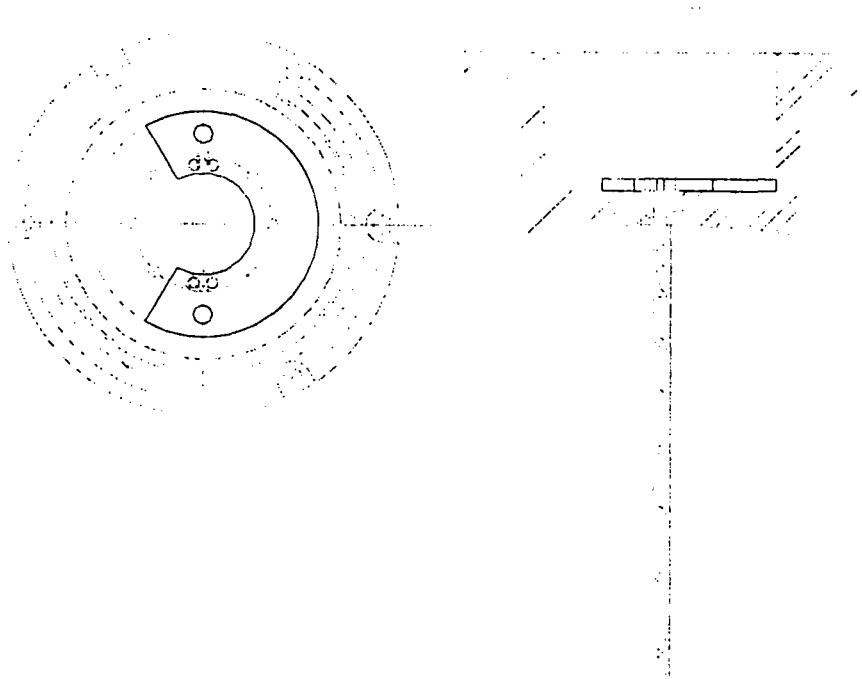


Figure D.1. – Upstream Total Pressure Measurement Rake Assembly.

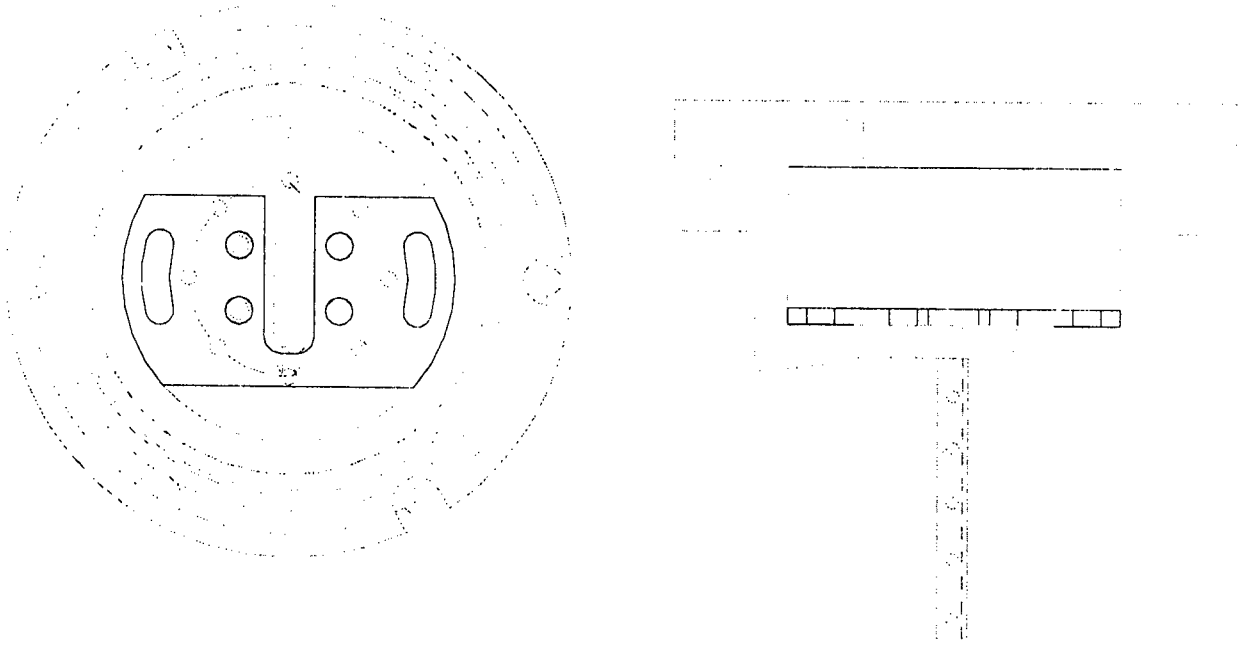


Figure D.2. – Downstream Total Pressure Measurement Rake Assembly.

12. Appendix E: Detailed Type-K Thermocouple Manufacturing Description

List of hardware components:

- Head casing (according to prints)
- Stainless steel spacer (according to prints)
- Type-K unsheathed fine gage thermocouples (0.0005" wire dia - Omega CHAL-0005)
- Thermocouple insulators (1/32" OD - .020" ID – Omega ORX-020132)
- Thermocouple insulated wires (0.010" wire dia – Omega TFCY-010 (Chromel) & TFAL-010 (Alumel))
- Thermocouple wires, duplex insulated (Omega TT-K-20).
- Multipin design thermocouple connectors (Female flanged Omega MTC-24-FF)
- Thermocouple contact pins (Chromel MTC-CH-P and Alumel MTC-AL-P).
- ½"-thick Teflon pieces
- ½"-thick aluminum piece
- 3"x3"x¼" cork pads

Chemical and soldering materials:

- Epoxy Eccobond 104 and Eccobond 45 LV
- Solder (HMP alloy – Type 366 Flux from Vishay Micro Measurements)
- All Purpose Flux LA-CO N-3
- M-Line Rosine Solvent (from Vishay Micro Measurements)
- M-Line AR Activated Rosin Soldering Flux (from Vishay Micro Measurements)
- Acetone

1st Step: Assembling the thermocouple insulators to the stainless steel spacer:

1. In the ½"-thick Teflon pieces, drill clearance holes for the stainless steel spacers. (0.177" for 3/16-probes and 0.211" for ¼ probes)
2. Using a diamond file, cut 0.510" long pieces of thermocouple insulators.
3. Drill a clearance hole for these ceramic tubes in the ½"-thick piece of aluminum.
4. Insert the ceramic piece in the clearance hole and grind both ends against sandpaper, to give clean and square edges to the tubes. The aluminum piece acts

as a holder and guarantees that the tubes will be brought down to the correct length.

5. Using the Teflon pad as a jig, epoxy the ceramic tubes with Eccobond 104 in the grooves of the stainless steel spacer. The ceramic tube edges must be flush with one end of the aluminum piece.
6. Cure it for 3 hours at 300 degrees F.
7. Gently remove the assembled spacers from the jig using a small arbor press. Shocks may damage the ceramic tubes in that process.
8. Under the microscope, check that the ceramic tubes are parallel. Scrape away the excess of epoxy, using a diamond file. Check the OD of the spacer against the ID of the head casing.

2nd Step: Mounting the thermocouple gage on the spacer:

1. Tape down the spacer on a stainless steel holder. Put a piece of 0.010" alumel wire through one ceramic tube and a piece of 0.010" chromel wire through the other ceramic tube. Strip them back 0.125", making sure the insulation does not ball up and allows the wire to move through the ceramic tubes without constraints. The wires should be 10" long for 3/16 probes and 24" long for ¼ probes.
2. Remove the gage from the package. Move the red and yellow dots to about 2" from the gage junction. Remove the white dot using acetone.
3. Tack the gage red wire and yellow wire gage to the 0.010" wires mounted on the spacers, using All Purpose Flux LA-CO N-3 and multicore 570-28R solder.
4. Turn the small gage wire at least four times around the large wire and solder, using again All Purpose Flux LA-CO N-3 and multicore 570-28R solder.
5. Put small droplets of Eccobond 104. Gently draw the wires in so as straighten the gage wire and center the junction between the ceramic tubes.
6. Tape down the 0.010" wires to stress relieve the gage and prevent it from moving during the curing period.
7. Cure the assembly for 3 hours at 300 degrees F.

8. Let the assembly cool down and check the continuity between the 2 wires. Add epoxy and cure again to cover any contacts between the edge of the ceramic tube and the gage (Figure E.1).

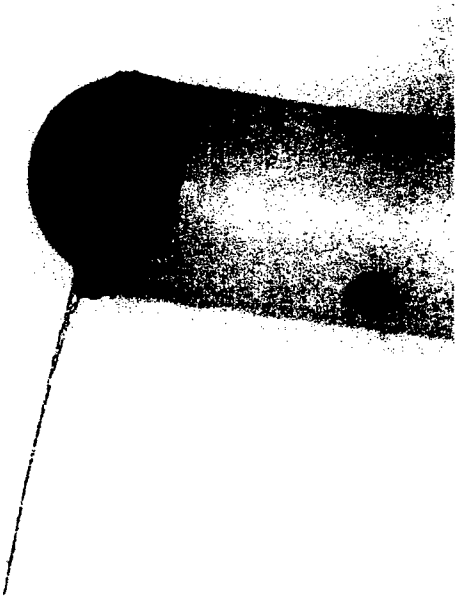


Figure E.1. – Close-Up View of the Thermocouple Gage Wire Epoxied to the Ceramic Stem.

3rd Step: Mounting the thermocouple insert on the head casing:

For 3/16" probes:

1. Drill a clearance hole for the 3/16" heads in the cork pad. Insert the head casing until the flange meets the cork. This piece serves as a holder in the process.
2. Coat the thermocouple spacer with Eccobond 104 epoxy and insert it into the head. Make sure the rear of the spacer is flush with the rear face of the head. Turn the insert inside the head so that the gage wire is perpendicular to the vent hole axis.
3. Tape down the wires to prevent the insert from moving during the curing process.
4. Cure for 3 hours at 300 degrees F.
5. Let the assembly cool down. Check the continuity. Put the TC head in a small graduated cylinder with acetone for one hour, to clean the gage. Check the result under the microscope.

For ¼" probes:

1. Measure 10.250" from the spacer rear side and strip the wire insulation over 0.250". Put Eccobond 104 epoxy and slide ½" ceramic tubes over the exposed wire.
2. Coat the thermocouple spacer with epoxy 104 and put into the head. The rear face must be flush with the inside of the stem piece and the gage must be perpendicular to the vent hole axis. Tape the wires down around the exterior of the stem tube. Cure for 3 hours at 300 degreed F.
3. Let the probe cool. Then run the wires down the stem, one at a time, and make sure they are not stressed by leaving a small loop behind the spacer face.
4. Using a syringe, fill the stem with Eccobond from the bottom end to seal the probe. Cure for 3 hours and add epoxy as needed.

4th Step: Building the leak-proof connectors for the rakes:

1. Remove the rubber part from the side that will accommodate the thermocouple wires on the thermocouple connector. Remove 3/16" of metal from the casing on the lathe and take of the paint from the inside area.
2. Cut 1 ¼" pieces of TT-K-20 wires. Strip back 3/16" of insulation on both ends and crimp them to the appropriate pins. Insert the pin on the connector according to a predetermined pattern.
3. Fill a plastic syringe with Eccobond 45LV epoxy and inject epoxy between the mounted pins, under the microscope. Once the bottom of the connector is covered, place the connector in a vacuum pump to degas the epoxy. This will cause the epoxy to bubble and overflow from the connector. To minimize the loss of epoxy and keep the connector as clean as possible, form a small chimney around the connector using aluminum foil. Cover also each wire with a transparent plastic tube. Repeat this process 4 consecutive times until the level of epoxy reaches the metallic edge of the connector. Remove the transparent tubes from the wires and cure the connector for 45 minutes at 200 degrees F.

4. Put vacuum seal around the O-ring of the connector and place it on the connector. Hook it to a vacuum pump, pull vacuum on the wire side of the connector and register the pressure variation overnight.

5th Step: Mounting the 3/16 probes on the rakes:

1. Insert the heads on the rake and put 2 drops of Eccobond 104 on the side of the flange that will be in contact with the rake. Tape down the wires to the trailing edge of the airfoil and cure for 3 hours at 300 degrees F.
2. File the flange and the excess of epoxy off the cover groove, so as to allow that cover to slide in smoothly. Check the continuity of each probe.
3. To remove a broken head, scrape away the epoxy, with a diamond file, as much as possible. Finish removing with a hammer. It is crucial to remove as much epoxy as possible so as to avoid hammering the rake too strongly. The shocks caused by the hammer can break the neighboring gages. Repeat the process to insert a new head.
4. Label each thermocouple wire and lace them together for easier and safer handling (Figure E.2)
5. Close the airfoil and screw it to the front canister piece. Pass the wires through the aft canister piece.
6. Cut ½"-long pieces of shrink tubes and place them over each wire. Strip back the wires' ends over 1/8". Using multicore 570-28R and M-Line AR Activated Rosin Soldering Flux, solder these ends to the cables on the connector cables, according to the laying pattern. For easier handling, bend the TT-K-20 wires to space their extremities. Clean with M-Line Rosine Solvent. Cover the soldered area with the shrink tubes and shrink them with the heat gun. Close the entire assembly.



Figure E.2. – View of the Thermocouple Extension Cables Laced Together in the Rake Airfoil Cavity.

References and Bibliography

[1] Kerrebrock Jack L.. *The Prospects for Aspirated Compressors.* MIT – AIAA-2000-2472. 2000

[2] Parker David V.. *Design and Operation of a Counter-Rotating Aspirated Compressor Blow-Down Test Facility.* Master's thesis, Massachusetts Institute Technology, 2005.

[3] Cai Yi. *Aerodynamic Performance Measurements in A Fully Scaled Turbine.* Master's thesis, Massachusetts Institute Technology, 1998.

[4] American Society for testing and Materials, 1916 Race Street, Philadelphia, PA 19103. *Manual on the Use of Thermocouple in a Temperature Measurements.* 1970.

[5] Cattafesta L.N.. *An Experimental Investigation of the Effects of Inlet Radial Temperature Profiles on the Aerodynamic Performance of a Transonic Turbine Stage.* Master's thesis, Massachusetts Institute Technology, 1988.

[6] Whitman, Gayne. *The Effects of the Reynolds and Mach Number on the Recovery Factor of Cylindrical Thermocouples Immersed in a Rapidly Moving Air Stream.* Master's thesis, Massachusetts Institute of Technology, 1950.

[7] Mills A.F. *Heat and Mass Transfer.* Ed. Irwin, 1995.

[8] http://www.hartscientific.com/products/bathfluid.htm

[9] DeWitt D.P. Incropera F.P. *Fundamentals of Heat and Mass Transfer.* Wiley and Sons, Inc, second edition, 1985.

[10] Russell Walter R. Gracey William, Letko William. *Wind tunnel investigation of a number of total pressure tubes at high angles of attack.* Technical Report, 2331, National Advisory Committee for Aeronautics, 1951.

[11] Pankhurst R.C. Ower E. *The Measurement of Air Flow.* Pergamon Press, fifth edition, 1977.

[12] Coleman H.W. *Experimentation and Uncertainty Analysis for Engineers.* Wiley, 1999.

[13] http://www.unitedsensorcorp.com/kiel.html

[14] http://www.unitedsensorcorp.com/pitot.html

[15] http://www.omega.com/Temperature/pdf/TRCIII.pdf

[16] Merchant Ali. *Aerodynamic Design and Performance of Aspirated Airfoils.* Proceedings of Turbo Expo 2002, 2002.

[17] Merchant Ali. *MAFC Aero Design.* Massachusetts Institute of Technology. 2004.

[18] http://sine.ni.com/nips/cds/view/p/lang/en/nid/1055

[19] http://sine.ni.com/nips/cds/view/p/lang/en/nid/13677

[20] http://sine.ni.com/nips/cds/view/p/lang/en/nid/12785

[21] White F.M. *Fluid Mechanics.* McGraw-Hill Series in Mechanical Engincering, 1999.

[22] Carslaw H.S. and Jaeger J.C. *Conduction of Heat in Solids.* Oxford University Press, 1986.